Short-lived radioactive isotopes from massive single and binary stellar winds

PhD Thesis

Hannah Elisabeth Brinkman

Konkoly Observatory,

ELKH CSFK, Research Centre for Astronomy and Earth Sciences

Konkoly Thege Miklos ut 15-17, H-1121 Budapest, Hungary

and

Doctoral School of Physics, University of Szeged, Dom tér 9, Szeged, 6720 Hungary

Supervisor: Dr. Maria Lugaro

Konkoly Observatory,

ELKH CSFK, Research Centre for Astronomy and Earth Sciences

Konkoly Thege Miklos ut 15-17, H-1121 Budapest, Hungary

ELTE Eötvös Loránd University, Institute of Physics, Budapest 1117,

Pázmány Péter sétány 1/A, Hungary

Monash Center for Astrophysics, Monash University, VIC3800, Australia

Advisor: Dr. József Vinkó

Department of Optics and Quantum Electronics, University of Szeged,

Dom tér 9, Szeged, 6720 Hungary

Doctoral School of Physics, Department of Optics and Quantum Electronics, Faculty of Science and Informatics,

University of Szeged, Hungary

April 2022

Abstract

During their lives and deaths stars turn the lightest elements, hydrogen and helium, into heavier elements, such as carbon and oxygen, the building blocks of life. Many stars have lived and died since the beginning of the Universe, and their nuclear burning products have been ejected into the interstellar medium and incorporated into new generations stars. Eventually, this process led to the formation of the Sun and the Solar System. To understand where the isotopes that formed the Sun and the Solar System come from, here I study a special group of isotopes; short-lived radio-active isotopes. These are radioactive isotopes with half-lives up to a few Myr, which makes them short-lived compared to the Galaxy and the lifetimes of most stars. Because of their relative short half-lives compared to the age of the Universe and their production in specific processes, these short-lived radioactive isotopes can point us to the sources that polluted the early Solar System. They can provide us information about the environment and circumstances of the birth of the Sun, as they represent the fingerprint of the local nucleosynthesis that occurred nearby at the time and place of the birth of the Sun. Their presence and abundances in the early Solar System have been inferred from meteoretic data reporting excesses in their daughter nuclei. In this work I study four short-lived radioactive isotopes, and specifically the heating source ^{26}Al with a half life of 0.72 Myr. The other three short-lived radioactive isotopes considered are ^{36}Cl, ^{41}Ca, and ^{60}Fe.

The four short-lived radioactive isotopes are all produced in massive stars and they can be expelled into the interstellar medium by the stellar winds, by mass-transfer between the components of massive binary systems, and by the final explosions of such stars. Massive stars are one of the main contributors to the conversion of elements and the production of these isotopes, because they undergo all burning phases until their cores become made of iron-group elements. At this point, fusion does not generate any more energy to counter the gravitational collapse of the core. The core then contracts further until it turns into a neutron star. The material outside of the core falls onto the neutron star and bounces back, which is observed as the supernova explosion. If enough material is accreted onto the neutron star, it will turn into a black hole instead of a neutron star. In some other cases, the star will directly turn into a black hole. The outcome of the evolution depends therefore on the initial mass of the star. My work focuses on the production of ^{26}Al in massive binaries, and then on the production of ^{26}Al, ^{36}Cl, ^{41}Ca, and ^{60}Fe in massive rotating and non-rotating single stars, and the resulting wind yields. I do not consider the contribution of the supernovae. I also consider the wind yields of the stable isotopes that are part of the CNO-cycle, as well as ^{19}F and ^{22}Ne, for which the astrophysical sources are still uncertain.

For this work, I use the MESA stellar evolution code with a nuclear network of 63 isotopes for the first part of my research, and of 209 isotopes for the second part, to compute massive (10-80 $M_\odot$), rotating (with initial velocities of 150 and 300 km/s) and non-rotating single stars at solar metallicity (Z=0.014), as well as non-rotating binary stars with initial masses 10-50 $M_\odot$. First, the models are evolved up to the onset of carbon burning to study only ^{26}Al. Then I compute a second set of models to study the four short-lived radioactive isotopes and the stable isotopes, which are evolved to the onset of core collapse.

In Chapter 1, I introduce the short-lived radioactive isotopes, and give an overview of the theory relevant for this thesis. In Chapter 2, I describe the method. In Chapter 3, I present the results of the stellar evolution of the different sets of models, and compared them to studies from the literature. In Chapter 4, I present the wind yields for the various

isotopes, discuss the trends in their yields, and again compare them to studies from the literature. In Chapter 5, I discuss the impact of the binary wind yields on the overall galactic budget of ^{26}Al, and how massive stars might be the source of ^{26}Al, ^{41}Ca, and ^{36}Cl in the early Solar System. In Chapter 6, I discuss various uncertainties connected to binary evolution, as well as uncertainties connected to the reaction rates involved in the production and destruction of the short-lived radioactive isotopes. I also present the first results of binaries evolved up to the onset of core-collapse. In Chapter 7, I end with the summary and conclusions, as well as a list of future work. In Chapter 8 the summary and conclusions are given in Hungarian.

Contents

Abstract **I**

List of Figures **V**

List of Tables **VII**

1 Introduction **1**

1.1 Short-lived radioactive isotopes: characteristics and nucleosynthesis 1

1.2 Stellar evolution of single stars and nucleosynthesis 5

1.2.1 Main nuclear burning cycles and their nucleosynthesis 9

1.2.2 Mass loss and stellar winds 16

1.2.3 Internal mixing 20

1.2.4 Rotation 23

1.3 Binary evolution 26

1.4 Aim and overview of the thesis 32

2 Method **33**

2.1 Input physics for Sets 1 and 2 34

2.2 Treatment of binary interactions in Set 2 36

2.2.1 The semi-numerical binary analytic scheme 36

2.2.2 The numerical binary input physics 39

2.3 Input physics for Set 3 40

2.3.1 Input physics for the evolution up to the core-collapse 40

2.3.2 Input physics for rotation 41

2.4 Yield calculations 42

3 Stellar structure and evolution: results and discussion **44**

3.1 Single and binary evolution for a 20 $M_\odot$ star to the onset of carbon burning . . . 44

3.1.1 Single star 45

3.1.2 Detailed description of selected numerical binaries 46

3.2 Single and binary evolution for a 50 $M_\odot$ star to the onset of carbon burning . . . 50

3.2.1 Single star 51

3.2.2 Detailed description of selected numerical binaries 51

3.3 Stellar evolution for single star and binaries up to carbon burning 54

3.4 Stellar evolution up to the core-collapse with rotation 60

3.4.1 Comparison to other data sets 63

4 Stellar yields: results and discussion **66**

4.1 Yields from single and binary stars to the onset of carbon burning 66
4.1.1 20 $M_\odot$ 67
4.1.2 50 $M_\odot$ 69
4.1.3 Other primary masses 70
4.2 Yields from single, rotating stars up to the core collapse 73
4.2.1 The short-lived radioactive isotopes 73
4.2.2 Stable isotopes 77
4.2.3 Comparison to other studies 80
4.2.4 Stable isotopes of the CNO-cycle 81

5 Implications for the galactic ^{26}Al abundance and for the early Solar System 90
5.1 Implications of binary yields for the galactic abundance of ^{26}Al 90
5.1.1 Impact of binary yields for the early Solar System 93
5.2 Implications of the wind yields for the early Solar System 94
5.2.1 Calculation of dilution factor and the delay time 95
5.2.2 Results and comparison to other studies 98
5.2.3 Oxygen isotopic ratios 100

6 Discussion 102
6.1 Uncertainties in binary evolution 102
6.1.1 The effect of the secondary and reverse mass-transfer 102
6.1.2 Mass-transfer efficiency 103
6.1.3 The influence of the mass ratio 104
6.2 Effects of the uncertainties in reaction rates 105
6.2.1 Aluminium-26 105
6.2.2 Chlorine-36 and calcium-41 109
6.2.3 Chromium-53,54 and titanium-49,50 110
6.3 Yields from non-rotating binary stars up till core collapse 114
6.3.1 Short-lived radioactive isotopes 115
6.3.2 Stable isotopes ^{19}F and ^{22}Ne 117

7 Summary, conclusions, and future work 125
7.1 Summary and conclusions 125
7.2 Future work 128

8 Összefoglalás, következtetések és további tervek 131
8.1 Összefoglalás és következtetések 131
8.2 További tervek 134

Publications 136

Acknowledgments 137

References 139

List of Figures

1.1 Modified sections from the nuclide chart for ^{26}Al, ^{36}Cl, ^{41}Ca, and ^{60}Fe. . . 4
1.2 Annotated Kippenhahn diagram for a 20M$_\odot$ star 11
1.3 The ρ_cT$_c$ diagram for the 20 M$_\odot$, non-rotating, single star. 12
1.4 The HRD for the 20 M$_\odot$, non-rotating, single star. 12
1.5 The AlMg-cycle 14
1.6 The three pp-chain branches. 14
1.7 The four CNO cycles 15
1.8 Evolutionary stages for a 60 M$_\odot$ star 20
1.9 HRD for three 50 M$_\odot$ stars at different rotational velocities 25
1.10 Nitrogen-14 surface mass-fraction for a 20 M$_\odot$ and 50 M$_\odot$ star at different rotational velocities 26
1.11 Schematic figure of the Roche potential of a binary 29

2.1 Principle of the semi-numerical binary scheme. 37

3.1 HRDs and KHDs for 20 M$_\odot$ single and binary stars 47
3.2 HRDs and KHDs for 50 M$_\odot$ single and binary stars 52
3.3 Hydrogen and helium burning lifetimes for Set 1 and selected binary systems of Set 2 56
3.4 Size of the helium core for Set 1 and selected systems of Set 2 57
3.5 Total mass loss for Set 1 and selected binary systems of Set 2 57
3.6 Hydrogen and helium burning lifetimes for Set 3 61
3.7 Stellar mass and core mass at the end of the main sequence 62
3.8 Mass loss for central hydrogen, helium, and carbon burning 63

4.1 ^{26}Al yields for a 20 M$_\odot$ star and a 50 M$_\odot$ star and their associated binary yields. 67
4.2 ^{26}Al wind yields for single, non-rotating single stars 71
4.3 ^{26}Al wind yields for non-rotating single and binary stars 72
4.4 ^{26}Al yields for single (non-) rotating massive stars 74
4.5 ^{36}Cl and ^{41}Ca yields for single (non-) rotating massive stars 75
4.6 KHDs for a 30 and 50 M$_\odot$ star with the ^{41}Ca mass-fraction on the colour-scale 76
4.7 ^{60}Fe yields for single (non-) rotating massive stars 77
4.8 Production chains for ^{19}F during He-burning. 78

4.9 KHDs for a 20$M_\odot$ star, non-rotating (a) and rotating (b), with the ^{19}F mass-fraction on the colour-scale 78
4.10 ^{19}F yields for single (non-) rotating massive stars 79
4.11 ^{22}Ne yields for single (non-) rotating massive stars 80
4.12 ^{12}C and ^{13}C yields for single (non-) rotating massive stars 83
4.13 ^{14}N and ^{15}N yields for single (non-) rotating massive stars 84
4.14 ^{16}O, ^{17}O, and ^{18}O yields for single (non-) rotating massive stars 86

5.1 Effective binary yields of ^{26}Al (left) and the impact on the galactic ^{26}Al budget (right) 91
5.2 Evolution of the abundance ratios of ^{26}Al, ^{36}Cl, and ^{41}Ca for three different initial masses 101

6.1 Effect of varying binary parameters on the ^{26}Al wind yields 104
6.2 Mass-fraction of ^{26}Al in the core of a 30 $M_\odot$ star for varied production rates 105
6.3 Effect of varying reaction rates on the ^{26}Al mass-fraction in the core 106
6.4 Evolution of the central temperature of single stars 106
6.5 Effect of varying the neutron capture rate on ^{36}Cl and ^{41}Ca for the ESS . . 110
6.6 Cr isotopic compositions for varied neutron-capture rates 113
6.7 Ti and Cr isotopic compositions for varied neutron-capture rates 113
6.8 Yields for ^{26}Al for Set 1, Set 3, and the effective binary yields of Set 4 . . . 116
6.9 Yields for ^{36}Cl, ^{41}Ca, and ^{60}Fe for Set 3, and the effective binary yields of Set 4 118
6.10 KHDs for 10, 15, and 25$M_\odot$, single and binary stars with ^{41}Ca on the colour scale 119
6.11 Yields for ^{19}F and ^{22}Ne for Set 3, and the effective binary yields of Set 4 . 120
6.12 KHDs for 10, 20, and 40$M_\odot$ single and binary stars with ^{22}Ne on the colour-scale 122

List of Tables

2.1 Input for the three sets of models 34

3.1 Tabulated stellar evolution results for single and binary stars up till carbon burning 58
3.2 Selected details of the stellar evolution of the single (non-) rotating models 65

4.1 Wind yields for the single (non-) rotating models: ^{19}F, ^{22}Ne, ^{26}Al, ^{36}Cl, ^{41}Ca, and ^{60}Fe 87
4.2 Wind yields for the single (non-)rotating models: ^{12}C, ^{13}C, ^{14}N, and ^{15}N of Set 3 88
4.3 Wind yields for the single (non-)rotating models: ^{16}O, ^{17}O, and ^{18}O of Set 3 89

5.1 The binary enhancement factor for the different primary masses 92
5.2 The three SLRs in the ESS and their characteristics 95

6.1 Neutron-capture rate changes for ^{36}Cl and ^{41}Ca 109
6.2 Neutron capture rate changes for ^{53}Cr, ^{54}Cr, ^{48}Ti, and ^{50}Ti 112
6.3 Wind yields for the binary models up to core-collapse 123

Chapter 1

Introduction

In this introductory chapter, I discuss the theory relevant for this thesis. This includes a general introduction to stellar evolution of single stars, the evolution of binary systems, and the nucleosynthesis and characteristics of short-lived radioactive isotopes. I highlight the most important input for single star models and the main uncertainties for these models, such as stellar winds and stellar rotation, as well as those impacting binary evolution.

1.1 Short-lived radioactive isotopes: characteristics and nucleosynthesis

The information presented in this section was also included in the introductions of Brinkman et al. (2019) and Brinkman et al. (2021), but has been adapted and expanded from these two works.

The products of stellar nucleosynthesis, the process of creating new atomic nuclei in the stellar interior, are expelled into the interstellar medium by stellar winds (see Section 1.2.2) and/or binary mass-transfer (see Section 1.3), and supernova explosions, and then incorporated into a younger generation of stars, such as the Sun. Radioactive isotopes play an important role in the field of astrophysics. For example, the radioactive isotopes produced in supernova explosions power the light emitted by these events, and this radiation can been seen throughout the Galaxy and even beyond. A special class of radioactive isotopes are the so-called short-lived radioactive isotopes (SLRs). These radioactive isotopes, with short half-lives of less than a few Myr were present in the early Solar System (ESS), specifically the famous heating source ^{26}Al, with a half life of 0.72 Myr, as inferred from meteoritic data of excess in the ratios between their daughter nuclei to a stable isotope of the same element (e.g., excess in ^{26}Mg/^{24}Mg, from the decay of ^{26}Al in ^{26}Mg, Lee et al. 1977). These radioactive isotopes live such short lives that they represent the fingerprint of the local nucleosynthesis that occurred at the time and place of the birth of the Sun, and therefore they give us clues on the environment and the

circumstances of such birth (Adams, 2010; Lugaro et al., 2018).

Aside from ^{26}Al, ^{36}Cl and ^{41}Ca are interesting for the ESS. All three can be formed in the early phases of the evolution of massive stars and can be expelled from these stars through stellar winds. ^{60}Fe is also important, but likely comes from a different stellar source than the three other isotopes mentioned, due to its production during the later evolutionary phases. Below the synthesis and characteristics of each of these isotopes are briefly described.

Aluminium-26

Aluminium-26, a short-lived radioactive isotope with a half-life of 0.72 Myr (Basunia & Hurst, 2016), decays to an excited state of ^{26}Mg, and the quick, subsequent decay to the ground state releases a γ-photon at an energy of 1.81 MeV (red and white arrow in the top left panel of Figure 1.1). These photons, and thus the decay of ^{26}Al, have been detected in the Galaxy in γ-ray spectroscopic observations by the Imaging Compton Telescope (COMPTEL) on board the Compton Gamma Ray Observatory (CGRO) and the International Gamma-Ray Astrophysics Laboratory (INTEGRAL) satellite. From these observations it has been determined that the Galaxy contains about 2-3 $M_\odot$ of ^{26}Al (Diehl, 2013). Considering the short half-life of this isotope, the production of ^{26}Al is an ongoing process in the Galaxy. By mapping the distribution of the observed γ-rays, it has been shown that most of the ^{26}Al is confined to the plane of the Galaxy, and there are clumps that coincide with known OB-associations, i.e., groups of stars with masses $\geq$10 $M_\odot$ (see Figure 16 of Diehl 2013), such as the Cygnus region (Martin et al., 2009), the Scorpius-Centaurus region (Diehl et al., 2010), and the Carina region (Voss et al., 2012). The observations indicate that massive stars are the main source of ^{26}Al in the Galaxy, which expel the ^{26}Al isotope through winds and supernova explosions.

^{26}Al was also present in the ESS as inferred from ^{26}Mg excess in meteorites (Lee et al., 1977). From this excess the ^{26}Al/^{27}Al ratio at the time of the formation of the Solar System is determined. This ratio is currently reported to be $(5.23\pm0.13)\times10^{-5}$ (Jacobsen et al., 2008). ^{26}Al played an important role in the early stages of our Solar System because its decay has been linked to the heating of planetesimals (Lichtenberg et al., 2016), the first rocks with sizes between 10-100 km, from which the rocky planets such as our Earth are believed to have formed. Due to the large amount of ^{26}Al present in the ESS, its radioactive heating was dominant over the contribution of other radionuclides, however, its origin is still unclear. The abundance of ^{26}Al in the ESS was higher than the γ-ray observed abundance of ^{26}Al currently in the interstellar medium, and an extra source of ^{26}Al is needed (Lugaro et al. 2018; Côté et al. 2019a).

^{26}Al is significantly produced in massive stars by proton captures on ^{25}Mg during core and shell hydrogen-burning, and during carbon/neon convective shell burning, and explosive neon burning during the supernova (Limongi & Chieffi, 2006). The top left panel of Figure 1.1 shows the production and destruction channels of ^{26}Al. An important factor in the production of ^{26}Al that has to be mentioned is the presence of an isomeric state. This isomeric state has a much shorter half-life than the ground state, of the order of 6 seconds. The presence of this isomeric state reduces the amount of this isotope in the ground state. The interaction between the isomeric and the ground state of ^{26}Al is relatively well understood (Iliadis et al., 2010). However, at the temperatures of the production phases discussed in this work (hydrogen core and shell burning), the two states can be treated as two separate isotopes (see for a recent overview of ^{26}Al; Diehl et al., 2021).

The ^{26}Al produced during the core hydrogen-burning stage is mainly ejected through stellar winds driven by radiative pressure (see Section 1.2.2). Only the ^{26}Al remaining in the envelope, that has not decayed or been destroyed by then, is expelled by the supernova explosion. Some of the ^{26}Al produced during shell hydrogen-burning is expelled over time by the winds as well. The ^{26}Al produced in the other phases is expelled during the supernova explosion. The stellar winds, depending on the initial mass and metallicity, can be rather strong, leading to mass-loss rates ($\dot{M}$) ranging from 10^{-7} $M_\odot$/yr to 10^{-4} $M_\odot$/yr. In some cases these winds can drive off the entire envelope of the star. For the most massive stars the winds can be so strong that when the star leaves the main sequence, the hydrogen burning shell is stripped away as well. What is left of the star is an exposed helium core. Through these two mechanisms, winds and supernova explosions, massive stars are the main contributors of ^{26}Al in the Galaxy. For overviews of massive star evolution and their supernovae, see, e.g., Langer (2012) and Woosley et al. (2002). A general overview of the evolution of (massive) stars is given in Section 1.2.

In this thesis, I investigate ^{26}Al-production not only in massive stars, but also in massive binary stars, in which the ^{26}Al production can be enhanced, as will be further described in Section 1.3 and Chapters 4 6.

Chlorine-36 and Calcium-41

Like ^{26}Al, ^{36}Cl and ^{41}Ca have a half-life of less than 1 Myr, and specifically only of a few 10^5 yr (0.301 Myr, Nica et al. 2012 and 0.0994 Myr, Nesaraja & McCutchan 2016, respectively). Both are mainly produced by neutron captures on the stable isotopes, ^{35}Cl and ^{40}Ca, respectively (see the top right and bottom left panel of Figure 1.1). The neutrons are mainly produced by the ^{22}Ne(α,n) reaction (Arnould et al., 1997). For both ^{36}Cl and ^{41}Ca the main destruction is via (n,γ) or (n,α) reactions. The ^{36}Cl and ^{41}Ca

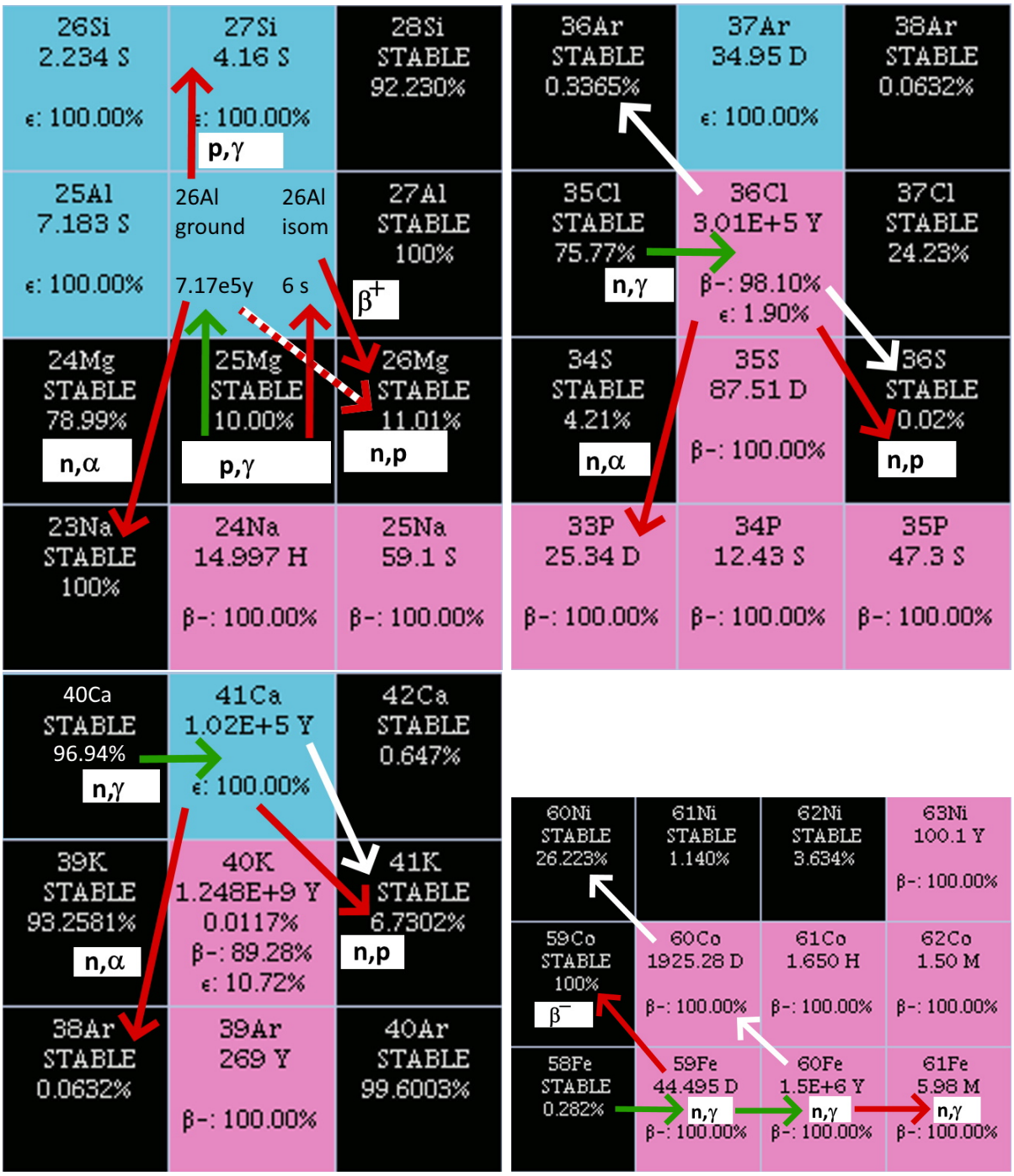

Figure 1.1: Modified sections from the nuclide chart (the original chart can be found at the website of the National Nuclear Data Center, `www.nndc.bnl.gov`). The four sections illustrate the nuclear-reaction paths leading to the creation (green arrows) or destruction (red arrows) of the four SLRs discussed in this section, in clockwise order starting from the top left; ^{26}Al, ^{36}Cl, ^{41}Ca, and ^{60}Fe. The white arrows represented the natural radioactive decay of each SLR, mind that for ^{26}Al the arrow is overlaid with the main destruction channel through neutron captures. (*This figure was reproduced from Figure 7 of Lugaro et al. (2018).)*

produced by the neutron-captures during helium burning can be expelled by massive star winds, most importantly the Wolf-Rayet winds (see Section 1.2.2), and these wind yields might be affected by rotational mixing and/or binary interactions. In core collapse supernovae a considerable amount of ^{36}Cl and ^{41}Ca is produced as well, especially for the low mass massive stars (up to 35 $M_{\odot}$, see, e.g., Pignatari et al., 2016; Limongi & Chieffi, 2018).

Iron-60

The fourth SLR I study in this thesis is ^{60}Fe with a half-life of 2.62 Myr, which makes it the longest lived SLR considered in this study. Like the decay of ^{26}Al, ^{60}Fe-decay can can be observed in γ-rays at energies of 1.173 and 1.332 MeV (Wang et al., 2020, and references therein). It is expected that the production of ^{60}Fe in stellar winds is negligible compared to the supernova ejecta. Indeed, ^{60}Fe is produced via neutron captures on the unstable ^{59}Fe (see bottom right panel of Figure 1.1), and for this nucleus to capture a neutron instead of decaying higher neutron densities ($> 10^{10-11}$ cm^{-3}) are required than those produced during core helium burning. Unlike the SLRs discussed earlier, ^{60}Fe is mainly produced in carbon shell-burning and in explosive helium- and carbon-burning conditions (Limongi & Chieffi, 2006; Tur et al., 2010; Jones et al., 2019) towards the end of the evolution. The production of ^{26}Al coupled with the limited production of ^{60}Fe in massive star winds makes this stellar site a potential source of the ^{60}Fe/^{26}Al ratio observed in the ESS (Trappitsch et al., 2018), which is about a factor of 300 lower than γ-ray observations from the interstellar medium and supernova models (Austin et al., 2017; Sukhbold et al., 2016). This suggests that either ^{60}Fe is less injected into the ESS compared to the galactic average, or that a different source of ^{26}Al was present at the time of the birth of the Sun. This different source has been suggested to be the winds of Wolf-Rayet stars (see ,e.g., Gounelle & Meynet, 2012), which is the reason why I focus my work on massive stars.

1.2 Stellar evolution of single stars and nucleosynthesis

To understand the production of the SLRs mentioned above, it is necessary to understand the basics of stellar and binary evolution, and the nucleosynthesis taking place in their interiors. In this section I cover the evolution of single stars and nucleosynthesis. Binary evolution is covered in Section 1.3.

The evolution of stars can be divided into three stages: their formation, or birth, their life, and their death. The formation of a star starts with the collapse of a cloud of interstellar gas due to a perturbation, such as a nearby supernova, a collision with another cloud, or another kind of turbulence inducing process. A cloud of interstellar gas collapses when the condition for pressure equilibrium in the cloud is violated, leading to a critical mass for clouds to be stable to perturbations, the Jeans mass M_J, which is defined as:

$$M_J \approx 4 \times 10^4 M_\odot \left(\frac{T}{100K}\right)^{3/2} \left(\frac{n}{cm^{-3}}\right)^{-1/2} \tag{1.1}$$

where, $M_\odot$ is the mass in solar masses, T the temperature in Kelvin, and n the molecular density by number (see, e.g., Maeder, 2009, Section 18.2.1). As the cloud collapses, the density increases, and the Jeans mass decreases. This leads to the violation of the stability criterion not only for the cloud as a whole, but also within the cloud. This leads to fragmentation of the cloud into smaller pieces, which then continue to collapse. As the fragments continue to collapse, the increasing density makes the gas opaque, which means that it traps photons inside the fragment. Due to this, hydrostatic equilibrium is reached and the fragment is now a protostar, where hydrostatic equilibrium refers to a state where the forces working on gas elements inside the cloud or star are (almost) cancelling each other out. From this point onward, the mass of the object grows due to accretion from a disk of gas and dust. This disk is formed due to original rotation of the collapsing cloud. The gravitational energy generated by the accretion either heats up the core of the protostar or is radiated away from the object. Due to the heating, the molecular hydrogen the gas is made up of, is dissociating. Hydrostatic equilibrium is then violated, and a new phase of collapse starts. Once all molecular hydrogen is turned into atomic hydrogen, a new equilibrium is found. This process repeats when first hydrogen, and later on helium is ionised. As the protostar regains equilibrium and the accretion stops, the star has reached the so-called "pre-main sequence" phase.

For low- and intermediate mass stars, $\geq$8 $M_\odot$[1], the formation scenario as described above is generally well understood (see ,e.g., McKee & Ostriker, 2007, for a theoretical review on the subject of star formation). The formation of more massive stars is more complicated, due to mechanisms such as radiation pressure, that hamper the growth of the stellar mass through accretion. A full discussion of the subject is beyond the scope of this thesis a review of the formation of massive stars (for of the formation of massive stars see, e.g., Zinnecker & Yorke 2007; Tan et al. 2014; Krumholz 2015 for a theoretical review and Motte et al. 2018 for an observational review).

As the star reaches the pre-main sequence, the internal temperature is still too low for nuclear burning. During this phase, the luminosity comes from further gravitational

[1]The definition of the mass-ranges for the different types of stars can be found in Box 2 at the end of this section.

contraction. This leads to an increase of the density and the temperature of the gas. The process of contraction continues until the core reaches a high enough temperature (4×10^6 K for hydrogen burning) for nuclear fusion reactions to start taking place. As soon as the energy generated by hydrogen fusion compensates for the loss of energy from the stellar surface, the contraction stops. The star has now reached the zero-age main-sequence.

On the zero-age main-sequence, stars are almost homogeneous in their composition and are in complete equilibrium, which means that they are both in hydrostatic and thermal equilibrium. A star in thermal equilibrium loses as much energy at its surface as is produced in its centre by nuclear reactions. When the star has reached this state of equilibrium, the subsequent life of the star can be modelled. For a more detailed description of stellar formation and the path to the zero-age main sequence see, e.g., Maeder (2009) Chapters 18-20.

Box 1: When the star is on the zero-age main sequence (in hydrostatic and thermal equilibrium) and spherical symmetry is assumed, its structure can be described by the following set of differential equations:

$$\frac{\partial r}{\partial m} = \frac{1}{4\pi r^2 \rho} \tag{1.2}$$

$$\frac{\partial P}{\partial m} = -\frac{Gm}{4\pi r^4} \tag{1.3}$$

$$\frac{\partial L}{\partial m} = \epsilon_{nuc} - \epsilon_\nu + \epsilon_g \tag{1.4}$$

$$\frac{\partial T}{\partial m} = -\frac{Gm}{4\pi r^4}\frac{T}{P}\nabla_{rad} \tag{1.5}$$

or

$$\frac{\partial T}{\partial m} = -\frac{Gm}{4\pi r^4}\frac{T}{P}\nabla_{ad} \tag{1.6}$$

These are the equations of continuity or mass conservation (Equation 1.2), of hydrostatic equilibrium (Equation 1.3), of energy equilibrium (Equation 1.4), and of energy transport (Equation 1.5 for the radiative case and Equation 1.6 for the convective case). In this equations, r is the radius, m the mass, ρ the density, P the pressure, G the gravitational constant, l the local luminosity, ϵ_{nuc} the nuclear energy produced per unit mass and per second, ϵ_ν the energy carried away by neutrinos per unit mass and per second, ϵ_g the energy generated by gravity per unit mass and per second, T the temperature, ∇_{rad} the radiative temperature gradient with respect to pressure, and ∇_{ad} the adiabatic temperature gradient with respect to pressure.

Once the star is on the main sequence, the evolution is driven by subsequent nuclear burning stages and mass loss. On the main sequence stars convert hydrogen into helium

in their cores, either through the pp-chains (like our Sun) or the CNO-cycle (see Section 1.2.1 for more details). This process is very efficient and can power the star for a long time. Most stars spend about 90% of their total lifetimes on the main sequence. Exactly how long this phase lasts depends on the initial mass of the star. Stars with initial masses similar to our Sun go through their hydrogen fuel very slowly and the main sequence phase lasts about 10 Gyr. In the case of our Sun, this means that it is about half-way through its main sequence phase. For more massive stars, this phase is much shorter, for example it lasts 3 and 20 Myr for stars with an initial mass of 80 $M_{\odot}$ and 10 $M_{\odot}$, respectively.

When all hydrogen in the core of the star has been converted into helium, the core starts to contract again under the force of gravity. At the same time, the envelope of the star expands, and the outer envelope cools (see Figure 1.4). The initial expansion goes rapidly, and the star crosses the so-called Hertzsprung-Gap, before helium is ignited in the core. It is during this evolutionary phase, commonly referred to the red giant or supergiant phase, that stars start losing some of their mass. To counteract gravitational collapse, first hydrogen is ignited in a shell around the core, and when later the temperature in the centre of the star rises enough to ignite helium (to $15{\times}10^8$ K for the triple-α process, see Section 1.2.1). As soon as helium is ignited, the star returns to its state of hydrostatic and thermal equilibrium. Towards the end of helium burning, the hydrogen burning shell extinguishes. For massive stars, once the helium in the core is exhausted, the core contracts again, and the central temperature increases until carbon is ignited. Helium is further burned in a shell around the core, and this shell can remain active till the end of the evolution. This process is repeated for neon, oxygen, and finally silicon burning. The carbon burning shells slowly move outwards (see Figure 1.2 for more details), with short pauses in between. This also happens for the oxygen burning shells. Both the carbon burning shell and the oxygen burning shell are active till the end of the life of the star. The final product of these burning cycles is a core formed of the iron group elements, which have the highest binding energy and further fusion does not release more energy.

Low-mass stars like the Sun, with initial masses in the range 0.8-2 $M_{\odot}$ do not go through all these burning stages, their evolution ends shortly after helium is ignited in their cores. The helium burning for these stars happens under unstable conditions. These stars end their lives as carbon-oxygen white dwarfs. The lowest mass stars, 0.08-0.5 $M_{\odot}$ do not even ignite helium and end their lives as helium white dwarfs, as their cores cannot reach the temperatures required for further burning. Stars with masses from $\simeq 2$ up to 8-10 $M_{\odot}$ (also known as intermediate-mass stars) ignite helium in a stable way and form a carbon-oxygen core. For most of these stars this is the end of their evolution, and they end their lives as carbon-oxygen white dwarfs as well. At the top of this mass range, the stars may ignite carbon, and end their lives as oxygen-neon white dwarfs instead (see, e.g, Herwig, 2005; Karakas & Lattanzio, 2014).

Finally, high-mass stars, stars with initial masses of $\simeq$10-12 $M_\odot$ and higher, at solar metallicity, undergo all nuclear burning stages described above and end their lives when their cores collapse, leaving a neutron star, or a black hole, or potentially no remnant behind (see, e.g., Heger et al., 2003; Langer, 2012).

While these basics of the theory of stellar evolution are well understood, there are still many uncertain processes that can alter the evolution of a star. For example, due to their high luminosities, massive stars have strong stellar winds that blow off their outermost layers, uncovering the processed layers within. Stars with initial masses of 35 $M_\odot$ and higher lose the majority or even the whole hydrogen envelope already during their main sequence phase, leaving the inner layers exposed. These stars are the so-called Wolf-Rayet stars. Not only the mass loss is important for the evolution, but also the internal mixing, the presence of rotation, and the treatment of convective overshooting and semi-convection have an impact. Another factor is the metallicity, however, in this work I will focus only on stars of solar metallicity.

Box 2: In the following, the mass ranges for the different types of stars are used:

- Very low-mass stars: 0.08-0.5 $M_\odot$
- Low-mass stars: 0.5-2 $M_\odot$
- Intermediate-mass stars: $\simeq$ 2 to 8-10 $M_\odot$
- High-mass stars or massive stars: $\simeq$10-12 and up, generally to $\sim$100-120 $M_\odot$
- Very massive stars: 120 $M_\odot$ and higher

Mind that these are rough borders and depend on the stellar physics and the initial metallicity of the stars.

In the following subsections, I will cover the main nuclear burning cycles and their nucleosynthesis, mass loss through stellar winds, the internal mixing of stars, and rotation.

1.2.1 Main nuclear burning cycles and their nucleosynthesis

An overview of the theory of nucleosynthesis in stars was first written down in the famous paper by Burbidge, Burbidge, Fowler, & Hoyle, 1957, also known as B^2FH, where the authors identified the different processes that lead to the production of all different elements and isotopes in the Universe. In the context of this thesis, the main interest is the production of the selected SLRs, however, to understand their production, it is important to understand the general nucleosynthesis in stars. The material covered in this section is also covered in more detail in (for example Maeder, 2009, Chapter 9).

As mentioned before, during their lifetimes, massive stars burn lighter elements, such as hydrogen, into heavier elements until the iron-group elements are reached and nuclear fusion no longer generates energy. These nuclear reactions generally takes place during the hydrostatic burning phases of the star, as well as during the supernova explosion.

Figures 1.2 and 1.3 show the internal evolution of a 20 $M_\odot$ star taken from Brinkman et al. (2021). Figure 1.2 shows a Kippenhahn diagram (KHD) representing the internal structure of the star. The x-axis is the log of time till the core collapse, which allows to show all burning cycles with a similar amount of space in the figure. The y-axis is the internal mass coordinate. The different shaded areas indicated different types of mixing, which will be discussed further in Section 1.2.3.

Like a KHD, the $\rho_c T_c$ diagram of Figure 1.3 also gives information about the interior of the star, in this case the density and the temperature of the center of the star. Four areas separated by the dashed lines based on the equations of state can be distinguished: radiation dominated, (classical) ideal gas, non-relativistic electron degeneracy, and extremely relativistic electron degeneracy (the equations for these regimes are given in Box 3). Due to the dependence on the mean molecular weight (μ) and the mean molecular weight by free electron (μ_e) of the equations of state, these borders should be considered as guidelines. For most of the their evolution, stars are in the ideal gas regime. In this diagram, the onset of the core burning phases are indicated by the same capital letter as in Figure 1.2, while the end of the same burning stage is indicated by lower case letters.

Box 3: The formulas for the equations of state that are used to determine the borders for the different internal regimes in the $\rho_c T_c$ diagram are the following (see for a derivation, e.g., Maeder, 2009, Chapter 7):

$$P = \frac{1}{3} a T^4 \tag{1.7}$$

$$P = \frac{\mathfrak{R}}{\mu} \rho T \tag{1.8}$$

$$P = K_{NR} (\rho/\mu_e)^{5/3} \text{with } K_{NR} = \frac{h^2}{20 m_e m_u^{5/3}} \left(\frac{3}{\pi}\right)^{2/3} \tag{1.9}$$

$$P = K_{ER} (\rho/\mu_e)^{4/3} \text{with } K_{ER} = \frac{hc}{8 m_u^{4/3}} \left(\frac{3}{\pi}\right)^{1/3} \tag{1.10}$$

These are the equations for a regime dominated by radiation pressure (Equation 1.7), by (classical) ideal gas (Equation 1.8), and by non-relativistic and relativistic electron degeneracy (Equation 1.9 and 1.10, respectively). In these equations, P is the pressure, a is the radiation density constant, T is the temperature in Kelvin, $\mathfrak{R}$ is the gas constant, μ is the mean molecular weight, ρ is the density, μ_e is the mean molecular weight per free electron, h is the Planck constant, m_e is the electron mass, and m_u is the atomic mass unit.

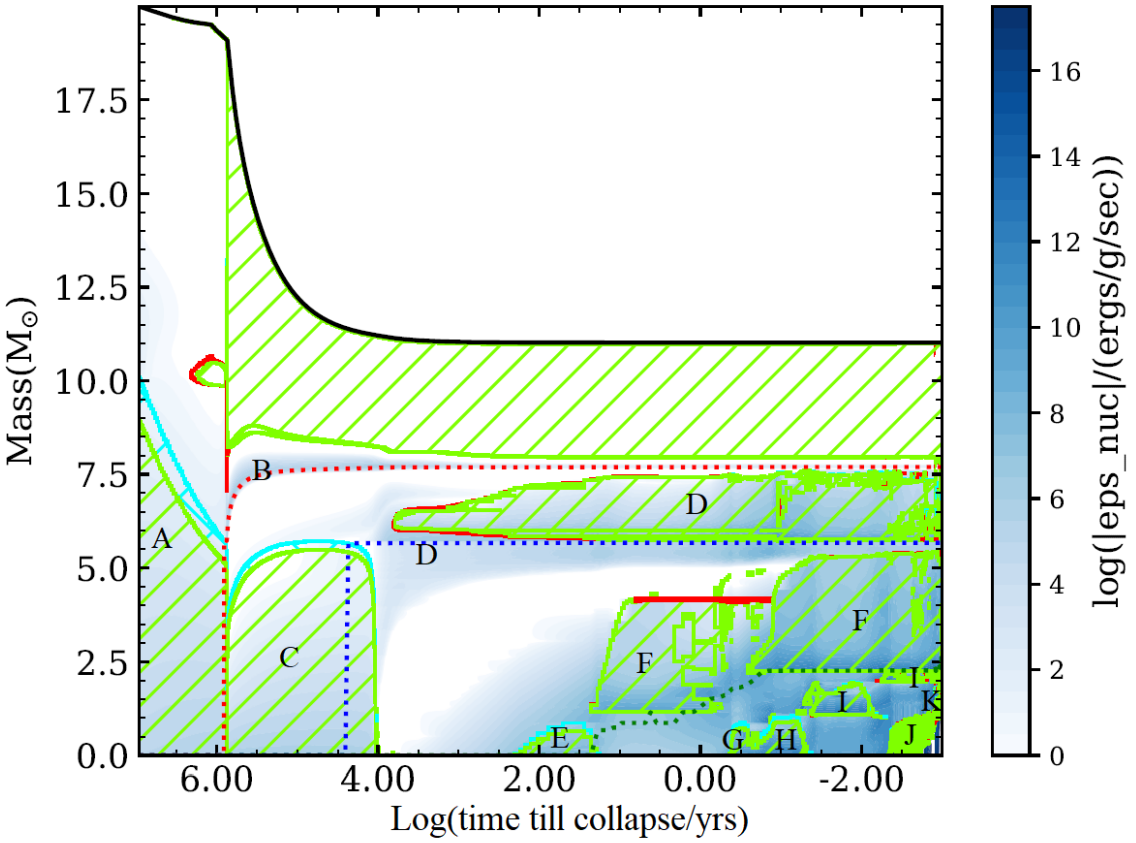

Figure 1.2: The Kippenhahn diagram for a 20 $M_{\odot}$, non-rotating single star (calculated for Brinkman et al., 2021). The x-axis gives the log of the time till the end of the simulation at the collapse of the core, and the y-axis the mass-coordinate. The green shaded areas correspond to areas of convection, the cyan shaded areas to overshooting, and the red shaded areas to semi-convection. The red dotted line indicates the hydrogen depleted core, or helium core, where the hydrogen content is below 0.01 and the helium content is above 0.1. The blue dotted line indicates the helium depleted, or carbon core, and the green dotted line the carbon depleted, or oxygen core. The blue colour scale shows the nuclear energy production at the mass coordinate and time. The different hydrostatic core- and shell-burning phases are indicated by the capital letters A-J, where A is core hydrogen burning, B is hydrogen shell burning, C is core helium burning, D is helium shell burning, E is core carbon burning, F is carbon shell burning, G is core neon burning, H is core oxygen burning, I is oxygen shell burning, J is silicon burning, and K is silicon shell burning.

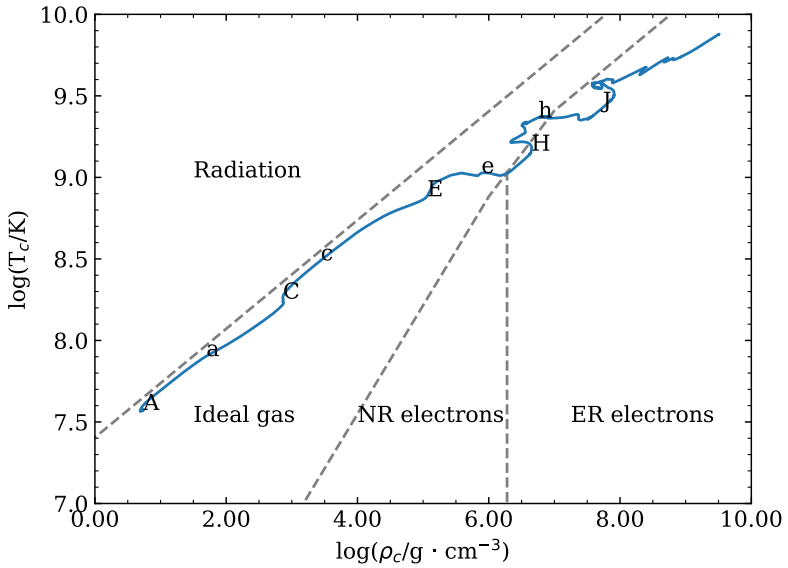

Figure 1.3: The $\rho_c T_c$ diagram for the 20 $M_\odot$, non-rotating, single star. The x-axis gives the log of the central density of the star, the y-axis the log of the central temperature. The capital letters indicate the onset of the nuclear burning stages, the lower case letters the end point. These are the same as in Figure 1.2. The areas dominated by one of the four equations of state are indicated, where NR and ER stand for non-relativistic and extremely relativistic, respectively (see Box 3 for more details).

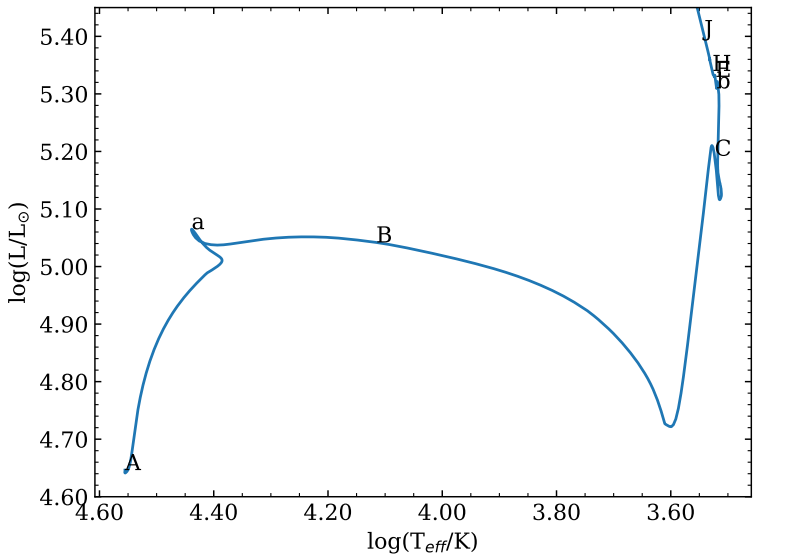

Figure 1.4: The HRD for the 20 $M_\odot$, non-rotating, single star. The x-axis gives the log of the effective temperature, the y-axis the log of the luminosity in solar luminosities. The capital letters indicate the onset of the central nuclear burning stages, as well as the onset of hydrogen shell-burning, the lower case letters the end point. The letters are the same as for Figure 1.2.

Finally, in Figure 1.4, I present the Hertzsprung-Russell diagram (HRD) of the same star, which gives the luminosity and effective temperature and shows how these external properties evolve in time. The different burning phases are annotated using the same letters as in Figures 1.2 and Figure 1.3, with the capital letters indicating the onset of a burning phase and the corresponding lower case letter the end of the same phase.

On the zero-age main sequence, the star is burning hydrogen. During this hydrogen burning phase (A in Figures 1.2-1.4), hydrogen is converted into helium either through one of the pp-chains or through the CNO-cycle. Low mass-stars burn most of their hydrogen through the pp-chain (see Figure 1.6) and shift to the CNO-cycle (see Figure 1.7) only at the very end of their hydrogen burning phase when their central temperatures reach 1.5-2 $\times 10^7$ K for stars with initial masses larger than 1.3 $M_\odot$, at which the CNO-cycle becomes more efficient at generating energy than the pp-chain. Massive stars however, burn hydrogen purely through the CNO-cycle. It should be noted that Cycle 1 is also referred to as the CN-cycle, and Cycle 2 is also referred to as the NO-cycle.

Due to the different reaction rates associated to each of the proton-capture reactions, this cycle turns the CNO isotopes into ^{14}N aside from turning ^{1}H into ^{4}He, because the ^{14}N(p,γ)-reaction is the slowest reaction. This makes the ^{14}N(p,γ)^{15}O one of the most important reactions to know to high accuracy for stellar evolution in this phase. The hydrogen burning process continues in the hydrogen burning shell (B) after hydrogen burning in the core ends. During core hydrogen burning, ^{26}Al is formed through the magnesium-aluminium cycle, as shown in Figure 1.5.

Helium burning (C) takes place through the triple-α reaction: ^{4}He + ^{4}He $\rightarrow$ ^{8}Be, followed by ^{8}Be + ^{4}He $\rightarrow$ ^{12}C + 2γ, and through α-captures on ^{12}C forming ^{16}O as soon as the abundance of this isotope is high enough. The main products of this burning process are ^{12}C and ^{16}O. Helium burning continues in the helium shell (D) after all helium in the core is exhausted. The helium shell remains active till the end of the evolution. During helium burning neutrons are produced by α-captures on ^{13}C and ^{22}Ne via the ^{13}C(α,n)^{16}O and the ^{22}Ne(α,n)^{25}Mg reactions, respectively. For massive stars during helium burning, the neutrons produced through ^{22}Ne are most important (see, e.g., Pignatari et al., 2010; Chieffi & Limongi, 2013, and references therein). The ^{22}Ne is produced by a sequence of α-captures on ^{14}N: ^{14}N(α,γ)^{18}F($\beta^+\nu$)^{18}O(α,γ)^{22}Ne. The neutrons produced by this reaction give rise to the slow neutron capture process (s process). In this process, nuclei capture a neutron, then (if they are unstable) experience β-decay, after which another neutron is captured. This s process then can continue to produce nuclei all the way up to ^{209}Bi. Though this takes place mostly in stars on the asymptotic giant branch, massive stars also undergo the "weak" s-process, which traditionally produces the isotopes between iron and strontium (see, e.g., Pignatari et al., 2010). This process takes place in the late stages of core helium burning with ^{22}Ne as main neutron source and during convective carbon shell burning with ^{13}C as main neutron source.

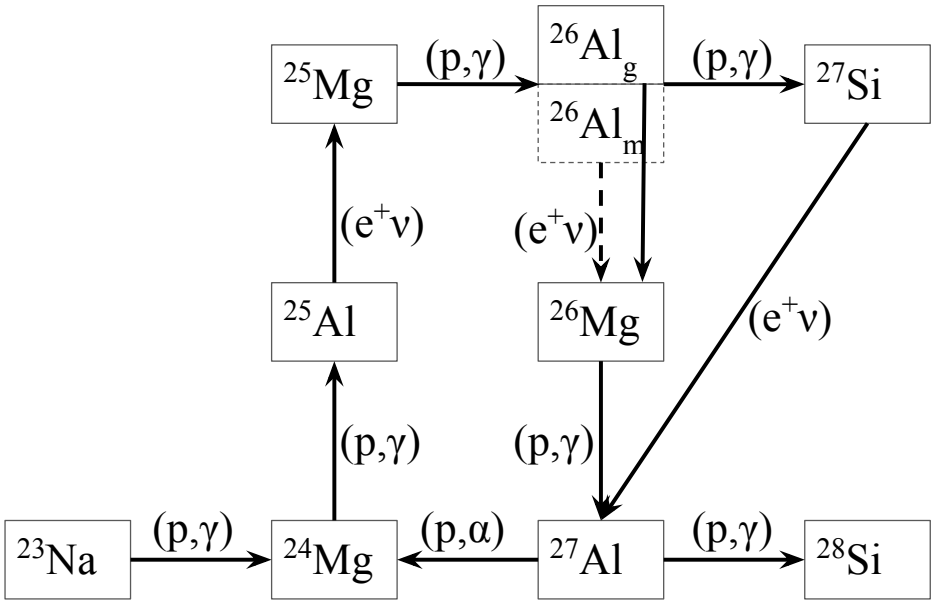

Figure 1.5: The AlMg-cycle, which is active during hydrogen burning and produces ^{26}Al in both the ground state and the isomeric state. The amount of ^{26}Al that can potentially be produced in a massive star and subsequently expelled by the winds depends mainly on the initial abundance of ^{25}Mg. This is not the case for the ^{26}Al expelled by the supernova explosion, or produced by asymptotic-giant branch stars.

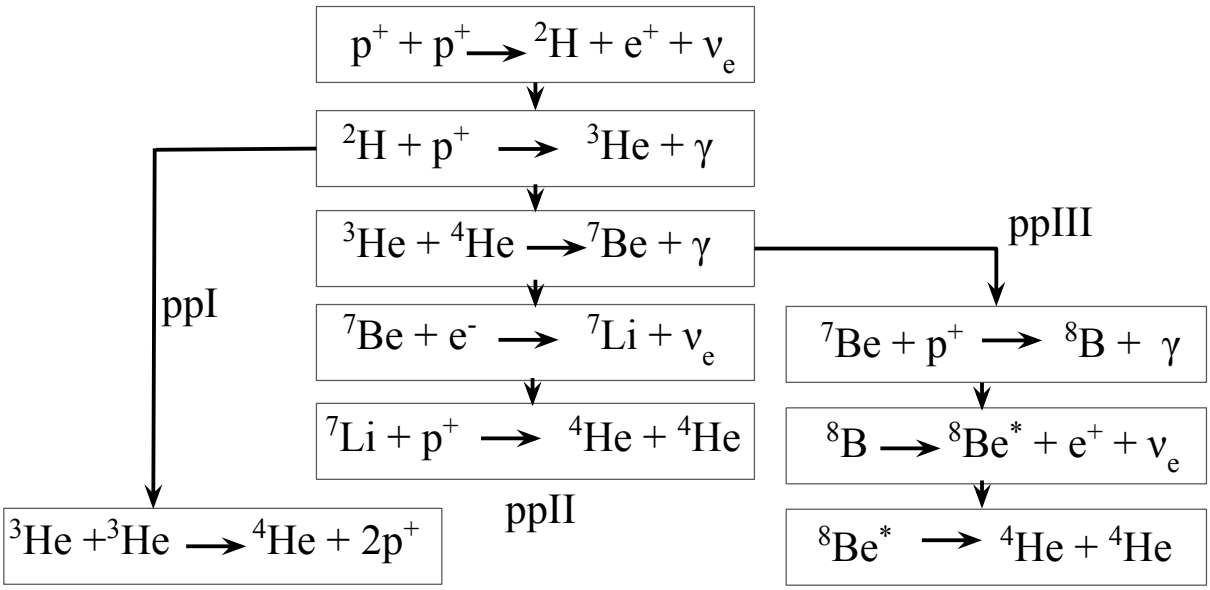

Figure 1.6: The three pp-chain branches. The ppI chain needs two ^{3}He nuclei, while ppII and ppIII both only need one. Which of the three chains is dominant, depends on the temperature and the chemical composition of the star. The ^{3}He+^{4}He reaction has a higher sensitivity to temperature compared to the ^{3}He + ^{3}He reaction. Therefore, the ppI chain is dominant at relatively low temperatures (T $\leq 1.5\times10^7$K). ^{8}Be* is an unstable isotope, and decays quickly into two ^{4}He.

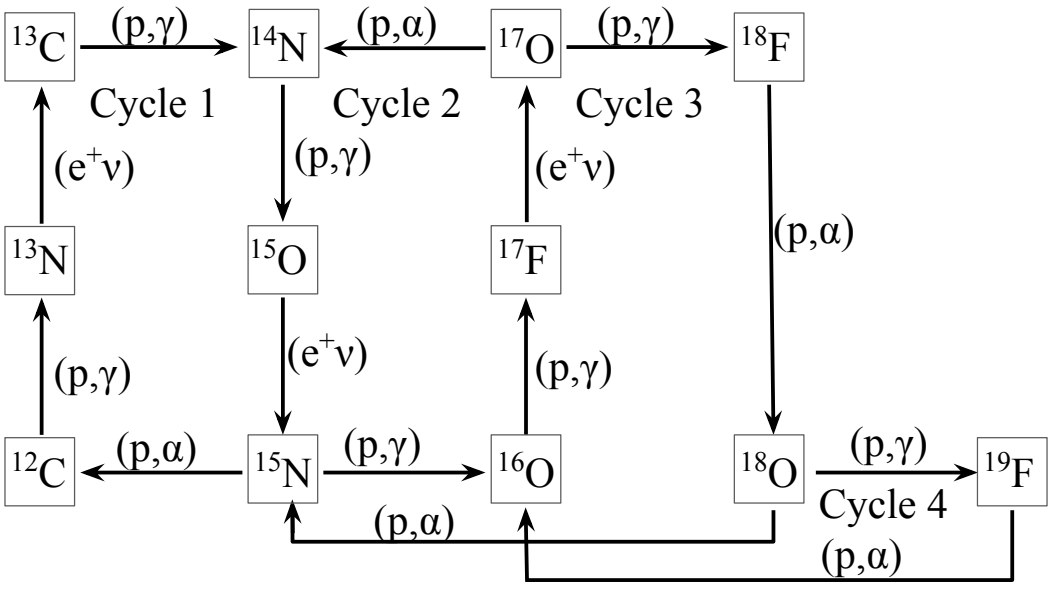

Figure 1.7: The four CNO cycles, where different isotopes of C, N, and O are cycled through as catalysts while turning hydrogen into helium. Cycle 1 is responsible for most of the hydrogen burning, with a contribution of Cycle 2. Cycles 3 and 4 are not active at the temperatures of hydrogen burning. The ^{17}O(p,α)-reaction is dominant over the ^{17}O(p,γ)-reaction. ^{19}F and ^{18}O are effectively destroyed in this phase.

The next burning phase is carbon burning (E), where the main reactions are ^{12}C(^{12}C,α)^{20}Ne and the ^{12}C(^{12}C,p)^{23}Na. Due to the high temperatures in the core at this point, 5×10^8 K, the protons and α-particles produced by these reactions quickly react with other nuclei via, e.g., the ^{20}Ne(α,γ)^{24}Mg, ^{23}Na(p,α)^{20}Ne, and ^{23}Na(p,γ)^{24}Mg reactions. The main products of carbon burning are ^{20}Ne, ^{23}Na, and ^{24}Mg. Carbon burning continues then in shells (F), moving slowly outwards.

After carbon burning, one would expect the next burning phase to be oxygen burning (H). However, neon burning (G) happens earlier at a temperature of 1.5×10^9K. Unlike the burning phases before, neon burning is not the fusion of two neon nuclei, but is rather a combination of photo-disintegration of ^{20}Ne and subsequent α-captures. The main reactions are ^{20}Ne(γ,α)^{16}O, ^{20}Ne(α,γ)^{24}Mg, and ^{24}Mg(α,γ)^{28}Si. The main products of this burning phase are ^{16}O, ^{24}Mg, and ^{28}Si.

The next burning phase is oxygen burning (H), where two ^{16}O fuse together, at a temperature of 2×10^9 K. The main reactions for oxygen burning are ^{16}O(^{16}O,α)^{28}Si and ^{16}O(^{16}O,p)^{31}P, however just as before for carbon burning, other reactions take place as well. The main final products of oxygen burning are ^{28}Si and ^{32}S. Oxygen burning continues in shells that move outwards (I), comparable to the carbon shells.

The last burning phase is silicon burning (J), at temperatures $\geq3\times10^8$ K. Like neon burning, silicon burning takes place as a series of photo-disintegrations and α-captures.

There are two sequences of reactions taking place, the first 'melts' silicon down to lighter nuclei:
^{28}Si(γ,α)^{24}Mg(γ,α)^{20}Ne(γ,α)^{16}O(γ,α)^{12}C(γ,α)2α,
while the other sequence picks up the released α-particles:
^{28}Si(α,γ)^{32}S(α,γ)^{36}Ar(α,γ)^{40}Ca(α,γ)^{44}Ti(α,γ)...^{56}Ni.

Most of these reactions are in equilibrium with each other, i.e., the reactions occur both forward and backward. In the end, a state of "nuclear statistical equilibrium" is reached, with as the main products nuclei belonging to the iron group and α-particles. The most abundant nuclei are those with the lowest binding energy, which means the core is mostly made of ^{56}Fe by the end of the stars lifetime. Silicon burning continues in a shell as well (K). At this point the star is very close to the end of the evolution.

After silicon burning has finished and the core has turned into mostly α-particles and iron, the core starts to collapse and a supernova explosion will take place. During the explosion, explosive nucleosynthesis can also occur due to the shock wave passing through the star. In this thesis, I focus on the previous hydrostatic phases of the evolution, and specifically hydrogen and helium burning. For more details on explosive nucleosynthesis see, e.g., Rauscher et al. (2002).

1.2.2 Mass loss and stellar winds

Stars do not only change inside due to conversion of hydrogen into heavier elements, but also on the outside, as shown in Figure 1.4. Aside from the luminosity and the effective temperature, also the radius and the total mass change over time. In fact, all stars lose mass during their lives. This may happen through stellar winds, eruptive episodes, and explosions (such as a supernova), as well as due to interactions in a binary system (as described in more detail in Section 1.3). For low-mass stars, mass loss through stellar winds has a limited impact on the evolution until the very final red giant stages of their lives. For massive stars ($\geq$8 $M_\odot$) instead, the mass loss through stellar winds can start as early as the main sequence. These stellar winds do not only impact the evolution of the massive stars themselves and their final fates (see, e.g., Smith, 2014, for a review), but they also impact their environment, as the products of their nuclear burning are expelled into the interstellar medium.

Depending on the initial mass of the star, massive stars may lose only a fraction of their initial mass ($\sim$1 $M_\odot$ for a 10 $M_\odot$ single, non-rotating star) to losing over half of it ($\sim$56 $M_\odot$ for a 80 $M_\odot$ non-rotating star), see Section 3.4 and see, e.g., Ekström et al. 2012; Sukhbold et al. 2016; Pignatari et al. 2016; Ritter et al. 2018b; Limongi & Chieffi 2018 and many others in the literature. In the latter case, these stars become Wolf-Rayet stars, a spectroscopic designation for stars that have lost (most of) their hydrogen envelopes and

show the products of CNO burning and/or helium burning at the surface. For Wolf-Rayet stars, with initial masses above 30-35 $M_\odot$ (depending on the initial conditions), the mass loss during the main-sequence can already be significant and will impact their lives, while for stars at the lower mass-end of massive stars, up to ∼20-30 $M_\odot$, mass loss happens mainly after the main-sequence and has a limited impact on their central evolution (see Section 3.4).

The stellar winds of stars are mainly driven by line-absorption of photons, where the photons interact with metallic ions in the envelope and push the gas outwards (see, e.g., Puls et al., 2008). This means that these winds depend on the chemical composition and the ionisation of the outer layers of the star. For the stars considered in this thesis, the mass-loss rates due to the stellar winds are between 10^{-10} and 10^{-5} $M_\odot$/yr (de Jager et al., 1988; Vink et al., 2001), while the mass-loss rate for the Sun is around 10^{-14} $M_\odot$/yr for comparison.

In stellar evolution codes, winds are implemented by relatively simple parametric prescriptions for the different phases of the evolution based on theoretical formulas or empirical relations. The mass loss is generally described as a function of the mass of the star (M), the luminosity (L), the effective temperature ($T_{\rm eff}$), and the metallicity (Z). Due to the uncertainty of the mass-loss prescriptions, often a scaling factor is added as well. An overview of mass-loss prescriptions for massive stars can be found in, e.g., Renzo et al. (2017).

Generally, there are three phases of mass loss for massive stars; the hot phase ($T_{\rm eff} \geq 1.1 \times 10^4$ K), the cold phase ($T_{\rm eff} \leq 1.1 \times 10^4$ K), and the Wolf-Rayet phase (with a surface hydrogen mass-fraction of $X_s < 0.4$). The transition between the phases is often done by interpolation, though the borders of the three phases can be somewhat arbitrary (Glebbeek et al., 2009; Brott et al., 2011; Renzo et al., 2017). For the hot phase, commonly either the wind prescription by Vink et al. (2000, 2001) or that by Kudritzki et al. (1989) is used. For the cold phase, there are three commonly used prescriptions: de Jager et al. (1988), Nieuwenhuijzen & de Jager (1990), and van Loon et al. (2005). Finally, for the Wolf-Rayet phase, either Nugis & Lamers (2000) or Hamann et al. (1995) are used for calculating the wind. The prescription by Vink et al. (2000, 2001) also includes the so-called "bi-stability jump", a strong increase in the mass loss around an effective temperature of 25,000 K, due to the recombination of Fe VI ions into Fe III ions by capturing a free electron ions (Lamers et al., 1995; Vink et al., 1999; Vink, 2021).

These prescriptions however do not take into account recent findings of for example clumping (inhomogeneities) in the wind, see Vink (2021) for a recent review , and often a scaling factor is used to account for this (see, e.g., Hamann & Koesterke, 1998; Yoon et al., 2006). Also, recent modelling of stellar winds has questioned the presence of the bi-stability jumps (Björklund et al., 2021), which are still included in most wind prescriptions, including those used for this thesis. Finally, there is discussion on whether

stripped helium-stars (stars that have lost their hydrogen-rich envelopes due to binary interactions) should be calculated with the same wind as Wolf-Rayet stars, which have lost their hydrogen-rich envelopes due to stellar winds instead (Vink, 2017; Sander & Vink, 2020).

Types of Wolf-Rayet stars

As mentioned previously, Wolf-Rayet stars are those which have lost (most) of their hydrogen-rich envelopes, and are now very hot and luminous stars, with clear emission lines (most importantly of helium) in their spectra. Generally, these stars are burning helium in their cores, but the most massive of them can still be at the end of hydrogen burning. The highest wind mass loss rates for single stars are found in Wolf-Rayet stars. Their mass loss rates are very high, 10^{-5}-10^{-4} $M_{\odot}$/yr (see, e.g., Maeder 2009 Chapter 27 and Crowther 2007). As the winds for generic O-type stars (i.e., hot, blue stars with initial masses > 15 $M_{\odot}$), Wolf-Rayet winds are driven by radiation pressure, but they are stronger due to their optically thick outflows which increases the photon scattering. Because of the strong mass loss, Wolf-Rayet stars are important for the enrichment of the interstellar medium with newly synthesised elements in the stellar interior.

In the spectrum of Wolf-Rayet stars, the products of the CNO-cycle are higher compared to O-stars, indicating that the surface of these stars is in fact the exposed hydrogen- or helium- burning core. The border between O-stars and Wolf-Rayet stars is often set at either a hydrogen surface mass-fraction of X_s=0.4 (see, e.g., Meynet & Maeder, 2005; Limongi & Chieffi, 2006), in agreement with observations by Hamann et al. (1995), who showed that in their sample, most WN stars (a sub-type of Wolf-Rayet stars, see below) have hydrogen surface mass-fractions of 10-30%, or at a helium surface mass-fraction of Y_s=0.7 (see, e.g., Yoon et al., 2006).

Wolf-Rayet stars are classified also based on their surface mass-fractions (see, e.g., Smith, 2014) as:

- WNL stars (or late WN): hydrogen is still present at the surface, though with a mass fraction below 0.4, and the helium and nitrogen mass fractions are increased relative to the solar values, and in agreement with their equilibrium values from the CNO-cycle.
- WNE stars (or early WN): Same as the WNL stars, but without the presence of any hydrogen.
- WC stars: No hydrogen, little or no nitrogen present, and while the helium, carbon, and oxygen mass fractions are increased relative to the solar values, which indicate partial helium burning.

- WO stars: Similar to the WC stars, though the oxygen mass fraction is higher. These stars are thought to be at the end of helium burning.

In the models, the transition between the WNL and WNE classes is often set at X_s=10^{-5} (Limongi & Chieffi, 2006). For the WC and WO phases, the transition is based on the enrichment of CNO at the surface. Following Maeder & Meynet (1994); Eldridge & Vink (2006), the following definition is used; ζ=$(\chi_C + \chi_O)/Y$, where χ_C and χ_O are the surface mass-fractions of carbon and oxygen, respectively, and Y is the surface mass-fraction of helium. A Wolf-Rayet star is a WC star if X_s=0 and $\zeta > 0.03$, and a WO star if X_s=0 and $\zeta > 1$. Limongi & Chieffi (2006) use a slightly different definition, based on N and C, defining a star as a WC when $X_s = 0$ and $0.1 < (\mathrm{C/N})_s < 10$, and a star as a WC when $X_s = 0$ and $(\mathrm{C/N})_s > 10$.

Generally, because the winds peel off more and more mass of the stars, the different subtypes of WR stars can be seen in the models as an evolutionary sequence. This interpretation is also known as the Conti scenario (Conti, 1975) and results in the following evolutionary pathways for stars with different initial masses[2]. The proposed evolutionary sequences listed below for the different initial masses are adapted from Ekström et al. (2019):

- M $\leq$ 15 $M_\odot$: O/B (main sequence) $\rightarrow$ RSG $\rightarrow$ BSG in a blue loop? $\rightarrow$ RSG $\rightarrow$ CCSN
- M = 15-25 $M_\odot$: O/B (main sequence) $\rightarrow$ BSG $\rightarrow$ RSG $\rightarrow$ CCSN
- M = 25-30 $M_\odot$: O (main sequence) $\rightarrow$ BSG $\rightarrow$ RSG $\rightarrow$ YSG? LBV? $\rightarrow$ CCSN
- M = 30-40 $M_\odot$: O (main sequence) $\rightarrow$ BSG $\rightarrow$ RSG $\rightarrow$ WNE $\rightarrow$ WC
- M = 40-60 $M_\odot$: O (main sequence) $\rightarrow$ BSG $\rightarrow$ LBV $\rightarrow$ WNL $\rightarrow$ WNE $\rightarrow$ WC
- M > 60 $M_\odot$: O (main sequence) $\rightarrow$ WNL $\rightarrow$ LBV $\rightarrow$ WNL $\rightarrow$ WC $\rightarrow$ WO

where RSG stands for red supergiant ($\log_{10}(T_{\mathrm{eff}}/\mathrm{K}) \leq 3.6$), BSG for blue supergiant ($3.6 \leq \log_{10}(T_{\mathrm{eff}}/\mathrm{K}) \leq 3.8$), and YSG stands for yellow super giant ($\log_{10}(T_{\mathrm{eff}}/\mathrm{K}) \geq 3.8$), based on the surface temperature before the explosion, as defined in, e.g., Georgy (2012). LBV stands for luminous blue variable, which is a bright blue star experiencing periodic and often violent mass-loss episodes. CCSN stands for core-collapse supernova. It should also be noted that generally it is assumed that stars with initial masses $\geq$ 30 $M_\odot$ do not

[2]mind that these masses are a rough indication because mixing, rotation, and mass loss prescription impact the parameters used for identifying the different stages

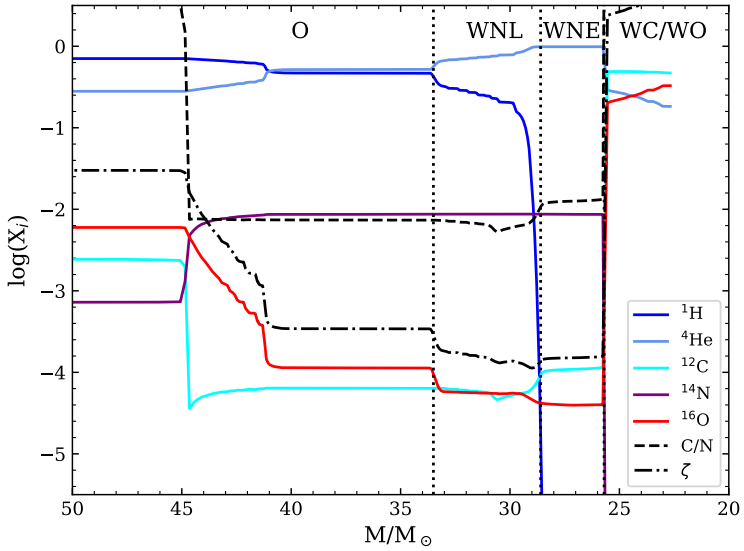

Figure 1.8: Surface mass-fractions of H, He, C, N, and O for the non-rotating 60 $M_\odot$ from Brinkman et al. (2021), as well as ζ and C/N. The different phases of the star are indicated at the top. The WC phase is very short and turns into a WO phase quickly, and is therefore not indicated separately. The LBV phase is not indicated as in the scheme because this phase was not modelled.

explode in a CCSN but directly collapse into a black hole (see, e.g., Sukhbold et al., 2016).

The evolution of the surface mass-fractions illustrating the last listed sequence for a 60$M_\odot$ star as a function of the current, evolving mass calculated by Brinkman et al. (2021) is shown in Figure 1.8 (see also, e.g., Figure 1 of Lamers et al. 1991 for a 60 $M_\odot$ model and Figure 14 of Meynet & Maeder 2005 for a 40 $M_\odot$ model). The C/N ratio and ζ, as defined above, are also plotted and the vertical dashed lines indicate roughly the transition between the different phases. Both the definition based on $(C/N)_s$ and that based on ζ, of the borders between the later Wolf-Rayet types occur at a very close time in the evolution, and the final transition from WC to WO is very rapid.

1.2.3 Internal mixing

While winds strip off the external layers of the star and expose the deeper, processed layers to the surface, the products of nucleosynthesis can also be brought to the surface by mixing processes. These mixing processes have an impact on the duration of the hydrostatic burning stages as well because they mix in fresh fuel from the envelope into the core, mostly during hydrogen burning. The main mixing process inside stars is convective mixing, which is the process by which bubbles of gas float up (relatively hot bubbles) or down (relatively cold bubbles). Convective motions are both an effective way of heat

transportation (the other being radiative transport, which is the repeated absorption and emission of photons) and an efficient mixing mechanism. Therefore, convective regions in stellar models are usually considered to be fully mixed and therefore fully homogeneous in their composition. Because of the upwards and downwards motion of mass-elements, there is no net mass flow and the condition of hydrostatic equilibrium is not violated, while heat is transported effectively by the gas elements. Convection occurs in regions with a strong temperature gradient, for example the cores of massive stars, or in regions with a high opacity, such as the envelopes of low-mass stars. In most stellar evolution codes, convection is modelled based on the so-called "mixing-length theory" (Böhm-Vitense, 1958). This theory gives the following equation for diffusive mixing in stars:

$$D_{conv} = \frac{1}{3}\alpha_{mlt} H_p v_{conv}, \tag{1.11}$$

where D_{conv} is the diffusive mixing coefficient, α_{mlt} a free scaling parameter, H_p the pressure scale height, and v_{conv} the convective velocity.

To determine whether a region in a star is stable against convection or whether convective motions will develop, either the Schwarzschild criterion or the Ledoux criterion is used. The Schwarzschild criterion states that a region is unstable against convection when the following holds true;

$$\nabla_{rad} > \nabla_{ad}, \tag{1.12}$$

i.e.,

$$\left(\frac{\mathrm{d\,lnT}}{\mathrm{d\,lnP}}\right)_{rad} > \left(\frac{\mathrm{d\,lnT}}{\mathrm{d\,lnP}}\right)_{ad} \tag{1.13}$$

where ∇_{rad} is the temperature gradient relative to pressure and ∇_{ad} the adiabatic temperature variation in a specific element. The Ledoux criterion also takes the chemical composition into account, following the definition as given by Salaris & Cassisi (2017):

$$\nabla_{rad} > \nabla_{ad} + \frac{\chi_\mu}{\chi_T}\nabla_\mu \equiv \nabla_L, \tag{1.14}$$

i.e.,

$$\left(\frac{\mathrm{d\,lnT}}{\mathrm{d\,lnP}}\right)_{rad} > \left(\frac{\mathrm{d\,lnT}}{\mathrm{d\,nP}}\right)_{ad} - \frac{\chi_\mu}{\chi_T}\left(\frac{\mathrm{d\,ln}\mu}{\mathrm{d\,lnP}}\right) \tag{1.15}$$

where ∇_μ is the gradient of the molecular weight, i.e., the mean mass of the gas particles in atomic mass units, $\chi_\mu = \left(\frac{\mathrm{d\,lnP}}{\mathrm{d\,ln}\mu}\right)_{\rho,T}$, and $\chi_T = \left(\frac{\mathrm{d\,lnP}}{\mathrm{d\,lnT}}\right)_{\rho,\mu}$ (see, e.g., Maeder, 2009; Salaris & Cassisi, 2017, for more details). For a chemically homogeneous layer, i.e., a layer where no chemical gradient is present, the Ledoux criterion reduces to the Schwarzschild criterion.

This divides the interior of a star into four different regimes, a regime where the interior is radiative, and thus stable, according to both the Ledoux and the Schwarzschild criteria ($\nabla_\mu \geq 0$ and $\nabla_{rad} < \nabla_{ad}$), a regime where the interior is convective, a regime

where the interior undergoes semiconvection, and a regime where the interior undergoes thermohaline mixing (see also Figure 3 of Salaris & Cassisi, 2017). Convection occurs when $\nabla_\mu > 0$ and $\nabla_{rad} > \nabla_{ad}$. Semiconvection occurs because there is a difference between the border determined by the Schwarzschild and that determined by the Ledoux criterion (the term including ∇_μ). Semiconvection occurs in a layer that is stable according to the Ledoux criterion, but unstable according to the Schwarzschild criterion (Kato, 1966), i.e., $\nabla_\mu \geq 0$ and $\nabla_{ad} < \nabla_{rad} < \nabla_L$. The material in such a region is slowly mixed. The last regime is where thermohaline mixing takes place. This happens when ∇_μ is negative, for example due to accretion of material from another star during binary interactions, or due to off-center ignition of a nuclear burning cycle. In this case, the condition is $\nabla_\mu < 0$ and $\nabla_{rad} < \nabla_L$.

For massive stars, it is not simple to determine which of the two criteria should be used (see, e.g., Langer & Maeder 1995 and Salaris & Cassisi 2017 for a review). The main difference is that the Ledoux criterion shortens the lifetimes of hydrogen and helium burning (Robertson & Faulkner, 1972; Paxton et al., 2013; Salaris & Cassisi, 2017).

The upwards moving bubbles are strongly braked as soon as they cross the convective border determined by either the Schwarzschild or the Ledoux criterion. However, due to their non-zero velocity, they will move beyond this boundary by some extent. This process is generally called overshooting. It is often implemented in stellar evolution codes by either "step-overshoot" (see, e.g., Maeder, 2009, Chapter 6), or by "exponential overshoot" (Herwig, 2000).

For step-overshoot, the overshoot is modelled by a simple, free parameter, called α_{ov}. The overshoot distance, l, is then determined by this free parameter and the local pressure scale height H_p at the border of the convective region. The extent of the overshoot region is then $l = \alpha_{ov} H_p$. For exponential overshoot, a diffusive coefficient, D_{ov}, or an overshooting velocity is determined and used beyond the convective border. This approach has also has a free parameter, f_{ov}, and then the expression becomes $D_{ov} = D_0 exp(\frac{-2z}{f_{ov} H_p})$ (Herwig et al., 1997), and equivalent for the velocity (Cristallo et al., 2009) where z is the radial distance from the edge of the convective zone.

In most models of stellar evolution, the amount of applied overshoot is based on the combination of different observational constraints, such a the width of the main sequence in stellar clusters, the properties of eclipsing binary systems (see, e.g., Schaller et al., 1992; Schroder et al., 1997; Claret, 2007; Stancliffe et al., 2015), and asteroseismic observations (see, e.g., Montalbán et al., 2013; Aerts, 2013).

In general, to obtain the same effect, the values of f_{ov} are a factor of 10 smaller than α_{ov} (see, e.g., Doherty et al., 2017, and references therein), with the values for α_{ov} typically in the range 0.1-0.4 (see, e.g., Schaller et al., 1992; Claret & Torres, 2016; Stancliffe et al., 2015), and f_{ov} of the order 0.016 (Herwig, 2000; Stancliffe et al., 2015).

Aside from convection and semi-convection, other processes of internal mixing are mainly linked to stellar rotation, aside from thermohaline mixing.

The mixing described above changes the composition of regions in the star, along with the nuclear burning, following the equation for the change in the chemical composition:

$$\frac{\partial X_i}{\partial t} = \left(\frac{\partial}{\partial m}\right)_t \left((4\pi r^2 \rho)^2 D_{mix} \left(\frac{\partial X_n}{\partial m}\right)_t\right) + \frac{m_i}{\rho}\left(\sum_j r_{ji} - \sum_k r_{ik}\right) \tag{1.16}$$

where the first term is the change due to mixing and the second term is the change due to nuclear burning. In these equation, m_i is the mass of element i, X_i the mass fraction of the same element, D_{mix} is the diffusion coefficient of all mixing processes included in the calculation, and r_{ji} and r_{ik} are the reaction rates for creating and destroying element i, respectively. D_{mix} includes D_{conv} as defined by Equation 1.11, but also a term related to semi-convection (D_{semi}), and terms connected to the various types of rotational mixing (see next Section).

1.2.4 Rotation

As a result of their formation process, all stars rotate. Massive stars are generally observed to rotate at a velocity within a range of 0-300 km/s on the main sequence (see, e.g., Hunter et al., 2008). Endal & Sofia (1976) identified four ways in which rotation might affect the equations of stellar structure:

1. The centrifugal forces lower the effective gravity anywhere except on the axis of rotation.

2. Due to the centrifugal forces not being parallel to the gravitational force, the equipotential surfaces in the star are no longer spherical, and thus spherical symmetry, which is assumed for stellar calculations, is broken.

3. The radiative flux varies with the local gravity (the von Zeipel effect), the radiative force is no longer constant on an equipotential surface (von Zeipel, 1924; Maeder, 2009).

4. Rotation affects the criteria for convection, and changes how chemical elements and angular momentum are transported in the star.

For calculating stellar structure, this means that instead of the spherical surfaces that are generally used, isobars should be used. However, this means that the stellar structure equations as shown in Box 1 are no longer accurate and the equations cannot be expressed

in one dimension anymore. By implementing shellular rotation, which enforces a rotation that is constant as a function of the radius, the equations can be simplified (Meynet & Maeder, 1997). Due to strong horizontal turbulence, there is no chemical gradient on the isobars. Therefore, the problem becomes one-dimensional again.

Box 4: When the star is on the zero-age main sequence (in hydrostatic and thermal equilibrium) and the star is rotating, its structure can be described by the following set of differential equations, which have small alterations compared to the equations given in Box 1:

$$\frac{\partial r_P}{\partial m_P} = \frac{1}{4\pi r_P^2 \bar{\rho}} \tag{1.17}$$

$$\frac{\partial P}{\partial m_P} = -\frac{G m_P}{4\pi r_P^4} f_P \tag{1.18}$$

$$\frac{\partial L_P}{\partial m_P} = \epsilon_{nuc} - \epsilon_\nu + \epsilon_g \tag{1.19}$$

$$\frac{\partial \bar{T}}{\partial m_P} = -\frac{G m_P}{4\pi r_P^4} f_P \min\left[\nabla_{ad}, \nabla_{rad}\frac{f_T}{f_P}\right] \tag{1.20}$$

where

$$f_P = \frac{4\pi r_P^4}{G m_P S_P} \frac{1}{< g_{\rm eff}^{-1} >} \tag{1.21}$$

and

$$f_T = \left(\frac{4\pi r_P^2}{S_P}\right)^2 \frac{1}{< g_{\rm eff} >< g_{\rm eff}^{-1} >} \tag{1.22}$$

These are the adjusted equations of continuity or mass conservation (Equation 1.17), of hydrostatic equilibrium (Equation 1.18), of energy equilibrium (Equation 1.19), and of energy transport (Equation 1.20). In these equations, the subscript 'P' refers to the isobar with a pressure equal to P (this takes the effect of point 2 above into account), S_P is the surface of an area of equal pressure, $g_{\rm eff}$ is the effective gravity, and $< g_{\rm eff} >$ is $g_{\rm eff}$ averaged over the isobaric surface, $\bar{\rho}$ and $\bar{T}$ are the averages of the density and temperature in the volume between two isobars, all the other symbols are the same as in Box 1. f_P is a factor to account for the change in the centrifugal forces (number 1 above), and f_T is a factor to account for variations in the flux due to changes in the local gravity (number 3 above). The fourth point is taken into account by adding more terms to D_{mix} in Equation 1.16

Stellar rotation has several effects that are significant within this thesis: that it induces mixing and also that it has an effect on the shape of the star (flattening), the temperature and luminosity, and the mass-loss. Rotation leads to deformation of the star due to the centrifugal effects. The polar radius becomes smaller and the equatorial radius becomes larger. This effect is most visible in modelled stars that rotate close to their critical rotational velocity, i.e., the rotational velocity at the surface of the star for which the centrifugal force equals the gravitational force. If the star rotates faster than this, its

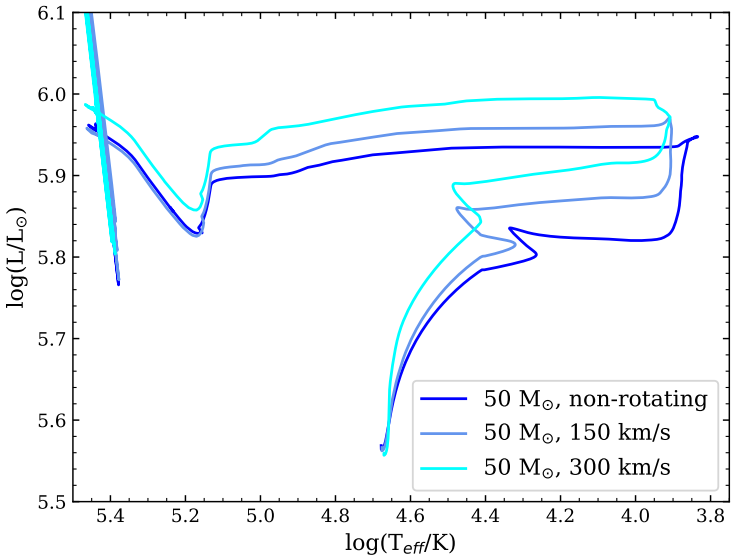

Figure 1.9: HRD for a 50 $M_\odot$ stars with three different initial rotational velocities, 0 km/s (blue), 150 km/s (light blue), and 300 km/s (cyan). These models were taken from Brinkman et al. (2021).

surface becomes unbound. For stars that rotate at lower velocities, the deviation from spherical symmetry is much smaller and the surface remains bound to the star.

The second factor of rotation relevant here is that on the temperature and the luminosity of the star. Figure 1.9 shows the HRD for a 50 $M_\odot$ star with three different initial rotational velocities. Initially, the star rotating at the highest initial rotational velocity is slightly cooler and dimmer than its non-rotating counterpart. This is due to expansion as a result of the centrifugal effects, which leads to a cooler and more opaque envelope, which, in turn, leads to a lower luminosity. Later in the evolution, however, the rotating stars have a higher luminosity than their non-rotating counterpart, and cool less when moving to the right of the HRD.

Rotation and the mass loss also affect each other. Overall, rotating enhances the mass loss through stellar winds. This boost is described by Langer (1998), who gives the following equation for the enhancement (Equation 4.20 in the paper):

$$\frac{\dot{M}}{\dot{M}_{v_{rot}=0}} = \left(\frac{1}{1-\Omega}\right)^{\xi} \tag{1.23}$$

where Ω is the angular velocity and ξ=0.43 (see Langer, 1998, for the full derivation) However, Maeder & Meynet (2000a) pointed out that some effects have been excluded in this treatment, and they give an adjusted equation (Equation 4.30 in their paper):

$$\frac{\dot{M}}{\dot{M}_{v_{rot}=0}} \simeq \frac{(1-\Gamma)^{\frac{1}{\alpha}-1}}{\left(1-\frac{4}{9}\left(\frac{v}{v_{crit}}\right)^2\right)^{\frac{1}{\alpha}-1}} \tag{1.24}$$

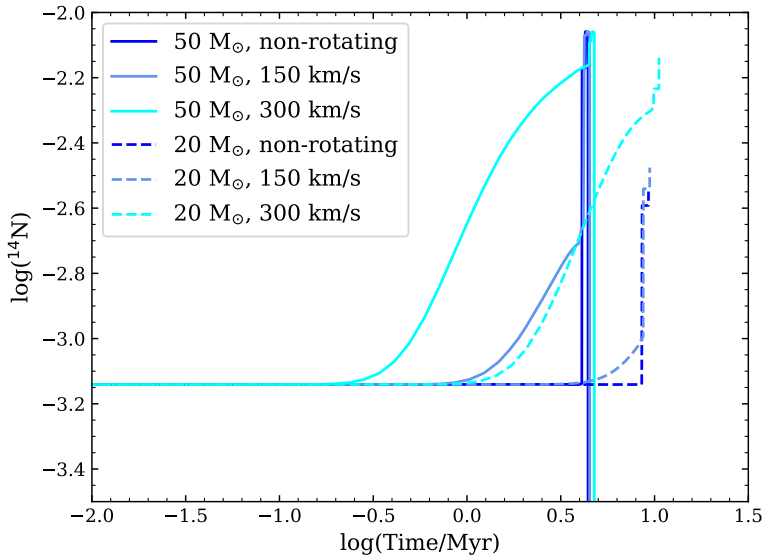

Figure 1.10: Nitrogen-14 surface mass-fraction as a function of time for a 20 and a 50 $M_\odot$ star, dashed and solid lines, respectively, with three different initial rotational velocities, 0 km/s (blue), 150 km/s (light blue), and 300 km/s (cyan). These models were taken from Brinkman et al. (2021).

in which Γ is the Eddington factor, and α a temperature-dependent empirical parameter from Lamers et al. (1995). This effect will be considered in this thesis (see for more details Chapter 2)

Finally, rotation affects the internal mixing of the star through various processes. This is observed through an enhancement in the surface nitrogen (^{14}N) mass-fraction in rotating stars. ^{14}N is used as a proxy because, as mentioned before, the ^{14}N(p,γ) reaction is the slowest of the CNO-cycle and leads to a build-up of this isotope. This effect is illustrated in Figure 1.10, where the surface mass-fraction of ^{14}N is shown as a function of time for a 20 and a 50 $M_\odot$ star with initial rotational velocities of 0, 150, and 300 km/s. For the rotating models, there is a slow increase of the surface mass-fraction, followed by a sharper increase as the deeper layers of the star are exposed by the winds. The main instabilities responsible for the redistribution of chemical elements and angular momentum often used in stellar evolution calculations are: the Solberg-Hoiland instability, the dynamical shear instability, the secular shear instability, the Eddington-Sweet circulation, and the Goldreich-Schubert-Fricke instability (for more details see, e.g., Maeder, 2009).

1.3 Binary evolution

The information presented in this section was also included in the introduction of Brinkman et al. (2019), but has been adapted and expanded from this work.

Stars, and especially massive stars, are seldom found alone, and often have one or more companions (see, e.g., Sana et al. 2012a and Duchêne & Kraus 2013). Depending on the period of the system, the stars can either interact, or evolve as if they were single stars.

These interactions can simply circularise the orbit and lead to tidal synchronisation, or can also include mass transfer between the components of the binary system, which may lead to a common envelope where the envelope of one of the stars engulfs both, or even a merger of the two stars. Sana et al. (2012a) found that more than 70% of all O-type stars ($\gtrsim 15\,M_\odot$) interact with their companion during their lifetimes (see also Kiminki & Kobulnicky 2012, Kobulnicky et al. 2012, Kobulnicky et al. 2014, and Duchêne & Kraus 2013). The binary systems show a strong preference for close orbits: Sana et al. (2012a) found that 71% of the O stars with a companion have periods shorter than 1500 days and will interact with their companion within their lifetimes. Of these systems, roughly 1/3 will eventually merge. More than 25% of O-stars will interact with a companion before the end of hydrogen burning in their cores (Sana et al., 2012a). Duchêne & Kraus (2013) determined that the binary fraction for B-stars is $\simeq 60\%$ and $\simeq 80\%$ for O stars, with no difference from whether these stars are in clusters or in the field. From the initial period distribution (i.e., the period on the main sequence), there is a peak at shorter periods (see, e.g., Sana et al., 2012b; Moe & Di Stefano, 2017). Instead, the binary systems do not show a clear preference for the mass ratio between the two stars (Moe & Di Stefano, 2017).

The recent detection of gravitational waves from merging binary black holes and binary neutron stars (see, e.g., Abbott et al., 2016, 2017) have further highlighted the astrophysical relevance of massive binary stars. Interestingly, binary interactions between massive stars can also influence the nucleosynthetic yields, such as of ^{26}Al (and other SLRs), as originally proposed by Braun & Langer (1995), and also for stable isotopes such as ^{12}C (see, e.g., Farmer et al., 2021). Mass transfer between the components of the binary system has a strong impact on the wind isotopic wind yields because it can radically alter the way stars in binaries lose mass as compared to single stars. Mass transfer between the stars can change the time at which mass loss starts as compared to a single star, as well as the amount of mass that is lost from the star (see Section 3.4, for more details and examples). Because of this difference, investigating massive binary systems is important for understanding both the Galactic distribution of ^{26}Al and other isotopes, as well as the possible stellar sources that produced the ^{26}Al, ^{36}Cl, and ^{41}Ca that was present in the ESS.

Binary systems are characterised by several parameters: stellar parameters, such as the masses of the individual stars (M_1 and M_2) and their metallicity, and the orbital parameters, such as the orbital separation (a) or period (P), the eccentricity (e), and the spin alignment (Hut, 1981). In this work, I always refer to the initially more massive star the "primary" with mass M_1, and the initially less massive star as the "secondary" with mass M_2. I define the mass ratio as $q{=}M_2/M_1$ unless otherwise specified.

For systems that undergo interactions, it is often assumed that their orbits have been circularised (Zahn, 1977), which sets the eccentricity to 0. The circularisation of the

system does not depend on the initial masses, since it is a dynamical process rather than a star formation process (Hurley et al., 2002). In this case, and under the assumption that the two stars can be treated as point masses, as well as that the stars are in rigid rotation and synchronised with the orbital motion, the Roche model can be applied to the binary system (Eggleton, 1983). With this model, it is possible to calculate the equipotential surfaces between the two stars, and most importantly, the equipotential surface that touches in the inner Langrangian point, which is commonly referred to as the Roche lobe (see Figure 1.11). During the evolution of a star, the radius changes in size. Mass transfer takes place when the radius of the star is equal to the radius of the Roche lobe, so when the star fills its Roche lobe. Then, mass will flow from one star to the other through the L1 point. If the star becomes so large that it overflows the outer Lagrange points (L2 or L3, see Figure 1.11), the matter will flow out of the system.

The radius of the Roche lobes (R_L) for either star can be calculated by using Eggelton's approximation for the Roche lobe:

$$\frac{R_{L1}}{a} = \frac{0.49q^{-\frac{2}{3}}}{0.6q^{-\frac{2}{3}} + ln(1 + q^{-\frac{1}{3}})} \tag{1.25}$$

where q is defined as above. To calculate the Roche lobe of the secondary star, q is simply inverted (i.e., M_1/M_2). When the orbital period is given instead of the orbital separation, the two can be converted by applying Kepler's Third Law:

$$\frac{a^3}{P^2} = \frac{G(M_1 + M_2)}{4\pi^2}. \tag{1.26}$$

By comparing the radius of the star and the size of the Roche lobe, it can be determined when mass transfer is expected to take place in a binary system with a given set of parameters. The mass transferred between the stars can be accreted by the secondary, which is called conservative mass-transfer, or the mass is fully or partially expelled from the system, which is called (fully) non-conservative mass-transfer. The primary generally loses the majority of its hydrogen envelope in this process. This can have major consequences for the rest of the evolution of both stars. For example, a secondary star that would under single star circumstances become a white dwarf could accrete enough mass to become a supernova instead, and a primary could turn into a helium star, instead of becoming a giant.

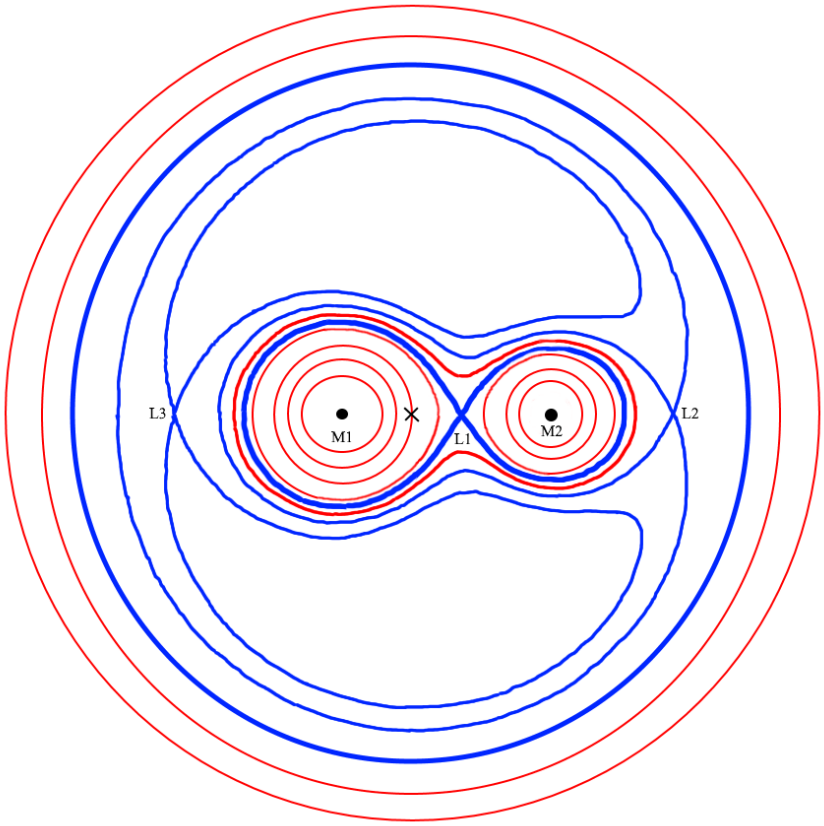

Figure 1.11: Schematic figure of the Roche potential of a binary with (point) masses M_1 and M_2. The blue lines indicated the surfaces going through the Lagrange points, the red lines are normal equipotential surfaces. The x marks the orbital axis. M_1 and M_2 are the stars represented as point masses. In this example, $M_1 > M_2$ so $q < 1$. The red and blue lines show the equipotential surfaces of the Roche potential, with the blue lines the surfaces passing through the Lagrange points (where the gravitational and centrifugal forces balance each other out). These points are marked with L1, L2, and L3. The Roche lobe is the surface passing through the L1 point. *This figure was adapted from Figure 11.3 of Prialnik (2009)*

One way to classify binary systems is the following, where they are divided into three groups (Kopal, 1955);

- Detached, when there is no mass transfer between the stars through Roche lobe overflow.
- Semi-detached, when one of the stars fills its Roche lobe.
- Contact, when both of the stars fill their Roche lobe.

However, even in the detached phase there can be exchange of mass between the stars, if the stellar winds are funnelled through the L1 point between the stars (Mohamed & Podsiadlowski, 2007, 2012). This is, for example, the pathway to form so-called carbon enhanced metal poor (CEMP)-stars, for which matter from an asymptotic giant branch star is accreted onto their companion. However, for the scenario in this thesis, this mass transfer is not important and not studied here.

In the literature, also different cases of mass transfer have been distinguished for semi-detached binary systems (Kippenhahn & Weigert, 1967; Lauterborn, 1970):

- Case A: occurring during core hydrogen burning, as the star expands on the main sequence.
- Case B: occurring after core hydrogen burning and during hydrogen-shell burning, as the star expands after the core hydrogen exhaustion.
- Case C: occurring after core helium burning, as the star expands after helium exhaustion in the core or during the asymptotic giant branch phase, for low-mass stars

Case A mass transfer requires short orbital periods, up to a few days. Case B mass transfer occurs over a larger range of orbital periods. Many systems that undergo Case A mass transfer also undergo a later Case B mass transfer, referred as Case AB (Wellstein et al., 2001). For massive stars, helium burning can occur at a larger radius than helium ignition. When this leads to mass transfer, it is between Case B and Case C, and is sometimes referred to as Case BC. Case C systems interact very late in the evolution and are not considered in the scope of this work because their impact on the chemical and isotopic yields is very minimal. It is also possible for the stars to be too far apart, in this case, the stars will be in a binary system, but evolve as if they were single stars. In the context of the research presented here, the interest is mainly in systems undergoing Case A or Case B mass transfer, because during those stages, the products of hydrogen and

helium burning can be expelled from the star through non-conservative mass-transfer. In Sections 3.1 and 3.2, I will discuss in detail binary systems undergoing Case A and Case B mass transfer with initial primary masses of 20 $M_\odot$ and 50 $M_\odot$.

What happens to the system during the mass transfer depends partially on whether the secondary star accretes matter or not, as mentioned earlier. This is called the "conservativeness" of the mass transfer, or the mass-transfer efficiency. Conservative mass-transfer means that all the mass that is lost from the primary star is accreted by the secondary. At the other extreme is fully non-conservative mass-transfer, which means all mass is lost from the binary system. There are several different ways to model how the mass is lost from the system, for example, the fast or Jean's mode in which the mass is lost like a wind from the primary, isotropic re-emmission, where the mass is ejected by the secondary star, and a circumbinary ring where the ejected mass forms a ring around the binary system. If the secondary star instead accretes a large amount of mass, the mass ratio of the system can even be inverted. This happens for example in the so-called Algol systems (van Rensbergen et al., 2011). The other major factor in determining the fate of the system is how the orbit changes as mass is transferred and/or lost from the system (Soberman et al., 1997). The response of the system can lead to the formation of a so-called common envelope (Paczynski, 1976; Dominik et al., 2012), i.e., a system in which both the primary and the secondary star are inside the envelope of the primary star. This configuration can lead either to a merger, or to the formation of a very close system with a very short orbital period (see Ivanova et al., 2013, for a review). The lack of knowledge of the interaction between the two stars and their shared envelope makes this phase of the current challenges of binary evolution (De Marco & Izzard, 2017).

Aside from the transport of mass between the stars and the interstellar medium, mass transfer is also a means of angular momentum transport. This limits the amount of mass that can be accreted by the secondary star. Packet (1981) state that accretion of 10% of the mass of a star will lead to a spin-up to the break-up velocity of a star (see also Section 1.2.4). Tidal interaction and mass loss through stellar winds can eject some of this angular momentum (de Mink et al., 2014).

Due to the interactions between the stars in a binary configuration, the outcomes of the stellar evolution as sketched earlier in this chapter do not always hold. Especially for supernovae, in a binary configuration, the mass limit for these events can shift to higher initial masses depending on the initial parameters of the binary system (see, e.g., Podsiadlowski et al., 2004; Tauris et al., 2015; Poelarends et al., 2017), especially for the stars on the supernova boundary, 8-15 $M_\odot$ for single stars (see, e.g., Doherty et al., 2015), due to mass transfer between the components of the system.

In this thesis, I consider in detail the coupling between nucleosynthesis and binary interactions.

1.4 Aim and overview of the thesis

The goal of the thesis is to determine the wind yields of ^{26}Al, ^{36}Cl, ^{41}Ca, and ^{60}Fe of massive stars, under different circumstances, such as for rotating and non-rotating stars, as well as for the primary stars in a binary system, and how these different configurations (rotation, binarity) affect the yields. With these yields, I can determine the impact on the interpretation of the SLR abundances in the ESS and whether binary systems are able to explain the abundances of these isotopes. I achieve this by calculating full stellar and binary evolution models with the MESA stellar evolution code. In Chapter 2, I discuss the input physics for the models used for my research presented here. In Chapter 3, I discuss the stellar evolution details of the models and compare them to studies from the literature. In Chapter 4, I discuss the yields for these models and again compare them to yields from the literature. In Chapter 5, I discuss the impact of the single star models on the SLR origin for the ESS and discuss which stellar models are the potential sources to have polluted the ESS with ^{26}Al, ^{36}Cl, and ^{41}Ca. In Chapter 6, I discuss the uncertainties attached to binary evolution, the effects of uncertainties in reaction rates. I also present the first results of the effect of binary interactions on the yields of ^{36}Cl, ^{41}Ca, ^{60}Fe, ^{19}F, and ^{22}Ne, as well as a brief reminder of those effects on ^{26}Al, when the primary stars are evolved up to the core collapse. In Chapter 7, I give a summary and the conclusions of this work, as well as a list of future work. In Chapter 8, I present the same summary and conclusions in Hungarian.

Chapter 2

Method

The method presented in this chapter is adapted and expanded from the methods as presented in Brinkman et al. (2019) and Brinkman et al. (2021).

For the research presented in this thesis I have calculated stellar and binary evolution models with the 1D code Modules for Experiments in Stellar Astrophysics (hereafter MESA), version 10398 (Paxton et al., 2011, 2013, 2015, 2018). While several other stellar evolution codes allow for modelling of stellar and binary evolution (see for an overview De Marco & Izzard, 2017, Table 2), for the work presented in this thesis, MESA was used because it is a widely supported tool. It also includes the option of future work on modelling the supernova explosions, as well as of extending the nuclear networks, and tune the numerical recipes used, for example, for mass loss. The input physics I have used for the calculations of the single stars and the binary systems is described in the next sections.

Three sets of models have been calculated with MESA: 1) a set of massive, non-rotating, *single* star models up to the onset of carbon burning (hereafter Set 1), 2) a set of massive, non-rotating, *binary* models up to the onset of carbon burning (hereafter Set 2), and 3) a set of massive, *rotating* and non-rotating, single star models up to core-collapse (hereafter Set 3).

For the first two sets of models, the focus is on calculating the wind yields for ^{26}Al. For Set 3, the other three SLRs (^{36}Cl, ^{41}Ca, and ^{60}Fe), as well as the stable isotopes ^{19}F and ^{22}Ne, are also considered. In Section 2.1, I discuss the input physics for Set 1 and Set 2. In Section 2.2, I discuss the additional physics for the binary models of Set 2. In Section 2.3, I discuss the changes made for Set 3 compared to Set 1, as well as the input physics for the rotating models. The most important settings for these three sets are given in Table 2.1). In Section 2.4, I discuss how the yields were calculated.

The initial masses for the models of Set 1 and Set 3 were 10, 15, 20, 25, 30, 35, 40, 45, 50, 60, 70, and 80 $M_\odot$. For Set 2, the primary masses of the binary systems are the same, except that there are no binary systems with initial primary masses of 70 and 80 $M_\odot$. The masses of the secondary stars are set by the mass ratio, $q = \frac{M_2}{M_1}$. The mass ratio used here is $q = 0.9$, unless otherwise indicated. I have used only one mass ratio for the

Table 2.1: Input physics for the three sets of stellar models.

	Set 1	Set 2	Set 3
Paper	Brinkman et al. (2019)	Brinkman et al. (2019)	Brinkman et al. (2021)
Type	single, non-rotating	binary, non-rotating	single, rotating
Initial masses ($M_\odot$)	10, 15, 20, 25, 30, 35, 40 45, 50, 60, 70, 80	10, 15, 20, 25, 30, 35, 40 45, 50	10, 15, 20, 25, 30, 35, 40 45, 50, 60, 70, 80
Nuclear network Reaclib	63 NACRE	63 NACRE	97 JINA
α_{mlt}	1.5	1.5	1.5
α_{ov}	0.2	0.2	0.2 for core burning 0.1 for hydrogen shell 0 for other shells
α_{sc}	0.1	0.1	0.1
Rotation	0	0	0, 150, and 300 km/s
Stop	carbon ignition or 10^4 time steps	carbon ignition or 10^4 time steps or reverse mass-transfer	core-infall of 300 km/s

calculations to limit the parameter space, even though the mass ratio will have different values in nature. The mass ratio of 0.9 was chosen to compare directly to the two models calculated by Braun & Langer (1995).

2.1 Input physics for Sets 1 and 2

Within MESA a large number of choices can be made for the input physics (see Paxton et al., 2011, 2013, 2015, 2018). Here I briefly describe and motivate my main choices.

For the calculation of the ^{26}Al-yield, I have evolved the stars of Set 1 up to the onset of carbon burning. At this point the further evolution will only take a few thousand years or less before the explosion, and this is not enough time for either the winds to expel much more mass from the star, or for ^{26}Al to decay further. Therefore, the ^{26}Al yield is the same as it would be if the whole evolution was calculated to core collapse. Also, because ^{26}Al is destroyed during helium burning by neutron-capture reactions (see Figure 1.1), there is almost no ^{26}Al left in the stellar core at the onset of carbon burning and therefore it is not needed to evolve the stars past this stage for this particular isotope. If the stars do not reach the onset of carbon burning due to computational difficulties, the simulations were stopped after a total of 10^4 time steps from the beginning of the calculation.

The initial composition used in this study is solar with Z=0.014, following the abundances as given by Asplund et al. (2009). For the initial helium content I have used Y=0.28. The nuclear network used for Set 1 and Set 2 contains all the relevant isotopes for hydrogen, helium burning, and early carbon burning, as well as all relevant isotopes

connected to the production and destruction of ^{26}Al, including the both ground and isomeric states of ^{26}Al. For a visual representation of the isotopes and reactions connected to ^{26}Al production and destruction, see the top right panel of Figure 1.1, and Figure 1.5. This network thus contains the following 63 isotopes: n, ^{1,2}H, ^{3,4}He, ^{6,7}Li, ^{7,8}Be, ^{8}B, $^{12-14}$C, $^{13-15}$N, $^{14-19}$O, $^{17-20}$F, $^{19-23}$Ne, $^{21-24}$Na,$^{23-26}$ Mg, ^{25}Al, ^{26}Al$_g$,^{26}Al$_m$,^{27,28}Al, $^{27-30}$Si, $^{28-31}$P, $^{30-34}$S, $^{32-35}$Cl, and ^{56,57}Fe.

The reaction rates are based on the compilation of thermonuclear rates by Angulo et al. (1999, NACRE), and when not available on that by Caughlan & Fowler (1988), see Section 4.4 of Paxton et al. (2011). In the version 10398 of MESA the isomeric states are implemented in the code. The reaction rates for the interactions between the ground state and the isomeric state of ^{26}Al, ^{26}Al$_g$ $\leftrightarrow$ ^{26}Al$_m$, are taken from Gupta & Meyer (2001). The other reactions involving ^{26}Al states are taken from Straniero et al. (2013) and Iliadis et al. (2010), which are the most up-to-date rates for ^{26}Al. In Section 6.2.1, I discuss the uncertainties in the reaction rates and their influence on the production and yields of ^{26}Al.

Several free parameters need to be set in MESA to model convection and mixing and a choice can be made between the Ledoux and Schwarzschild criterion for convection. I have used the Ledoux criterion (Equation 1.14) to establish the location of convective boundaries. The mixing-length parameter, α_{mlt}, was set to 1.5. Semi-convection, which occurs in a region that is stable according to the Ledoux criterion but unstable according to the Schwarzschild criterion, is modelled by a free parameter α_{sc}. I have used α_{sc} = 0.1, which I found to give results that best resemble the non-rotating tracks in the Hertzsprung-Russell diagram by Maeder & Meynet (2000b, Figure 6). I made use of convective overshooting via the "step-overshoot" scheme, where the overshoot region extends above the convective border by a length l, given by $l = \alpha_{ov} H_p$, where H_p is the pressure scale height at the convective border and α_{ov} is a free parameter. The exact value of this parameter is uncertain (see, e.g., Brott et al. 2011, Section 2.4). I have chosen to use α_{ov} = 0.2, which gives moderate overshooting and is within the uncertainties given by Brott et al. (2011). This value is commonly used by other groups to compute massive stars (Claret & Torres 2016, and references therein). In this work, I only consider overshoot above a convective core or shell, and do not consider an overshoot region below a convective shell.

I have used the wind mass-loss scheme as described in Brott et al. (2011) and implemented by Schootemeijer & Langer (2018) for MESA. This mass-loss scheme is a combination of the prescriptions by Nieuwenhuijzen & de Jager (1990); Hamann et al. (1995); Vink et al. (2000), and Vink et al. (2001) and is commonly used to parametrise mass loss from massive stars (see also Section 1.2.2).

I did not include stellar rotation in my first 2 sets of models. The focus of Set 2 is the potential impact of binary interactions on the yields, compared to the non-rotating

single star models of Set 1. In Set 3 rotation is included to study the associated additional complications and uncertainties (for more details see, e.g., Maeder, 2009).

2.2 Treatment of binary interactions in Set 2

2.2.1 The semi-numerical binary analytic scheme

To explore the influence of the initial period of the binary systems on the ^{26}Al yields for a given initial mass of the primary star, I have first applied an analytical binary scheme to the simulation of the single stars. This analytical scheme I have called the semi-numerical binary (SNB) scheme. In this scheme, I vary the two parameters that I expect to have the greatest impact on the yields: the primary mass, M_1, and the orbital period, P, while I keep the mass ratio constant, $q = 0.9$. By combining Kepler's Third law (Equation 1.26) and Eggleton's approximation of the size of the Roche lobe (Equation 1.25) relative to the period, the size of the Roche lobe for a given period and combination of stellar masses can be determined from these two parameters.
The definition of the orbital separation (a) is:

$$a = \sqrt[3]{\frac{G(M_1 + M_2)P^2}{4\pi^2}} \tag{2.1}$$

and then the size of the Roche lobe (R_L) is:

$$R_L = \left(\frac{0.49q^{-\frac{2}{3}}}{0.6q^{-\frac{2}{3}} + ln(1 + q^{-\frac{1}{3}})} \right) a. \tag{2.2}$$

The comparison between the size of the Roche lobe with the radius of the fully evolved single star gives an estimate on when the binary interaction will take place. There is likely to be a small off-set compared to the fully numerical binary simulations, because the change in the size of the Roche lobe due to mass loss through winds of either star is not taken into account in this approach, and neither is the change in the orbital period due to mass loss. Therefore, the size of the Roche lobe is determined only by the initial configuration of the system. The duration of the mass transfer phase is not taken into account either, as the envelope is stripped instantaneously. This SNB method allows an initial estimation of the amount of ^{26}Al that can potentially be the ejected by a binary system, which I then use to target the range and compare to the full numerical models described in Section 2.2.2 (See Chapters 3 and 4 for the comparison).

With Equation 2.2, I calculate the size of the Roche lobe for systems with periods ranging from a few to ∼100 days. The limits for the period were chosen based on the stellar radius of the primary stars and in such a way that the mass transfer is either a Case A (occurring

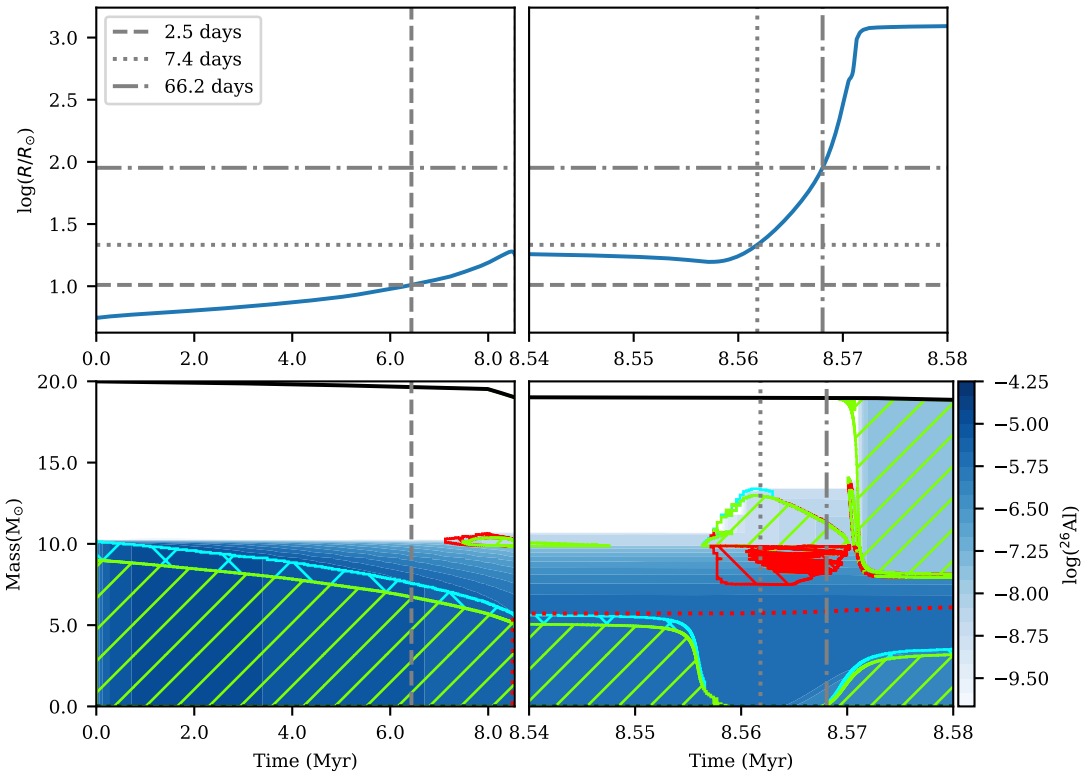

Figure 2.1: Evolution of the mass regions (lower panels) and the radius (upper panels) of a 20 $M_\odot$ star from Set 1 in time to illustrate the principle of the semi-numerical binary scheme. The upper left panel shows the slow expansion of the radius during the main sequence. The upper right panel shows the rapid expansion at the end of hydrogen burning and the onset of helium burning. The horizontal lines represent the size of the Roche lobe for three periods, 2.5, 7.4, and 66.2 days. The time when the size of the Roche lobe crosses the radius (grey, vertical lines), represents the time when the mass transfer would start if the system was a binary and therefore the envelope is stripped here. The bottom panels present the corresponding KHD (see also Figure 1.2 in Section 1.2.1). The green shaded areas correspond to areas of convection, the cyan shaded areas to overshooting, and the red shaded areas to semi-convection. The red dotted line in the lower right panel indicates the hydrogen depleted core, or helium core, where the hydrogen content is below 0.01 and the helium content is above 0.1. The colour scale shows the ^{26}Al mass fraction as a function of the mass coordinate and time. The vertical lines in the lower panels correspond to the vertical lines in the top panels, showing where in the evolution the envelope is stripped.

during hydrogen burning) or a Case B (occurring after hydrogen, but before the central ignition of helium). To determine the shortest possible orbital period for a binary system to use in the SNB scheme, it is assumed that the star fills its Roche lobe directly at the start of the main sequence. This value was then multiplied by 2 to give the shortest period used here, such that the stars are not touching each other from the start. This shortest period is around 2-3 days depending on the initial mass of the model. The longest period was chosen to be that of the widest orbit in which the system undergoes Case B mass transfer without the primary star having a convective envelope, which is ∼100 days. The convective envelope develops during helium burning (see also Figure 1.2 and the lower panels of Figure 2.1). Mass transfer cases with a convective envelope are between Case B and Case C, where Case C mass transfer refers to all mass transfer that occurs after core helium burning has finished. The reason for choosing to consider only Case A and Case B mass transfer is that the ^{26}Al in the envelope decays after hydrogen burning. This can be seen in the lower left panel of Figure 2.1, where the mass fraction of ^{26}Al is already decreasing in the areas where the hydrogen burning core has retreated. Because the strongest mass loss in massive stars occurs after the main sequence and during helium burning, mass transfer occurring after helium burning will have yields almost identical to the single star (further details can be found in Chapters 3 and 4). Aside from this reasoning to choose relative close orbital separations, the observational evidences by Sana et al. (2012a) show that massive star binaries preferentially have short orbital periods.

Within the SNB scheme, at the time when the stellar radius equals the size of the Roche lobe for a given orbital period, I assume that the full envelope of the star is stripped away. Depending on the evolutionary stage, this stripping is either down to the upper border of the overshoot region, for mass transfer during hydrogen burning (cyan dashed area in the lower panels of Figure 2.1), or down to the top of the hydrogen-depleted or helium core, for mass transfer after hydrogen burning (red dashed line in the bottom right panel of Figure 2.1). The helium core is defined as the part of the star where the hydrogen mass-fraction is below 0.01 and the helium mass-fraction is above 0.1, following the definition used in MESA. For these stripped regions, I calculate the ^{26}Al yield by summing the amount of ^{26}Al in all the mass stripped away. Figure 2.1 illustrates the procedure for a 20 $M_\odot$ star. The horizontal lines are the sizes of the Roche lobes for initial orbital periods of 2.5, 7.4, and 88.2 days. The vertical lines (dashed, dotted, and dashed-dotted for the respective periods) show where the envelope is stripped for these initial periods. For the system with an initial period of 2.5 days, the envelope is stripped down to the top of the overshoot region (cyan dashed area). For the other two periods, the envelope is stripped down to the hydrogen depleted core (red dotted line).

2.2.2 The numerical binary input physics

After exploring the period parameter space with SNBs, I made a selection of systems to use for a fully numerical, more computationally demanding, binary simulation with MESA. In the SNB scheme, assumptions are made that are not fully physical, such as the instantaneous and complete stripping of the envelope, and changes in the orbital parameters and in the masses of the stars are not taken into account when calculating the Roche lobe. Therefore, the yields of the numerical binaries will be somewhat different, and likely lower than the yields calculated following the SNB scheme, as less material may be removed and decay of ^{26}Al will take place during the non-instantaneous mass-transfer phase.

To compare between the results of the SNB scheme and the fully numerical binary models ran with MESA, I have selected 3-6 initial periods from the 15-20 initial periods used in the SNB scheme. The periods for the fully numerical binary models are more sparsely sampled than for the SNBs, but also range from a few to $\sim$100 days. The 3-6 selected periods cover both cases of mass transfer, and I selected specifically the systems on the border of Case A and Case B to see the impact of the orbital adjustment. This means that out of the 3-6 periods, one is the Case A closest to the end of the main sequence, and one is the Case B closest to the beginning of the Hertzsprung Gap, where the star starts to expand rapidly, as determined by the SNB scheme. Also the second shortest period as determined by the SNB scheme was selected. The other periods fill up the rest of the period space. Because the radius of the Roche lobe is determined by the initial mass of the stars and the mass ratio, the periods are different for each system, just as for the SNB scheme. The set of initial periods used for the fully numerical binary simulations can be found in Table 3.3.

In these numerical simulations the focus is on the yields from the primary star, i.e., the secondary star is fully evolved as well and not treated as a point mass to take the orbital adjustments due to mass loss of the secondary into account, but its wind is not considered for the ^{26}Al yields of the system.

One of the most important, but also a very uncertain parameters in binary evolution is the efficiency of the mass transfer. The mass-transfer efficiency is the fraction of the mass lost by the primary star that is accreted by the secondary star. In MESA the parameter β is defined as the fraction of mass lost from the system, such that the mass-transfer efficiency is equal to 1-β. In this thesis I will follow the definition as used in MESA, but note that it is also quite common in the literature to use β for the mass-transfer efficiency itself. With the definition used in MESA, β=1 means that no mass is accreted by the secondary, and hence all the transferred mass is lost from the system, also known as fully non-conservative mass-transfer, while β=0 means that all mass is accreted by the secondary and hence none of the transferred mass is lost by the system, which is referred

to as conservative mass-transfer. Observational evidence suggests that different values for β occur in nature, from rather conservative to non-conservative mass-transfer (see, e.g, Pols et al., 1991; de Mink et al., 2007; Schootemeijer et al., 2018). Main evidence that for massive binaries ($\gtrsim$ 20 $M_\odot$) the mass-transfer efficiency is low, comes from from attempts to reproduce the galactic population of Wolf-Rayet+O-star binaries. These systems require a $\beta \gtrsim 0.8$ (Petrovic et al., 2005; Shao & Li, 2016). For this thesis, I have chosen to use fully non-conservative mass-transfer, β=1. Using this gives an upper limit of the amount of ^{26}Al ejected from the binary systems, since nothing is accreted by the secondary. For a few selected systems I have also tested the effect of varying the mass-transfer efficiency (Section 6.1.2), as well as the mass ratio (Section 6.1.3). The eccentricity of the systems was not varied because it is reasonable to assume that all systems are circularised by tidal friction (Zahn, 1977) by the time the interaction between the stars takes place.

2.3 Input physics for Set 3

As for the models of Sets 1 and 2 described above, for Set 3 I have also used version 10398 of MESA (Paxton et al., 2011, 2013, 2015, 2018) to calculate massive star models with and without rotation. The key input parameters and the changes compared to the input physics given in Section 2.1 are discussed below.

2.3.1 Input physics for the evolution up to the core-collapse

The initial masses of the models are 10, 15, 20, 25, 30, 35, 40, 45, 50, 60, 70, and 80 $M_\odot$. The initial composition used is the same as mentioned before for Set 1 and Set 2, i.e., solar composition with Z=0.014 (Asplund et al., 2009). To model all burning cycles beyond hydrogen, helium, and early carbon burning up to the core-collapse, the nuclear network was extended from the network described in Section 2.1. The extended nuclear network contains all the relevant isotopes for the main burning cycles (H, He, C, Ne, O, and Si), as well as all the relevant isotopes connected to the production and destruction of ^{26}Al, ^{36}Cl, ^{41}Ca, ^{19}F, ^{22}Ne, and ^{60}Fe. Including the ground and isomeric states of ^{26}Al, the total nuclear network contains therefore the following 209 isotopes: n, ^{1,2}H, ^{3,4}He, ^{6,7}Li, $^{7-10}$Be, $^{8-11}$B, $^{12-14}$C, $^{13-16}$N, $^{14-19}$O, $^{17-20}$F, $^{19-23}$Ne, $^{21-24}$Na,$^{23-27}$ Mg, ^{25}Al, ^{26}Al$_g$,^{26}Al$_m$,^{27,28}Al, $^{27-33}$Si, $^{30-34}$P, $^{31-37}$S, $^{35-38}$Cl, $^{35-41}$Ar, $^{39-44}$K, $^{39-49}$Ca, $^{43-51}$Sc, $^{43-54}$Ti, $^{47-58}$V, $^{47-58}$Cr, $^{51-59}$Mn, $^{51-66}$Fe, $^{55-67}$Co, $^{55-69}$Ni, $^{59-66}$Cu, and $^{59-66}$Zn. Following Farmer et al. (2016, and references therein) a nuclear network of 204 isotopes is optimal for following the full evolution of a star, especially because it includes isotopes that influence Y_e, the electron

fraction, which profile is important for determining the core collapse (see Heger et al., 2000) and the results of the explosive nucleosynthesis (see, e.g., Chieffi & Limongi, 2013).

In Set 3, I have changed the reaction rate library from NACRE, which was used for the first two sets of models, to the latest JINA reaclib (Cyburt et al., 2010), version 2.2. The main difference that affects the stellar evolution is the ^{14}N(p,γ)^{15}O, rate which is updated to (Imbriani et al., 2005).

As for Set 1 and 2, I make use of overshooting via the "step-overshoot" scheme for Set 3 with $\alpha_{ov} = 0.2$ for the central burning stages. For better convergence of the models, especially in the later stages of the evolution, I switched off the overshoot on the helium burning shell and the later burning shells and the overshoot on the hydrogen shell was reduced to $\alpha_{ov} = 0.1$.

I have also changed the earlier mentioned wind mass-loss scheme from what was used for the first two sets of models. For the hot phase ($T_{\rm eff} \geq 11$ kK) I use again the prescription given by Vink et al. (2000, 2001) and for the cold phase ($T_{\rm eff} \leq 10$ kK) I use Nieuwenhuijzen & de Jager (1990). For the Wolf-Rayet phase in Set 3 I use Nugis & Lamers (2000) instead of Hamann et al. (1995).

I have evolved the stars to the onset of core collapse, using an (iron-)core infall velocity of 300 km/s as the termination point of the simulations. At this point the mass loss through winds is over, which is the main focus here. Other studies use a core infall velocity of 1000 km/s, however, the core structure is well established at 300 km/s and it can be used for further studies of the core collapse and supernova explosion (A. Sieverding, private communication).

2.3.2 Input physics for rotation

From observations, it is well known that massive stars rotate, and often at rates high enough to influence their evolution (see, e.g., Maeder & Meynet, 2000b, for a review). In the first two sets of models, rotation was not included because I focused on the impact of binary interactions instead. For the third set of models, I do include rotation but do not consider full binary interactions.

Rotation in MESA is implemented as in Heger et al. (2000) (see also Paxton et al., 2013). The two free parameters $f_{\rm c}$ and f_μ, as introduced by Pinsonneault et al. (1989), are set to their commonly used values 1/30 and 0.05 (as calibrated by Heger et al., 2000) to match the solar ^{7}Li surface abundance, as well as the increase of CNO elements at the surface of rotating massive stars. The contribution of the mixing processes induced by rotation are reduced by a $f_{\rm c}$ before they are added to the total diffusion coefficient for the transport of chemical elements, which gives then $D_{mix} = D_{conv} + D_{sem} + f_c(\sum D_{rot})$ (see, e.g., Heger et al., 2000). The term f_μ describes the sensitivity of the rotationally

induced mixing to gradients in the molecular weight, i.e., ∇_μ is replaced by $f_\mu \nabla_\mu$.

I included the Taylor-Spruit dynamo for angular momentum transport, following the implementation of Heger et al. (2005), because this mechanism allows for efficient transport of angular momentum, which is needed to allow for stellar evolution models to match observed rotation rates in many different stellar objects in different stellar evolutionary phases (see, e.g., recent publications of Aerts et al. 2019 and Belczynski et al. 2020). It does not impact the transport of chemical elements.

I have used initial rotational velocities of 150 and 300 km/s, to cover the rotational velocities observed on the main-sequence (see, e.g., Hunter et al., 2008) and for easier comparison to the yield sets of Limongi & Chieffi (2018). For the models that include the effects of rotation, the wind will receive a rotational boost. MESA includes the boost as given by Langer (1998). However, Maeder & Meynet (2000a) pointed out that some effects have been excluded in this treatment, and therefore I implemented the rotational boost as in their Equation 4.30 (see also Equation 1.24 in Section 1.2.4), following the initial implementation for MESA by Keszthelyi et al. (2020), to which I have added the temperature-dependence of an empirical "alpha-parameter", determined by Lamers et al. (1995). I implemented a step-function to connect Equations 2 and 3 from Lamers et al. (1995) at $\log(T_{\rm eff}) = 4.325$, to match the data presented in Figure 7 by the same authors. Below $\log(T_{\rm eff}) = 3.90$, the alpha-parameter is undefined and I have set it to 1, which makes the boost disappear. Above $\log(T_{\rm eff}) = 4.7$, the alpha-parameter is again undefined. Here I have set it to 0.52, extrapolating the results of Lamers et al. (1995).

2.4 Yield calculations

My first focus is on calculating M_{26}^{wind}, i.e., the amount of ^{26}Al in $M_\odot$ that is carried by massive star winds and by binary mass transfer into the interstellar medium. To calculate these yields, I need to integrate over time because unlike a supernova explosion which happens on very short timescales (the collapse taking a few seconds and the shock wave reaching the surface a couple of hours), stellar winds take place over a longer timescale (order of Myr, depending on the initial mass of the star). This yield is calculated as (see, e.g., Palacios et al., 2005b, Equation 1):

$$M_{26}^{wind}(M_i) = \int_0^{\tau(M_i)} {}^{26}Al_s(M_i,t)|\dot{M}(M_{ini},t)|dt \tag{2.3}$$

where $M_{26}^{wind}(M_i)$ is the wind yield for a certain initial mass M_i, $\tau(M_i)$ is the total lifetime of a certain of initial mass M_i, ${}^{26}Al_s(M_i,t)$ is the surface mass-fraction of ^{26}Al at time t, and $\dot{M}(M_{ini},t)$ is the mass loss rate at a given time t. This translates to the following

equation when applied to the MESA output:

$$M_{26}^{wind}(M_i) = \sum_{0}^{n} {}^{26}Al_s(n)[M(n) - M(n+1)] \tag{2.4}$$

where n equals the amount of time steps taken in the calculation, $^{26}\mathrm{Al}_s(n)$ is the surface mass-fraction of ^{26}Al at a given time step n, and $[M(n) - M(n+1)]$ is the mass lost between two time steps.

Because ^{26}Al is radioactive, part of the expelled ^{26}Al decays in the interstellar medium after it is expelled from the star. This adds an extra time-dependence to the yield, (see, e.g, Figure 17 of Limongi & Chieffi, 2006). I have not taken this decay into account in the time-integrated yields presented in this thesis. For the other SLRs which are included in the models of Set 3, the equations are the same.

My next focus is on the pre-supernova isotopic yields from stable isotopes in the winds. As mentioned before, these are calculated by integrating over time (Equation 2.3 or 2.4), because wind mass-loss is a continuous process. Unlike ^{26}Al, which is not present in the star from the beginning, there are two types of yields to consider for the stable isotopes, the "total" yield and the "net" yield. The total yield is calculated as described above, which ignores the initial amount of the stable isotope present in the star. The net yield is the total yield minus the initial amount of the isotope that was present in the star, see for example Equation 1 of Meynet & Arnould (2000):

$$M_{19}^{wind}(M_i) = \int_{0}^{\tau(M_i)} \dot{M}(M_{ini}, t)[{}^{19}F_s(M_i, t) - {}^{19}F_s(0)]dt \tag{2.5}$$

where $M_{19}^{wind}(M_i)$ the wind yield for a certain initial mass M_i, $^{19}F_s(M_i, t)$ the surface mass-fraction of ^{19}F at a certain time t, and $^{19}F_s(0)$ the initial surface mass-fraction of the star. This translates to the following equation when applied to the MESA output:

$$M_{19}^{wind}(M_i) = \left(\sum_{0}^{n} {}^{19}F_s(n)[M(n) - M(n+1)] \right) - {}^{19}F(n=0) \times M_i \tag{2.6}$$

where $^{19}\mathrm{F}_s$ is the surface mass-fraction of ^{19}F at a given time step n, ^{19}F(n=0) the mass fraction of ^{19}F in the star, and M_i is the initial mass of the star. The calculation is the same for the other stable isotopes. For the SLRs the net yield is identical to the total yield, because there is no initial amount of these isotopes present in the stars. The total yields and the relevant initial amounts of the earlier mentioned isotopes are presented in Section 4.2.

Chapter 3

Stellar structure and evolution: results and discussion

In this chapter, I present the results of the evolution of the stellar models described in the previous section. First, I discuss the differences between the evolution of a single star and the primary star of a binary system (Section 3.1 for a 20 $M_\odot$ star and Section 3.2 for a 50 $M_\odot$ star), and how this impacts the ^{26}Al yields for these stars. I also consider the effect of different orbital periods (P) using the models from Set 1 and Set 2 for these two masses. Section 3.3 gives the results for the stellar evolution for all the models in Set 1 and Set 2, and a more general overview of the impact of binary interactions. In Section 3.4, I discuss the differences between the rotating and the non-rotating single stars of Set 3, and I again compare these results with other studies from the literature.

3.1 Single and binary evolution for a 20 $M_\odot$ star to the onset of carbon burning

The results discussed in this section were published in Brinkman et al. (2019).

To understand how binary interactions influence the evolution of a massive star, and ultimately its ^{26}Al yield, I compare here the non-rotating, single star with an initial mass of 20 $M_\odot$ from Set 1 to three binary systems with a 20 $M_\odot$ primary star and a 18 $M_\odot$ companion from Set 2: one Case A system (P = 2.5 days), and two Case B systems (P = 7.4, 66.2 days). I selected this initial mass as an example because it was one of the two systems used by Braun & Langer (1995) to show the potential impact of binary interactions on the ^{26}Al yield (the other being a 50+45 $M_\odot$ binary system, see the next section). The period of their system is not specified in their paper, though it was confirmed to undergo Case B mass transfer (Braun & Langer 1995; Langer, private communication).

This section is structured as follows: In Section 3.1.1, I describe the evolution of the 20 $M_\odot$ single star using its Hertzsprung-Russell diagram (HRD) and Kippenhahn diagram (KHD) (Figure 3.1a,b). In Section 3.1.2, I describe the three binary systems with different

periods and cases of mass transfer and also show their HRDs and KHDs (Figure 3.1c-h). All the relevant information regarding stellar evolution is given in Table 3.1 in Section 3.3. This information includes the duration of the core hydrogen burning and core helium burning, the sizes of the cores at the end of these burning cycles, the total duration of the evolution, either till the onset of carbon burning or the end of the simulation, and the total amount of mass lost during the evolution. Table 3.1 also gives the ^{26}Al yields for the numerical single stars and binaries, as well as the SNB yields, which will be further discussed in Section 4.1 of the next chapter.

3.1.1 Single star

Figure 3.1a shows the HRD for the 20 $M_\odot$ single star from Set 1. Figure 3.1b shows the KHD of the same 20 $M_\odot$ star with the ^{26}Al content on the colour scale. The ^{26}Al content reaches a maximum value in the centre through proton captures on ^{25}Mg early on in the main sequence, within 1 Myr. After the maximum is reached, around 3 Myr, the ^{26}Al decay is getting faster than the production of ^{26}Al through proton captures. ^{25}Mg is still abundantly present, which keeps ^{26}Al from fully disappearing (see Figure 1.5), and the slope of the decline of the central mass-fraction of ^{26}Al never gets to a true β^+ decay for this isotope (see also Figure 6.2, and Figure 1 of Limongi & Chieffi 2006). The decay of ^{26}Al is more visible in the area where the convective core has retreated (between mass-coordinate 10 and 7 $M_\odot$ in Figure 3.1b). At the end of the main sequence ($\sim$8.5 Myr) the top layer of the former hydrogen burning core (around a mass-coordinate of 10 $M_\odot$) has gone through several half-lives of ^{26}Al and the ^{26}Al content has decreased. The layers deeper in the star have been part of the convective hydrogen burning core for longer, and therefore the ^{26}Al content is higher in these layers (compare, e.g., mass-coordinate 10 $M_\odot$ with 7.5 $M_\odot$ at 8.5 Myr in Figure 3.1b).

As soon as the star moves off the main sequence (Point 2 in Figure 3.1a), the mass-loss rate increases. This is visible in the KHD (Figure 3.1b) by the steep decrease in the total mass during the helium-burning phase (see also Figure 1.2). Between the main sequence and the end of helium burning (Point 4), the star loses 9.43 $M_\odot$. The majority of the mass loss takes place after hydrogen burning, when the star is a red supergiant. From Figure 3.1b it is clear that the majority of the ^{26}Al-rich region is not expelled by the mass loss through stellar winds for this particular mass. The ^{26}Al that is produced in the hydrogen-burning shell and visible as the darker blue region close to the top of the hydrogen depleted core (red dotted line in Figure 3.1b), is too deep into the star to be reached and expelled by the stellar winds. The ^{26}Al in this region will be expelled by the subsequent supernova, which will happen in a few thousand years after the end of my simulation. The yields from the supernova for this particular mass will be larger than the

yields from the wind (see, e.g., Chieffi & Limongi, 2013; Sukhbold et al., 2016). In Table 3 of Limongi & Chieffi (2006), the authors split out the total yield of their 20 $M_\odot$ single star, and show that the total yield is 5.43×10^{-5} $M_\odot$, while the wind yield is only 4.32×10^{-8}. The bulk of the total ^{26}Al yield for this particular mass is produced in neon/carbon shell burning and by explosive burning (see for more details Limongi & Chieffi, 2006). The ^{26}Al remaining in the H-shell is insignificant compared to these two other contributions.

Figure 3.1b also shows that during helium burning ^{26}Al is destroyed in the core of the star. This destruction takes place via neutron capture reactions, (n,p) and (n,α), producing ^{26}Mg and ^{23}Na, respectively (see also the top right panel of Figure 1.1). These neutrons are mainly produced by the ^{22}Ne(α,n)^{25}Mg reaction (Pignatari et al., 2010), and only in a small amount by the ^{13}C (α,n) ^{16}O reaction (Limongi & Chieffi, 2006), depending on the temperature and the region of the star. The ^{13}C, which is produced in the CNO cycle-1, is mainly an active neutron source in the later shell-burning stages. During helium burning, ^{22}Ne, produced by two alpha capture-reactions: ^{14}N(α,n)^{18}O(α,n)^{22}Ne. Due to ^{14}N being the main product of the CNO-cycle, aside from turning hydrogen into helium, this isotope is abundantly present in the core, leading to ^{22}Ne as the main neutron source in this phase.

3.1.2 Detailed description of selected numerical binaries

In this section I discuss three binary systems in detail, representing three different cases of mass transfer: a Case A, an early Case B, and a late Case B. All primaries have a mass of 20 $M_\odot$, all secondaries have a mass of 18 $M_\odot$.

Case A

As an example of Case A mass transfer, I consider here the system with a period of 2.5 days. Both stars start on the main sequence, where the heavier star has a higher luminosity and effective temperature. In the HRD (Figure 3.1c) this point in time is indicated with 1 for the primary (blue track) and for the secondary (orange track). The mass transfer starts while the primary is still on the main sequence (Point A in Figure 3.1c), and it ends at the point indicated with a. The drop in the luminosity is caused by the mass loss. The main effect of mass transfer occurring early in the evolution is the shrinking of the hydrogen burning core. As can be seen in the KHD of the primary star (Figure 3.1d), the core becomes about half the original mass. This leads to a longer hydrogen burning phase for this star than for the single star by ≈ 0.7 Myr, which can be seen from comparing panels b and d in Figure 3.1. The length of the main sequence can also be found in the tables in Table 3.1.

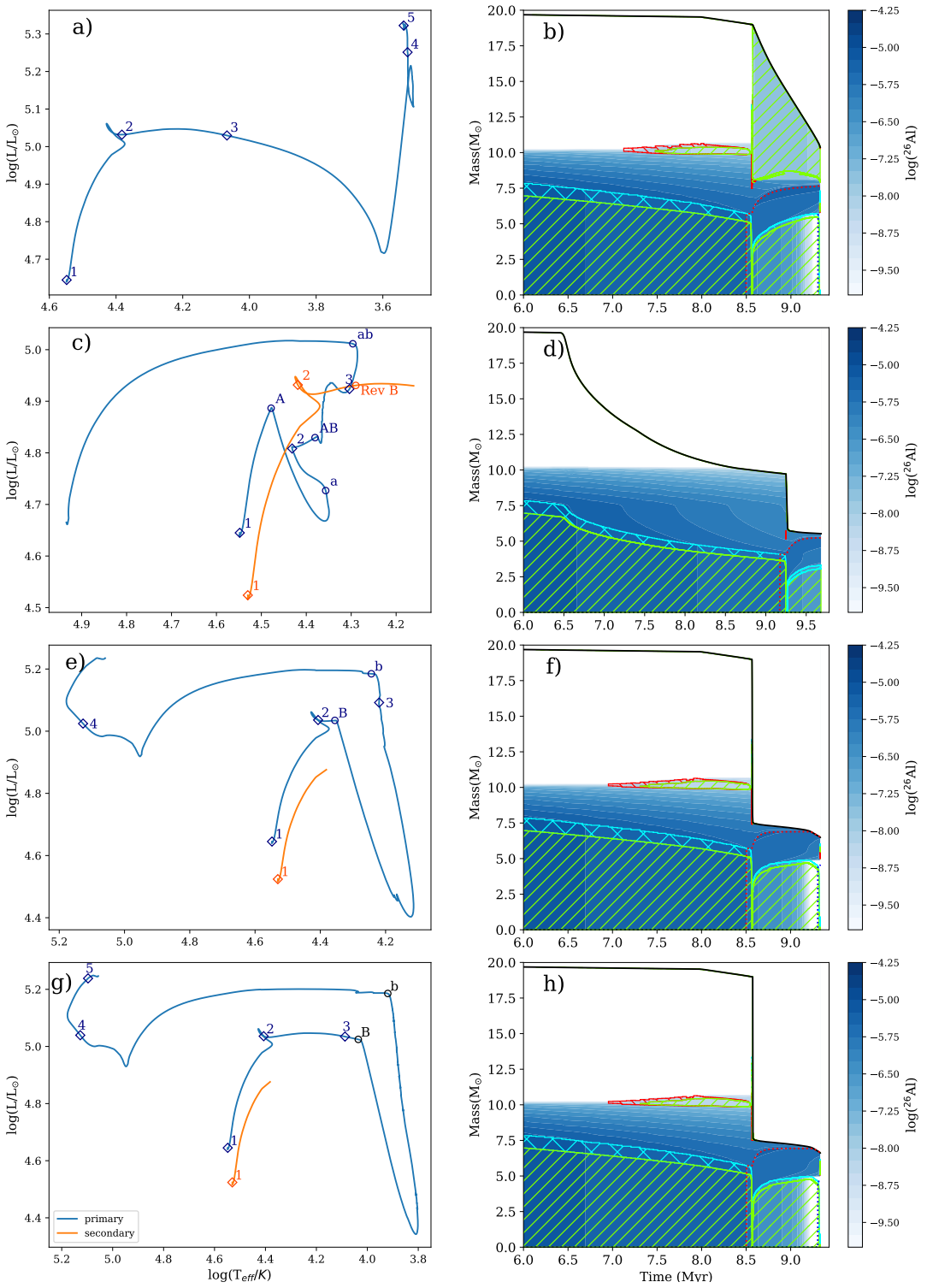

Figure 3.1: HRDs (left panels) and KHDs (right panels) for the 20 $M_{\odot}$ single star (a,b) of Set 1 and binary systems with a period of 2.5(c,d), 7.4(e,f), and 66.6(g,h) days of Set 2. The main stages of stellar evolution are indicated with numbers and open diamonds on the track in the HRDs: the start of the main sequence (1), the end of the main sequence (2), helium ignition (3), end of helium burning (4), and the onset of carbon burning (5) (corresponding to A, a, C, c, and E in Figure 1.4). In panels c, e, and g, I indicate the stages of binary mass-transfer with the open circles and letters on the track, where the letters correspond to the respective type of mass transfer phase. The mass transfer phases start at the capital letters and end at the lower case letters. For the KHDs all colours and shadings are the same as in Figure 2.1

At the end of the mass-transfer phase the primary is still burning hydrogen in its core, and thus still on the main sequence. The end of the main sequence is indicated with 2 on the track in the HRD (Figure 3.1c). A second phase of mass transfer starts at Point AB in the HRD. This mass transfer phase is called Case AB, because it takes place during the same phase in the stellar evolution as a Case B, after hydrogen burning (see next sections), but had a Case A mass-transfer phase preceding it. During this phase the star is out of thermal equilibrium, which results in a faster mass-loss rate than for the earlier mass-loss phase. This can be seen by comparing the gradual mass loss between 6.5-8.5 Myr, and the sharp decrease of the mass at ∼9.25 Myr in Figure 3.1d.

At the point indicated with 3 in Figure 3.1c helium is ignited in the core. The mass transfer continues during the first part of helium burning and stops as soon as the star has regained equilibrium (Point ab in the HRD). At this point nearly the whole hydrogen envelope is lost (Figure 3.1d at ∼9.25 Myr). During helium burning, after the mass transfer, the star moves to the left in the HRD, to higher effective temperatures because the mass of the hydrogen-rich envelope is decreasing as a result of hydrogen-shell burning and mass loss through winds. During this phase the last part of the hydrogen envelope is lost and the hydrogen shell is extinguished, though the simulation ends before this has taken place.

As mentioned in Chapter 2, I assumed in this study that the mass-transfer is fully non-conservative, and thus the secondary star does not accrete any mass. Because the main-sequence lifetime of the primary star has been extended by the first mass-transfer phase, the secondary star evolves off the main sequence before either of the stopping criteria of Set 1 are met (see Table 2.1). As the secondary star moves of the main sequence, it starts expanding and fills its own Roche lobe, leading to a case of reverse mass-transfer while the primary is burning helium. This mass-transfer phase is called reverse Case B (indicated by Rev B in Figure 3.1c). As soon as the secondary star overfills its Roche lobe, the simulation was stopped. When the simulations are continued past this point, they often quickly evolve into a common envelope system which cannot be modelled with the MESA version used here. All the information for the ^{26}Al and the evolution of the primary star is therefore as complete as possible at this ending point. In Section 6.1.1 I will briefly discuss reverse mass-transfer in a bit more detail.

This binary system gives an ^{26}Al yield of 1.63×10^{-6} $M_\odot$ (Table 3.1), an order of magnitude higher than that of the single star (2.01×10^{-7} $M_\odot$), but lower than that given by the semi-numerical binary (7.69×10^{-6} $M_\odot$) by a factor of ∼5. By comparing Figure 3.1b and d, it becomes clear that even though the single star mixes the ^{26}Al through the whole envelope, the Case AB mass transfer reaches deeper layers of the star and the primary loses almost 5 $M_\odot$ more material than the single star. This leads to the higher yields for the binary system. For the SNB and the binary, the difference in the way the mass loss is treated is the reason for the difference in the yields. For the SNB the

whole envelope is stripped in one go, while the numerical binary undergoes two separate mass-transfer phases. Even though the numerical binary loses more mass, the most ^{26}Al-rich region is expelled during the Case AB, and at this point ^{26}Al has already decayed substantially.

Early Case B

When the mass transfer occurs soon after the end of hydrogen burning, it is called early Case B mass transfer, and an example of this is the system with a period of 7.4 days. This system goes through one mass-transfer event. This mass transfer is rapid, which explains the sudden decrease in mass at ∼8.5 Myr in Figure 3.1f. The star is strongly out of thermal equilibrium, which leads to the strong decrease in luminosity between Point B and b in Figure 3.1e. The ignition of helium, at indicated with 3 in the HRD shown in Figure 3.1e, happens just before the mass-transfer phase ends at the point indicated with b. When the star starts to regain equilibrium it detaches from its Roche lobe and the evolution continues towards higher effective temperatures. The luminosity decreases because the hydrogen-burning shell is stripped away due to mass loss by winds during core helium burning, as can be seen in Figure 3.1f where the star becomes smaller than the hydrogen-depleted core, indicated by the red dotted line.

This binary system gives an ^{26}Al yield of 2.39 $\times 10^{-6}$ $M_\odot$. Just as for the system described above, the yield of the binary system is an order of magnitude larger than for the single star. The primary star loses ∼4 $M_\odot$ more mass than the single star, which causes the difference in the yield. For this system, the difference between the yield from the SNB and the binary system is ∼2, which is smaller than for the Case A system (see Table 3.1) because a fraction of the ^{26}Al has already decayed by the time the mass transfer occurs. The total mass loss for the SNB is ∼14.25 $M_\odot$, which is a combination of wind loss before Roche lobe overflow and then the mass loss due to the binary interactions. The numerical binary loses mass due to winds as well, and then goes through Roche lobe overflow, losing a total amount of ∼13.51 $M_\odot$. However, only ∼11.5 $M_\odot$ is lost during the Roche lobe overflow, and the remaining amount is lost through winds after. These factors combined lead to a lower yield for the numerical binary compared to the SNB.

Late Case B

The system with a period of 66.2 days is an example of late Case B mass transfer. From the definition, Case B mass transfer takes place between the end of core hydrogen-burning and the start of core helium-burning. However, as it can be seen from Figure 2.1, the expansion of the star does not stop at helium ignition, but continues until the star has

reached the red supergiant branch. Therefore, some systems start their mass transfer during or shortly after the ignition of helium, where the ignition of helium is defined as the point where the luminosity from the triple-α reaction is larger than the luminosity from the pp-chain or CNO-cycle. These systems fall between the definitions of Case B and Case C, as defined in Section 1.3. In this work, I refer to these systems as late Case B systems.

When comparing the KHD for this system, Figure 3.1h, with the KHD in Figure 3.1f, the difference is very small, since all Case B mass transfer phases occur within a time span of 0.01 Myr. However, when comparing the HRDs, Figures 3.1e and 3.1g, there is a clear difference. In the latter figure, the primary star evolves further along the Hertzsprung gap than in the former. This leads to a small difference in the final yield for the stars, 2.17×10^{-6} $M_\odot$ for the 66.2 day period and 2.39×10^{-6} $M_\odot$ for the 7.4 day period. This difference is rather small, because both systems are very similar up to the time of mass transfer and the times at which the mass transfer starts are close. However, for the wider system the envelope is slightly less stripped.

As for the early Case B system, the yield of the binary system is an order of magnitude larger than the single star yield. The total mass loss from the primary star is again $\sim$4 $M_\odot$ more than for the single star. Because the Case B systems enter all enter the Roche-lobe overflow phase in a relatively small time space, the yield for this system is again $\sim$2 times smaller than the SNB yield for the same period.

3.2 Single and binary evolution for a 50 $M_\odot$ star to the onset of carbon burning

The results discussed in this section were published in Brinkman et al. (2019).

As in the previous section, I compare the evolution of a single, non-rotating star from Set 1 to its binary counterparts from Set 2. Here, the initial mass of the single star and the primary stars is 50 $M_\odot$, and I consider two binary systems: a Case A system ($P = 8.1$ days) and a Case B system ($P = 72.3$ days), both with a secondary star with a mass of 45 $M_\odot$. Braun & Langer (1995) suggested that at this initial mass for the primary star, the impact of binary interactions is limited as compared to the 20 $M_\odot$ case. The system they presented is also a 50 $M_\odot$ primary star with an 45 $M_\odot$ companion. The period is not specified in the paper, though it was confirmed to be a Case B system as well (Braun & Langer 1995; Langer, private communication).

This section is structured as follows: In Section 3.2.1, I describe the evolution of the single star using the HRD and KHDs of this star, Figure 3.2a,b. In Section 3.2.2 I describe two systems with different cases of mass transfer and show HRDs and KHDs as

well, Figure 3.2c-f. The yields for the single and binary stars are tabulated in Table 3.1.

3.2.1 Single star

Figure 3.2a shows the HRD for the single star of 50 $M_\odot$. Figure 3.2b shows the KHD for this star with the ^{26}Al content on the colour scale. The difference from the 20 $M_\odot$ star is that, even before the main sequence ends, the mass-loss rate increases significantly (at ∼3.85 Myr in Figure 3.2b). This is due to a change in the opacity of the envelope at $T_{\rm eff} \approx 25000$K, also known as the bi-stability jump (see Table 2 of Vink et al. 2000). As soon as the star moves off the main sequence, at the point indicated by 2 in Figure 3.2a, the mass-loss rate increases even more, as can be seen in Figure 3.2b at $\sim$ 4.1 Myr. The mass-loss rate is higher for this star than for the 20 $M_\odot$ star in Section 3.1.1 because its luminosity and effective temperature are higher. By the time the whole envelope is stripped away, the hydrogen-burning shell is extinguished and then this region is stripped away as well. What is left is the hydrogen-depleted core of the star, and the star has become a Wolf-Rayet star. The star loses 29.24 $M_\odot$ through these stellar winds, more than half of its initial mass. The ^{26}Al yield for this single star is 4.47×10^{-5} $M_\odot$.

As can be seen in Figure 3.2b, the star does not reach the end the helium-burning phase during the simulation, which is due to convergence issues. However, from the same figure it can also be seen that very little ^{26}Al is left in the star at this point in time, and therefore the wind yields are not impacted significantly.

Compared to the 20 $M_\odot$ star, the winds of the 50 $M_\odot$ star contribute much more significantly to the total ^{26}Al yield. Following again Table 1 of Limongi & Chieffi (2006), the total ^{26}Al for their 40 and 60 $M_\odot$ models are 1.21×10^{-4} and 2.52×10^{-4}, respectively. These authors do not present a 50 $M_\odot$ model, so I compare with the models closest in mass. Wind yields are 2.06×10^{-5} and 6.94×10^{-5}, respectively. While the production in the neon/carbon shell and the later explosive burning are still the main sources of ^{26}Al for these stars, the contribution of the wind to the total yield is 17-27%, while it was insignificant for the 20 $M_\odot$ model (0.1%).

3.2.2 Detailed description of selected numerical binaries

In this section, I discuss two binary systems in detail, representing two different cases of mass transfer, a Case A and a late Case B. All primaries have a mass of 50 $M_\odot$, all secondaries have a mass of 45 $M_\odot$. Braun & Langer (1995) found that for masses $\gtrsim$ 40 $M_\odot$, the binary systems give lower yields than the single stars. Here, I discuss this statement as well.

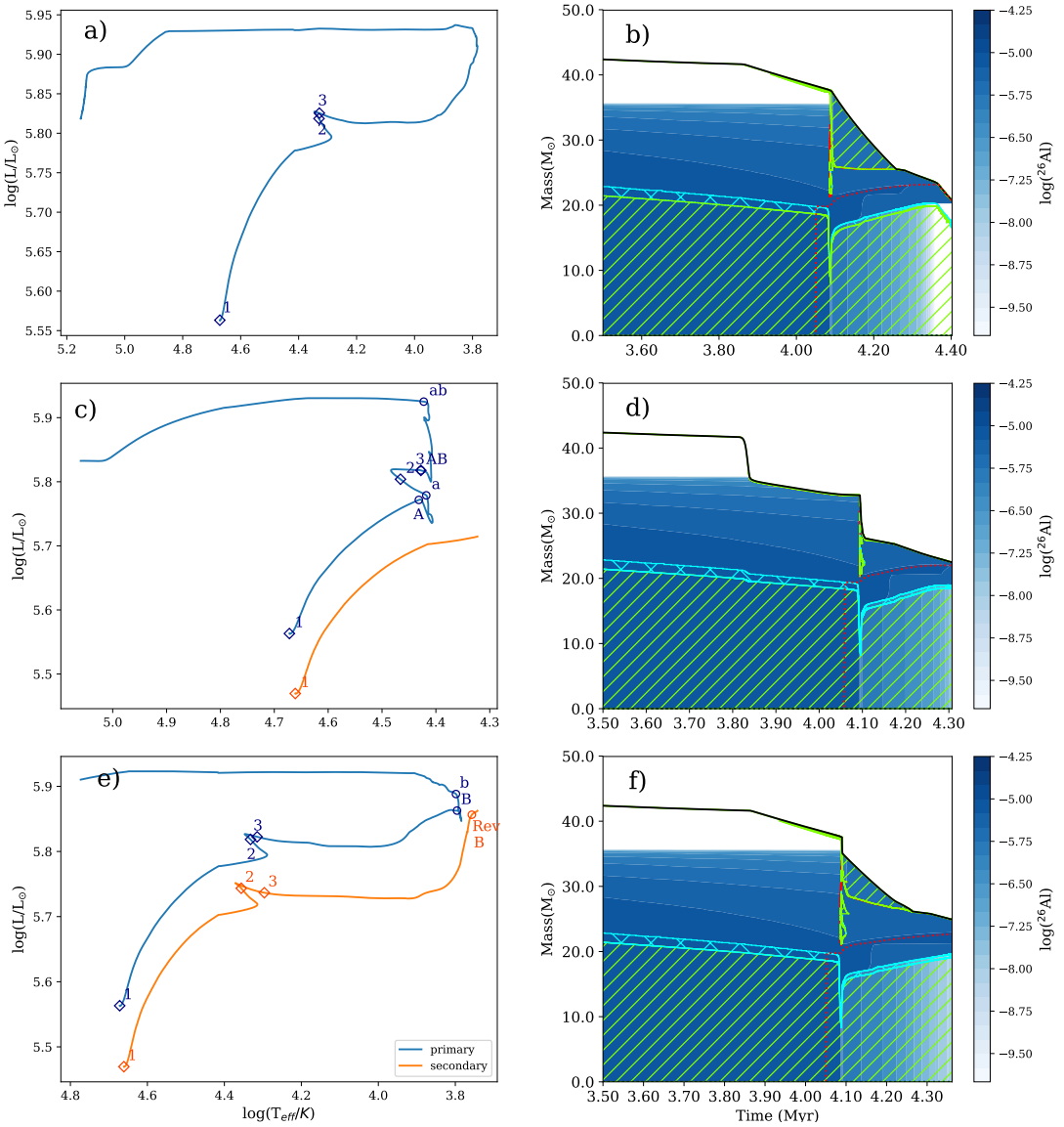

Figure 3.2: HRDs (left panels) and KHDs (right panels) for the 50 $M_{\odot}$ single star (a,b) of Set 1 and binary systems with a period of 8.1(c,d), and 72.3(e,f) days, both from Set 2. The main stages of stellar evolution are indicated with numbers and open diamonds on the track: Point 1 is the start of the main sequence, at Point 2 the hydrogen-burning phase has ended and the star leaves the main sequence, at Point 3 helium is ignited in the core. The stages of binary evolution are indicated with the open circles and letters on the track. The mass transfer phases start at the capital letters and end at the lower case letters. For the KHDs all colours and shadings are the same as in Figure 2.1.

Case A

The system with an initial period of 8.1 days described in this section undergoes Case A mass transfer. Both stars start on the main sequence in Figure 3.2c at the points indicated by 1. The mass transfer starts at the point indicated by A, before the primary has finished hydrogen burning (indicated by 2) and ends at the point indicated by a. Compared to the primary in Figure 3.1c, the drop in the luminosity due to the mass transfer is a lot smaller. As for the primary in Figure 3.1d, the hydrogen-burning core becomes less massive than for the single star (see the small dip at ∼3.8 Myr in Figure 3.2), though not as noticeable as for the 20 $M_\odot$ case. The first mass transfer phase ends when the primary star contracts as it regains equilibrium due to helium burning in its core. The star moves to the left in the HRD, to higher effective temperatures, and the star loses more mass due to the stellar winds active during this phase. Then, a second mass transfer starts at the point indicated with AB, which is after helium ignition (indicated with 3) and ends at the point indicated with ab. As explained in Section 3.1.2, I refer to this mass transfer as a Case AB. This is visible in Figure 3.2d, where the first of the near vertical decreases corresponds to fast phase of the Case A mass transfer, the slower decrease after that is a combination of the slower phase of the Case A mass transfer and mass loss through winds, and the second near vertical decrease corresponds to the Case AB mass transfer. All mass lost after this (beyond ∼4.1 Myr), is due to the winds. The total amount of mass lost by the primary star in the binary system is lower than the mass lost by the single star, 27.49 $M_\odot$ instead of 29.24 $M_\odot$, leading to a 15% smaller ^{26}Al yield (or 3.82×10^{-5} $M_\odot$ less). However, this star does not proceed as far into helium burning as the single star before the calculation stops, which can be seen from comparing Figure 3.2b and d. Additional mass will be lost in the wind during the rest of the helium-burning phase, which will likely bring the yields closer to each other. This result is different from the 20 $M_\odot$ case, where there was a strong increase between the binary and the single star yield. This is because for the 50 $M_\odot$ star the mass-loss history between the single star and the Case A primary is more similar, and the mass loss through winds and the mass loss through Roche lobe overflow have a similar effect. This result is in agreement with Braun & Langer (1995).

The SNB yield for this model is 6.76 $\times10^{-5}$ $M_\odot$. This is higher than the single star yield, though the difference between the SNB and the full simulation is much smaller than for the 20 $M_\odot$ Case A system. This is because the mass loss of the single star and the mass loss in the SNB scheme are very similar. The difference is due to the earlier removal of the entire envelope, which means that less ^{26}Al has decayed.

Case B

The system with an initial period of 72.3 days described in this section undergoes late Case B mass transfer. In the HRD (Figure 3.2e) the mass-transfer phase (Points B to b) is not as recognisable as in all of the previous HRDs for the binary systems. There is only a small dip in the luminosity. The secondary overflows the Roche lobe at the end of the simulation, leading to reverse Case B mass transfer. Compared the to Case A system described above, the binary star loses even less mass, $\sim$25 $M_\odot$ instead of 29.24 $M_\odot$ for the single star. The yield is also lower, 2.59×10^{-5} $M_\odot$, $\sim$43% less than the single star yield. However, a significant amount of ^{26}Al is still left in the envelope at the end of the simulation (see the dark blue shade of the top of the star in Figure 3.2f), which could increase the yield to a similar level as the single star if the evolution was followed through the entire helium-burning phase. Overall, for the Case B system the mass-loss history is almost identical to the mass-loss history of the single star. This is because the mass transfer happens during a phase when the star is already rapidly losing mass due to the red supergiant wind, as can be seen from comparing panels b and d of Figure 3.2. Therefore, the effect of the mass transfer is relatively small, as can also be seen when comparing panels a and e of Figure 3.2, which show that also the tracks in the HRD are very similar. The main effect of the mass transfer is that the red supergiant phase is shortened, turning the primary into a Wolf-Rayet at an earlier stage. The second effect is that the primary has a slightly lower luminosity on the track back to the hotter side of the HRD, leading to a slightly lower mass-loss rate than for the single star. This explains why the primary star of the binary loses less mass than the single star. However, since neither of the stars have finished helium burning, there is still future mass loss that has not been taken into account.

3.3 Stellar evolution for single star and binaries up to carbon burning

The results discussed in this section were published in Brinkman et al. (2019). Here I present the results in a bit more detail.

In this section I discuss the stellar evolution details of Set 1 compared to representative binary systems undergoing Case A and Case B mass transfer. For the Case A systems, I selected the either the shortest period (for 10 and 15 $M_\odot$) or the second shortest period (all other masses), except for the 45 and 60 $M_\odot$ systems since none of the Case A systems for this primary mass evolved up to carbon burning. For the Case B systems, I selected the third widest system except for the 10, 15, and 50 $M_\odot$ primary stars, because there is

only one Case B system for 10 and 15 $M_\odot$ and because for the 50 $M_\odot$ the period of the second widest system is more comparable to the other periods.

In Table 3.1, selected relevant information of all the models of Set 1 and Set 2 regarding the stellar evolution is presented: the core mass at the end of H and He burning, the duration of these burning phases, the total lifetime of the star, the total mass loss, the ^{26}Al yield and for the binary systems, also ^{26}Al yield as determined by the SNB-method.

In the previous sections, the effects of binary interactions, such as a change in the duration of core hydrogen-burning or the size of the hydrogen-burning core, on the evolution of a 20 $M_\odot$ and 50 $M_\odot$ star were discussed. Figures 3.3-3.4 show these effects in a more general way. The duration hydrogen burning, t_H, (Column 4 of Table 3.1), is shown in Figure 3.3a. Only for the Case A systems at the lowest masses. 10-25 $M_\odot$, the hydrogen burning timescale changes significantly. For the other masses, 30-60 $M_\odot$, there is no difference between duration of the hydrogen burning phase between the single and the primary stars. The difference in the duration of the hydrogen burning phase is due to a change in the size of the hydrogen burning core due to the mass transfer, as was shown in Section 3.1.2. It was also shown in Section 3.2.2 that for this primary mass, the change in the size of the hydrogen core is much smaller, and thus the effect on the duration of the core hydrogen-burning will be less as well. Figure 3.4a shows the size of the hydrogen-depleted core for the single stars and the selected binary systems. For all the systems undergoing Case A mass-transfer, the size of the hydrogen-depleted core is smaller than the same core for the single stars. Figure 3.4b shows the difference between this core for the single star and the representative binary system for a better comparison. For the Case A systems, the core is between 0.5-1 $M_\odot$ smaller, depending on the initial mass of the primary. However, for the Case B systems, there is barely any difference between the single star and the primary star, as for the duration of this burning phase. This is because for Case B systems, the hydrogen burning core is unaffected, and thus also the duration of core hydrogen burning.

Figure 3.3b shows the duration of core helium burning. One should keep in mind that for the Case B systems with initial primary masses of 35 $M_\odot$ and higher this phase is not completed. And the same goes for most Case A systems with initial primary masses of 25 $M_\odot$ and higher. For 45 $M_\odot$ both simulations of Case A systems failed, and therefore it is missing in the figure. For the lowest mass models, 10-20 $M_\odot$, the duration of core helium burning is extended for the Case A system, which is a result of the smaller core mass at the end of core hydrogen burning for these systems. For the models with an initial mass of 25 $M_\odot$ and higher, the duration of core helium-burning is shorter, and would likely be similar to the single star case if the phase was finished. For the Case B systems the duration of helium burning is slightly extended due to smaller total stellar mass for the 10-20 $M_\odot$ models. From $\sim$25 $M_\odot$, the duration of core helium burning is identical in most cases to the single star case, except for those models that ended at an earlier stage.

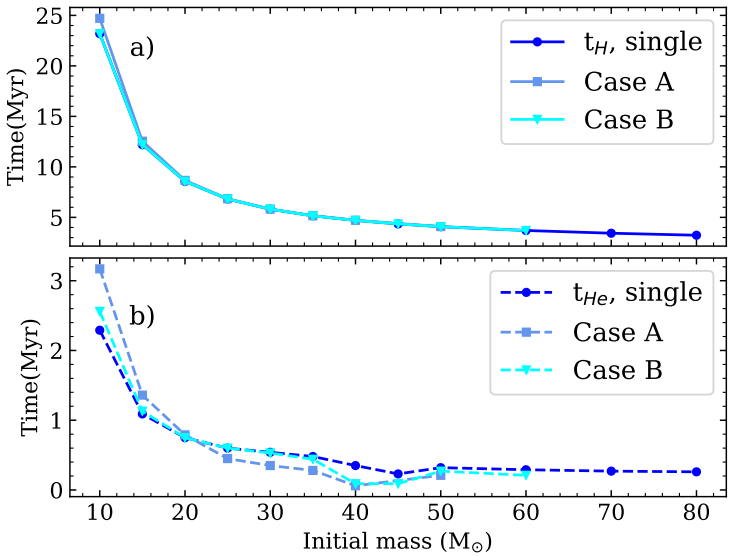

Figure 3.3: The duration of core hydrogen burning, t_H (solid lines in the top panel) and the duration of core helium burning t_{He} (dashed lines in the bottom panel) for the single stars of Set 1 and representative binary systems undergoing Case A and Case B mass transfer from Set 2.

Finally, Figure 3.5 shows the total mass lost over the whole simulation. For the binaries with initial masses below ∼40 $M_\odot$, the total mass loss is larger than for the single stars, especially for the Case A systems. However, at ∼50 $M_\odot$, the binaries start losing less mass than the single stars, though the selected system for 60 $M_\odot$ loses slightly more mass than the single star model. It should again be noted that there is still a possibility for the stars to lose mass after the simulation has ended since not all models have finished helium burning. However, the overall picture remains that below 35-40 $M_\odot$ the binaries have a large impact on the mass loss, and above this threshold, the impact of the binary interactions becomes negligible, since the mass loss through stellar winds becomes similar to the mass loss through binary interactions. The yields will be discussed in Chapter 4.

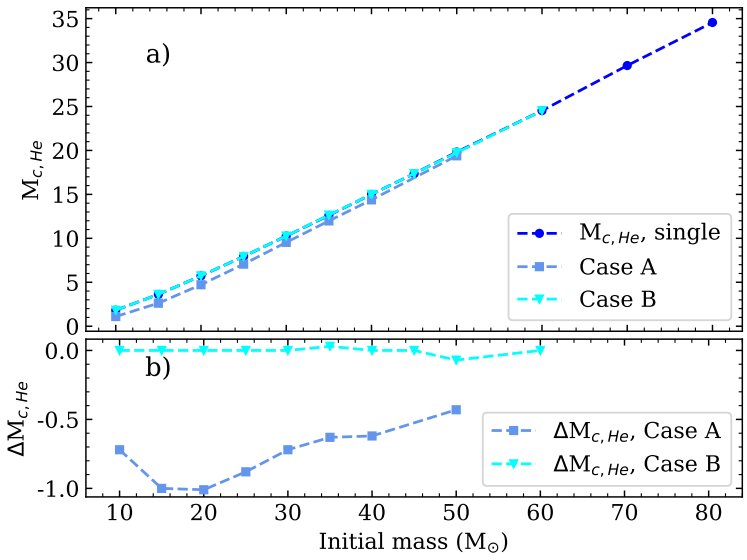

Figure 3.4: The top panel shows the size of the hydrogen-depleted core ($M_{c,He}$) for the single stars of Set 1 and representative binary systems undergoing Case A and Case B mass transfer from Set 2. The bottom panel shows the relative difference in the size of the helium cores when comparing the cores of the primary stars to those of the single stars, where $\Delta M_{c,He}$ = $M_{c,He}$(bin)-$M_{c,He}$(single).

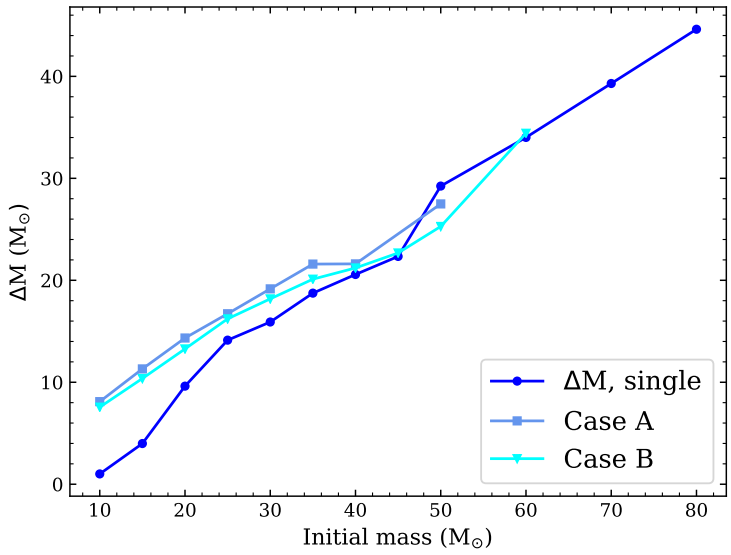

Figure 3.5: Total mass loss for Set 1 and representative binary systems undergoing Case A and Case B mass transfer from Set 2.

Table 3.1: Stellar evolution results for Set 1 and Set 2. $M_{\rm ini}$ is the initial (primary) mass in $M_\odot$. For all binary systems the initial mass ratio is the same, $q = 0.9$. $P_{\rm ini}$ is the initial period in days. The symbol "-" indicates the single star in the period and case columns. The case of the mass transfer is given in the next column. $t_{\rm H}$, $t_{\rm He}$, and $t_{\rm tot}$ are the duration of hydrogen burning, helium burning, and the whole simulation in Myr, respectively. $M_{\rm c,He}$ and $M_{\rm C,c}$ are the masses of the hydrogen-depleted core and the helium-depleted core at the end of the corresponding burning phases in $M_\odot$. $Y_{\rm c}$ gives the final helium mass-fraction in the core, if core helium burning had not ended. ΔM is the total mass lost in $M_\odot$. ^{26}Al and ^{26}Al (SNB) give the ^{26}Al yields for the numerical stars and the SNBs in $M_\odot$, respectively.

$M_{\rm ini}$ ($M_\odot$)	$P_{\rm ini}$ (days)	Case	$t_{\rm H}$ (Myr)	$M_{\rm c,He}$ ($M_\odot$)	$t_{\rm He}$ (Myr)	$M_{\rm C,c}$ ($M_\odot$)	$Y_{\rm c}$	$t_{\rm tot}$ (Myr)	ΔM ($M_\odot$)	^{26}Al ($M_\odot$)	^{26}Al (SNB) ($M_\odot$)
10	-	-	23.19	1.82	2.29	1.52	-	25.61	1.01	2.62e-10	-
	2.8[1]	A	24.71	1.10	3.17	-	0.18	28.05	8.10	5.22e-08	8.13e-07
	4.9	B	23.19	1.82	2.60	1.17	-	25.97	7.60	5.56e-08	5.93e-07
	13.1	B	23.19	1.82	2.56	1.19	-	25.93	7.56	2.60e-08	6.23e-07
15	-	-	12.20	3.62	1.09	3.40	-	13.33	3.99	9.06e-09	-
	3.8	A	12.54	2.62	1.36	2.095	-	13.97	11.31	9.74e-07	2.81e-06
	6.7	B	12.20	3.62	1.14	2.79	-	13.39	10.43	2.98e-07	1.95e-06
	16.8	B	12.20	3.62	1.13	2.83	-	13.38	10.37	2.59e-07	1.87e-06
20	-	-	8.56	5.73	0.75	5.65	-	9.33	9.62	2.01e-07	-
	2.5[1,2]	A	9.25	4.07	0.42	-	0.52	9.68	14.47	1.63e-06	7.69e-06
	5.1	A	8.66	4.72	0.79	3.73	-	9.48	14.34	3.51e-06	5.86e-06
	6.2	B[6]	8.56	5.71	0.75	4.46	-	9.33	13.53	2.43e-06	5.65e-06
	7.4	B	8.56	5.73	0.75	4.48	-	9.33	13.51	2.39e-06	4.49e-06
	18.4	B	8.56	5.73	0.75	4.71	-	9.33	13.27	1.99e-06	4.38e-06
	66.2	B	8.56	5.73	0.75	4.62	-	9.33	13.38	2.17e-06	4.20e-06
25	-	-	6.81	7.94	0.60	7.95	-	7.43	14.13	1.32e-06	-
	2.7[2]	A	7.24	6.20	0.32	-	0.49	7.56	16.95	4.24e-06	7.35e-06
	6.7[2]	A	6.85	7.06	0.45	-	0.18	7.31	16.72	6.68e-06	1.07e-05
	8.9[4]	B	-	-	-	-	-	-	-	failed	8.59e-06
	17.8[4]	B	-	-	-	-	-	-	-	failed	8.39e-06
	71.3	B	6.81	7.94	0.60	6.58	-	7.42	16.22	5.62e-06	8.12e-06
30	-	-	5.81	10.26	0.54	10.27	-	6.36	15.91	3.27e-06	-
	2.8[1,3]	A	-	-	-	-	-	-	13.38	2.79e-07	2.36e-05
	8.4[2]	A	5.82	9.54	0.35	-	0.23	6.18	19.16	1.14e-05	1.73e-05
	10.1[1]	B[6]	5.81	10.26	0.55	8.88	-	6.37	18.38	1.04e-05	1.71e-05
	12.2[1]	B	5.81	10.26	0.55	8.94	-	6.36	17.88	1.00e-05	1.45e-05
	30.3	B	5.81	10.26	0.53	9.15	-	6.36	18.18	9.25e-06	1.41e-05
	75.4[1]	B	5.81	10.26	0.55	9.24	-	6.37	17.83	7.91e-06	1.40e-05
35	-	-	5.16	12.61	0.48	12.57	-	5.65	18.74	7.52e-06	-
	2.9[1,3]	A	-	-	-	-	-	-	14.52	7.04e-07	3.58e-05
	8.8[2]	A	5.16	11.98	0.28	-	0.30	5.45	21.59	1.77e-05	2.58e-05
	10.6[2]	B[6]	5.16	12.57	0.30	-	0.25	5.46	21.41	1.70e-05	2.54e-05
	12.7[1,2]	B	5.15	12.64	0.43	-	0.08	5.59	19.04	1.17e-05	2.17e-05
	31.5[1,2]	B	5.15	12.64	0.44	-	0.04	5.59	20.11	1.27e-05	2.14e-05
	78.6[1,2]	B	5.15	12.64	0.44	-	0.04	5.59	20.01	1.22e-05	2.10e-05
40[2]	-	-	4.70	15.00	0.35	-	0.12	5.06	20.57	1.06e-05	-
	3.1[4]	A	-	-	-	-	-	-	-	failed	4.88e-05
	7.6[2]	A	4.71	14.38	0.06	-	0.83	4.78	21.61	1.55e-05	3.82e-05
	15.8[1,2]	B[6]	4.70	15.00	0.36	-	0.13	5.06	21.15	1.92e-05	3.55e-05
	20.4[2]	B	4.70	15.00	0.24	-	0.35	4.94	21.50	1.73e-05	3.11e-05
	32.8[2]	B	4.70	15.00	0.09	-	0.74	4.79	21.21	1.44e-05	3.10e-05
	81.7[2]	B	4.70	15.00	0.12	-	0.68	4.82	21.01	1.35e-05	3.06e-05

Table 3.1 continued.

$M_{\rm ini}$ ($M_\odot$)	$P_{\rm init}$ (days)	Case	$t_{\rm H}$ (Myr)	$M_{\rm C,He}$ ($M_\odot$)	$t_{\rm He}$ (Myr)	$M_{\rm C,c}$ ($M_\odot$)	$Y_{\rm c}$	$t_{\rm tot}$ (Myr)	ΔM ($M_\odot$)	^{26}Al ($M_\odot$)	^{26}Al (SNB) ($M_\odot$)
45[2]	-	-	4.35	17.36	0.23	-	0.34	4.58	22.34	1.53e-05	-
	3.2[4]	A	-	-	-	-	-	-	-	failed	6.54e-05
	7.8[3]	A	-	-	-	-	-	-	16.28	1.54e-06	5.14e-05
	19.5[2]	B[6]	4.35	17.36	0.30	-	0.19	4.65	22.04	2.01e-05	4.73e-05
	23.4[2]	B	4.35	17.36	0.29	-	0.20	4.65	22.22	2.08e-05	4.20e-05
	42.0[2]	B	4.35	17.36	0.09	-	0.74	4.44	22.68	1.79e-05	4.18e-05
	69.9[2]	B	4.35	17.36	0.12	-	0.63	4.48	22.59	1.73e-05	4.17e-05
50[2]	-	-	4.08	19.82	0.32	-	0.12	4.40	29.24	4.47e-05	-
	8.1[2]	A	4.09	19.39	0.21	-	0.36	4.31	27.49	3.82e-05	6.76e-05
	14.0[2]	A	4.09	19.58	0.17	-	0.45	4.26	27.28	3.67e-05	6.29e-05
	21.7[1,2]	B	4.08	19.75	0.27	-	0.22	4.35	25.51	3.02e-05	6.14e-05
	29.1[1,2]	B	4.08	19.75	0.27	-	0.22	4.35	25.28	2.92e-05	5.48e-05
	72.3[2]	B	4.08	19.75	0.27	-	0.21	4.36	25.03	2.59e-05	5.46e-05
60[2]	-	-	3.70	24.53	0.29	-	0.13	3.99	34.01	6.83e-05	-
	3.5[1,3]	A	-	-	-	-	-	-	18.09	4.33e-06	1.24e-04
	7.2[1,3]	A	-	-	-	-	-	-	19.65	6.21e-06	1.05e-04
	14.9[1,2]	B[6]	3.70	24.53	0.21	-	0.30	3.91	28.81	4.28e-05	9.53e-05
	17.8[2]	B	3.70	24.53	0.20	-	0.32	3.90	34.75	7.65e-05	7.91e-05
	37.0[2]	B	3.70	24.53	0.21	-	0.31	3.91	34.42	7.43e-05	7.87e-05
	92.2[1,2]	B	3.70	24.53	0.21	-	0.30	3.91	28.29	3.90e-05	7.80e-05
70[2,5]	-	-	3.43	29.66	0.27	-	0.13	3.70	39.30	9.89e-05	-
80[2,5]	-	-	3.23	34.56	0.26	-	0.14	3.49	44.62	1.40e-4	-

[1]Terminated early due to reverse mass transfer.
[2]Terminated before the end of helium burning.
[3]Terminated before the end of hydrogen burning.
[4]Terminated due to convergence issues.
[5]Calculated for Section 6.2.
[6]These systems are Case A according to the SNBs, but in the detailed simulations they are Case B.

3.4 Stellar evolution up to the core-collapse with rotation

The results discussed in this section were published in Brinkman et al. (2021).

In this section, I discuss the stellar evolution details of the single star models evolved till core collapse and the impact of rotation on these models (Set 3). In Table 3.2, selected relevant information of these models regarding the stellar evolution is presented: the total stellar mass and core mass at the end of the hydrogen, helium, and carbon core-burning, the duration of these burning phases, the total lifetime, the total mass-loss, and the compactness parameter (see described below). The start and end points of the different burning phases are defined as in Götberg et al. (2018)[1]. By the end of carbon burning the mass-loss phase has mostly ended, since the stellar mass does not change between the end of helium burning ($M_{*,He}$) and the end of the simulations ($M_{*,f}$) (see the dotted lines Figure 3.8). All models of Set 3 have reached the end of the mass loss stage. I then continued the evolution of these models until a core-infall velocity of 300 km/s, which corresponds to the core collapse. In total, 31 out of the 36 models have reached this point, with numerical issues halting the calculations of the remaining 5 models slightly prior to this stage.

The duration of hydrogen burning, $t_{\rm H}$ (Column 3 of Table 3.2), is shown in Figure 3.6a. For all initial masses, $t_{\rm H}$ increases with the rotational velocity. The effect is the strongest at the lower mass end (17% for 10 $M_\odot$) and the smallest for the three highest masses of my grid (9% for 80 $M_\odot$). The increasing duration of the main sequence is due to rotational mixing. More hydrogen is mixed into the core from the envelope, adding more fuel to the core, and thus extending this burning phase. Together, this leads to larger hydrogen-depleted cores, $M_{c,\rm He}$, at the end of the main sequence (dotted lines in Figure 3.7 and Column 4 in Table 3.2).

The only exceptions to this trend are the two most massive models, 70 and 80 $M_\odot$, which have a longer main sequence yet smaller helium-core masses at the end of hydrogen burning when rotating. This is especially noticeable for the highest initial rotational velocity. In these two most massive models, the increased mass loss due to rotation limits the core growth. With more mass lost from the star, there is less fuel to add to the core to increase its mass. This is shown by the solid lines in Figures 3.7 and 3.8, which give the final mass at the end of the main sequence, $M_{*,\rm H}$ (Column 5 of Table 3.2) and the mass loss on the main sequence ($M_{\rm ini}$-$M_{*,\rm H}$), respectively. For the models below ∼50 $M_\odot$,

[1]i.e., the end of the core hydrogen burning stage is defined as the time when the central helium mass-fraction is larger than 0.98 and the total luminosity produced by nuclear burning is larger than 0.5 the luminosity of the star, the end of helium core-burning when the central carbon mass-fraction is 0.4, the end of carbon burning when the central carbon mass-fraction is 0.01, and the end of oxygen burning when the central oxygen mass-fraction is 0.04.

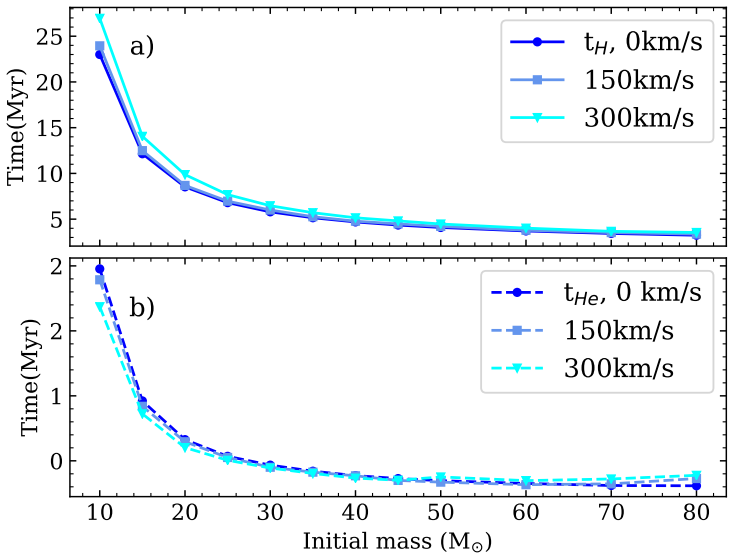

Figure 3.6: The duration of core hydrogen burning, $t_{\rm H}$ (solid lines in the top panel) and the duration of core helium burning, $t_{\rm He}$ (dashed lines in the bottom panel) for the three rotational velocities as a function of the initial mass for the stars of Set 3.

there is little difference (1-4%)in the total amount of mass lost by the rotating models and the non-rotating models. Above ∼50 M$_\odot$, the extra amount of mass lost from the rotating stars as compared to the non-rotating stars becomes more significant, up to 50% more for the most massive model.

The mass loss between the end of the main sequence and the end of helium burning ($M_{*,\rm H}$-$M_{*,\rm He}$), represented by the dashed lines in Figure 3.8, is comparable between the rotating and non-rotating models with the same initial mass. The exceptions are again the two most massive models, for which the mass loss between the end of hydrogen and the end of helium burning reduces with the increasing rotational velocity. This is because these models have already lost more mass on their main sequence (solid lines in Figure 3.8), and as a consequence experience less mass loss afterwards.

As a result of the larger core masses at the end of hydrogen burning, the helium burning life-time, $t_{\rm He}$, becomes shorter for most of the models with rotation (Figure 3.6b and Column 6 of Table 3.2). This is because the heavier the cores, the faster the burning. For the three most massive models, however, the rotating models have smaller helium core masses at the end of hydrogen burning compared to their non-rotating counterparts. For these masses, the rotating models have longer $t_{\rm He}$ than their non-rotating counterparts. The turn-over mass at which this happens is around ∼50 M$_\odot$, as can be seen in Figure 3.6b.

After helium burning, barely any mass is lost from the stars (dotted lines in Figure 3.8). The helium-depleted core at the end of helium burning, $M_{c,\rm C}$ (Column 7 in Table 3.2) increases in mass for the models below ∼50 M$_\odot$. For the three highest masses, however, the mass of the helium-depleted cores decreases with the initial rotational velocity, which is a direct result of the smaller helium cores mentioned earlier.

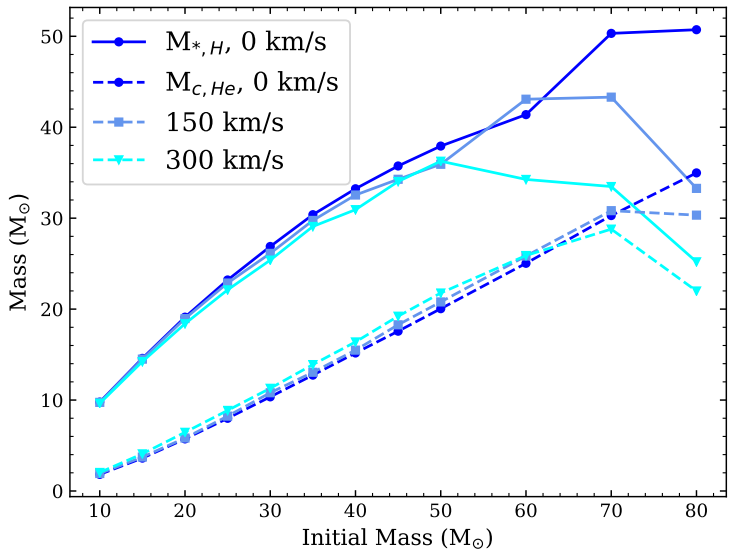

Figure 3.7: The total stellar mass $M_{*,\mathrm{H}}$, (solid lines) and the hydrogen depleted core mass $M_{*,\mathrm{He}}$, (dashed lines) at the end of the main sequence for the three rotational velocities as a function of the initial mass for the stars of Set 3.

I note that the mass of the carbon depleted core, $M_{c,\mathrm{O}}$ (reported in Column 10 of Table 3.2) is very sensitive to mixing in the final phases of the stellar evolution and small fluctuations in for example the mixing can easily change its size.

The mass loss during the main sequence always increases with higher rotational velocities (solid lines in Figure 3.8). The same applies to the total lifetime of the star, t_{tot} (Column 9 of Table 3.2). On the other hand, the total mass loss during the whole evolution, ΔM, (Column 12 of Table 3.2) is not always larger for the higher rotation rates.

The final column of Table 3.2 gives the compactness-parameter, $\xi_{2.5}$. This parameter, as defined by O'Connor & Ott (2011) in their Equation 10, determines how compact the core of the star is just before the collapse and therefore how difficult it is to explode the star, i.e., high values of ξ_M indicate compacter pre-SN structure which is more difficult to explode than a low value of ξ_M which indicates a pre-SN structure that is easier to explode. The definition is:

$$\xi_M = \frac{M/M_\odot}{R(M)/1000\,\mathrm{km}} \tag{3.1}$$

where M is the mass of the inner region of the star of which the compactness is to be calculated, which was set to 2.5 $\mathrm{M}_\odot$ by O'Connor & Ott (2011), and $R(M)$ the radius of this chosen mass, i.e., the radial coordinate of mass coordinate 2.5. The compactness is sensitive to small changes in the structure, and is therefore strongly dependent on the model parameters and the codes used (see, e.g., Sukhbold et al. 2016; Limongi & Chieffi 2018 and Schneider et al. 2021). Overall, the compactness parameters calculated from Set 3 are comparable to those by the other authors mentioned. However, there are some differences, some that can be attributed to the fact that the models of Set 3 were evolved only to an infall-velocity of the iron-core of 300 km/s while other studies compute their models up to 1000 km/s. However, I can conclude that the values I have computed for

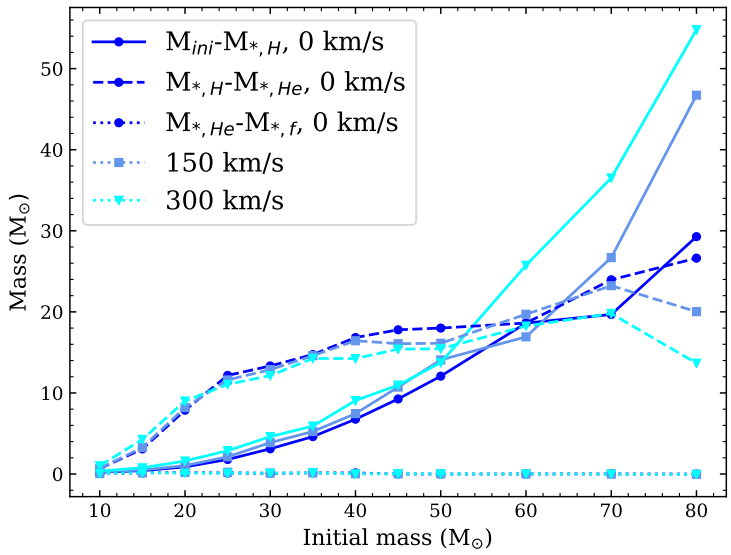

Figure 3.8: Mass loss for three different phases for the stars of Set 3, the main sequence (solid lines, $M_{\rm ini}$-$M_{*,\rm H}$), helium burning (dashed lines, $M_{*,\rm H}$-$M_{*,\rm He}$) and carbon burning and beyond (dotted lines, $M_{*,\rm He}$-$M_{*,\rm f}$), as a function of the initial mass. The final mass ($M_{*,\rm f}$) is the difference between the initial mass and the total mass loss, $M_{\rm ini}$-ΔM.

$\xi_{2.5}$ are reasonable for the models of Set 3.

3.4.1 Comparison to other data sets

I compare the results of Set 3 primarily to those of Ekström et al. (2012), calculated using the GENEC stellar evolution code (hereafter GENEC), and Limongi & Chieffi (2018) calculated with the FRANEC stellar evolution code (hereafter FRANEC), for three reasons. The first is that both studies present rotating and non-rotating massive star models until the late phases of evolution. The second is that the implementation of rotation differs in these codes compared to what is used in MESA. Specifically, the treatment of rotation in MESA is based on a diffusive approximation, while in GENEC and FRANEC it is based on diffusion–advection approach (Maeder & Zahn, 1998; Paxton et al., 2013). Since it is well established that the impact of rotation on stellar model computations varies depending on which rotational mixing approach is used (see, e.g, Maeder & Meynet, 2000b), comparison of these three sets can provide insight in the quantitative impact of the different methods. Third, all the stellar evolution details from these two studies are publicly available (although for Ekström et al. (2012) I do not have yields for ^{36}Cl, ^{41}Ca, and ^{60}Fe). I compare the models of Set 3 to those from these papers at solar metallicity, Z=0.014 and Y=0.266 for Ekström et al. (2012), and Z=0.01345 for Limongi & Chieffi (2018), and both following Asplund et al. (2009) for the mixture of elements.

Table 2 of Ekström et al. (2012) and Table 5 of Limongi & Chieffi (2018) show the properties of their non-rotating and rotating models. The former models an initial rotational velocity of $0.4\omega_{\rm crit}$ (corresponding to 260-350 km/s for 10-80 M$_\odot$), where $\omega_{\rm crit}$ is the

critical angular velocity, i.e., the angular velocity at the surface of the star for which the centrifugal force equals the gravitational force. The latter models have initial rotational velocities of 150 and 300 km/s, like the models of Set 3.

These two works show similar trends as my models, such as the extended duration of the main sequence and the increased mass-loss in the early phases of the evolution. Overall, all three different sets of models show similar main-sequence lifetimes. However, even though the mass loss prescriptions are rather similar between the three sets of models (mainly a combination of Vink et al. 2000, 2001; de Jager et al. 1988; Nieuwenhuijzen & de Jager 1990 and Nugis & Lamers 2000), the implementation of the effects of rotation and internal mixing can make a big difference in the total mass loss between models of a similar initial mass, as well as how these prescriptions are implemented into the code. The models by Limongi & Chieffi (2018) especially lose much more mass in the early phases when rotation is included, while the mass loss for the non-rotating models is comparable. When looking at their Figure 7, their lowest mass models including rotation move up almost vertically in the Hertzsprung-Russell diagram at the end of the main sequence, due a difference in the way the bi-stability jump is treated (Limongi and Chieffi, private communication). Another important difference with those models is that for the coolest phases, they implement the mass-loss prescription of van Loon et al. (2005), which is a dust-driven wind for the red supergiant phase. This leads to a strong increase in the mass loss for the rotating models on the lower mass end of the stars discussed here, which is not seen in my models nor in those by Ekström et al. (2012). Only the rotating models pass the threshold for the dust-driven wind to activate. The non-rotating models behave quite similar to my models and those by Ekström et al. (2012) over the whole mass-range. The 20 and 25 $M_{\odot}$ models by Ekström et al. (2012) also lose more mass compared to my models due to an additional boost on the mass loss rate which they describe in their paper. It is thus important to keep in mind that even though the physical input of different sets of models looks similar, the exact implementation and the combination of the implementations can have large effects on the outcome, which is most clearly visible for the rotating models by Limongi & Chieffi (2018).

Table 3.2: Selected details of the stellar evolution of my stellar models for Set 3. $M_{\rm ini}$ is the initial mass in $M_\odot$. $V_{\rm ini}$ is the initial rotational velocity in km/s. $t_{\rm H}$, $t_{\rm He}$, and $t_{\rm tot}$ are the duration of hydrogen burning, helium burning, and the total evolution time in Myr, respectively. $M_{*,\rm H}$, $M_{*,\rm He}$, and $M_{*,\rm C}$ are the masses of the stars at the end of their respective burning phases. $M_{c,\rm He}$, $M_{c,\rm C}$, and $M_{c,\rm O}$ are the masses of the hydrogen-depleted core, the helium-depleted core, and the carbon depleted core at the end of the corresponding burning phases in $\rm M_\odot$. ΔM is the total mass lost in $\rm M_\odot$. $\xi_{2.5}$ is the compactness of the star at the final model.

$M_{\rm ini}$ ($\rm M_\odot$)	$V_{\rm ini}$ (km/s)	$t_{\rm H}$ (Myr)	$M_{c,\rm He}$ ($\rm M_\odot$)	$M_{*,\rm H}$ ($\rm M_\odot$)	$t_{\rm He}$ (Myr)	$M_{c,\rm C}$ ($\rm M_\odot$)	$M_{*,\rm He}$ ($\rm M_\odot$)	$t_{\rm tot}$ (Myr)	$M_{c,\rm O}$ ($\rm M_\odot$)	$M_{*,\rm C}$ ($\rm M_\odot$)	ΔM ($\rm M_\odot$)	$\xi_{2.5}$ -
10	0[1]	23.00	1.83	9.78	1.98	1.52	9.11	25.37	1.38	9.04	0.96	6.09e-3
	150[1]	23.95	1.92	9.75	1.89	1.58	9.06	26.21	1.34	8.99	1.01	7.69e-3
	300	26.96	2.04	9.64	1.69	1.84	8.62	28.99	1.91	8.55	1.45	0.017
15	0	12.15	3.62	14.58	0.96	3.41	11.49	13.26	1.71	11.35	3.65	0.098
	150	12.49	3.73	14.50	0.92	3.54	11.22	13.56	1.60	11.08	3.91	0.078
	300	14.05	4.09	14.23	0.86	4.04	9.96	15.03	1.66	9.80	5.20	0.086
20	0	8.53	5.73	19.12	0.66	5.66	11.24	9.29	2.49	11.02	8.98	0.23
	150	8.68	5.82	18.96	0.65	5.83	10.77	9.43	1.92	10.55	9.44	0.16
	300[1]	9.87	6.45	18.39	0.60	6.62	9.39	10.55	2.99	9.28	10.71	0.40
25	0[1]	6.80	7.99	23.20	0.53	8.13	11.04	7.41	1.71	10.92	14.07	0.12
	150	6.96	8.23	22.87	0.53	8.06	11.27	7.56	1.77	11.04	13.95	0.11
	300	7.68	8.86	22.12	0.50	8.63	11.06	8.25	1.90	10.96	14.03	0.11
30	0[1]	5.80	10.35	26.89	0.47	10.73	13.56	6.32	2.44	13.47	16.52	0.23
	150	6.00	10.80	26.13	0.45	10.70	13.25	6.50	2.23	13.12	16.87	0.22
	300	6.47	11.29	25.39	0.44	10.81	13.24	6.96	2.16	13.12	16.86	0.19
35	0	5.15	12.74	30.38	0.42	12.95	15.64	5.62	3.00	15.46	19.51	0.18
	150	5.27	13.05	29.75	0.41	12.55	15.15	5.73	2.79	15.00	19.98	0.23
	300	5.70	13.90	29.09	0.40	12.12	14.83	6.15	2.69	14.65	20.33	0.29
40	0	4.69	15.17	33.23	0.39	13.63	16.40	5.12	3.21	16.24	23.74	0.19
	150	4.78	15.49	32.55	0.38	13.21	16.11	5.20	3.07	16.04	23.93	0.23
	300	5.15	16.39	30.94	0.37	13.72	16.70	5.56	3.09	16.65	23.32	0.26
45	0	4.35	17.57	35.74	0.36	14.85	17.95	4.76	3.43	17.90	27.06	0.26
	150	4.48	18.28	34.28	0.35	15.26	18.20	4.88	3.28	18.13	26.82	0.26
	300	4.81	19.22	34.03	0.35	15.57	18.63	5.20	3.62	18.55	26.41	0.31
50	0	4.09	20.05	37.93	0.35	16.84	19.92	4.48	3.77	19.87	30.07	0.31
	150	4.21	20.79	35.93	0.34	16.68	19.80	4.59	3.53	19.71	30.23	0.30
	300	4.47	21.77	36.26	0.38	17.70	20.81	4.85	3.99	20.73	29.21	0.33
60	0	3.71	25.04	41.39	0.33	19.49	22.76	4.07	4.53	22.67	37.25	0.31
	150	3.78	25.84	43.08	0.32	20.09	23.37	4.14	4.60	23.29	36.63	0.32
	300	4.02	25.89	34.26	0.35	13.19	16.01	4.40	3.15	15.93	43.99	0.23
70	0	3.43	30.29	50.32	0.31	22.86	26.36	3.78	15.14[2]	26.25	43.65	0.46
	150	3.53	30.82	43.31	0.32	16.89	20.08	3.89	3.88	19.99	49.92	0.32
	300	3.67	28.80	33.48	0.36	11.10	13.68	4.07	2.74	13.60	56.30	0.29
80	0	3.24	34.98	50.72	0.31	20.68	24.10	3.58	4.84	23.99	55.90	0.36
	150	3.36	30.33	33.28	0.36	10.67	13.24	3.76	2.45	13.17	66.72	0.25
	300	3.54	21.99	25.20	0.39	9.10	11.54	3.97	2.06	11.46	68.42	0.16

[1] Terminated before core collapse was reached due to numerical difficulties. The mass loss was complete. [2] This run experienced computational difficulties in the final phases, leading to a much larger $\rm M_{c,O}$ than for any of the other models.

Chapter 4

Stellar yields: results and discussion

In this chapter, I present the stellar yields calculated by the models described in the previous two chapters. First, in Section 4.1, I discuss the yields from the stars of Set 1 and Set 2, as well as the SNB yields and what causes the differences between the SNB yields and those of Set 2. The latter was already briefly touched on in Chapter 3. As in Chapter 3, the 20 $M_\odot$ and 50 $M_\odot$ stars and their binary counterparts are used as examples to compare Set 1 and Set 2 in Sections 4.1.1 and 4.1.2. Then, in Section 4.1.3, I present all models of Sets 1 and 2. In Section 4.2, I discuss the yields from the models of Set 3. In both Section 4.1 and Section 4.2, the yields are compared to those from various studies in the literature.

4.1 Yields from single and binary stars to the onset of carbon burning

The results presented in this section were published in Brinkman et al. (2019).

As mentioned in Chapter 3, to understand how the ^{26}Al yields are affected by binary interactions, I compare the yields of Set 1 to the yields of Set 2, and to the results of the SNB-scheme. In Section 4.1.1, I do this first for the 20 $M_\odot$ model, similar to Section 3.1. I compare the yields to those by Limongi & Chieffi (2006, 2018); Woosley & Heger (2007) and Ekström et al. (2012), as well as to the binary system presented by Braun & Langer (1995). In Section 4.1.2, I do the same for the 50 $M_\odot$ model, similar to Section 3.2. In Section 4.1.3, I compare all the results of the other masses of Sets 1 and 2 to each other, as well as to the various studies from the literature. The ^{26}Al yields for all systems of Set 1 and Set 2 are provided in the Table 3.1 in Section 3.3, as well as information on the evolutionary stages of all stars.

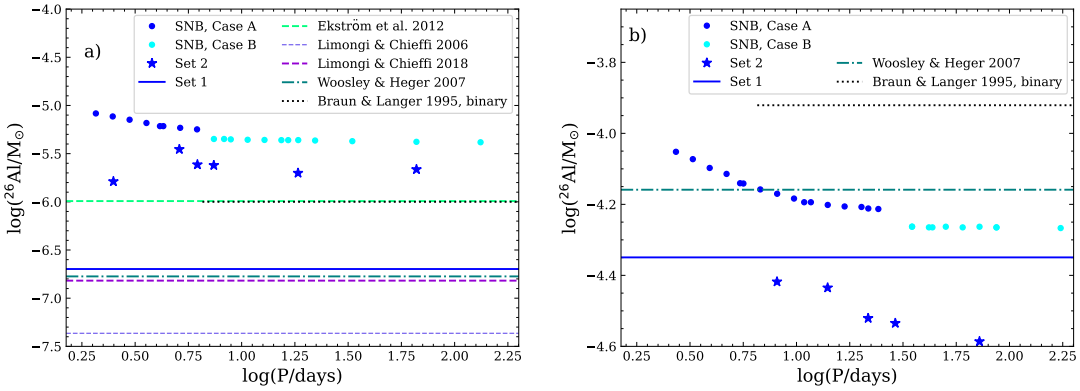

Figure 4.1: (a) ^{26}Al yields for a 20 $M_\odot$ single, non-rotating star from Set 1 (blue solid line) and various other studies. Note that the yield from Ekström et al. (2012) is almost identical to the yield by Braun & Langer (1995). The black dotted line indicates the yield from the binary by Braun & Langer (1995) given as a line starting at the first period for a Case B system, because the exact period of this Case B system is unknown. The dots are the yields of my SNBs, blue for Case A and cyan for Case B. The stars indicate the yields for the numerical binaries of Set 2. (b) Same as Figure 4.1a for the 50 $M_\odot$ primary. Note the difference in the y-scale, where the left panel covers more than 3 orders of magnitude due to the large difference between the single star and the binary, the right panel less than one order of magnitude because the single star yields and binary yields are more similar.

4.1.1 20 $M_\odot$

Figure 4.1a shows the ^{26}Al yields for a 20 $M_\odot$ single star from Set 1, as well as the yields from single stars from the literature as horizontal lines. The yields from the numerical binaries (Set 2) and the SNBs with a companion of 18 $M_\odot$ are given as stars and dots as function of the period, respectively. Compared to the single star models of Set 1, the yields from the SNBs are a factor of 20-40 higher. The SNB yields decrease until an orbital period of ∼6.2 days is reached and then the yield plateaus. This is caused by the transition in the type of mass transfer: the systems with periods shorter than ∼6.2 days undergo Case A mass transfer (blue dots in Figure 4.1), those with longer orbital periods undergo Case B mass transfer (cyan dots in Figure 4.1). The yields from SNB Case A systems are more sensitive to the orbital period, and they decrease as the orbital period increases. This is due to the slow increase of radius over the duration of the main sequence, as can be seen in the upper left panel of Figure 2.1. While the hydrogen-burning core slowly decreases in size, the ^{26}Al in the areas that belonged to the hydrogen-burning core now decays (see bottom left panel of Figure 2.1). Because the half-life of ^{26}Al is 0.72 Myr, a significant part of the ^{26}Al that was present in the core has decayed by the time the latest Case A system is modelled, as compared to the shorter Case A systems. The Case B systems have a lower yield than the Case A systems by a factor up to 2 because for the Case B systems more ^{26}Al has already decayed, relative to the Case A systems.

However, because mass transfer for all the Case B systems occurs at a very similar time, between 8.56-8.57 Myr (see right panels of Figure 2.1), the orbital period has almost no influence on the yields from these systems.

Compared to their SNB counterparts, the numerical binary systems undergoing Case B mass transfer follow a similar trend: there is only a small variation in the yields between the Case B system with the shortest and the longest orbital period. However, the ^{26}Al yields are lower for the numerical binary systems in all cases. This is because the orbital adjustment during the mass-transfer phase changes the size of the Roche lobe (see Equations 1.25 and 1.26). This causes the star to detach ($R < R_L$) from its Roche lobe when a smaller amount of mass is lost, as compared to the SNBs. The numerical Case A systems follow a different trend than their SNB counterparts. For systems with short orbital periods, the change in the orbital period plays a larger role. Unlike the SNBs, where the mass is lost in one instantaneous event, the numerical Case A binary systems go through two phases of mass transfer prior to the end of helium burning (Case A and Case AB, see Figure 3.1d in Section 3.1). Close to the end of helium burning of the primary star in the closest period systems, the secondary star starts to evolve off the main sequence and fills its Roche lobe, starting a phase of reverse mass-transfer (see also Section 6.1.1). In my set-up this ends the evolution of the system. The shorter the period, the earlier the Roche lobe overflow for the secondary takes place, leading to a lower yield. For the wider Case A systems, which do not go through reverse mass-transfer prior to the end of helium burning of primary, the ^{26}Al yield goes down again due to the internal decay of the ^{26}Al, just as for the SNBs.

To put the single and binary yields from Sets 1 and 2 in perspective, Figure 4.1a also shows the results by Limongi & Chieffi (2006, 2018); Woosley & Heger (2007) and Ekström et al. (2012). My single star wind yield is in agreement with the yield found by Woosley & Heger (2007) and Limongi & Chieffi (2018). The yield given by Ekström et al. (2012), instead, is higher by almost an order of magnitude. This is because, as they mention in their Section 2.6.2, these authors have artificially increased their mass-loss rate for their 20 and 25 $M_\odot$ models. They remark that this leads to an order of magnitude larger mass-loss rate, when averaged over time, than the rate by de Jager et al. (1988). The yields for the binary systems, both numerical and semi-numerical, are still higher than this single star result, showing that even for a different wind prescription, the effects of the binary interactions have a stronger impact.

I also compare my results to the yield given by Braun & Langer (1995). The wind yield they find is comparable to the single star yield found by Ekström et al. (2012). Compared to the Case B binary yields I present, this is a factor of $\sim$2 smaller. While the mass-transfer efficiency for the systems is the same and both studies used the Ledoux criterion, the metallicity is slightly different (Z=0.02) and the mass-loss prescriptions are different as well. Another difference is that the secondary is not fully evolved but treated

as a point mass. However, it is difficult to say exactly which of these differences leads to the subsequent difference in the yield.

4.1.2 50 $M_\odot$

Figure 4.1b shows the results for the 50 $M_\odot$ single star model of Set 1, as well as for the binaries of Set 2 with a companion of 45 $M_\odot$ and the SNBs for the same initial mass. Note the difference in the vertical scale compared to Figure 4.1a, 3.5 orders of magnitude versus ∼1 order of magnitude for panel b. This is because the binary yields for the 50 $M_\odot$ models are much closer to the single star yield than for the 20 $M_\odot$ models, as was shown as well in Sections 3.1 and 3.2. In Figure 4.1b, it is visible that the ^{26}Al yields from the SNBs are in general up to a factor of 2 higher than the ^{26}Al yield of the single star model (see also Table 3.1). This increase is significantly less than for the 20 $M_\odot$ binaries, where the increase is between a factor of 20-40 (Figure 4.1a).

More interestingly, as can be seen in Figure 4.1b, the yields from the numerical binary systems are lower than for the single star model, by up to a factor of 2. It has to be noted however, that neither the single star, nor any of the binary systems reached the end of helium burning. These stars are indicated by ^{2} in Table 3.1, where the value of Y_c is a proxy for the stage of helium burning, i.e., the lower the central helium mass-fraction, the closer to the end of helium burning. During helium burning, more mass will be lost from all 50 $M_\odot$ stars (see also the discussion on Set 3 in Section 3.4). This will lead to a yield higher than shown in Figure 4.1b. The increase will be the largest for the systems that stopped the evolution in an earlier stage of helium burning. This may push a few of the binary systems closer to the single star yield, but some might still remain below it. However, also the single star yield will still increase due to further mass loss. Only completing helium burning for both the binary systems and the single stars will give a final answer. For the SNB yields, it does not matter that helium burning was not finished since these yields are calculated either during hydrogen burning or between hydrogen and helium burning. This leads to a higher yield for the SNB systems than for the numerical binaries.

Considering this result, I confirm the conclusion of Braun & Langer (1995) that, above a given mass, the effect of binary interaction no longer significantly increases the ^{26}Al yield, but keeps it at the same level or decreases it compared to the single star yield. This is because the mass-loss rate by wind is comparable to the mass-loss rates due to binary interaction at this stellar mass. This leads to a similar amount of mass lost from the stars, independent of whether the star has a companion or not. The general trend is that for a system with a 50 $M_\odot$ primary, the binary interaction does not increase the ^{26}Al yield compared to the single star.

I compare my results to the one given by Braun & Langer (1995). The wind yield for their binary system is higher than for all the SNBs. Compared to my single star model, their binary system has a yield of a factor of ∼2.5 larger, and it is a factor of ∼3-4.5 larger than for my binary systems. As stated in Section 4.1.1, it is difficult to say exactly which of the differences between the model set-ups is the source of the difference in the yield.

Only Woosley & Heger (2007), of the studies compared to here, consider a 50 $M_\odot$ model. The yield of this model is higher than the Case B SNB yields, and also higher than my single star yield. It is lower than the yield from the binary model by Braun & Langer (1995).

4.1.3 Other primary masses

Figure 4.2 shows the ^{26}Al wind yields for all the single stars from Set 1, as well as from various studies in the literature. All studies show the same trend of increasing ^{26}Al yield with increasing stellar mass. The spread in the yields converges towards the same value at the highest masses in the sample. The convergence of the yields shows that at lower masses, the models, and thus the yields are more sensitive to the physical input than at higher masses. For the lower mass end of the mass range, below 20 $M_\odot$, my single star yields are higher than for the other studies, by between a factor 3-10. However, even then the yields are much lower than the supernova yields, so it has no big impact on the overall ^{26}Al yield of these stars. From 20 $M_\odot$ to 30 $M_\odot$ my single star yields are comparable to most of the other yields. Above 30 $M_\odot$ my yields are slightly lower than Woosley & Heger (2007), but comparable to Limongi & Chieffi (2018). An explanation for this difference is that not all of my stellar models completed helium burning and a small amount of extra envelope lost can increase the ^{26}Al yields. From this figure it is also clear that the 20 $M_\odot$ and 25 $M_\odot$ models of Ekström et al. (2012) give much higher yields compared to all other studies, for the reasons already discussed in Section 4.1.1 for the 20 $M_\odot$ case.

Figure 4.3 shows my results for all the other different primary masses of Set 2, as well as the single stars of Set 1 and the various studies from the literature. It is important to notice the difference in the vertical scale for the different initial primary masses. For the lowest masses in my range (10 and 15 $M_\odot$), the variations are the largest and the vertical scale covers three orders of magnitude. This is due to the fact that for these masses the mass-loss rate for the single star is very small. For example, for the 10 $M_\odot$ single star, it is between 3×10^{-9}-3×10^{-8} $M_\odot$/yr on the main sequence, and has a maximum value of 2×10^{-6} $M_\odot$/yr at the end of the simulation. This is roughly one and two orders of magnitude lower than for the 20 $M_\odot$ and 50 $M_\odot$ single stars, respectively. This difference makes the effect of binarity on the total mass lost from the stars much more noticeable for the lowest masses in my range, relatively to mass loss from the single star. As a

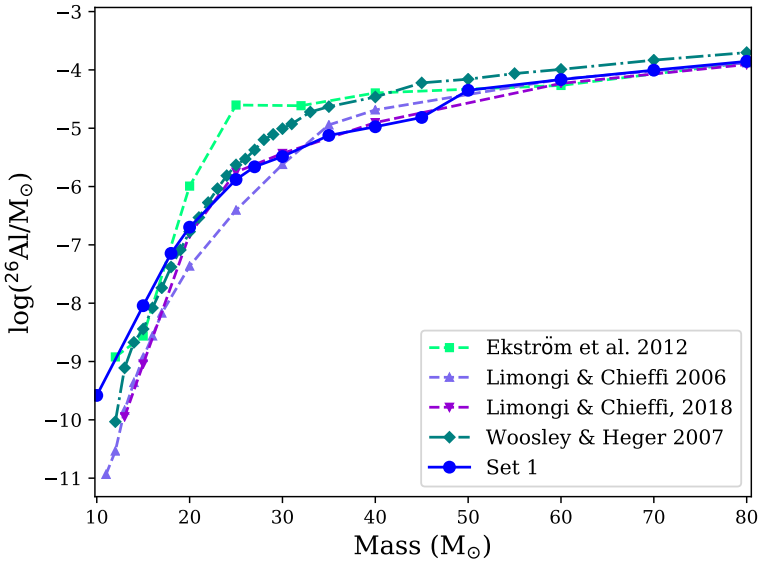

Figure 4.2: ^{26}Al wind yields for single, non-rotating single stars from Set 1 and from literature.

consequence, when the stellar mass increases the variations in the ^{26}Al yield decrease. For the lowest masses (10 and 15 M$_\odot$), all the binary yields are larger than the single star yields from all the studies reported here. For stellar masses of 25 and 30 M$_\odot$, the vertical scale covers two and one order of magnitudes, respectively, and the numerical binary yields are in some cases very similar to the single star yields, or even lower, when considering the 25 M$_\odot$ yield from Ekström et al. (2012). For masses from 35 M$_\odot$ and above the vertical scale covers a range of yield variation of a factor 3 to 5 only, and in several instances the binary yields, both numerical and semi-numerical, are similar to or even lower than the single star yields, as predicted by Braun & Langer (1995). For these cases, binarity effectively produces variations in the yields that cannot be distinguished from variations due to uncertainties in the stellar models of single stars.

For all the masses considered, the yields from the SNBs are always, by construction, higher than the numerical binary yields. The SNB yields show a clear pattern, Case A mass-transfer produces yields that decrease smoothly with orbital period and are always higher than those of the Case B mass-transfer models, where the yields are not affected by the period. For the numerical binaries, the Case B systems follow the same trend as their SNB counterparts while for the Case A systems, the yields of very short orbital period models are affected by reverse mass-transfer, as explained in Section 4.1.1 (see also Section 6.1.1).

In summary, the increase in the ^{26}Al yield in the binary system, relative to the single star, decreases with the mass - with typical multiplication factors of roughly 150, 50, 10-20, 5, 3, and 2 for stars with initial masses of 10, 15, 20, 25, 30, 35 M$_\odot$ (see Table 5.1 for the factors for all initial masses), and no significant changes for higher masses. The yields per system are tabulated in Table 3.1.

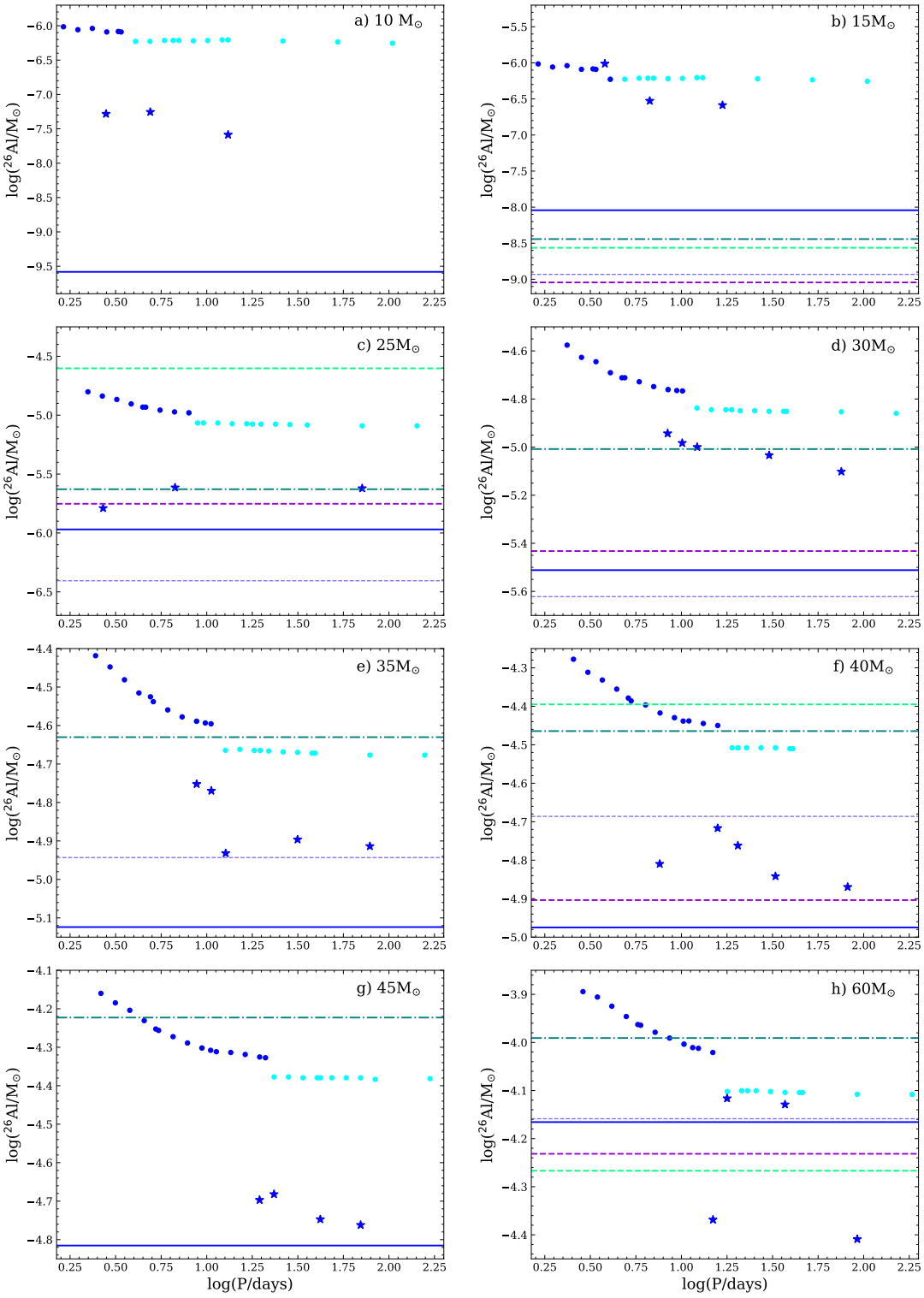

Figure 4.3: Same as Figure 4.1 but for the other masses of Set 1 and Set 2. The colours and the symbols indicate the same as in these two panels. Note that while the extend of the horizontal axis is the same for all of them, the vertical axis changes from 2 orders of magnitude to 0.5 orders of magnitude.

4.2 Yields from single, rotating stars up to the core collapse

The majority of the results discussed in this section were published in Brinkman et al. (2021). Not all isotopes were discussed in the main part of this paper, but were presented in the supplementary material. Here, I also highlight some of the other isotopes aside from the four SLRs, and the stable isotopes ^{19}F and ^{22}Ne.

In this section, I present and discuss the wind yields for ^{26}Al, ^{19}F, ^{22}Ne, ^{36}Cl, ^{41}Ca, and ^{60}Fe from Set 3 and compare them to various other studies in the literature. In Table 4.1 the yields of the four isotopes and the initial amounts of ^{19}F and ^{22}Ne present in the stars are presented. I also briefly discuss several other stable isotopes from the CNO-cycle that are of interest for galactic chemical evolution and galactic archaeology[1]

As discussed in Section 3.4, for the low mass end, 10-35 $M_\odot$, of the stars I investigated, most of the mass loss due to winds occurs between the main sequence and the onset of helium-burning. At the high mass end, ∼35-80 $M_\odot$, instead, the stars become Wolf-Rayet stars and continue to lose mass even during and shortly after helium burning, stripping away not only the hydrogen-rich envelope, but also the top of the hydrogen-depleted core. This strongly impacts the yields of these stars, especially for the isotopes synthesised after hydrogen burning.

4.2.1 The short-lived radioactive isotopes

Aluminium-26

For ^{26}Al (Figure 4.4a), the non-rotating yields are comparable to those from Set 1, with the exceptions of the 10, 40, and 45 $M_\odot$ models. The reason is that the 10 $M_\odot$ model of Set 1 loses more mass than the 10 $M_\odot$ model of Set 3 due to a longer main sequence lifetime, leading to a slightly higher yield. The 40 and 45 $M_\odot$ models of Set 3 are evolved until core collapse, while for Set 1 they did not finish helium burning. This leads to a larger mass loss and therefore a higher yield.

To estimate the effect of the binary interactions on the yields when the models include rotation, I again apply the SNB-scheme to these models. Then, to estimate the general effect, I calculate the "effective SNB yield". The effective SNB yield is defined as the single star yield multiplied by the arithmetic average increase (over all periods considered) of the yield of the single star compared to the yield of the SNBs, which cover multiple periods. I assume a flat period-distribution for this, giving all systems an equal weight in the

[1]The complete set of wind yields for all isotopes and models presented here, are available on Zenodo under a Creative Commons 4.0432 license: `https://doi.org/10.5281/zenodo.5497258`.

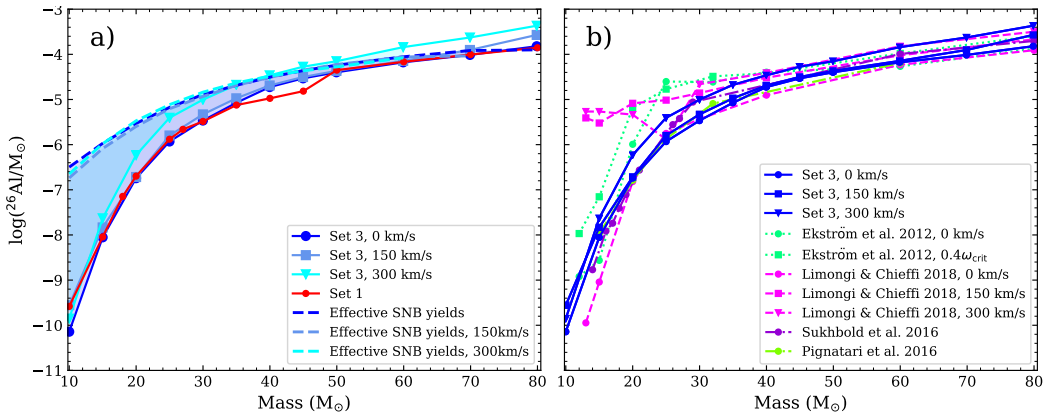

Figure 4.4: The left panel shows my ^{26}Al yields for the single star models (solid lines with symbols) at the three different initial rotational velocities. The red line shows the yields from Set 1. The dashed lines give the effective SNB yields for the different initial rotation velocities. The shaded area between the single star models and the effective binary yields is therefore the potential parameter space covered by binary systems. The right panel shows the single star models of Set 3 together with the yields of various other studies, as listed in the legend.

calculation. This allows for comparing the single star yields and the binary yields in the same figure for all masses.

The largest impact of the SNBs is at the lower mass-end, 10-35 M$_\odot$ (as shown in Section 4.1.3). However, here I also find that, because both rotation and binary interactions lead to an increased mass loss at similar points in the evolution, the impact of binarity, as estimated by using the SNB method, becomes relatively smaller with increasing initial rotational velocity. The effect of binary interactions becomes negligible for models with initial masses of 40-45 M$_\odot$, depending on the initial rotational velocity. Overall, as shown in Figure 4.4,my ^{26}Al yields are only mildly sensitive to rotation. Unlike in Set 1, where I used Hamann et al. (1995) for the Wolf-Rayet phase, for Set 3, I have changed this to Nugis & Lamers (2000). Even though this was changed, the ^{26}Al yields did not, and I conclude that the yields are therefore not sensitive to this change. Overall, the effect of the binary interactions is stronger than the effect of rotation or changing the wind.

Chlorine-36 and Calcium-41

Figures 4.5a and 4.5c show respectively the ^{36}Cl and ^{41}Ca wind yields for the models of Set 3. Unlike ^{26}Al, where the yield increases gradually with increasing mass, these yields show a sharp rise of almost 15 orders of magnitude at masses between 20-30 M$_\odot$, depending on initial rotational velocity. This is easily understood when considering Figure 4.6, which shows the KHDs for non-rotating 30 M$_\odot$ and 50 M$_\odot$ models, with the ^{41}Ca mass-fraction on the colourscale (^{36}Cl looks similar). Prior to core helium burning, there is no ^{41}Ca (or

^{36}Cl) present within these stars, as they are unstable. The mass fraction of ^{41}Ca (and ^{36}Cl) increases due to neutron captures during helium burning on ^{40}Ca (and ^{35}Cl), and it is also destroyed by neutron capture reactions, see the lower left (or upper right) panel of Figure 1.1. These neutrons are produced by the ^{22}Ne(α,n) reaction[2]. The ^{22}Ne itself is produced by the ^{14}N(α,n)^{18}O(α,n)^{22}Ne reactions, with the ^{14}N being produced in CNO cycles 1 and 2 (see Figure 1.7) during hydrogen burning. For the 30 $M_\odot$ model, this ^{41}Ca (and ^{36}Cl) barely reaches the surface, leading to a very low yield (2.22×10^{-19} and 6.76×10^{-21} for ^{41}Ca and ^{36}Cl, respectively). However, for the 50 $M_\odot$ model the top layers of the helium burning core are stripped away, leading to a more significant ^{41}Ca (and ^{36}Cl) yield (6.89×10^{-7} and 4.18×10^{-7} for ^{41}Ca and ^{36}Cl, respectively). For the rotating models, the Wolf-Rayet phase is reached at a lower initial mass due to an increase in the mass-loss rate. Therefore, the increase in the yields also moves towards lower initial masses. This means that unlike the ^{26}Al yields these yields are highly sensitive to the wind prescription used, especially for the Wolf-Rayet phase.

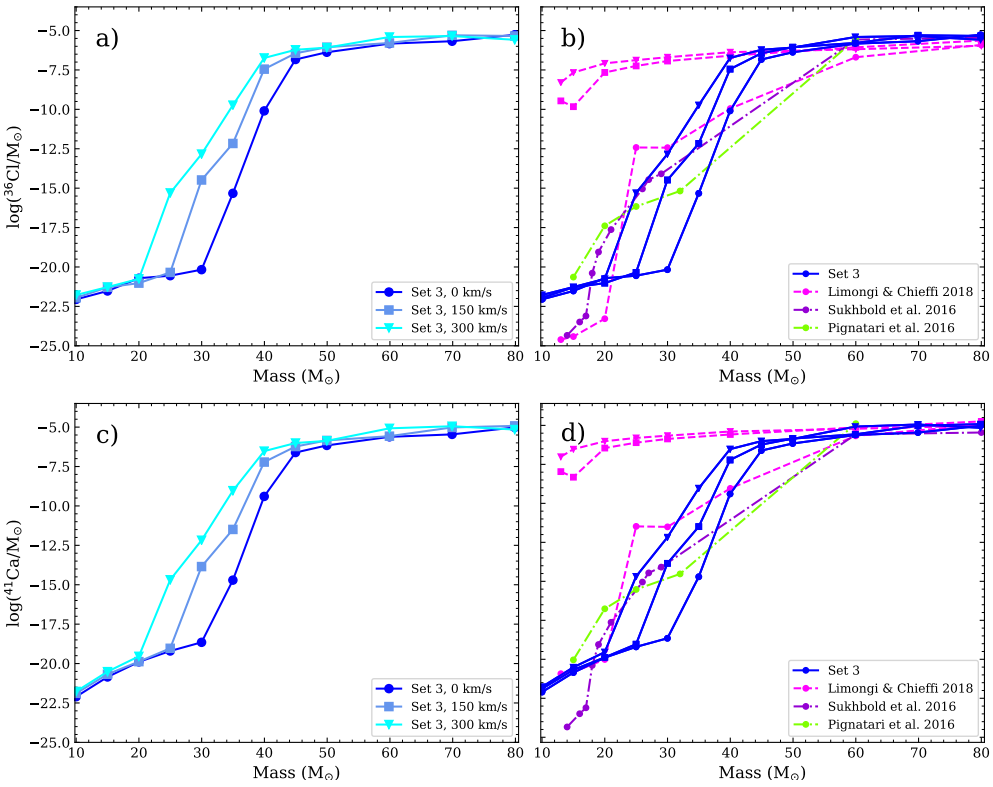

Figure 4.5: The left panel shows the ^{36}Cl yields. All colours and symbols are the same as for Figure 4.4. There is no initial amount of ^{36}Cl present in the star. The right panel shows the single star models of Set 3, together with the yields of various other studies where for Limongi & Chieffi (2018) and Ekström et al. (2012) the rotating models have the same symbols as in Figure 4.4.

[2]in Limongi & Chieffi (2006) it is mentioned that some of these neutrons are coming from the ^{13}C(α,n)-reaction. However, this reaction is only briefly active at the very beginning of helium burning and does not play a significant role for ^{36}Cl, ^{41}Ca, or ^{60}Fe (see also next section).

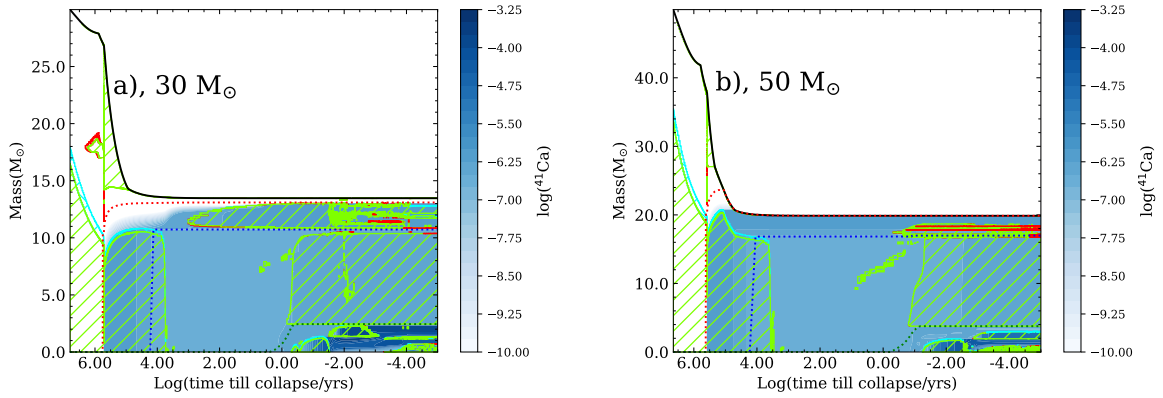

Figure 4.6: Kippenhahn diagrams for a 30 $M_\odot$ star in the left panel and for a 50 $M_\odot$ the right panel, both non-rotating. The colour-scale shows the ^{41}Ca-content. The green-hatched area is convective, the blue hatched area is overshoot, and the red areas are semi-convective. The red dotted line is the size of the hydrogen-depleted core.

Iron-60

The content of this section was originally included in Brinkman et al. (2021). However, during the revision process this was removed because the ^{60}Fe yields are very low and the full discussion was not necessary for the paper. Here, I do discuss these yields, as they are, mostly to show that these models do not produce any significant amount of ^{60}Fe, which is in favour for the origin of ^{26}Al in the early Solar System (see also Chapter 5).

Figure 4.7a shows the ^{60}Fe wind yields for the models of Set 3 with the three different rotational velocities. Most of the ^{60}Fe produced by massive stars is expelled during the supernova explosion (see, e.g., Table 3 of Limongi & Chieffi, 2006) and the wind yields for this isotope are generally very low, virtually zero for the three lowest masses considered here. This is because neutron captures on the unstable ^{59}Fe are needed to produce ^{60}Fe (see the lower right panel of Figure 1.1), and the neutron density during helium burning is not high enough for these reaction to significantly take place. As for ^{36}Cl and ^{41}Ca, the ^{22}Ne(α,n) reaction creates the neutrons needed for the production of ^{60}Fe. This produces only a small amount of this isotope that can be expelled by the winds. The steep increase in yields moves to lower masses with rotation because the Wolf-Rayet phase starts at a lower mass. However, even at the highest initial masses and including rotation, the yields do not exceed $\sim 10^{-9}$ $M_\odot$. The supernova yields are significantly larger, between 10^{-6}-10^{-5} $M_\odot$ (see, e.g., Limongi & Chieffi, 2018). The bulk of the ^{60}Fe expelled by the explosion is produced in the convective helium-shell (see, e.g., Table 3 of Limongi & Chieffi, 2006). This material will not be expelled by the winds, and will leave the star during the explosion. This shows that stellar winds yields will add little to the overall ^{60}Fe budget.

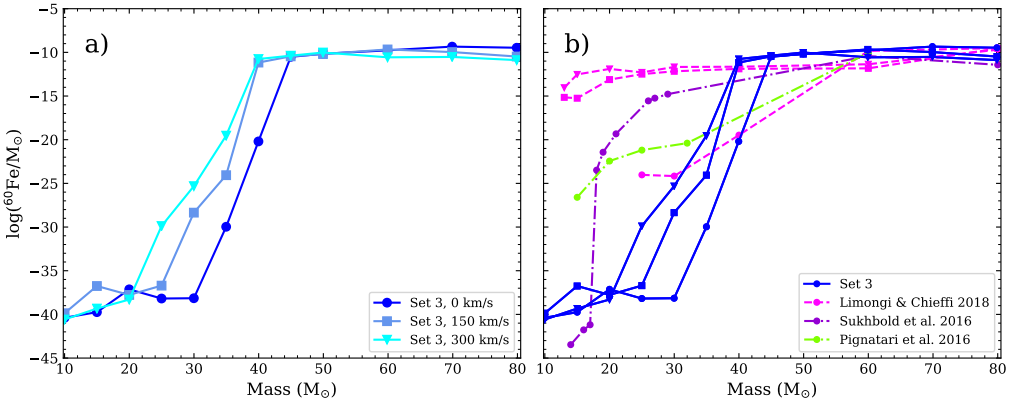

Figure 4.7: Same as Figure 4.5, but for ^{60}Fe. Note that while the horizontal axis is the same as for all the previous figures, the vertical axis covers about 40 orders of magnitude here.

4.2.2 Stable isotopes

Fluorine-19

^{19}F is a stable isotope and is already present in the star at the time of its birth depending on its metallicity. It is typically destroyed by proton captures during hydrostatic hydrogen-burning as part of the CNO-cycle (see Figure 1.7). The dominant destruction channel is ^{19}F(p,α)^{16}O during this phase. During helium burning, ^{19}F is produced by α-captures on ^{15}N (see Figure 4.8). In this figure, the top channel via the β^+ decay of ^{18}F is the dominant production channel for ^{19}F. The α-particles are present since this takes place during helium burning, while the neutrons and protons are produced by the ^{13}C(α,n) and ^{14}N(n,p) reactions, respectively. After its production, ^{19}F is also destroyed by α-captures, producing ^{22}Ne (Meynet & Arnould, 2000).

Figure 4.9 shows the KHDs for two 20 M$_\odot$ models, non-rotating on the left and with an initial rotational velocity of 300 km/s on the right. The colour-scale shows the ^{19}F mass-fraction in the star. For the non-rotating model, the initial ^{19}F present in the core is rapidly destroyed, while in the envelope it remains unprocessed until it is expelled from the star. For the rotating model, it takes longer to destroy all ^{19}F in the core, because fresh ^{19}F is being mixed in from the envelope. As a result of the rotational mixing, the ^{19}F mass-fraction decreases in the envelope. For both models the ^{19}F mass-fraction increases again in the core during helium burning, but by the end of this burning phase, most of it is destroyed again.

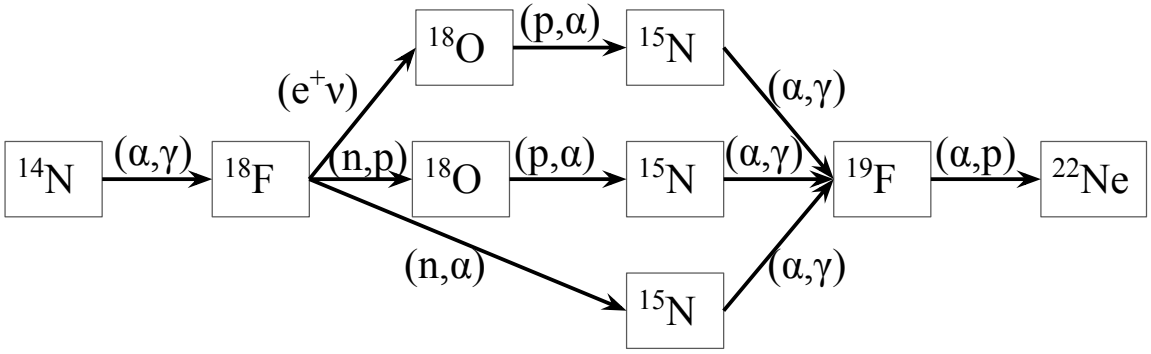

Figure 4.8: Production chains for ^{19}F during He-burning. The production of ^{19}F mainly happens through the top channel, since the β^+ decay of ^{18}F is the most efficient of the three channels. The protons and neutrons are produced by the ^{13}C(α,n) and ^{14}N(n,p) reactions, respectively.

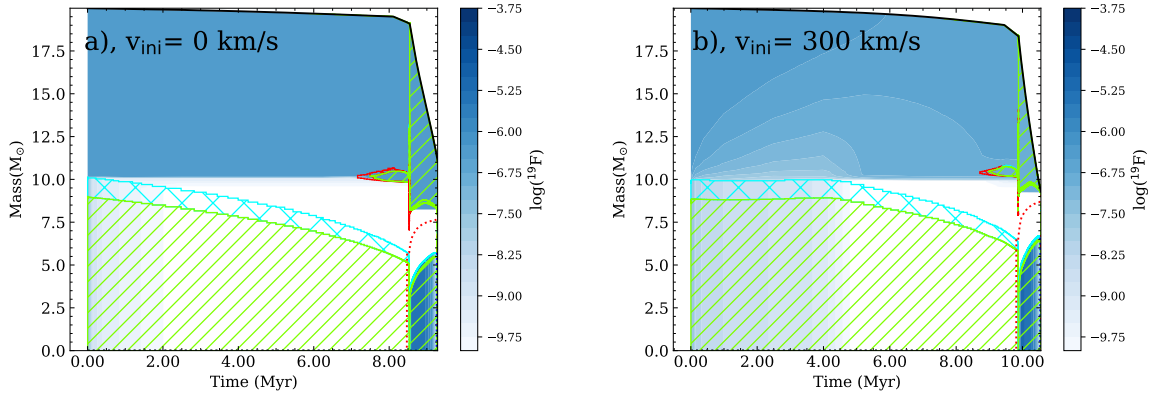

Figure 4.9: KHDs for a 20 M$_\odot$ star of Set 3, the left panel without rotation and the right panel with an initial rotation of 300 km/s. The colour-scale shows the ^{19}F mass-fraction. The green-hatched area is convective, the blue hatched area is overshoot, and the red areas are semi-convective. The red dotted line is the size of the hydrogen-depleted core.

The ^{19}F total wind yields are shown Figure 4.10a. The initial mass of ^{19}F present in the star is indicated as a solid red line to help visualise the net yields, which are difference between the total yields and this initial amount (see Section 2.4)[3]. For almost all models, the initial amount of ^{19}F present in the star is higher than the ^{19}F expelled and therefore the net yield is negative. only the 80 M$_\odot$ model with an initial rotational velocity of 150 km/s gives a positive yield. This is in agreement with the earlier results by Meynet & Arnould (2000) and Palacios et al. (2005a).

[3]In Brinkman et al. (2021), the initial amounts of ^{19}F and ^{22}Ne were not correct. They had been taken from the first main sequence model, but in the MESA code, some burning takes already place during the pre-main sequence. This means that some of the isotopes already got processed via the CNO-cycle. The values given in Figures 4.10 and 4.11, and in Table 4.1 have been corrected.

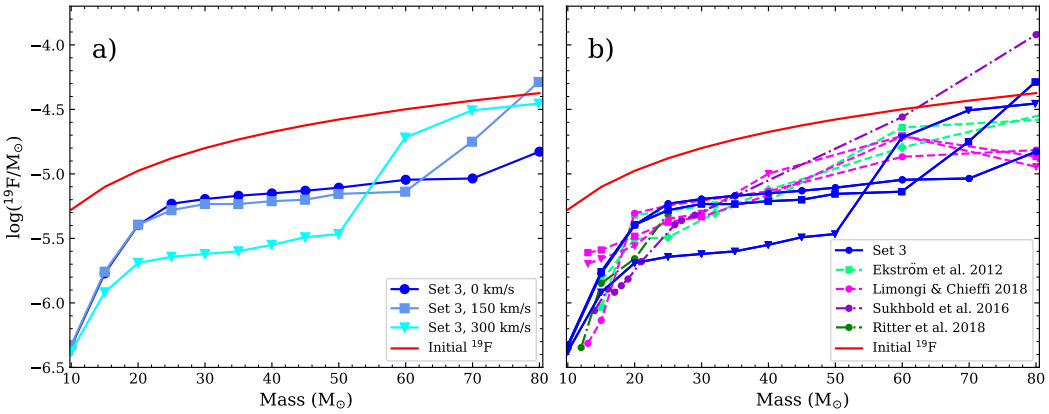

Figure 4.10: The left panel shows the ^{19}F yields for the models of Set 3. All colours and symbols are the same as for Figure 4.4. The red line indicates the initial amount of ^{19}F in $M_\odot$ in the models. The right panel shows the single star models of Set 3 together with the yields of various other studies, where for Limongi & Chieffi (2018) and Ekström et al. (2012) the rotating models have the same symbols as in Figure 4.4.

For the lowest masses in Figure 4.10, 10-35 $M_\odot$, all the expelled ^{19}F is not synthesised in the star itself, but it is the ^{19}F initially present in the star, minus the fraction destroyed by hydrogen and helium burning and thus the net yields are negative. Unlike for ^{26}Al, the yield does not increase when the stars are rotating faster because due to the rotational mixing ^{19}F is mixed into the core and destroyed instead of expelled from the star (see Figure 4.9). This leads to a lower ^{19}F yield for the rotating model compared to the non-rotating model. Also, for these models, the yield is lower than the initial amount of ^{19}F present in the star. This means that overall these massive stars are consumers of ^{19}F. For models with masses above ∼40 $M_\odot$ the ^{19}F synthesised in the helium core (and in the helium-burning shell during carbon burning) can be reached by the winds, leading to an increase in the yields. Yet, as pointed out before, for only one model this leads to a positive net yield.

Neon-22

Figure 4.11a shows the ^{22}Ne wind yields. Below 35 $M_\odot$, rotating models produce lower yields than the non-rotating models. The reason is similar as for ^{19}F: ^{22}Ne is destroyed inside the core during hydrogen burning, however, at a lower rate than ^{19}F. The destruction takes place via proton-captures in the NeNa-cycle. Rotation enhances the mixing between the envelope and the core and thus leads to more destruction of ^{22}Ne than for the non-rotating models, and thus to a lower yield. Unlike ^{19}F, where only one star in my grid gives a positive net yield (80 $M_\odot$with V_{ini}=150 km/s), for ^{22}Ne, stars with an initial mass of 45 $M_\odot$ and higher give a positive net yield, as well as the 40 $M_\odot$ model

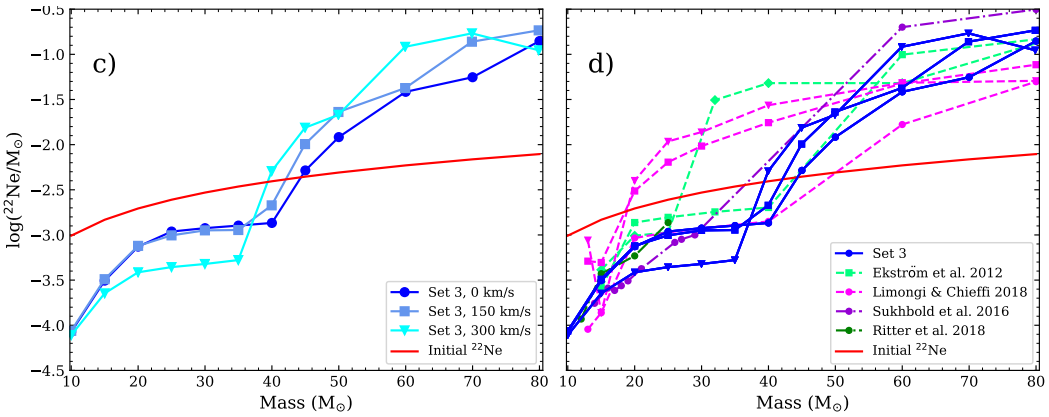

Figure 4.11: The left panel shows the ^{22}Ne yields for the models of Set 3. The red line indicates the initial amount of ^{22}Ne present in the stars. The right panel shows the stellar models of Set 3 together with the yields of various other studies.

with an initial rotational velocity of 300 km/s. This is because, unlike ^{19}F, ^{22}Ne is not destroyed during helium burning, but remains abundantly present until the end of this burning phase as it is produced via the ^{14}N(α,γ)^{18}F(,$\beta^+\nu$)^{18}O(α,γ)^{22}Ne reaction chain. Because of this, all the mass loss will contribute to the ^{22}Ne yield, while for ^{19}F it is only for a limited amount of time, until it is destroyed again.

4.2.3 Comparison to other studies

The right panels of Figures 4.4, 4.5, 4.7, 4.10, 4.10 and 4.11, show the results of the models of Set 3 (and Set 1 for ^{26}Al) along with several other studies from the literature. On top of the earlier considered studies, Limongi & Chieffi (2018) and Ekström et al. (2012), here I also consider the non-rotating models from Sukhbold et al. (2016), computed with the KEPLER stellar evolution code, Pignatari et al. (2016), computed with GENEC for the for mass range of interest, and from Ritter et al. (2018b), computed with MESA version 3709. I note that Ekström et al. (2012) and Pignatari et al. (2016) both use the GENEC code, however, the models of Pignatari et al. (2016) cover all burning stages, therefore all isotopes of interest are included, while for Ekström et al. (2012) I do not have yields for ^{36}Cl, ^{41}Ca, and ^{60}Fe. Overall, the yield sets are in broad agreement, within the uncertainties of the stellar evolution modelling. The models that stand out the most are the low-mass (10-30 M$_\odot$) models by Limongi & Chieffi (2018). These models show an increase in the SLR yields from non-rotating to rotating orders of magnitude higher than found by the other models. For ^{26}Al, the Limongi & Chieffi (2018) increase is comparable to the increase in the ^{26}Al yields I found for Set 1 to Set 2. This behaviour in the Limongi & Chieffi (2018) models is due to a very strong increase in the mass loss compared to their non-rotating models, leading to an increased yield. This difference in mass loss is due to

the treatment of rotational mixing and the formation of a dust driven wind following the wind prescription by van Loon et al. (2005), as explained in Chieffi & Limongi (2013). Limongi & Chieffi (2018) do not provide ^{60}Fe yields for their non-rotating models below 25 $M_\odot$.

As in the case of the other SLRs, the yields for their lowest masses increases significantly when rotation is included, while my models show similar yields for the rotating and non-rotating models. The models from Sukhbold et al. (2016) and Pignatari et al. (2016) behave in a similar way as for ^{36}Cl and ^{41}Ca. Above 60 $M_\odot$, the yields of the various studies become similar, and still much lower than the yields given by supernova explosions.

For the stable isotopes, the highest mass models by Sukhbold et al. (2016) stand out. These models lose much more mass than my 60-80 $M_\odot$ stars, especially their 80 $M_\odot$ model loses nearly 74 $M_\odot$, compared to $\simeq$56 $M_\odot$ for my non-rotating model. The 20 and 25 $M_\odot$ Ekström et al. (2012) models have higher yields than the overall trend for these two masses, because these stars have a slight boost to their winds, independent of rotation, as mentioned in Section 3.4.1.

4.2.4 Stable isotopes of the CNO-cycle

The results discussed in this section are part of the results of Brinkman et al. (2021), and the yields were published in the supplementary material of that paper. However, in the context of Brinkman et al. (2021), these yields were not explicitly discussed. The CNO-isotopes ($^{12,13}C$, $^{14,15}N$, and $^{16-18}O$) are interesting for stardust grains and galactic chemical evolution. Therefore, this information could be used in future works, I present the results here in more detail.

The CNO-isotopes (^{12,13}C, ^{14,15}N, and $^{16-18}$O) are interesting for stardust grains, material that originated in the cooling matter surrounding stars, which have the isotopic signature of their parent star, and for galactic chemical evolution. The origin of the CNO isotopic ratios have been studied extensively (see, e.g., Romano & Matteucci, 2003; Romano et al., 2019; Kobayashi et al., 2020, and references therein).

Romano & Matteucci (2003) state that low- and intermediate-mass stars are mainly responsible for the production of ^{12}C and ^{14}N, while massive stars produce most the ^{16}O. ^{13}C and ^{17}O have their origin in intermediate-mass stars, with small contributions of low-mass and massive stars. Kobayashi et al. (2020) do not split out the separate isotopes in their study. In their Figure 39, they show that asymptotic giant branch stars and core-collapse supernovae are the sources of the CNO elements. For carbon, massive stars and low mass asymptotic giant branch stars together are responsible for the production of carbon in the Universe, producing about half each of the total carbon budget. For nitrogen, the asymptotic giant branch stars have a stronger contribution than the massive

stars, while it is the other way around for oxygen, where the core-collapse supernovae are the main source. However, in neither of these studies, and there are many others, the contribution of binary stars has been taken into account. Recently, Farmer et al. (2021) have studied the impact of binary interactions on the carbon yields of massive binary stars and their supernovae, concluding that the yields of binary stars could be between 1.5-2.6 times higher than the single star yields. They have not expanded their study to the other isotopes in the CNO-cycles.

It is beyond the scope of this thesis to consider the impact of the yields of my models on either on the ESS or on galactic chemical evolution. Instead, I merely discuss the yields of the models of Set 3 and their trends, and compare them with the yields of various studies from the literature.

Carbon-12 and carbon-13

^{12}C and ^{13}C are both part of the CNO-cycle (see Figure 1.7). The initial amounts of these isotopes are are converted into ^{14}N in the hydrogen burning-core, though due to the nature of the CNO-cycles, not completely destroyed. Later on, during core helium-burning, ^{12}C is produced by the triple-α process. Some of this synthesised ^{12}C is subsequently turned into ^{16}O by α-captures, and later the rest is burned in core carbon-burning. Because of this, the behaviour of the ^{12}C yields is very similar to that of ^{22}Ne, which is produced in early helium burning. Aside from the shift of the y-axis, Figure 4.11a and Figure 4.12a look similar. Compared to the studies from the literature (see Figure 4.12b), the ^{12}C yields show a comparable behaviour. For the rotating models, first the ^{12}C yield is lower than the yield for the non-rotating model, and when the stars become Wolf-Rayet stars, the yields of the rotating models are generally higher. The models from Ekström et al. (2012) show an earlier strong increase in the ^{12}C yield. As for the other isotopes, the rotating models by Limongi & Chieffi (2018) show a different behaviour at the lower mass end.

The behaviour of ^{13}C is different from ^{12}C and ^{22}Ne. In Figure 4.12c, the yields for ^{13}C are plotted, as well as the initial amount of ^{13}C present in the stars. For the lowest two masses, 10 and 15 $M_\odot$, the net yields are negative. Then, for 20-60 $M_\odot$ the stars have positive net yields of ^{13}C for the non-rotating and rotating star at 150 km/s, and for 20-40 $M_\odot$ for the fastest rotating stars. At 80 $M_\odot$ all models have a positive net yield again.

^{13}C is initially converted into ^{14}N and then completely destroyed in early helium burning through α-captures. The complete destruction of the isotope explains why the yields even in the Wolf-Rayet phase are lower or comparable to the initial amount of ^{13}C in the star. This, however, does not explain the behaviour of the yields between 20-50 $M_\odot$. Rotation

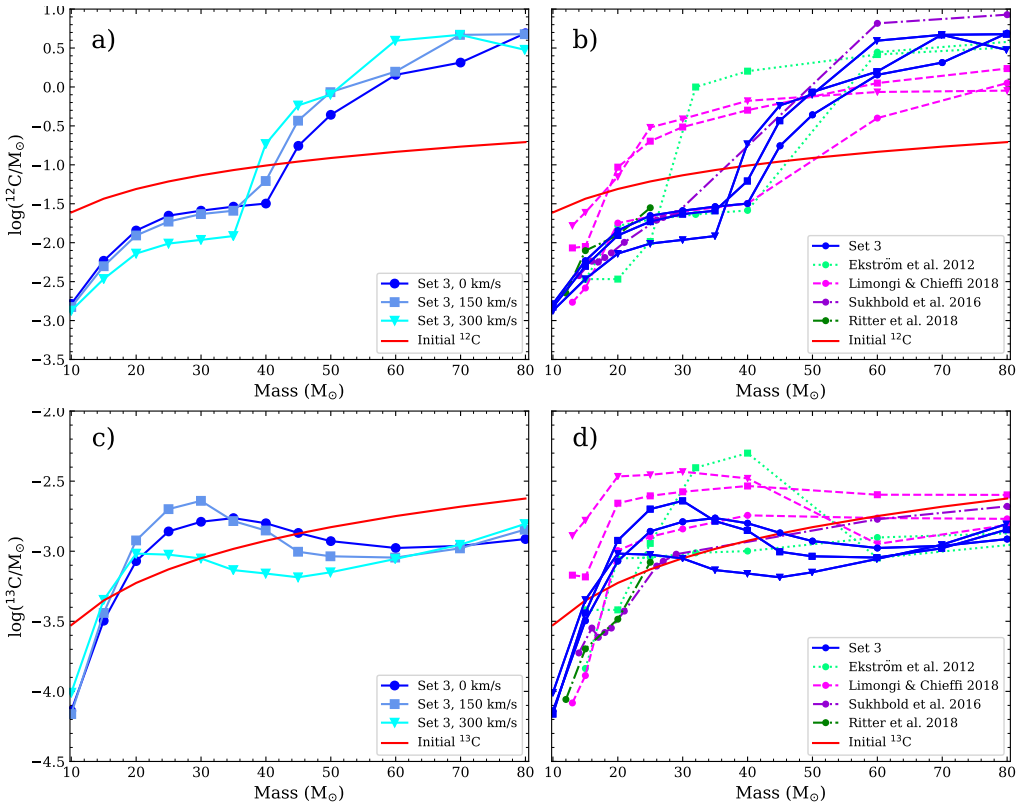

Figure 4.12: The left panels show the ^{12}C and ^{13}C yields for the models of Set 3. The red lines indicate the initial amounts of the isotope present in the models. The right panels show the stellar models of Set 3 together with the yields of various other studies.

has the same effect on ^{13}C as on the other CNO-isotopes, however, because the abundantly present ^{12}C is first converted to ^{13}N and then to ^{13}C, some of the conversion of ^{13}C into ^{14}N is compensated. This ^{13}C is then mixed out of the core into the envelope, leading to the increased yields. This effect is most prominent for the models with an initial rotational velocity of 150 km/s, and is the strongest at $\sim$30 M$_\odot$. For the faster rotating models, the conversion of ^{12}C in the CNO cycle is not enough to compensate for the conversion of ^{13}C, and the yields of these stars are below those of the non-rotating models. At $\sim$35 M$_\odot$, the yields of the moderately rotating model become lower than the yields of the non-rotating model, and the behaviour becomes relatively similar to ^{19}F, which is also completely destroyed in core helium-burning, and the net yield is negative for all models with initial masses above 45 M$_\odot$, and from 30 M$_\odot$ for the models with an initial rotational velocity of 300 km/s.

Compared to the studies from the literature (see Figure 4.12d), the rotating models by Ekström et al. (2012) and Limongi & Chieffi (2018) show a similar curve, the yields increasing first and then decreasing with mass. The spread in yields between 10-45 M$_\odot$ is about an order of magnitude, which shows that these yields are sensitive to the assumptions of the stellar models.

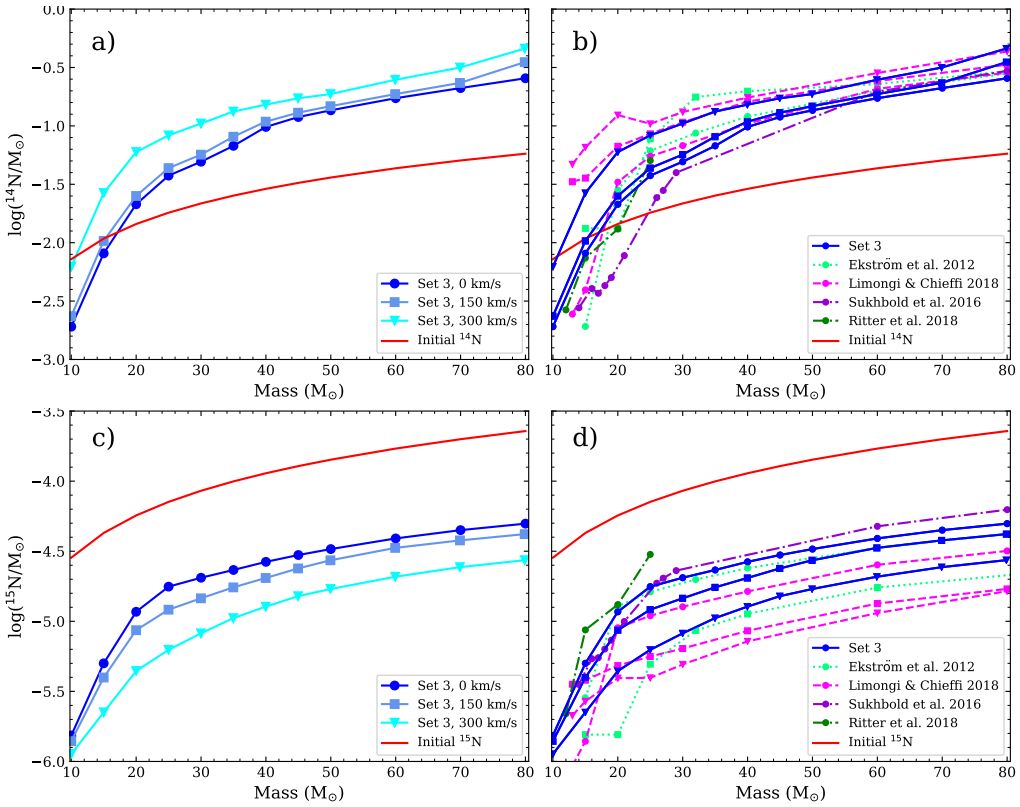

Figure 4.13: The left panels show the ^{14}N and ^{15}N yields of Set 3. The red lines indicate the initial amounts of the isotope present in the models. The right panels show the stellar models of Set 3 together with the yields of various other studies.

Nitrogen-14 and nitrogen-15

Unlike carbon, the nitrogen (mainly ^{14}N) in the Universe is mainly produced by intermediate mass asymptotic giant branch stars (4-7 M$_\odot$) Kobayashi et al. (2020). Still, ^{14}N is used often to calibrate the settings of rotation, as mentioned in Section 2.3.2. The isotope is used because the ^{14}N(p,γ) reaction is the slowest for the CNO and cycles 1 and 2 (see Figure 1.7). This means that during hydrogen burning, there is a significant production of ^{14}N from the other CNO isotopes. This ^{14}N is then mixed out of the core in larger quantities when rotational mixing occurs than when it does not. The effect is clearly visible in Figure 4.13a. The yield of ^{14}N increases steadily with initial mass, and with the initial rotational velocity. Unlike other isotopes, where rotation has a mixed effect on the yields (see, e.g., ^{19}F), the effect on ^{14}N is completely linear. The fastest rotating models have positive net yields for ^{14}N from 10 M$_\odot$, while for the non-rotating and the moderately rotating models the net yields are positive from $\sim$15M$_\odot$.

The net yields of ^{15}N are always negative because this isotope is destroyed both in hydrogen as in helium burning, and unlike ^{13} is not compensated by other reaction in the CNO-cycle. Due to the rotational mixing, the rotating models have lower yields than the non-rotating models, as is the case for ^{19}F and ^{22}Ne. ^{15}N is converted into ^{14}N, and only

a relatively small amount of ^{14}N is converted back into ^{15}N.

None of the studies in the literature give positive net yields for ^{15}N. The models by Ekström et al. (2012) and Limongi & Chieffi (2018) show a similar behaviour for the models including rotation, where the faster rotating models have lower yields than the non-rotating models, with the exception of the 10 and 15 $M_\odot$ models of Limongi & Chieffi (2018). The other studies from the literature show a similar curve, with the models by Sukhbold et al. (2016) having the highest yields of all sets presented here.

Oxygen-16, oxygen-17, and oxygen-18

In Figure 4.14, the yields for ^{16}O, ^{17}O, and ^{18}O are presented. ^{16}O behaves similar to ^{12}C and ^{22}Ne. Figure 4.14a shows the yields ^{16}O for the models of Set 3. As for the other isotopes produced during helium burning, at first, it is converted into ^{14}N during hydrogen burning. This leads to the lower yields for the rotating models below 35-40 $M_\odot$. As the stars enter the Wolf-Rayet phase, the products of helium burning are expelled and the yields increase, and the net yields become positive at 45-50 $M_\odot$ depending on the initial rotational velocity. For the highest 2 masses, 70 and 80 $M_\odot$, the yields are again lower for the rotating models compared to the non-rotating models. This is due to a difference in the size of the helium burning core.

The yields by Limongi & Chieffi (2018) are lower for the stars that enter the Wolf-Rayet phase, and before this point comparable to my yields. Overall, the various studies from the literature are in general agreement, though the final spread in yields in an order of magnitude.

The yields of ^{17}O and ^{18}O behave similarly to ^{15}N, and none of the models produces a positive net yield. ^{17}O is converted into ^{14}N in CNO cycle-2, and produced in the final stages of core helium-burning. However, this happens too late for the yields to be strongly affected by the winds. ^{18}O is also converted during core hydrogen burning. Then, in early helium burning it is produced by the conversion of ^{14}N into ^{22}Ne. Towards the end of helium burning it is therefore almost fully destroyed again. Due to this, the isotope behave like ^{15}N and not like for example ^{16}O.

For both ^{17}O and ^{18}O the yields of Set 3 are comparable to the yields from the other studies from the literature, showing the same overall trend. The spread in the yields is smaller than for ^{16}O, about one order of magnitude instead of 1.5 orders of magnitude.

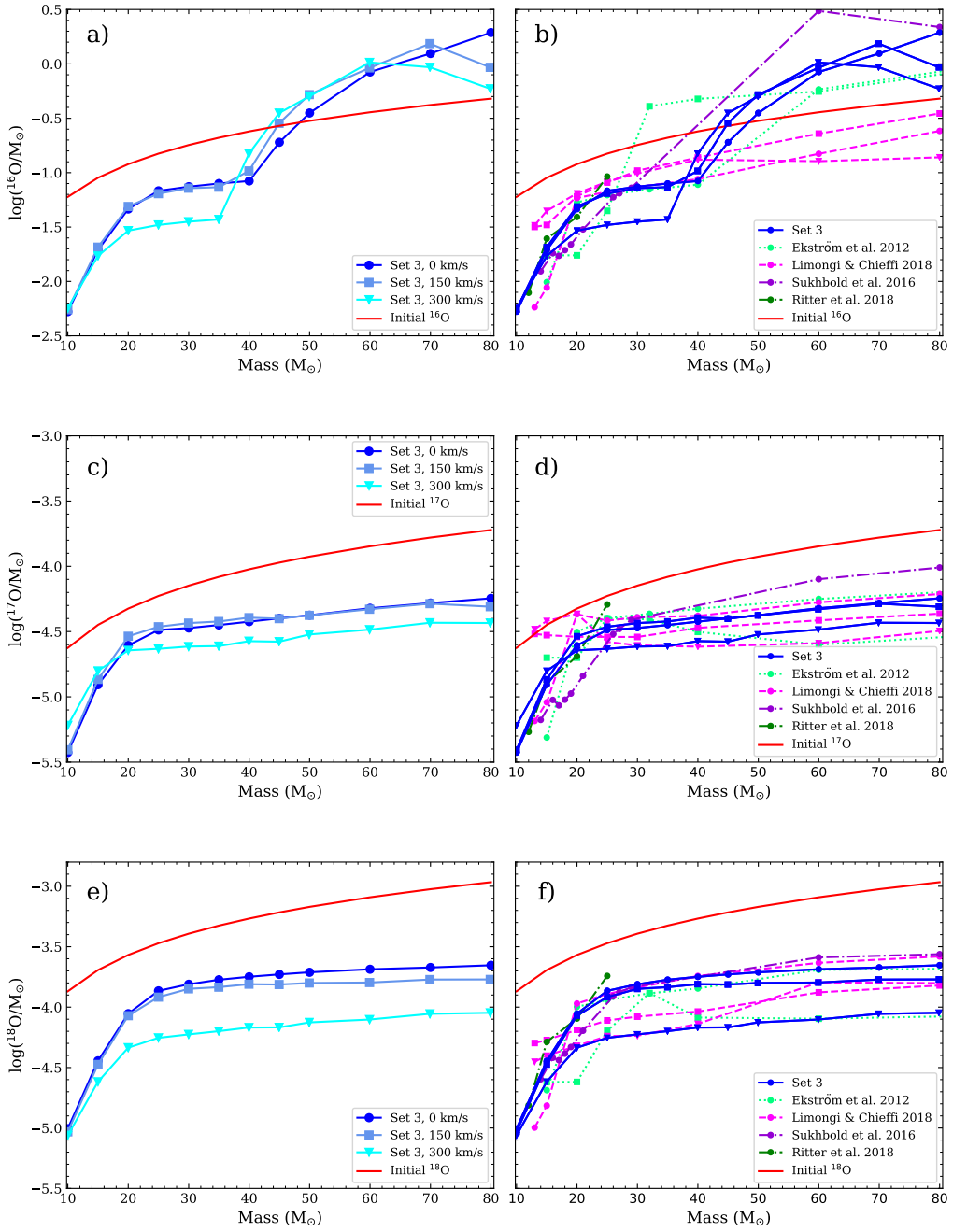

Figure 4.14: The left panels show the ^{16}O, ^{17}O, and ^{18}C yields for the models of Set 3. The red lines indicate the initial amounts of the isotope present in the models. The right panels show the stellar models of Set 3 together with the yields of various other studies.

Table 4.1: Wind yields for the single (non-) rotating models: ^{19}F, ^{22}Ne, ^{26}Al, ^{36}Cl, ^{41}Ca, and ^{60}Fe. $M_{\rm ini}$ is the initial mass in $M_\odot$. $V_{\rm ini}$ is the initial rotational velocity in km/s. The yields per isotope are given in $M_\odot$. For the stable isotopes, the initial amount present in the star is also given. The yields given here are not corrected for radioactive decay that might take place during the evolution of the star, and neither have I corrected the yields for the initial amount of the two stable isotopes present in the star, i.e., the total yields are given.

$M_{\rm ini}$ ($M_\odot$)	$V_{\rm ini}$ (km/s)	$^{19}F_{\rm ini}$ ($M_\odot$)	^{19}F ($M_\odot$)	$^{22}Ne_{\rm ini}$ ($M_\odot$)	^{22}Ne ($M_\odot$)	^{26}Al ($M_\odot$)	^{36}Cl ($M_\odot$)	^{41}Ca ($M_\odot$)	^{60}Fe ($M_\odot$)
10	0	5.28e-06	4.61e-07	9.82e-4	8.47e-05	7.19e-11	8.82e-23	7.90e-23	4.11e-41
	150	5.28e-06	4.71e-07	9.82e-4	8.68e-05	2.78e-10	1.11e-22	1.29e-22	1.36e-40
	300	5.28e-06	4.20e-07	9.82e-4	7.77e-05	1.40e-10	1.67e-22	1.70e-22	2.60-41
15	0	7.93e-06	1.69e-06	1.47e-3	3.12e-4	8.85e-09	3.00e-22	1.41e-21	1.81e-40
	150	7.93e-06	1.74e-06	1.47e-3	3.24e-4	1.47e-08	5.12e-22	2.10e-21	1.77e-37
	300	7.93e-06	1.21e-06	1.47e-3	2.26e-4	2.34e-08	5.32e-22	3.06e-21	4.67e-40
20	0	1.06e-05	4.01e-06	1.96e-3	7.43e-4	1.81e-07	1.94e-21	1.28e-20	7.40e-39
	150	1.06e-05	4.04e-06	1.96e-3	7.57e-4	1.92e-07	9.48e-22	1.33e-20	1.70e-38
	300	1.06e-05	2.04e-06	1.96e-3	3.86e-4	5.87e-07	1.75e-21	2.87e-20	5.01e-39
25	0	1.32e-05	5.87e-06	2.46e-3	1.09e-3	1.17e-06	2.80e-21	6.27e-20	6.56e-39
	150	1.32e-05	5.23e-06	2.46e-3	9.89e-4	1.59e-06	4.52e-21	9.28e-20	1.97e-37
	300	1.32e-05	2.28e-06	2.46e-3	4.41e-4	3.93e-06	4.98e-16	2.06e-15	1.30e-30
30	0	1.59e-05	6.38e-06	2.95e-3	1.19e-3	3.41e-06	6.76e-21	2.22e-19	7.10e-39
	150	1.59e-05	5.84e-06	2.95e-3	1.12e-3	4.68e-06	3.30e-15	1.42e-14	4.47e-29
	300	1.59e-05	2.39e-06	2.95e-3	4.77e-4	9.89e-06	1.45e-13	6.66e-13	4.84e-26
35	0	1.85e-05	6.77e-06	3.44e-3	1.27e-3	8.44e-06	4.70e-16	1.96e-15	1.08e-30
	150	1.85e-05	5.84e-06	3.44e-3	1.13e-3	1.06e-05	6.85e-13	3.23e-12	8.68e-25
	300	1.85e-05	2.51e-06	3.44e-3	5.27e-4	2.11e-05	1.85e-10	9.29e-10	2.92e-20
40	0	2.11e-05	7.06e-06	3.93e-3	1.36e-3	1.88e-05	7.99e-11	4.015e-10	6.37e-21
	150	2.11e-05	6.14e-06	3.93e-3	2.13e-3	2.05e-05	3.56e-08	6.07e-08	6.80e-12
	300	2.11e-05	2.82e-06	3.93e-3	5.09e-3	3.43e-05	1.82e-07	2.99e-07	1.72e-11
45	0	2.38e-05	7.40e-06	4.42e-3	5.18e-3	2.94e-05	1.45e-07	2.44e-07	3.09e-11
	150	2.38e-05	6.31e-06	4.42e-3	1.01e-2	3.15e-05	3.59e-07	5.86e-07	3.50e-11
	300	2.38e-05	3.23e-06	4.42e-3	1.54e-2	5.32e-05	5.99e-07	9.78e-07	4.18e-11
50	0	2.64e-05	7.82e-06	4.91e-3	1.21e-2	4.00e-05	4.18e-07	6.89e-07	6.88e-11
	150	2.64e-05	7.00e-06	4.91e-3	2.30e-2	4.30e-05	8.78e-07	1.43e-06	6.41e-11
	300	2.64e-05	3.42e-06	4.91e-3	2.14e-2	7.04e-05	8.26e-07	1.34e-06	9.58e-11
60	0	3.17e-05	9.00e-06	5.89e-3	3.84e-2	6.65e-05	1.48e-06	2.42e-06	1.71e-10
	150	3.17e-05	7.28e-06	5.89e-3	4.23e-2	7.16e-05	1.63e-06	2.67e-06	2.16e-10
	300	3.17e-05	1.91e-05	5.89e-3	0.12	1.44e-4	3.88e-06	8.37e-06	2.71e-11
70	0	3.70e-05	9.21e-06	6.88e-3	5.58e-2	9.70e-05	2.10e-06	3.46e-06	4.55e-10
	150	3.70e-05	1.78e-05	6.88e-3	1.38e-1	1.25e-4	5.00e-06	9.55e-06	1.08e-10
	300	3.70e-05	3.11e-05	6.88e-3	0.17	2.36e-4	4.48e-06	1.14e-05	2.99e-11
80	0	4.23e-05	1.49e-05	7.86e-3	0.14	1.51e-4	5.40e-06	9.55e-06	3.38e-10
	150	4.23e-05	5.16e-05	7.86e-3	0.18	2.69e-4	4.52e-06	1.20e-05	3.33e-11
	300	4.23e-05	3.51e-05	7.86e-3	0.11	4.29e-4	2.59e-06	6.99e-06	1.30e-11

Table 4.2: Wind yields for the single (non-)rotating models: ^{12}C, ^{13}C, ^{14}N, and ^{15}N of Set 3. $M_{\rm ini}$ is the initial mass in $M_\odot$. $V_{\rm ini}$ is the initial rotational velocity in km/s. The yields per isotope are given in $M_\odot$. For the stable isotopes, the initial amount present in the star is also given. The yields given here are not corrected for radioactive decay that might take place during the evolution of the star, and neither have I corrected the yields for the initial amount of the two stable isotopes present in the stars, i.e., the total yields are given.

$M_{\rm ini}$ ($M_\odot$)	$V_{\rm ini}$ (km/s)	$^{12}C_{\rm ini}$ ($M_\odot$)	^{12}C ($M_\odot$)	$^{13}C_{\rm ini}$ ($M_\odot$)	^{13}C ($M_\odot$)	$^{14}N_{\rm ini}$ ($M_\odot$)	^{14}N ($M_\odot$)	$^{15}N_{\rm ini}$ ($M_\odot$)	^{15}N ($M_\odot$)
10	0	2.44e-2	1.64e-3	2.97e-4	7.26e-05	7.23e-3	1.91e-3	2.85e-05	1.53e-06
	150	2.44e-2	1.49e-3	2.97e-4	6.89e-05	7.23e-3	2.35e-3	2.85e-05	1.40e-06
	300	2.44e-2	1.34e-3	2.97e-4	9.79e-05	7.23e-3	6.24e-3	2.85e-05	1.13e-06
15	0	3.67e-2	5.86e-3	4.46e-4	3.19e-4	1.08e-2	8.11e-3	4.27e-05	5.01e-06
	150	3.67e-2	4.99e-3	4.46e-4	3.63e-4	1.08e-2	1.04e-2	4.27e-05	3.97e-06
	300	3.67e-2	3.42e-3	4.46e-4	4.50e-4	1.08e-2	2.66e-2	4.27e-05	2.24e-06
20	0	4.89e-2	1.43e-2	5.94e-4	8.50e-4	1.45e-2	2.13e-2	5.69e-05	1.17e-05
	150	4.89e-2	1.24e-2	5.94e-4	1.19e-3	1.45e-2	2.51e-2	5.69e-05	8.64e-06
	300	4.89e-2	7.25e-3	5.94e-4	9.62e-4	1.45e-2	5.97e-2	5.69e-05	4.42e-06
25	0	6.12e-2	2.22e-2	7.43e-4	1.38e-3	1.81e-2	3.75e-2	7.11e-05	1.77e-05
	150	6.12e-2	1.87e-2	7.43e-4	2.00e-3	1.81e-2	4.35e-2	7.11e-05	1.21e-05
	300	6.12e-2	9.74e-3	7.43e-4	9.45e-4	1.81e-2	8.29e-2	7.11e-05	6.26e-06
30	0	7.34e-2	2.58e-2	8.91e-4	1.62e-3	2.17e-2	4.93e-2	8.54e-05	2.05e-05
	150	7.34e-2	2.33e-2	8.91e-4	2.29e-3	2.17e-2	5.67e-2	8.54e-05	1.46e-05
	300	7.34e-2	1.09e-2	8.91e-4	8.88e-4	2.17e-2	0.10	8.54e-05	8.20e-06
35	0	8.56e-2	2.90e-2	1.04e-3	1.72e-3	2.53e-2	6.75e-2	9.96e-05	2.32e-05
	150	8.56e-2	2.57e-2	1.04e-3	1.64e-3	2.53e-2	8.08e-2	9.96e-05	1.75e-05
	300	8.56e-2	1.22e-2	1.04e-3	7.34e-4	2.53e-2	0.13	9.96e-05	1.05e-05
40	0	9.79e-2	3.18e-2	1.19e-3	1.58e-3	2.89e-2	9.80e-2	1.14e-4	2.66e-05
	150	9.79e-2	6.19e-2	1.19e-3	1.41e-3	2.89e-2	0.11	1.14e-4	2.04e-05
	300	9.79e-2	0.19	1.19e-3	6.93e-4	2.89e-2	0.15	1.14e-4	1.27e-05
45	0	0.11	0.18	1.34e-3	1.35e-3	3.25e-2	0.12	1.28e-4	2.97e-05
	150	0.11	0.37	1.34e-3	9.92e-4	3.25e-2	0.13	1.28e-4	2.38e-05
	300	0.11	0.58	1.34e-3	6.51e-4	3.25e-2	0.17	1.28e-4	1.51e-05
50	0	0.12	0.44	1.49e-3	1.18e-3	3.61e-2	0.14	1.42e-4	3.28e-05
	150	0.12	0.86	1.49e-3	9.20e-4	3.61e-2	0.15	1.42e-4	2.72e-05
	300	0.12	0.80	1.49e-3	7.07e-4	3.61e-2	0.19	1.42e-4	1.70e-05
60	0	0.15	1.43	1.78e-3	1.05e-3	4.34e-2	0.17	1.71e-4	3.90e-05
	150	0.15	1.57	1.78e-3	9.01e-4	4.34e-2	0.19	1.71e-4	3.34e-05
	300	0.15	3.92	1.78e-3	8.80e-4	4.34e-2	0.25	1.71e-4	2.08e-05
70	0	0.17	2.06	2.08e-3	1.09e-3	5.06e-2	0.21	1.99e-4	4.47e-05
	150	0.17	4.67	2.08e-3	1.05e-3	5.06e-2	0.23	1.99e-4	3.78e-05
	300	0.17	4.67	2.08e-3	1.11e-3	5.06e-2	0.32	1.99e-4	2.43e-05
80	0	0.20	4.98	2.38e-3	1.22e-3	5.78e-2	0.26	2.28e-4	4.97e-05
	150	0.20	4.76	2.38e-3	1.42e-3	5.78e-2	0.35	2.28e-4	4.19e-05
	300	0.20	3.00	2.38e-3	1.56e-3	5.78e-2	0.46	2.28e-4	2.73e-05

Table 4.3: Wind yields for the single (non-)rotating models: ^{16}O, ^{17}O, and ^{18}O of Set 3. $M_{\rm ini}$ is the initial mass in $M_\odot$. $V_{\rm ini}$ is the initial rotational velocity in km/s. The yields per isotope are given in $M_\odot$. For the stable isotopes, the initial amount present in the star is also given. The yields given here are not corrected for radioactive decay that might take place during the evolution of the star, and neither have I corrected the yields for the initial amount of the two stable isotopes present in the stars, , i.e., the total yields are given.

$M_{\rm ini}$ ($M_\odot$)	$V_{\rm ini}$ (km/s)	$^{16}O_{\rm ini}$ ($M_\odot$)	^{16}O ($M_\odot$)	$^{17}O_{\rm ini}$ ($M_\odot$)	^{17}O ($M_\odot$)	$^{18}O_{\rm ini}$ ($M_\odot$)	^{18}O ($M_\odot$)
10	0	5.99e-2	5.28e-3	2.37e-05	3.75e-06	1.35e-4	9.88e-06
	150	5.99e-2	5.49e-3	2.37e-05	3.93e-06	1.35e-4	9.29e-06
	300	5.99e-2	5.68e-3	2.37e-05	6.05e-06	1.35e-4	8.68e-06
15	0	8.98e-2	1.95e-2	3.56e-05	1.24e-05	2.03e-4	3.60e-05
	150	8.98e-2	2.07e-2	3.56e-05	1.36e-05	2.03e-4	3.35e-05
	300	8.98e-2	1.72e-2	3.56e-05	1.58e-05	2.03e-4	2.41e-05
20	0	0.12	4.63e-2	4.75e-05	2.478e-05	2.70e-4	8.84e-05
	150	0.12	4.88e-2	4.75e-05	2.91e-05	2.70e-4	8.50e-05
	300	0.12	2.93e-2	4.75e-05	2.27e-05	2.70e-4	4.62e-05
25	0	0.15	6.81e-2	1 5.93e-05	3.25e-05	3.38e-4	1.36e-4
	150	0.15	6.41e-2	5.93e-05	3.44e-05	3.38e-4	1.21e-4
	300	0.15	3.31e-2	5.93e-05	2.33e-05	3.38e-4	5.57e-05
30	0	0.18	7.43e-2	7.12e-05	3.37e-05	4.05e-4	1.55e-4
	150	0.18	7.20e-2	7.12e-05	3.67e-05	4.05e-4	1.42e-4
	300	0.18	3.54e-2	7.12e-05	2.43e-05	4.05e-4	5.95e-05
35	0	0.21	7.95e-2	8.30e-05	3.55e-05	4.73e-4	1.68e-4
	150	0.21	7.36e-2	8.30e-05	3.78e-05	4.73e-4	1.46e-4
	300	0.21	3.71e-2	8.30e-05	2.45e-05	4.73e-4	6.32e-05
40	0	0.24	8.38e-2	9.49e-05	3.77e-05	5.40e-4	1.78e-4
	150	0.24	0.10	9.49e-05	4.05e-05	5.40e-4	1.55e-4
	300	0.24	0.15	9.49e-05	2.67e-05	5.40e-4	6.78e-05
45	0	0.27	0.19	1.07e-4	3.99e-05	6.08e-4	1.86e-4
	150	0.27	0.28	1.07e-4	3.97e-05	6.08e-4	1.54e-4
	300	0.27	0.35	1.07e-4	2.65e-05	6.08e-4	6.80e-05
50	0	0.30	0.35	1.19e-4	4.22e-05	6.75e-4	1.94e-4
	150	0.30	0.52	1.19e-4	4.21e-05	6.75e-4	1.58e-4
	300	0.30	0.50	1.19e-4	3.00e-05	6.75e-4	7.47e-05
60	0	0.36	0.84	1.42e-4	4.77e-05	8.11e-4	2.06e-4
	150	0.36	0.92	1.42e-4	4.69e-05	8.11e-4	1.60e-4
	300	0.36	1.03	1.42e-4	3.27e-05	8.11e-4	7.89e-05
70	0	0.42	1.25	1.66e-4	5.23e-05	9.46e-4	2.13e-4
	150	0.42	1.53	1.66e-4	5.18e-05	9.46e-4	1.69e-4
	300	0.42	0.93	1.66e-4	3.70e-05	9.46e-4	8.80e-05
80	0	0.48	1.94	1.90e-4	5.69e-05	1.08e-4	2.22e-4
	150	0.48	0.93	1.90e-4	4.91e-05	1.08e-4	1.69e-4
	300	0.48	0.59	1.90e-4	3.68e-05	1.08e-4	8.98e-05

Chapter 5

Implications for the galactic ^{26}Al abundance and for the early Solar System

The radioactive isotopes I have studied in the previous chapters were inferred to be present in the early Solar System (ESS) from observed excesses of their daughter nuclei in meteoritic inclusions. ^{26}Al is also observed in the Milky Way through its decay to an excited state of ^{26}Mg, and the quick, subsequent decay to the ground state that releases a γ-photon at an energy of 1.81 MeV. In the first section of this chapter, I discuss how the wind yields from binaries might impact the galactic ^{26}Al budget, as considered together with the yields from supernovae. In the second section of this chapter, I consider a simple dilution model for ^{26}Al, ^{36}Cl, and ^{41}Ca, to investigate if their abundances in the ESS can be explained self-consistently with the models of Set 3. I compare these results with those based on the yields by Limongi & Chieffi (2018). In the final part of the Section, I consider how the stars that could explain the ESS abundances impact the oxygen isotopic ratios.

5.1 Implications of binary yields for the galactic abundance of ^{26}Al

The work in this section was done by my collaborator, Benoit Côté, and published in Brinkman et al. (2019). Onno Pols contributed on dealing with the presence of binaries in this type of calculation. Some of the terminology as compared to the original work has been updated.

To bring my study of ^{26}Al from massive binary stars (Sets 1 and 2) into a galactic chemical evolution context, the yields must be integrated with the stellar initial mass function. To properly include binary yields in such a context, all possible mass ratios and orbital periods should be considered. In this section we use a simpler and preliminary

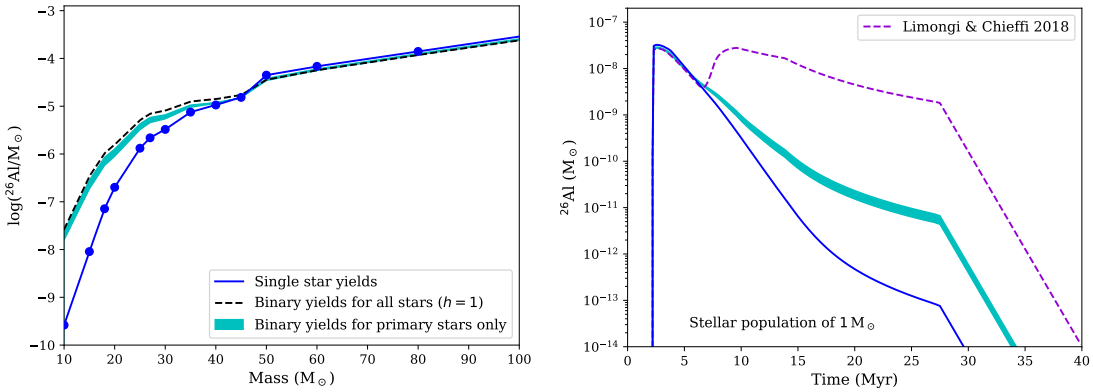

Figure 5.1: Left panel: The ^{26}Al wind yields as a function of stellar initial mass for single stars (blue dots and blue solid line, Set 1), and the effective stellar yields for stars in binary systems (cyan band, based on the results of Set 2). The thickness of the cyan band represents the range of solutions for the effective stellar yield (Equation 5.2) when assuming a binary fraction h between 0.5 and 0.9. The dashed black line represents the extreme case with $h = 1$ where the binary yields are applied to every star. Right panel: Evolution of the mass of ^{26}Al ejected by winds into the interstellar medium by a simple stellar population scaled to 1 $M_\odot$ as a function of time since the formation of the stellar population. The mass of ^{26}Al shown in this panel includes radioactive decay once it has been ejected by stars, as explained in Côté et al. (2019a), which is why the mass is decreasing over time. For comparison, the dashed violet line shows the result using the yields of Limongi & Chieffi (2018) for the single stars, which include both the wind and the supernova contribution.

approach, because we did not explore the complete parameter space for binary systems. Therefore, the results presented are first-order approximations. First, we determine the average increase in the ^{26}Al yield from binary systems as compared to the single star yields (listed in Table 3.1 of Section 3.3), which we call the "binary enhancement factor". This is defined as the arithmetic average increase (over all periods considered) of the yield of the single star compared to the yield of the binary systems, which cover multiple periods (as earlier described in Section 4.2.1). A flat period-distribution is assumed, giving all systems an equal weight in the calculation. The values we have calculated for this enhancement factor are given in Table 5.1. Second, we calculate an "effective stellar ^{26}Al yield" as a function of initial stellar mass by assuming that a fraction h of all massive stars are primary stars in a binary system. This fraction is connected to $f_{\rm binary}$, the fraction of all massive stars that are part of a binary system either as a primary or a secondary star, by:

$$f_{\rm binary} = \frac{2h}{(1+h)}. \tag{5.1}$$

For any given stellar mass, the effective stellar yield is defined as:

$$Y_{\rm eff} = \frac{(1-h)Y_{\rm single} + h(Y_{\rm prim} + \langle Y_{\rm sec}\rangle)}{1 + h\langle q\rangle}, \tag{5.2}$$

Table 5.1: The binary enhancement factor for the different primary masses. This is defined as the average increase (over all periods considered) of the yield of the single star compared to the yield of the binary systems, which cover multiple periods. A flat period-distribution is assumed, giving all systems an equal weight in the calculation.

M_{ini} ($M_\odot$)	factor	M_{ini} ($M_\odot$)	factor
10	150	35	2
15	50	40	1.5
20	10	45	1.25
25	5	50	1
30	3	60	1

where $Y_{\rm single}$, $Y_{\rm prim}$, and $Y_{\rm sec}$ are the yields of a single star and of the primary and secondary stars of a binary system, respectively, and they depend on the mass of the star. The derivation of the denominator factor is explained in the next paragraph. For all primary stars, we use the effective binary yield obtained by multiplying the yields of the single star by the binary enhancement factor. To calculate $Y_{\rm sec}$, we assume an average mass ratio of $\langle q \rangle = 0.5$ with a flat probability distribution between 0 and 1. For any primary mass $M_{\rm prim}$, $\langle Y_{\rm sec} \rangle$ represents the average yields of secondary stars in the mass range $M_{\rm sec} = [0 - M_{\rm prim}]$. For $M_{\rm sec}$ below 10 $M_\odot$, which is the assumed transition mass between super-AGB and massive stars (Doherty et al. 2015), no ^{26}Al is ejected. For $M_{\rm sec} > 10\,{\rm M}_\odot$, we use the single-star yields for a star with mass $M_{\rm sec}$ without the binary enhancement factor. Assuming a binary fraction $h = [0.5 - 0.9]$, our stellar effective yields are shown in the left panel of Figure 5.1 as the cyan band, while a binary fraction of h=1 is represented by the black dashed line.

We introduced these effective stellar yields at solar metallicity (Z=0.014) into the stellar population code `SYGMA` (Ritter et al., 2018a), assuming the initial mass function of Kroupa (2001) from 0.1 to 100 $M_\odot$. The total mass of our stellar population was set to 1 $M_\odot$, so that our results can be scaled and applied to any population mass. We took the stellar lifetimes from the NuGrid massive star models (Ritter et al., 2018b) and expelled all the ^{26}Al at the end of the life of the star, i.e., the wind and the supernova together if both yields are available. For any given stellar mass M the binary contribution included in the effective stellar yields (see Equation 5.2) represents the ^{26}Al ejected per binary system having a primary star with a mass M. Therefore, since $Y_{\rm eff}$ does not only account for the yields of single stars, but also for the yields of binary systems including the contribution of secondary stars, we introduced the correction factor $1 + h\langle q \rangle$ at the denominator of Equation 5.2. This regulates $Y_{\rm eff}$ once multiplied with the initial mass function, and ensures that the total mass of our stellar population is normalized to 1 $M_\odot$.

Assuming a binary fraction $h = [0.5 - 0.9]$ with $\langle q \rangle = 0.5$, the time evolution of the mass of ^{26}Al ejected by the stellar population is shown in the right panel of Figure 5.1.

After the initial rise of ^{26}Al, which is caused by the ejecta of the most massive stars, the amount of ^{26}Al starts to decline due to radioactive decay. The inclusion of the effective stellar yields significantly affects the amount of ^{26}Al produced by the winds when stars with initial mass below ~ 40 M$_\odot$ start to contribute after ~ 10 Myr.

However, the inclusion of effective stellar yields affects the total ejected mass of ^{26}Al through stellar winds only by about $5-10\%$. This is due to two reasons, i) the dominant contribution to the wind for ^{26}Al is from the most massive stars, which do not have any binary enhancement factor for their yields, and ii) even when the binary effect is taken into account the wind ejects $\sim$3 times less ^{26}Al than the total yields of Limongi & Chieffi (2018), which include both the wind and the supernovae components (violet dashed line in right panel of Figure 5.1). This suggests that even when including the enhancement to the wind yield of ^{26}Al due to the fact that massive stars are likely born as in a binary system, the major contribution to the total abundance of ^{26}Al produced by a stellar population would still come from core-collapse supernovae. I note that binary interactions can also modify the supernova yields. Therefore, the comparison with Limongi & Chieffi (2018) should be taken with caution.

Our preliminary conclusion is that mass loss from interacting binaries does not have a strong impact on the galactic ^{26}Al abundance and ^{60}Fe/^{26}Al ratio observed via γ-ray spectroscopy, and that solutions to the current mismatches between models and observations are to be looked for within the nucleosynthesis occurring just before or during the core-collapse supernova. This conclusion is preliminary because it needs to be tested against a more complete exploration of the parameter space (for example, the initial mass ratio, the stellar metallicity and the effect of rotation) and of the binary scenarios (for example, the effect of reverse mass-transfer), but also the inclusion of supernova yields for the binary systems. Once a more complete set of yields is available, we will introduce it into the galactic chemical evolution code `OMEGA` (Côté et al., 2017) to address more accurately the impact of binary stars on the total mass of ^{26}Al in the Milky Way, and its ratio to ^{60}Fe.

5.1.1 Impact of binary yields for the early Solar System

In relation to the presence of ^{26}Al in the ESS, the left panel of Figure 5.1 shows that binary stars could have a significantly impact. One of the currently favoured scenarios for the origin of ^{26}Al in the ESS attributes such origin to the winds of one or more massive stars (see, e.g., Gaidos et al., 2009; Gounelle & Meynet, 2012; Young, 2014). However, in the case of single stars, only those with initial mass larger than roughly 30 M$_\odot$ produce enough ^{26}Al in the wind to provide a plausible solution (see Section 5.2), and these stars are rare. Our calculations, on the other hand, show that also stars of lower mass, which

are more common, can expel significant amount of ^{26}Al via winds if they are in a binary system, which is expressed by the binary enhancement factor. The implications of this result will need to be considered carefully in the future in relation to ^{26}Al in the ESS, in terms of both the potential stellar source populations and the timescales of the ejection as compared to star formation timescales.

5.2 Implications of the wind yields for the early Solar System

The work in this section was published in Brinkman et al. (2021). For this section, I have expanded the explanation of the calculation to determine which stars are potential candidates for polluting the early Solar System with the SLRs.

In the previous section, I have shown that massive stars, and especially those in binaries, could have a significant impact on the amount of ^{26}Al that is found to be have been present in the ESS. However, ^{26}Al is often accompanied by ^{36}Cl and ^{41}Ca, which were not discussed in the context of Set 1 and Set 2. In Set 3, I do consider these isotopes, but I do not consider the binary interactions (see Section 6.3 for a discussion on the impact of binary interactions on the ^{36}Cl and ^{41}Ca yields). While other stellar objects in the Galaxy can produce these three SLRs, such as novae and asymptotic giant branch stars, much research has focused on massive stars as ESS polluters, because these stars live short enough to be able to eject material within star forming regions, which have typical lifetimes of at most a few tens of Myr (Murray, 2011). Furthermore, massive star winds are preferred by several authors (Gaidos et al. 2009; Gounelle & Meynet 2012; Young 2014 and Dwarkadas et al. 2017) as a most favoured site of origin for ^{26}Al (see discussion in Lugaro et al., 2018), because there are several difficulties for core-collapse supernovae to produce the abundances of the SLRs in the proportion required to match the ESS values. For example, core-collapse supernovae produce too high abundances of ^{60}Fe and ^{53}Mn, while the winds do not, as shown for ^{60}Fe in Section 4.2.1. These isotopes have half lives 4 to 50 times higher than the three SLRs that I consider in the calculation here, therefore, their abundances in the ESS can be explained, instead, by decaying their abundances in the interstellar medium as derived by galactic chemical evolution (see, e.g., Wasserburg et al. 2006; Tang & Dauphas 2012; Trappitsch et al. 2018; Côté et al. 2019a and Côté et al. 2019b).

Table 5.2: The three SLRs considered in the ESS calculation, the half life $T_{1/2}$ and the mean life τ in Myr of these isotopes, the mass of each isotope in the ESS (in units of $M_\odot$) assuming a mass of 1 $M_\odot$ to be polluted, their stable daughter nuclei, their stable reference, the mass of the reference isotope in the Solar System (in units of $M_\odot$), and the measured ESS number ratio between each SLR and their reference isotope.

SLR	$T_{1/2}$(Myr)	τ(Myr)	ESS value ($M_\odot$)	Daughter	Reference	Solar ($M_\odot$)	ESS ratio
^{26}Al	0.0717	1.035	3.1×10^{-9}	^{25}Mg	^{27}Al	6.22×10^{-5}	$(5.23 \pm 0.13)\times10^{-5a}$
^{36}Cl	0.301	0.434	8.49×10^{-11}	^{36}Ar (98%) ^{36}S (2%)	^{35}Cl	3.38×10^{-7}	$(2.44 \pm 0.65)\times10^{-5b}$
^{41}Ca	0.0994	0.1434	2.35×10^{-13}	^{41}K	^{40}Ca	5.68×10^{-5}	$(4.6 \pm 1.9)\times10^{-9c}$

[a] Jacobsen et al. (2008), [b] Tang et al. (2017), [c] Liu (2017)

5.2.1 Calculation of dilution factor and the delay time

To determine if the winds from the stars of Set 3 presented in Chapters 3 and 4 might be able to explain the abundances of ^{26}Al, ^{36}Cl, and ^{41}Ca in the ESS, I compare the yields of the stars of Set 3 to the inferred ESS initial abundances of the same SLRs. The SLRs and their characteristics are listed in Table 5.2. The methodology for the comparison between the yields and the ESS involves 4 steps, which I explain below.

Step 1 is to determine a "dilution factor", f for each stellar model. This is defined as:

$$f = \frac{M^{\rm ESS}_{\rm SLR}}{M^{*}_{\rm SLR}} \tag{5.3}$$

where $M^{\rm ESS}_{\rm SLR}$ is the mass of a given SLR in the ESS, and $M^{*}_{\rm SLR}$ is the mass of the same SLR ejected by the stellar wind, i.e., the total yield as given in the previous chapter. I use ^{26}Al to determine f and then apply the same value to ^{36}Cl and ^{41}Ca[1], this is because the ^{26}Al/^{27}Al ratio in the ESS is very well established to 5.23×10^{-5}, as reported by Jacobsen et al. (2008) and recently confirmed by Luu et al. (2019). I derive an ESS initial amount of ^{26}Al of 3.1×10^{-9} $M_\odot$ assuming the solar abundance of ^{27}Al of Lodders (2003) and a total mass of 1 $M_\odot$ to be polluted (see details in Lugaro et al., 2018).

The diluted amount of the other SLRs is then calculated as a simple multiplication factor of the yield to obtain the diluted amount of this isotopes:

$$M^{d}_{SLR} = M^{*}_{SLR} f_{26} \tag{5.4}$$

[1]If the injection of the SLRs occurred in the form of dust grains, chemistry and dust formation could lead to different f values for the different isotopes because Al, Ca, and Cl are different elements. While Al and Ca should behave chemically in a very similar way, the situation for Cl may be different. I do not consider these uncertainties here.

where M^d_{SLR} is the diluted amount of the SLR in solar masses and f_{26} the dilution factor based on ^{26}Al.

Step 2 is to determine the "delay time" (Δt), which is the time interval between the wind ejection and the formation of the first solids (the calcium-aluminium rich inclusions, CAIs) in the ESS, for which time the SLR values are given. The delay time is defined as:

$$\Delta t = ln\left(\frac{R/S}{(R/S)_{ESS}}\right)\tau_R \tag{5.5}$$

where R/S and $(R/S)_{ESS}$ are the number ratios of the radioactive isotope (R) over its reference(S), for the wind and for the ESS, respectively, and τ_R is the mean life for the SLR (see Table 5.2 for the values). The derivation of the equation for the delay time can be found in Box 5.

Box 5: The delay time is derived from the equation of radioactive decay;

$$\frac{dN_{SLR}}{dt} = -\lambda N_{SLR}, \tag{5.6}$$

where λ is defined as $1/\tau$, N_{SLR} is the number of SLR isotopes, λ is the decay rate of the SLR, and τ the mean life, i.e., the time interval needed to reduce N_{SLR} by a factor of $1/e$. Integrating this equation between time t_0 and t_1 gives the following expression:

$$N_{SLR}(t_1) = N_{SLR}(t_0)e^{-\lambda\Delta t} \tag{5.7}$$

where Δ t = t_1-t_0. To then determine Δt, the equation becomes:

$$\frac{N_{SLR}(t_1)}{N_{SLR}(t_0)} = e^{-\lambda\Delta t},$$
$$ln\left(\frac{N_{SLR}(t_1)}{N_{SLR}(t_0)}\right) = -\lambda\Delta t,$$
$$ln\left(\frac{N_{SLR}(t_0)}{N_{SLR}(t_1)}\right) = \lambda\Delta t.$$

And then Δt is defined as:

$$\Delta t = ln\left(\frac{N_{SLR}(t_0)}{N_{SLR}(t_1)}\right)\frac{1}{\lambda},$$
or
$$\Delta t = ln\left(\frac{N_{SLR}(t_0)}{N_{SLR}(t_1)}\right)\tau \tag{5.8}$$

Before the delay time can be calculated, both the yield and the ESS value of the reference isotope need to be converted to numbers, because i) the ESS ratio is a number

ratio, and ii) Equation 5.6 requires numbers, not masses. Therefore, before Step 2, I convert the mass ratio, M^d_{SLR}/M_S, where M_S is the mass of the reference isotope in the ESS, to the number ratio, R/S. M_S is determined by the solar abundances and the assumption of 1 $M_\odot$ to be polluted. To convert the solar masses to the amount of atoms, the yield first needs to be multiplied by the solar mass in grams. Then it is divided by the atomic mass (grams/mole) to get the amount of moles of the isotope, and finally it is multiplied by Avogadro's number N_A (atoms/mole) to get the final amount of atoms. Because these values are used in Equation 5.5 as a fraction, all factors except the atomic mass, A, cancel out. The final conversion between mass and number is thus:

$$R = M_R/A_R \tag{5.9}$$

where R is the converted yield, M_R the mass of isotope in solar masses, and A_R the atomic mass of the isotope.

With the converted yield, the delay time can be calculated by decaying the R/S ratio in the wind until the observed ESS value has been reached. To set the value of Δt I use the ^{41}Ca/^{40}Ca ratio of 4.6×10^{-9} because ^{41}Ca has the shortest half life of the three SLRs, and therefore it is the most sensitive to time.

Step 3 is to recalculate the dilution factor, f_{26}, once Δt is also applied to ^{26}Al. To do so, first a new amount R$'$ of ^{26}Al for the ESS has to be determined. This is done by reverse decaying the initial ESS amount of ^{26}Al by using the delay time from Step 2:

$$R^{'} = R_{ESS}e^{\Delta t/\tau_R} \tag{5.10}$$

And then the new value of the dilution factor is

$$f^{'}_{26} = (R^{'}A_R)/M^*_{ESS} \tag{5.11}$$

With this new value I repeat Step 2. I continue this iteration until we converge to a Δt within a 10% difference from the previous value.

Step 4 is to apply the final f_{26} and Δt to calculate the diluted ^{36}Cl abundance. I then also follow Step 2 again to determine a delay time for ^{36}Cl (Δt_{36}) using the ESS ^{36}Cl/^{35}Cl ratio of 2.44×10^{-5} measured in the *Curious Marie* calcium–aluminium-rich inclusion (CAI) (Tang et al., 2017).

A few remarks need to be made related to this method. First, even though ^{26}Al is not produced in the same evolutionary phase as ^{36}Cl and ^{41}Ca, here I assume that the bulk of these isotopes are expelled into the interstellar medium at the same time. Therefore, I do not take into account, for example, that some ^{26}Al might have decayed before ^{36}Cl and ^{41}Ca were ejected the star. This assumption is valid for the lowest mass stars of the sample, but might not be for the highest mass stars. This will require further

investigation. Second, I use the $^{41}Ca/^{40}Ca$ ratio to obtain Δt, even though this ratio is not well constrained in the ESS (Liu, 2017), because ^{41}Ca is the shortest lived of the three isotopes considered here. Therefore, it is the most sensitive chronometer to short timescales (see also Wasserburg et al., 2006).

Finally, the ESS abundances of both ^{36}Cl and ^{41}Ca can have a contribution from irradiation by solar cosmic rays. Higher values of ^{36}Cl than the ESS value used here have been measured in other meteoritic inclusions and can be produced by irradiation within the ESS. The value reported here was measured in a specific named CAI *Curious Marie* and probably represents the primordial value derived from a stellar source because ^{36}Cl coexists in this CAI with the canonical value of ^{26}Al (Tang et al., 2017). We note also that the measurements of the ESS values of ^{41}Ca and ^{36}Cl might be affected by systematic uncertainties, because the abundance of ^{41}Ca is very low and the abundance of ^{36}Cl is based on the measurement of its roughly 2% decay channel into ^{36}S. For ^{41}Ca the latest data on a handful of CAIs (Liu, 2017) demonstrate the presence of this very short-lived isotope in the ESS, however, the data precision is not high enough to be able to resolve possible heterogeneities.

5.2.2 Results and comparison to other studies

I apply the method described above to the models of Set 3 and consider them to be a solution for the ESS when the delay times for ^{41}Ca and ^{36}Cl are comparable with a factor of up to 5. For the non-rotating models of Set 3, a solution can be found for ^{26}Al and ^{41}Ca in the mass range 45-80 $M_\odot$ and Δt between 0.7 and 1 Myr. In order to also match the ^{36}Cl abundance, the mass range needs to be restricted to stars with an initial mass of 60 $M_\odot$ and higher. There still is a small inconsistency, because Δt needs to be lower for ^{36}Cl than for ^{41}Ca, as the delay time for ^{36}Cl is between 0.2 and 0.5 Myr. The results for the rotating models of Set 3 are similar, except that the mass range for which a solution is possible for ^{26}Al and ^{41}Ca may extend down to 40 $M_\odot$. If I consider the three isotopes, it is possible to find a solution for initial rotational velocity of 150 and 300 km/s at masses 50-80 $M_\odot$ and 60 and 70 $M_\odot$, respectively.

In Figure 5.2, I look more closely at a selected set of models. It shows the abundance ratios (R/S) for the three SLRs (R) over their stable reference isotope (S) versus delay time for the dilution factor f_{26}, for the stellar models with a mass of 40, 60, and 80 $M_\odot$. The horizontal bars represent the ESS ratios and their uncertainties (as given in Table 5.2). I compare my results with the results calculated from the models for the same initial masses from Limongi & Chieffi (2018).

For the 40 $M_\odot$ models (Figure 5.2a), the ^{36}Cl and ^{41}Ca yields from the non-rotating model (solid lines) are too low to match their ESS ratios. Only my rotating models

(dashed and dotted lines in panel a) can match both the $^{26}Al/^{27}Al$ and $^{41}Ca/^{40}Ca$ ratios (at $10^{5.9}$ yrs. i.e., 0.79 Myr), while the $^{36}Cl/^{35}Cl$ ratio is between one and two orders of magnitude too low. This excludes this star as a potential solution for the ESS. For the models of Limongi & Chieffi (2018), Figure 5.2b, the non-rotating model does not match $^{36}Cl/^{35}Cl$ or the $^{41}Ca/^{40}Ca$ ratio either. As for my models, the rotating models match both the $^{26}Al/^{27}Al$ and $^{41}Ca/^{40}Ca$ ratios. The difference is that in the models by Limongi & Chieffi (2018) the $^{36}Cl/^{35}Cl$ ratio is matched very early on in the calculation, at $10^{4.9}$ yrs, i.e., 7.9×10^4 yrs, and the other ratios are matched after 1 Myr (i.e., 10^6 yrs), while in my models the $^{36}Cl/^{35}Cl$ ratio cannot be matched at all. However, due to this large difference in Δt, these models can still not be considered a potential solution.

For the 60 $M_\odot$ models (Figure 5.2c), all of my models of Set 3 can match the three isotopic ratios, the $^{36}Cl/^{35}Cl$ ratio at $10^{5.5}$ yrs, i.e., 0.32 Myr and the other two ratios at 10^6 yrs, i.e., 1 Myr. For the models from Limongi & Chieffi (2018, Figure 5.2d), only their model with an initial rotational velocity of 150 km/s matches the $^{36}Cl/^{35}Cl$ ratio, but again too early ($10^{4-4.6}$ yrs, i.e., 1-3.9$\times$ 10^4 yrs) to be considered a solution together with the $^{26}Al/^{27}Al$ and $^{41}Ca/^{40}Ca$ ratios.

Finally, for the 80 $M_\odot$ (Figure 5.2e), I can match the ESS ratios of the SLRs with my non-rotating model and the model rotating at an initial velocity of 150 km/s. There is still a difference in the delay times for ^{41}Ca and ^{36}Cl of a factor of 2. For the 80 $M_\odot$ models from Limongi & Chieffi (2018), Figure 5.2f, only the non-rotating model matches all three ratios, but the $^{36}Cl/^{35}Cl$ ratio is matched at $10^{4.5}$ yrs, i.e., 0.03 Myr, while the other two are matched at $10^{6.05}$ yrs, i.e., 1.14 Myr. This difference is again too large to consider this as a solution. The rotating models cannot match the $^{36}Cl/^{35}Cl$ ratio.

The difference between the sets can be explained by considering Figures 4.5b and 4.5d. At 60 and 80 $M_\odot$ the ^{41}Ca yields are very comparable between my models and those by Limongi & Chieffi (2018), both for the rotating as for the non-rotating models. However, for ^{36}Cl the yields for the models by Limongi & Chieffi (2018) are slightly lower than for my models at the same mass and rotational velocity. Because ^{36}Cl and ^{41}Ca are produced in the same phase, the difference is unlikely to be due a different mass loss, because it is to be expected that ^{36}Cl and ^{41}Ca behave in a similar manner, as shown in Section 4.2.1. It could be that there is a difference in the reaction rates involving ^{36}Cl, though it is hard to say from the figures alone. However, this difference means that there is less ^{36}Cl compared to ^{41}Ca in these models for Limongi & Chieffi (2018) than in my models, making it harder to match both the ESS ratios within their respective uncertainties. For the 40 $M_\odot$ models, the rotating yields given by Limongi & Chieffi (2018) are higher than my rotating yields for ^{36}Cl, and ^{41}Ca which explains why their rotating models can match for the $^{36}Cl/^{35}Cl$ ratio, while my models can not.

My results that the three radionuclides ^{26}Al, ^{36}Cl, and ^{41}Ca can be ejected by the winds of a variety of Wolf-Rayet stars at relative levels compatible with the meteoritic

observations are also in qualitative agreement with the results of Arnould et al. (1997, 2006). Because these authors used ^{107}Pd to calculate f and do not produce enough ^{26}Al to match the ESS, my results are not directly comparable. However, if I consider the delay times shown in Figures 5-7 of Arnould et al. (2006), I find similar values for the delay time for the ^{41}Ca/^{40}Ca ratio, between $10^{5.5}$-10^{6} yrs, i.e., 0.32-1 Myr. The delay time for the ^{36}Cl/^{35}Cl ratio for their 40 $M_{\odot}$ model is much closer to their delay time for the ^{41}Ca/^{40}Ca ratio, compared to my models and those by Limongi & Chieffi (2018). However, the delay times for the ^{36}Cl/^{35}Cl ratio are shorter for their 60 and 85 $M_{\odot}$ models than for my models or those by Limongi & Chieffi (2018). My results also confirm the analysis of the production of ^{26}Al in Wolf-Rayet stars of mass between 32 and 120 $M_{\odot}$ by Gounelle & Meynet (2012). My f_{26} factor may be compared to their $\eta_{\rm wind}/1000$ in their Equation 2, for which they find values ranging down to 2×10^{-5}. For my models it is possible to find a solution for ^{26}Al and ^{41}Ca for models with initial masses 60-80 $M_{\odot}$ with dilution factors in the range 1.1×10^{-4} to 7.2×10^{-5} and Δt around 1 Myr.

Overall, I confirm that Wolf-Rayet stars are a robust candidate site for the production of ^{26}Al, ^{36}Cl, and ^{41}Ca in the ESS.

5.2.3 Oxygen isotopic ratios

For sake of completeness, I also checked if the models that reproduce ^{26}Al and ^{41}Ca affect the oxygen isotopic ratios. This is because a successful pollution model should avoid predicting a correlation between the presence of ^{26}Al and modification of the oxygen isotopes (Gounelle & Meibom, 2007) to match the observational evidence that some CAIs (the Fractionated and Unknown Nuclear anomalies, FUN, class) and some corundum grains are poor in ^{26}Al, but they have virtually the same oxygen isotopic composition as those that are rich in ^{26}Al (see, e.g., Makide et al., 2011).

The composition of the oxygen isotopes in the winds is dominated by hydrogen and helium burning. Its main features are production of ^{16}O and depletion of ^{17}O and ^{18}O, relative to their initial amounts in the star (see also Section 4.2.4), with ^{17}O/^{16}O and ^{18}O/^{16}O ratios at most roughly 8 and 20 times lower than solar. By adding the oxygen isotopic wind yields of the models diluted by f_{26} to the oxygen Solar System mass-ratios, I obtained a decrease of the order of 0.1 to 1.5% in both the ^{17}O/^{16}O and ^{18}O/^{16}O ratios, increasing the absolute value with increasing the stellar mass from 40-50 $M_{\odot}$ to 80 $M_{\odot}$. While variations at the lower values of this range would not be detectable, those at the upper values would be. Therefore, if I assume the specific scenario where the ^{26}Al-poor and ^{26}Al-rich grains formed before and after injection, respectively, then the lower masses would be favoured to avoid changes in the oxygen isotopic ratios. However, the higher masses reproduce the ^{36}Cl/^{35}Cl ratio. This discrepancy needs to be further investigated.

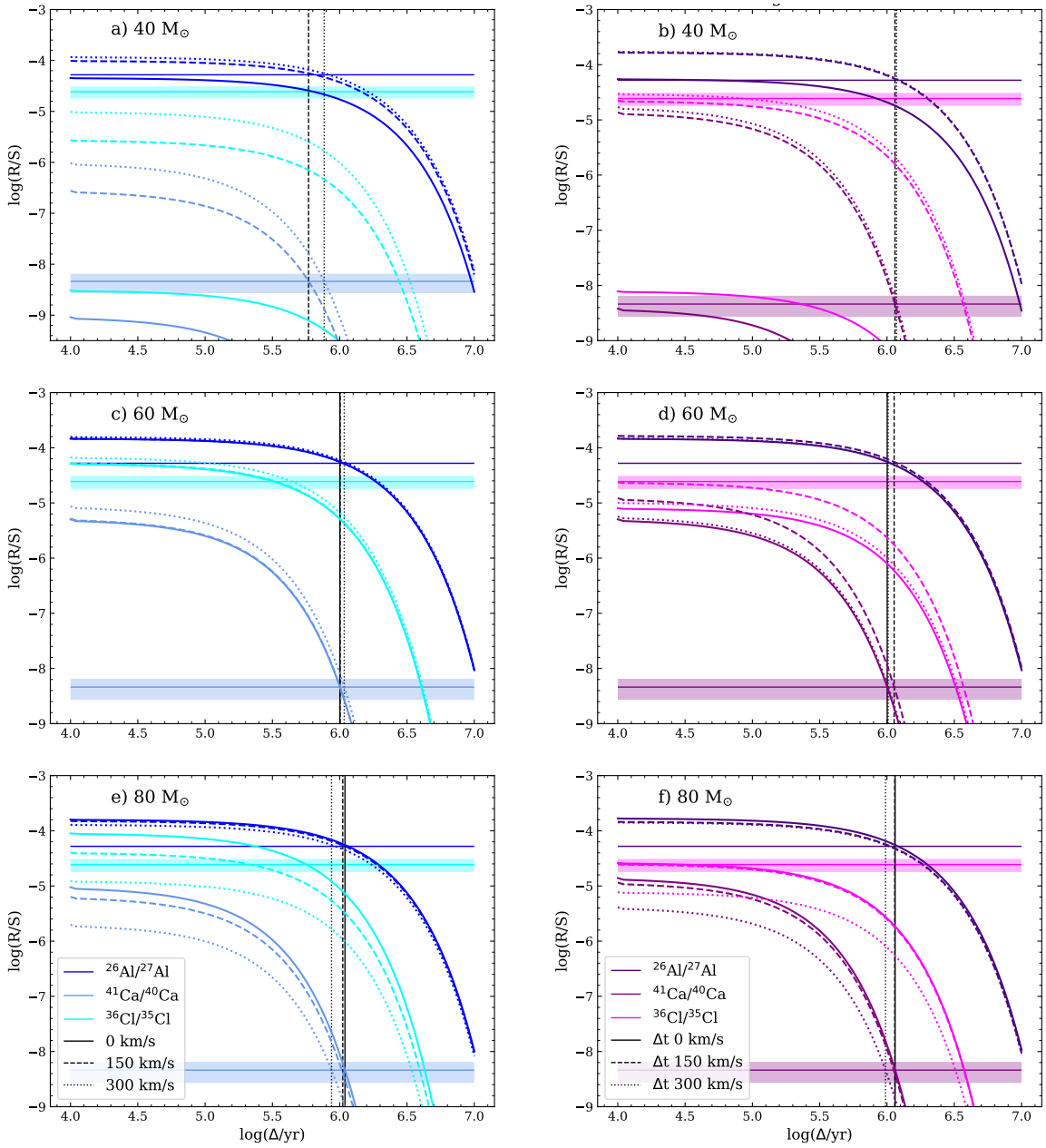

Figure 5.2: Abundance ratios (R/S) for the three SLRs (R) over their stable reference isotope (S) for the dilution factor f_{26} corresponding to each model. The range of values of f_{26} for each panel (in units of 10^{-4}) are: a) 1.32-2.64, b) 2.44-3.03, c) 0.60-1.13, d 0.54-1.37, e) 0.16-0.5, and f) 0.08-0.24. The solid lines represent the non-rotating models, the dashed lines the models with an initial rotational velocity of 150 km/s, and the dotted lines the models with an initial rotational velocity of 300 km/s. The horizontal bands represent the ESS ratios, with their respective errors. The vertical lines represent the delay time for the ^{41}Ca/^{40}Ca ratio. The left panels give the results for my models of Set 3 (40, 60, and 80 M$_\odot$), the right panels give the results for the models by Limongi & Chieffi (2018) for the same masses.

Chapter 6

Discussion

In this chapter I cover several topics that might affect the conclusions from Chapters 3, 4 and 5. In Section 6.1, I consider the effects of the uncertainties related to the binary interactions. In Section 6.2, I consider the effects of the uncertainties in the reaction rates related to production and/or destruction of ^{26}Al, ^{41}Ca, and ^{36}Cl, as well as of several isotopes of chromium and titanium. Finally, in Section 6.3, I consider the effect of binary interactions on the yields of ^{36}Cl, ^{41}Ca, ^{60}Fe, ^{19}F, and ^{22}Ne when these stars are evolved up to core-collapse.

6.1 Uncertainties in binary evolution

The work in this section was published in Brinkman et al. (2019).

In this section I discuss a few aspects of binary evolution that could influence the ^{26}Al yields of the systems: the effect of the secondary and reverse mass-transfer, the mass-transfer efficiency, and the mass ratio.

6.1.1 The effect of the secondary and reverse mass-transfer

Many of the binary systems of Set 2 start a phase of reverse mass-transfer before the end of the simulation (see Sections 3.1.2 and 3.3 for details). During this phase, mass is transferred from the secondary star to the primary star. The question that arises is how the further evolution of such a system will affect the ^{26}Al yield, both of the primary star and the secondary star. Reverse mass transfer is likely to result in a common-envelope phase, where the envelope of the star filling its Roche lobe engulfs both stars and the orbit shrinks substantially (Ivanova et al., 2013). If the system survives this phase as a close binary, the envelope of the secondary has to be expelled from the system. This can significantly increase the yield of the binary system as a whole. Furthermore, the close binary system that is left after this phase could eject more mass, and thus ^{26}Al, by either winds or further mass transfer in a close orbit. In case the common-envelope phase results

in the merger of the binary into a single star, part of the envelope may still be ejected, and the merged object could eject more ^{26}Al through stellar-wind mass loss.

The above considerations are likely to be relevant for a large fraction of the systems of Set 2, not only those in which I found reverse mass transfer during the evolution of the primary. This is because many of these systems might experience reverse mass transfer and a common-envelope phase at a later stage, after the primary star has finished its evolution and has become a compact object. This requires that the binary system is still bound after the supernova explosion, which depends on the dynamics of the supernova explosion and the resulting kick the compact object will receive. Altogether, the further evolution of the systems including that of the secondary star is complicated and subject to many uncertainties, and the resulting ^{26}Al yields are hard to predict but potentially very significant. The complete problem of the effect of binary evolution on the ^{26}Al yields can only be explored by a combination of binary population synthesis, which incorporates all these effects and allows the exploration of their uncertainties (see, e.g., Izzard et al. 2006, 2018), and further detailed binary calculations of selected interesting cases.

6.1.2 Mass-transfer efficiency

For the systems in Set 2, I have assumed that the mass transfer between the stars of the binary is fully non-conservative, meaning that all the mass transferred from the primary to the secondary is subsequently lost from the system. In reality, it is unclear how much mass is accreted and how much is lost, see Section 2.2.2.

In order to estimate the influence of the mass-transfer efficiency on my results, I take the following simplified approach. I consider the binary system with a primary mass of 20 $M_\odot$ and a secondary mass of 18 $M_\odot$ at a period of 18.4 days. I use an adjusted semi-numerical binary scheme to calculate the ^{26}Al yield for different values of β, using the mass stripped from the primary star in the numerical binary simulation for this system. I assumed that the ^{26}Al yield due to wind is not affected by β. I have used two approaches; i) I assume that initially the mass transfer is fully conservative until a fraction of 1-β of the total transferred mass is accreted, and the remaining part of the transferred mass is lost from the system, ii) I assume that β is constant in time during the mass-transfer phase. The mass accreted by the secondary is not added to the yield. As for the normal SNB scheme, I have not taken the changes of the orbit as a result of the change in mass of the secondary into account.

In Figure 6.1a the results of the two approaches are shown as a function of β, where the yield for β=1 is the same as in given in Table 3.1 in Section 3.3. Using the first approach, the yield is almost independent of β, because most of the ^{26}Al is located in the deeper layers of the star, and mostly ^{26}Al-poor material is transferred to the secondary.

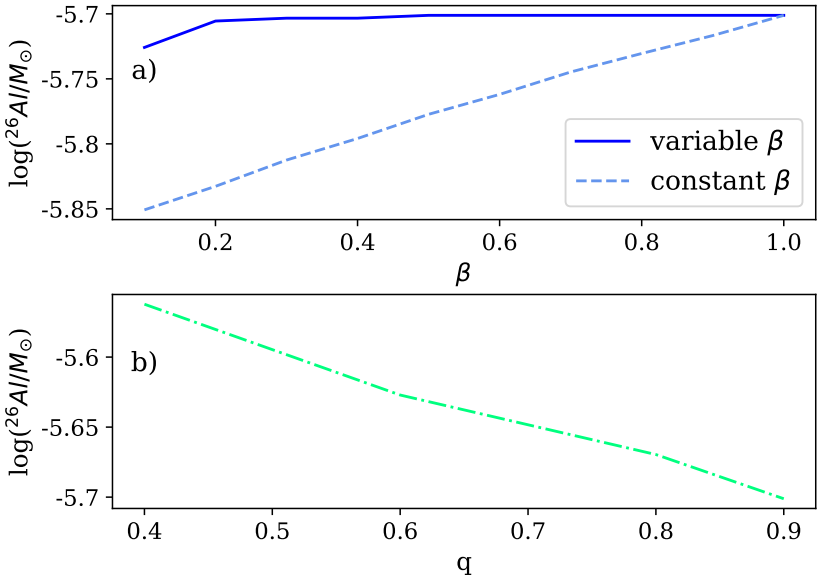

Figure 6.1: (a) effect of varying the mass-transfer efficiency, $1 - \beta$. The solid blue line is for a variable β and the dashed blue line is for a constant β. (b) effect of varying the mass ratio, q, on the ^{26}Al yield.

Using the second approach the effect is quite modest, mostly because most of the ^{26}Al yield (1.34×10^{-6} M$_\odot$) comes from the wind during helium burning after the mass-transfer phase. However, further investigation of the mass-transfer efficiency with more detailed simulations is needed.

6.1.3 The influence of the mass ratio

Apart from the initial primary mass and orbital period, the outcome of the binary evolution also depends on the initial mass ratio, $q = M_2/M_1$. All systems presented so far have an initial mass ratio of q=0.9, but this parameter can take on a wide range of values between close to 0 to 1. Here I briefly show the influence of varying the initial mass ratio between 0.4 and 0.9 on the final ^{26}Al yield for a few systems with a primary mass of 20 M$_\odot$ and a period of 18.4 days. For this, I preformed fully numerical simulations of binary systems with the same settings as for Set 2, though with a mass ratio of 0.4, 0.6, and 0.8.

For a fixed primary mass, a smaller mass ratio results in a smaller separation at the same orbital period (Equation 1.26), and in a larger ratio of the Roche-lobe radius to the separation (Equation 1.25). These effects nearly cancel each other, leading to only a slightly larger Roche-lobe radius for the same orbital period. This has a very small effect only on the time when mass transfer occurs in the system and thus on the ^{26}Al yield. A more substantial change in the yield comes from the different adjustment of the orbit to the mass loss. For the system with a mass ratio of 0.4, the orbit shrinks during the Roche lobe overflow, and then expands again. At the end of the simulation, the period is ∼15 days. For the system with a mass ratio of 0.6, the orbit shrinks only a little, and

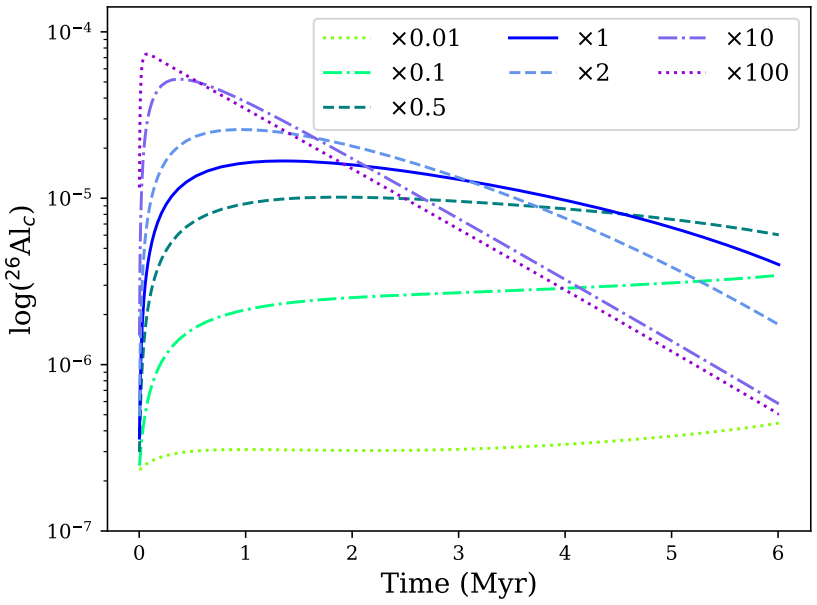

Figure 6.2: Time evolution of the mass fraction of $^{26}Al_g$ in the core of a 30 $M_\odot$ stellar model during the core hydrogen burning-phase. The $^{25}Mg(p,\gamma)^{26}Al_g$ rate is varied with a multiplication factor of 0.01-100 times the original rate.

at the end of the simulation, the orbit has expanded to a period of ∼50 days. For the other two mass ratios, 0.8 and 0.9, the orbit only expands, ending with periods of ∼85 and ∼101 days, respectively. These different responses to the Roche-lobe overflow lead to slightly more mass loss (by up to 0.5 $M_\odot$) for systems with a lower mass ratio during the mass-transfer phase. However, what causes the main difference to the yields is that systems with lower mass ratios lose more mass at the end of the helium-burning phase, where the ^{26}Al-rich region is stripped. Combined, this leads to the ^{26}Al yield increasing with decreasing initial mass ratio, as shown in Figure 6.1b. Because the mass ratio affects the orbital evolution of the system, this should be considered in future work, especially when considering the possibility of reverse mass-transfer as well.

6.2 Effects of the uncertainties in reaction rates

6.2.1 Aluminium-26

The work in this section was done by my collaborator Ertao Li and written in close collaboration with my supervisor Maria Lugaro. It is published in Brinkman et al. (2019). The models were done with the same settings as Set 1 (see Chapter 2).

We investigated the effect of varying the rates of the three reactions that are crucial for the production of ^{26}Al in the hydrogen-burning core of massive stars. These are the production channel of $^{26}Al_g$, $^{25}Mg(p,\gamma)^{26}Al_g$, the competing channel producing the isomer $^{26}Al_m$ that quickly decays into ^{26}Mg, $^{25}Mg(p,\gamma)^{26}Al_m$, and the main destruction channel of $^{26}Al_g$ in hydrogen burning conditions, $^{26}Al_g(p,\gamma)^{27}$Si, aside from the radioactive decay.

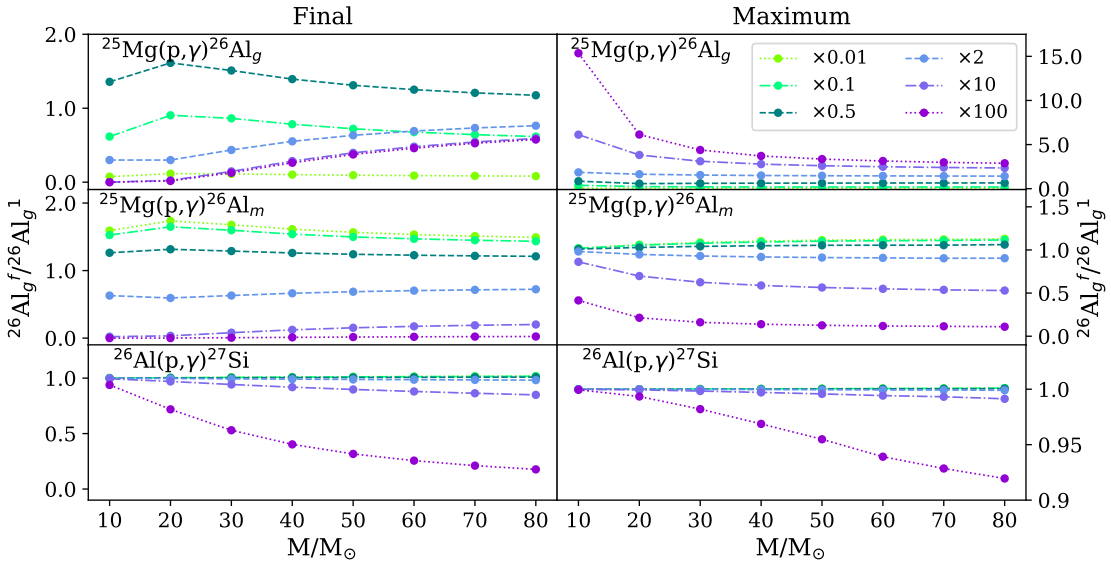

Figure 6.3: Effect of varying the three reaction rates for different initial stellar masses. The vertical axis shows the ratio of ^{26}Al$_g$ from the modified models (superscript f) to the standard models (superscript 1) within the core. The left panels show the ratios of the final mass fractions (end of hydrogen burning). The right panels show the ratios of the maximum mass fractions.

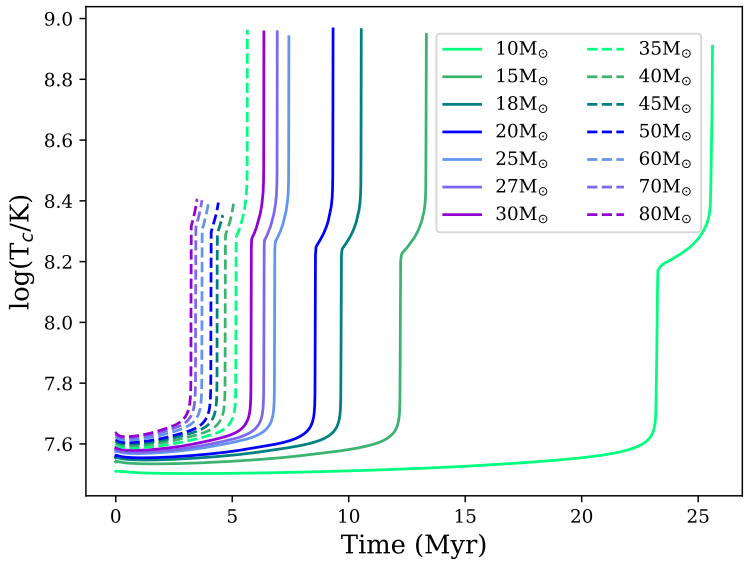

Figure 6.4: Evolution of the central temperature in the core of the single stars of Set 1 as function of time. The sharp increase in the temperature towards the end of the evolution corresponds to the end of hydrogen burning and the contraction of the core. The temperature range relevant to the production and destruction of ^{26}Al is that before this sharp increase.

The rates of the first two reactions are from the experiment performed underground by the LUNA collaboration (Straniero et al., 2013), which are provided with an uncertainty of roughly 40% and 30%, respectively, at a typical temperature of 50 MK. The third reaction is from the compilation of Iliadis et al. (2010), and the uncertainty at typical activation temperatures of 50, 60, and 70 MK is of a factor of 34, 20, and 8, respectively.

We tested variations of such rates by running the full evolutionary MESA models for the single stars with the same input settings as Set 1. Each time we multiplied one of the rates above by a multiplication factor ranging from 0.01 to 100, kept constant in the whole range of temperatures. This tested range is much larger than the uncertainties quoted above. However, for the ^{25}Mg(p,γ) reaction, of the two isolated narrow resonances at 57 keV and 92 keV that dominate the rate from roughly 30-80 MK, only the 92 keV resonance was directly measured by LUNA, while the 58 keV resonance is still inaccessible to direct experiments. Only indirect reaction data (Iliadis et al., 1996) and theoretical values (Li et al., 2015) are available to calculate the 58 keV resonance contribution. Furthermore, the relative importance of the two ^{25}Mg(p,γ) reaction channels is strongly affected by the value of the feeding factor to the ground state of ^{26}Al, which describes the probability of the ^{25}Mg(p,γ)^{26}Al resonances to decay through complex γ cascades to the ground state. The LUNA rates include the feeding factor of 0.6 for the 92 keV resonance provided by Strieder et al. (2001) with an uncertainty of roughly 30%. However, there are large discrepancies between this and the previous values, and there is no recent information on the feeding factor for the 58 keV resonance. The rate of the ^{26}Al$_g$(p,γ)^{27}Si reaction at low temperatures is strongly influenced by unobserved, low-energy resonances, whose contributions may modify the rate beyond the currently given lower and upper limits. Finally, the given reaction rates do not include the possible contribution of electron screening, except for the contribution of the 92 keV resonance in the ^{25}Mg(p,γ) reaction.

In Figure 6.2, we show how variations of the ^{25}Mg(p,γ)^{26}Al$_g$ reaction rates affect the time evolution of the central mass fraction of ^{26}Al in a 30 M$_\odot$ star. There is a striking difference between how the rate variations affect the maximum and the final mass fraction achieved. The maximum value for the mass fraction varies by orders of magnitude as the rate varies, and it is reached earlier in time as the rate increases, i.e., for the standard case (multiplication factor of 1) it is reached within 2 Myr, for the highest multiplication factor of 100 it is reached almost immediately, while for the lowest factor of 0.01, it is reached only at the end of the hydrogen burning phase. The final value of the mass fraction is also controlled by the decay of ^{26}Al$_g$, i.e., if ^{26}Mg is converted into a large amount of ^{26}Al$_g$ very early in time (multiplication factor of 100), there is more time for this ^{26}Al to decay and the final ^{26}Al$_g$ mass fraction is similar to the case when the rate is multiplied by 0.01. The standard case gives the same final ^{26}Al mass fraction as the case with a multiplication factor of 0.1, while the case that results in the highest final mass fraction (roughly a factor of 1.5 higher than the standard) corresponds to a multiplication factor

of 0.5.

Keeping these trends in mind, we show in Figure 6.3 the variations of the maximum and final mass fractions in the core during hydrogen burning for models of different masses. To help interpreting these results, we also show in Figure 6.4 the evolution of the central temperature during the computed evolution of all our single star models of Set 1. In the case of the ^{25}Mg(p,γ)^{26}Al$_g$ reaction, the variations in the final mass fraction do not show a significant trend with mass and the highest final mass fraction is achieved for every mass by the 0.5 multiplication factor. For the maximum mass fraction, instead, variations are more pronounced as the mass decreases and the rate increases. When the ^{26}Al$_g$(p,γ)^{27}Si reaction is varied, significant differences in the mass fraction appear only when the rate is multiplied by a factor of 100 and these differences are strongly dependent on the initial mass. Also, the maximum values of the mass fraction are not strongly affected in this case as the reaction becomes more activated later in the evolution as the temperature increases with time (Figure 6.4).

When comparing to the work of Iliadis et al. (2011), in particular their Section 3.4 reporting a sensitive study for a 80 M$_\odot$ star during core hydrogen burning, we find qualitatively similar results, although quantitatively there are differences. In the case of the ^{26}Al$_g$(p,γ)^{27}Si reaction multiplied by 100 we find a ratio with respect to the standard case of 0.18, while Iliadis et al. (2011) report 0.017. This is probably related to the fact that our core temperature is somewhat lower than that reported in Figure 10 of Iliadis et al. (2011): at a mass fraction of hydrogen of 10^{-4} we find a temperature of $\sim$ 75 MK, instead of $\sim$80 MK. Some differences may also be related to the fact that Iliadis et al. (2011) used a post-processing method, while we calculate a full evolutionary model for each rate variation. In the case of the ^{25}Mg(p,γ) reactions, it is not possible to make an exact comparison since we use the new rates by Straniero et al. (2013). However, we qualitatively agree on the result that variations larger than a factor of two appear only when the rates are changed by two orders of magnitude.

Finally, the temperature dependence of the decay rate of ^{26}Al is included in our calculations. This dependence arises as the ground and isomeric states of ^{26}Al, which are prohibited from communicating with each other due to the large spin difference, may communicate in hot stellar plasma via γ-transitions involving higher-lying energy levels. While the resulting effect is still debated (Gupta & Meyer, 2001; Reifarth et al., 2018; Banerjee et al., 2018), at the temperature range of interest here, between 30-80 MK, the communication between the two states is very weak, much lower than the β-decay rates. We have verified nevertheless that for using two very different rates (Gupta & Meyer, 2001; Reifarth et al., 2018) no change in the ^{26}Al mass fractions are seen in our models.

Table 6.1: Factors used to multiply the indicated reaction rates from their standard values in the 60 $M_\odot$ non-rotating models, and the wind yields of ^{36}Cl and ^{41}Ca for these models in $M_\odot$. Model 1 is the reference model as taken from Set 3.

	^{36}Cl(n,p)^{36}S	^{41}Ca(n,α)^{38}Ar	^{36}Cl ($M_\odot$)	^{41}Ca($M_\odot$)
Model 1	1	1	1.48e-06	2.42e-06
Model 2	0.5	1	2.47e-06	2.55e-06
Model 3	1	2	1.51e-06	1.29e-06
Model 4	0.5	2	2.41e-06	1.29e-06

6.2.2 Chlorine-36 and calcium-41

The work in this section was published in Brinkman et al. (2021).

From Figure 5.2 it becomes clear that to match the ^{26}Al/^{27}Al, ^{41}Ca/^{40}Ca, and ^{36}Cl/^{35}Cl ratios in the ESS by using a self-consistent delay time within the scenario sketched in Section 5.2.1, more ^{36}Cl and/or less ^{41}Ca is required. To look more closely at this, I performed a sensitivity study for the main destruction channel of these two isotopes. The dominant rates in the ^{36}Cl and ^{41}Ca destruction via neutron captures are the ^{36}Cl(n,p)^{36}S and ^{41}Ca(n,α)^{38}Ar rates, respectively. For the rate ^{36}Cl(n,p)^{36}S I use the reaclib label "ths8", which corresponds to a theoretical determination by Rauscher (2008). For ^{36}Cl(n,p)^{36}S, the reported experimental rates for this reaction are either similar (de Smet et al., 2007) or 30% lower (Koehler et al., 1993), at the temperature of interest here around 200-300 MK, as compared to the rate I use here. For the ^{41}Ca(n,α)^{38}Ar rate, the JINA reaclib reference I use is Sevior et al. (1986), which is roughly a factor of two higher than the theoretical rate by Rauscher (2008). Given that there are significant differences between the current estimates, I have computed three additional 60 $M_\odot$ non-rotating models with the settings of Set 3 where I multiplied the neutron-capture reaction rates of interest by different constants as indicated in Table 6.1.

The table also gives the yields for ^{36}Cl and ^{41}Ca for these extra models. The ^{36}Cl yield increases when the reaction rate is decreased, as expected (Models 2 and 4). For Model 2, the ^{41}Ca yield increases slightly as well, even though the reaction rate is unchanged. For Models 3 and 4, the ^{41}Ca yield decreases by about a factor 2, as expected as well. And also the ^{36}Cl yield changes slightly for Model 3. The changes in the yields are not fully linear due to other (neutron-capture) reactions also playing a minor role in the destruction of the these two isotopes. If I apply the delay time calculation to these new models, I find that for Model 1 (the original model of Set 3), the difference in the delay time between the ^{41}Ca/^{40}Ca ratio and the ^{36}Cl/^{35}Cl ratio is a factor of $\sim$3. For Model 2, the delay time difference is similar to that of Model 1. This is visible in Figure 6.5, where the solid lines (Model 1) and the dashed lines (Model 2) are more or less overlapping. Models 3 (dotted lines) and 4 (dashed-dotted lines), provide a better solution as the difference in the delay time is reduced to a factor 1.8. There is little difference between these two models. From

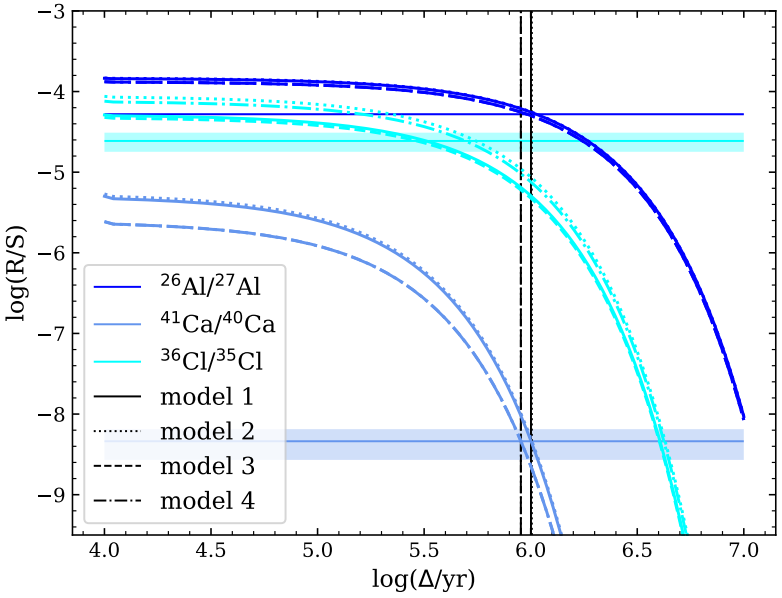

Figure 6.5: Results for the reaction rate tests. The colours and bands are the same as in Figure 5.2

this, I can conclude that to obtain a better match for all three SLR ratios, a decrease in the amount of ^{41}Ca has more impact than an increase in the amount of ^{36}Cl.

6.2.3 Chromium-53,54 and titanium-49,50

The work in this section was published in den Hartogh et al. (2022). The parts relevant for this thesis are from Section 5.1, to which I contributed to with my models, and are presented here. For more details, I refer the reader to the original work.

In the previous two sections, I presented tests on reaction rates related to SLRs of interest in this thesis. I also made such tests for selected stable isotopes, as I will show in this section. This was needed for the paper by Den Hartogh et al., who consider three sets of supernova yields (Sieverding et al. 2018; Ritter et al. 2018b and Lawson et al. 2022) to determine the different regions within these stars could be the origin site of pre-solar chromium-rich oxide (chromite) grains. These authors looked at models with initial masses of 15, 20, and 25 $M_\odot$ at solar metallicity (Z=0.014 or Z=0.02) and found that within the carbon-burning ashes there are regions that produce a good agreement with the observed ^{54}Cr/^{52}Cr and ^{53}Cr/^{52}Cr ratios, as well as the ^{50}Cr/^{52}Cr. Because the signal at atomic mass 50 could instead originate from ^{50}Ti, it is also possible to match the observed isotopic ratios in the ashes of explosive helium burning.

By considering three data sets from different stellar models, it is possible to derive a rough estimation of the effect of stellar physics uncertainties and of different computational approaches. This approach, however, does not provide us with a systematic way to check of the effect of nuclear uncertainties. I have considered these separately and I present the

results here.

As discussed in Section 3.1 of den Hartogh et al. (2022) (see also Table 6.2), the main channels of production of ^{53}Cr and ^{54}Cr in regions where the chromite grains potentially originated from are neutron captures on the Cr isotopes ^{52}Cr and ^{53}Cr. The final abundances of ^{53}Cr, ^{54}Cr, ^{48}Ti, and ^{50}Ti after a given neutron flux episode are controlled mostly by their neutron-capture rates. To test how variations in these rates affect the Cr and Ti isotopic ratios, I preformed several dedicated tests using the settings for the massive stars of Set 3 (see also Section 2). The considered models have an initial mass of 20 $M_\odot$ with Z=0.014 and are evolved up to the core-collapse. Unlike in the other models presented in den Hartogh et al. (2022), my models do not include the supernova explosion. However, the models from Ritter et al. (2018b); Sieverding et al. (2018) and Lawson et al. (2022), show that the chromium isotopes in the carbon- and helium-ashes are more significantly affected by the progenitor evolution for a 20 $M_\odot$ star than by the explosion (See Appendix A of den Hartogh et al. 2022). Because the supernova explosion has no significant impact on the mass fractions in the regions relevant for the analysis, a pre-supernova model of 20 $M_\odot$ can be used to investigate the impact of the reaction rates on the isotopic ratios.

I multiplied the neutron-capture reaction rates of interest by different constants, as indicated in Table 6.2. The variations of the reaction rates where chosen in such as they would help the models provide a better match to the most anomalous grain with ^{54}Cr/^{52}Cr > 1 (see Figure 6.6) and the rates were varied by up to a factor of 2. This is larger than the up to 50% uncertainty at 2σ reported for the recommended values in the KaDoNiS database[1] V0.2 (Dillmann et al., 2006, and therefore in the JINA reaclib database, which uses KaDoNiS). However, these reactions were measured several decades ago: these current recommended values are from Kenny et al. (1977) for the chromium isotopes, from Allen et al. (1977) for ^{48}Ti, and from Sedyshev et al. (1999) for ^{50}Ti. Therefore it is possible that systematic uncertainties are much higher than the reported uncertainty.

Figures 6.6 and 6.7 show the results for the Cr and Ti isotopic ratios from these tests, respectively. The figures show the carbon ashes (star symbols) and helium ashes (dotted symbols), which are the two possible sites of origin for the grains as described in Section 4 of den Hartogh et al. (2022). In the case of the Cr isotopic ratios, two expected main trends are visible:

i) in the models with an enhanced ^{53}Cr(n,γ)^{54}Cr rate only (Models 2 and 3) the ^{53}Cr/^{52}Cr ratio decreases relative to the standard Model 1 (taken from Set 3), for example from a maximum in the helium ashes around 0.16 to a minimum 0.07, i.e., roughly a factor of 2;

ii) in Model 4, with the reduced ^{54}Cr(n,γ)^{55}Cr rate, the ^{54}Cr/^{52}Cr ratio increases relative to Model 1, for example, in the carbon ashes from $\sim$1 to $\sim$2. In the combined

[1]See `https://kadonis.org/`

Table 6.2: Factors used to multiply the indicated reaction rates from their standard values in the 20 $M_\odot$ models considered in this section.

	^{53}Cr(n,γ)^{54}Cr	^{54}Cr(n,γ)^{55}Cr
Model 1[1]	1	1
Model 2	1.5	1
Model 3	2	1
Model 4	1	0.5
Model 5	2	0.5
	^{48}Ti(n,γ)^{49}Ti	^{50}Ti(n,γ)^{51}Ti
Model 6	2	1
Model 7	1	0.5
Model 8	2	0.5

[1] Using the KaDoNis database (Dillmann et al., 2006) values, which produces results very similar to those by Lawson et al. (2022) and Sieverding et al. (2018).

test (Model 5), the ^{54}Cr/^{52}Cr ratio increases further to $\sim$3 in the carbon ashes.

Although these tests are only meant to provide a basic estimation of the impact of nuclear uncertainties, it can already be derived that the uncertainties of the neutron-capture rates of Cr isotopes have a significant impact on stellar predictions. Therefore, new measurements of these neutron-capture rates are needed to reduce the uncertainty of the model predictions.

When considering the results of the Ti tests, I found that increasing the ^{48}Ti(n,γ)^{49}Ti reaction rate only (Model 6) leads to an increase of the ^{50}Ti/^{48}Ti ratio. Decreasing the ^{50}Ti(n,γ)^{51}Ti reaction rate only (Model 7) does not have a significant effect, because ^{50}Ti is a magic nucleus and therefore has a very low neutron-capture cross section in both the two nuclear reaction setups. As a consequence, when both rates are changed in Model 8, the result is very similar to Model 6.

I did not test the impact of other nuclear uncertainties affecting the production of these isotopes here, such as the production of the neutrons needed. In both the helium and the carbon ashes the ^{22}Ne(α,n)^{25}Mg reaction is the main neutron source. The impact of its present uncertainty on helium- and carbon-burning nucleosynthesis has been studied before (see, e.g., Kaeppeler et al., 1994; Heger et al., 2002; Pignatari et al., 2010). A more precise definition of the competing α-capture rates ^{22}Ne(α,n)^{25}Mg and ^{22}Ne(α,γ)^{26}Mg at relevant stellar temperatures is an open problem of nuclear astrophysics and has been an active line of research from many years (see, e.g., Longland et al., 2012; Talwar et al., 2016; Adsley et al., 2021).

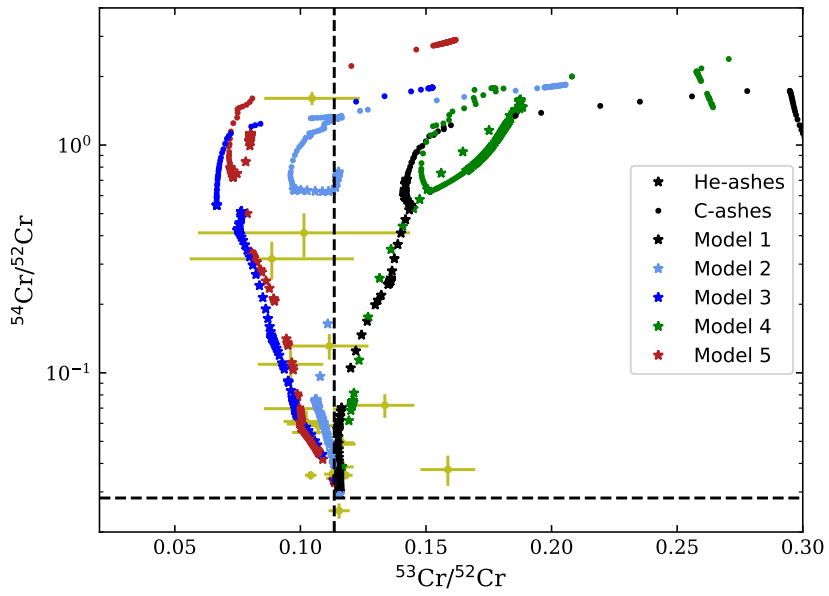

Figure 6.6: Cr isotopic compositions resulting from the five 20 $M_\odot$ models calculated using different neutron-capture rates for ^{52}Cr and ^{53}Cr, as listed in the top half of Table 6.2. The reference model is Model 1 taken from Set 3. The yellow points are the grain data from Nittler et al. (2018).

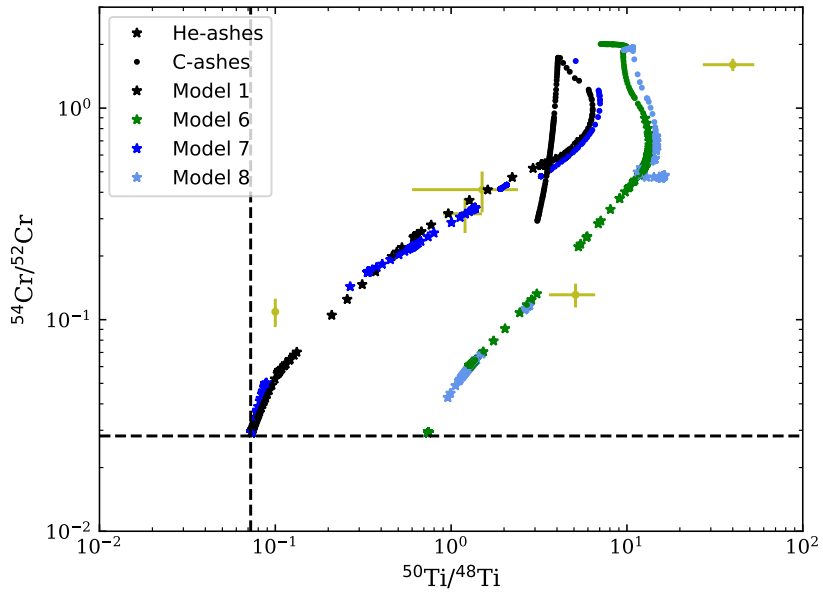

Figure 6.7: Same as Figure 6.6 but for the ^{50}Ti/^{48}Ti ratio resulting from the four 20 $M_\odot$ models calculated using different titanium neutron capture rates, and reference Model 1. The rates used in these tests are listed in the bottom half of Table 6.2.

6.3 Yields from non-rotating binary stars up till core collapse

The work in this section is part of Brinkman et al. in prep., and will be submitted after the completion of this thesis.

As I discussed in Chapters 3 and 4, binary interactions can have a large impact on the yields of massive stars by stripping off the envelope and exposing the deeper layers of the star, especially on the lower mass end of Set 1. In Set 2, I only considered the impact on ^{26}Al, and in Set 3, I considered more isotopes, but did not include the impact of binary interactions. In this section, I discuss how binary interactions impact the yields of the five other isotopes, ^{36}Cl, ^{41}Ca, ^{60}Fe, ^{22}Ne, and ^{19}F. The models discussed here will be referred to as Set 4, and have been calculated with the same settings as the non-rotating models of Set 3, and binary settings the same as for Set 2 (see Table 2.1), with initial masses from 10-50 $M_\odot$ for the primary stars. To produce as complete as possible yields, I uncoupled the binaries when reverse mass-transfer takes place in the system. This means that I stop the simulation at that point and then evolve the primary star further as if it were a single star to the onset of core collapse. This is possible because MESA stores a model when a simulation stops which can be restarted as a single star. This procedure will overlook some effects of the binary interactions, however, it is a step closer to producing full binary yields for these isotopes.

In this section, I use the following definitions:

- the effective binary yield, i.e., the single star yield multiplied by the binary enhancement factor, which is defined as the arithmetic average increase (over all periods considered) of the yield of the single star compared to the yield of the binary systems, which cover multiple periods (as earlier described in Section 4.2.1). A flat period-distribution is assumed, giving all systems an equal weight in the calculation,
- the maximum binary yield, i.e., the maximum value of the wind yields for the binary systems with a certain initial primary mass,
- and the minimum binary yield, i.e., the minimum value of the wind yields for the binary systems with a certain initial primary mass. This minimum binary yield includes systems that did not complete their evolution, for example, due to the formation of a common envelope.

6.3.1 Short-lived radioactive isotopes

In this section, I discuss the effects of the binary interactions on the SLRs of importance to this thesis.

Aluminium-26

Evolving the primary stars of the binaries up to core-collapse has a very limited impact on the ^{26}Al compared to the yields of Set 1 and Set 2, as was already shown in Chapter 4 for Sets 1 and 3. Figure 6.8a shows this again, with the single star yields of Set 1 and Set 3. The yields from Set 1 and the non-rotating yields for Set 3 are almost identical for the chosen mass-interval. Figure 6.8b shows the effective binary yields for Set 4, as well as the maximum binary yield and the minimum binary yield, as defined above. For most systems, the effective binary yield is very close to both the minimum and the maximum yield, except for the models at 30-45 $M_\odot$, where the system with the shortest initial period enters a common-envelope phase initiated by the primary star. The outcome of this phase is very uncertain and therefore I do not uncouple these systems. This cuts the evolution of the system short and thus the yields are strongly decreased compared to the yields of the other systems (see also Table 6.3). If the common envelope is the result of reverse mass-transfer however, I do uncouple the systems because the primary is unaffected by the reverse mass-transfer. Continuing these runs will give insight in the potential wind yields for such systems. However, uncoupling the binary does ignore the effects of changes in the orbital parameters.

Figure 6.8b also shows how both rotation and binary mass-transfer increase the yields of ^{26}Al for the stars on this mass interval, to the point that at ~ 30 $M_\odot$ the fastest rotating model of Set 3 already gives a similar yield to the binary system, while this happens only around ~ 40 $M_\odot$ for the other two initial rotational velocities of Set 3. This shows that for higher rotational velocities, the increase in the wind mass loss causes the effect of binary interactions to lose effect earlier than for the non-rotating models.

Chlorine-36, Calcium-41, and Iron-60

Unlike for ^{26}Al, there are no yields for ^{36}Cl and ^{41}Ca from Set 1, because these isotopes are produced during helium burning, and they were not part of the initial nuclear network. Panels a and c of Figure 6.9 show the yields from Set 3 for ^{36}Cl and ^{41}Ca respectively. As pointed out in Chapter 4, a higher initial rotational velocity decreases the initial mass for which the stars become Wolf-Rayet stars, leading to an earlier increase in the yields of these two SLRs. Panels b and d of Figure 6.9 show the single star yields of Set 3 in

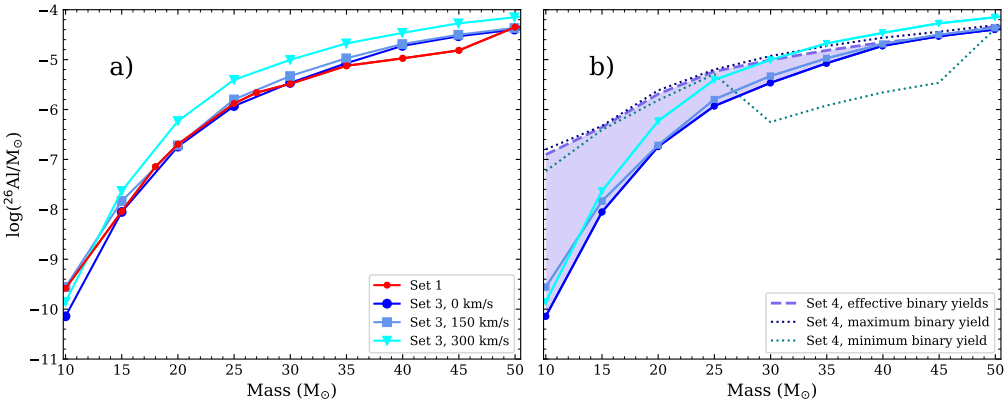

Figure 6.8: The figure shows the yields for Set 1 (red dots) and Set 3 (blue dots) in panel a, and the yields of Set 3 with the effective binary yield (dashed line), maximum binary yield (purple dotted line), and minimum binary yield (teal dotted line) for Set 4 for ^{26}Al in panel b. The yields for the separate binary systems are given in Table 6.3. The coloured area indicates the potential binary yields, assuming that they are between the effective binary yield and the single star yield.

combination with the effective binary yield, the maximum binary yield, and the minimum binary yield of Set 4. The difference between the maximum/effective binary yield and the minimum binary yield is larger for these two isotopes than for ^{26}Al. The sharp decrease in the minimum binary yield at 30 M$_\odot$ is caused by the systems with the shortest initial period undergoing a common-envelope phase initiated by the primary. As for ^{26}Al, the binary interactions have most effect at the lower masses, decreasing at the higher mass-end. For the rotating stars, the effective binary yields become similar to the single star yields at lower initial masses, as expected.

While the effective binary yields for ^{26}Al follow the same general trend as the single star yields, where the impact of the binaries is a strong increase at the lower mass end, slowly tapering off into no significant effect, the effective binary yields for ^{36}Cl and ^{41}Ca show a clear dip at 15 M$_\odot$ (see panels b and d of Figure 6.9), after which the trend looks similar again to that of ^{26}Al. The dip at 15 M$_\odot$ is caused by a difference in which layers are reached by the increased mass loss due to the binary interactions.

To illustrate this, Figure 6.10 shows the KHDs for 10, 15, and 25 M$_\odot$, the single star on the left (a, c, and e, respectively), and a binary system undergoing Case B mass-transfer on the right (b, d, and f, respectively), with the ^{41}Ca mass fraction on the colour scale (the ^{36}Cl mass fraction is similar). The 10 M$_\odot$ binary model loses more mass than the single star due to binary interactions. This exposes the deeper layers of the star where ^{41}Ca (and ^{36}Cl) can be found. Especially the final mass loss phase during carbon shell burning (between log(time till collapse/yrs) 4-2), the top the ^{41}Ca (and ^{36}Cl) enhanced layer is lost from the star (see Figure 6.10a and b).
This leads to a strong increase in the yield for ^{41}Ca (and ^{36}Cl). For the 15 M$_\odot$ star (panels

c and d of Figure 6.10), instead, the mass loss after the mass-transfer phase is not strong enough to remove the upper layers of the helium core and the ^{41}Ca (and ^{36}Cl) produced in the inner layers is not reached. This leads to smaller yields and a much smaller increase in the effective binary yield as compared to the 10 $M_\odot$ case. For the other single stars, 20-30 $M_\odot$, the helium burning core is barely reached as shown by the example of a 25 $M_\odot$ star. The resulting yields are below 10^{-20} (see also Table 6.3). For these masses, the increased mass loss leads to the exposure of the top of the helium burning core, just as for the 10 $M_\odot$ star, giving a larger effective binary yield. Around $\sim$40 $M_\odot$, the effect of the binary interactions becomes smaller again, especially compared to the rotating models of Set 3. I remind here that, to obtain a full picture of the interactions between binary mass-transfer and rotation, binary systems with a rotating primary star need to be calculated. While the wind yields for ^{60}Fe are very minor compared to the supernova yields, I still show the effects of binary evolution on these yields in Figure 6.9e and f. The effective binary yields behave the same as for ^{36}Cl and ^{41}Ca, with a dip at 15 $M_\odot$, and becoming equal to the single star yields between 40-45 $M_\odot$, depending on the initial rotational velocity.

6.3.2 Stable isotopes ^{19}F and ^{22}Ne

The results for ^{19}F and ^{22}Ne are shown in Figure 6.11. As in Figures 4.10 and 4.11, the red line gives the initial mass of the stable isotopes present in the stars at the beginning of the evolution. As I pointed out in Chapter 4, rotation decreases the yields on the mass interval studied here for the single stars.

At 25 $M_\odot$, the effective binary yield is nearly identical to the single star yield. This is because for both the single star and the binary, all ^{19}F present in the envelope is stripped off, but the binary mass loss is not strong enough to reach the helium burning core or the helium burning shell, where ^{19}F is produced. For the models with lower initial masses, the added mass loss through the binary interactions does increase the ^{19}F yields, and thus the effective binary yields are higher than the single star yields. For the models with higher initial masses, deeper layers of the star are reached, leading to an increase in the effective binary yields again as compared to the single star yields. Only the effective binary yield of the 35 and 40 $M_\odot$ models are larger than the initial amount of ^{19}F present in the star, giving a positive net yield. This is at a significantly lower mass than for the single stars of Set 3 studied in Chapter 4, where the only model to give positive ^{19}F yield is the 80 $M_\odot$ model rotating at 150 km/s. This means that the interval between 40-80 $M_\odot$ might be interesting for more binary simulations when considering the potential sources ^{19}F.

The results for ^{22}Ne (Figure 6.11c) are qualitatively similar to ^{19}F. The main difference is that for these models, the 40 $M_\odot$ star already has a positive net ^{22}Ne yield for the highest rotation rate. The binary models also have a positive yield at a lower mass, as

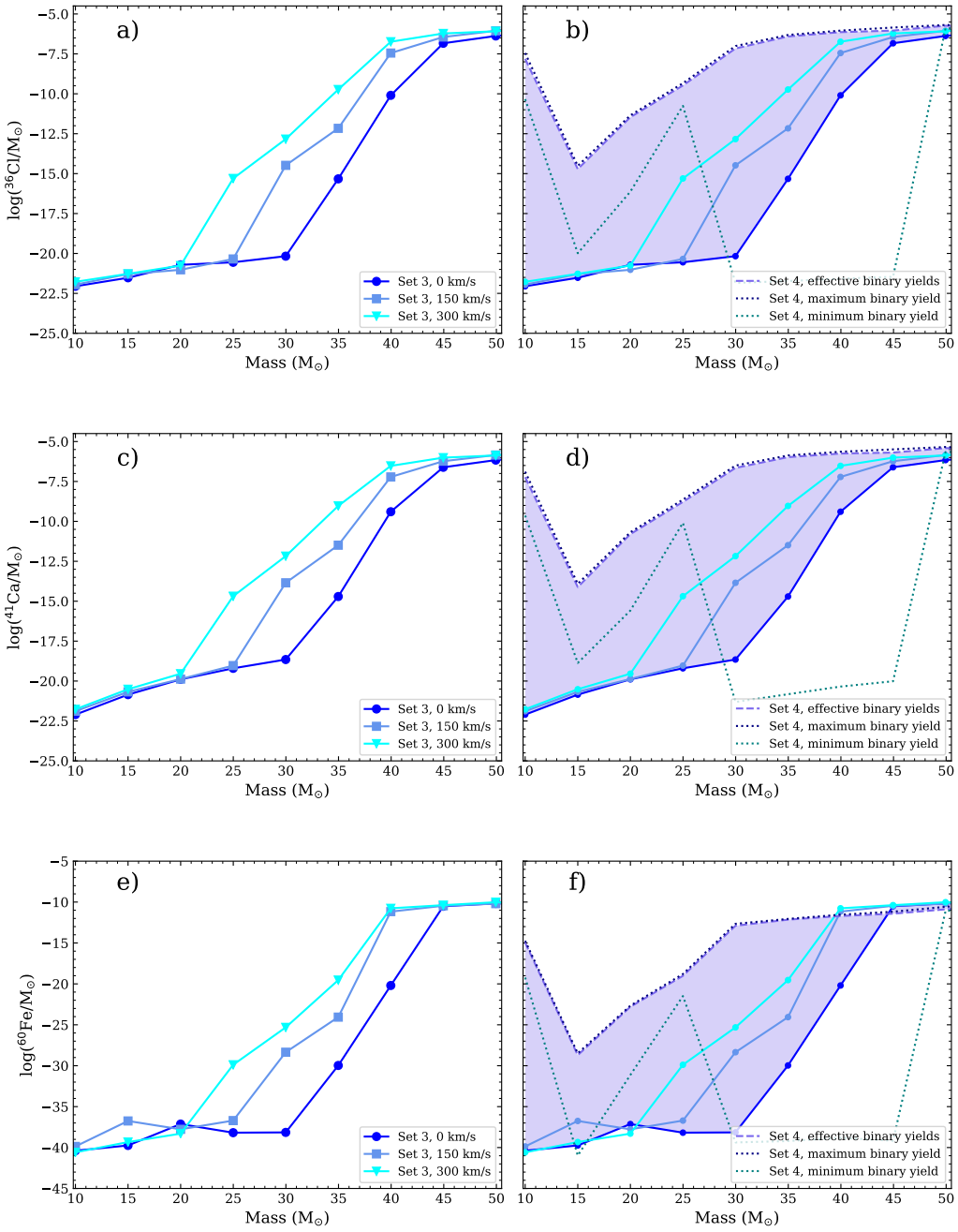

Figure 6.9: The figure shows the yields for only Set 3 (blue dots) in panels a, c, and e, and the yields of Set 3 with the effective binary yield (dashed line), maximum binary yield (purple dotted line), and minimum binary yield (teal dotted line) for Set 4 for ^{36}Cl, ^{41}Ca, and ^{60}Fe in panels b, d, and f, respectively. The yields for the separate binary systems are given in Table 4.1. The coloured area indicates the potential binary yields, assuming that they are between the effective binary yield and the single star yield.

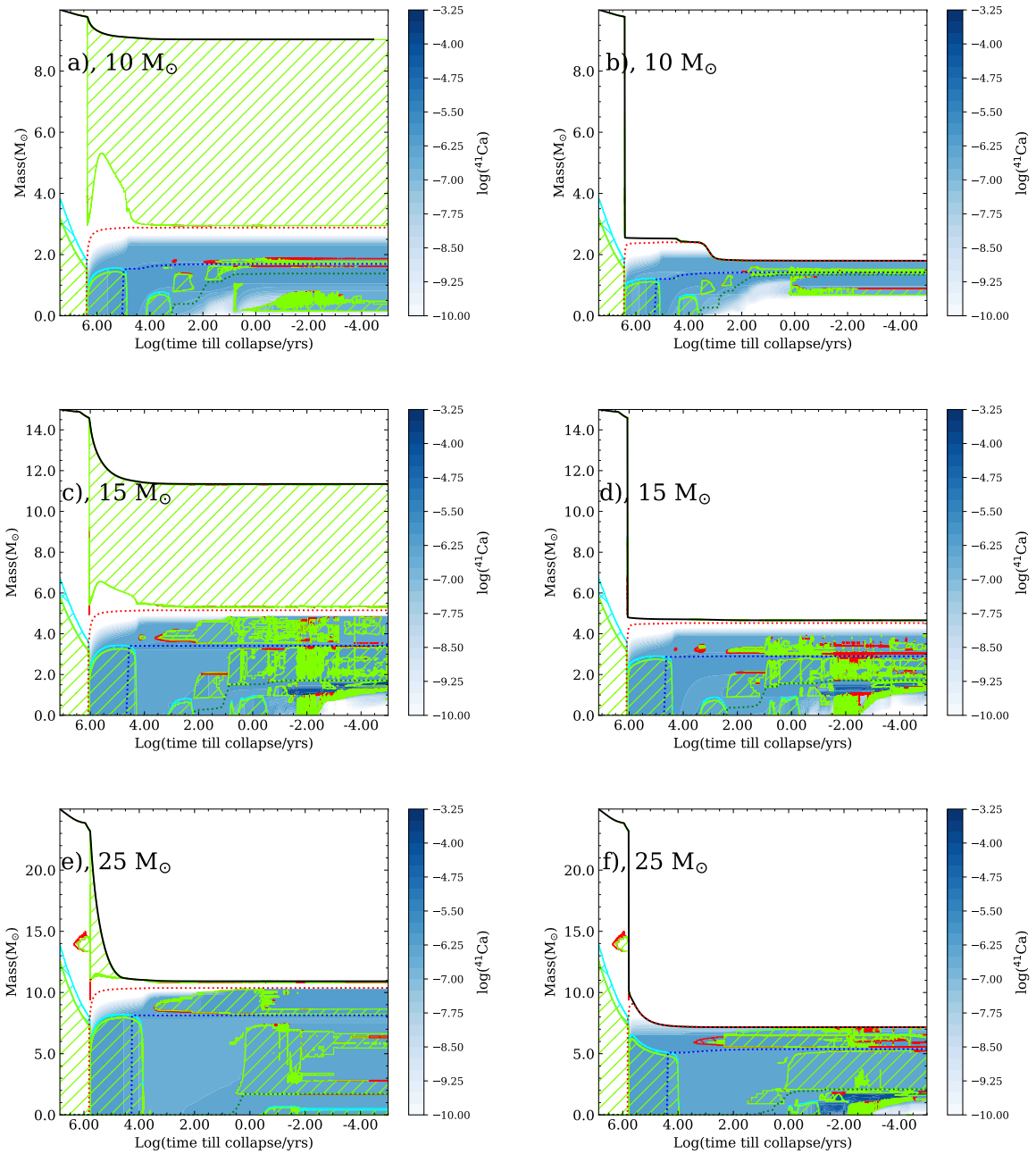

Figure 6.10: KHDs for 10, 15, and 25 $M_\odot$, single stars on the left (panels a, c, and e), binary stars on the right. The initial periods are 4.9 days for the 10 $M_\odot$ model (panel b), 6.7 days for the 15 $M_\odot$ model (panel d), and 8.9 days for the 25 $M_\odot$ model (panel f). All three systems undergo Case B mass transfer. The colour scale shows the ^{41}Ca mass fraction in the stars. All other colours and shadings are the same as in Figure 2.1.

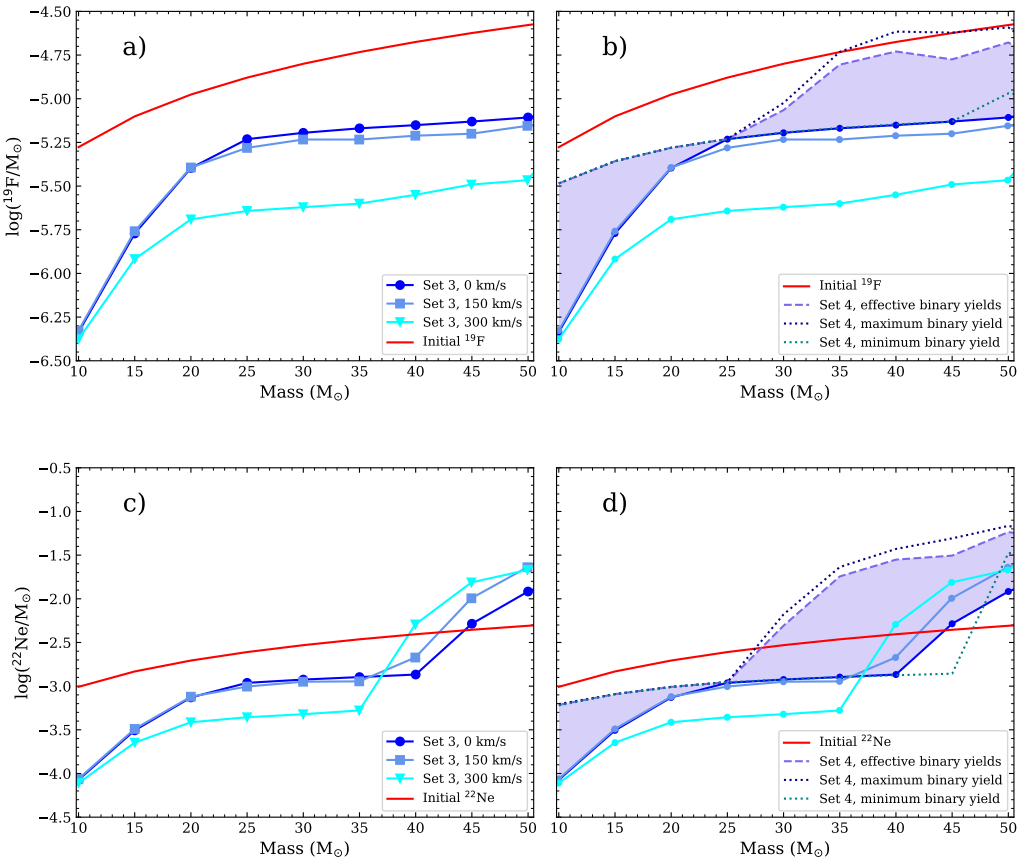

Figure 6.11: The figure shows the yields for Set 3 (blue dots) in panel a and c, and the yields of Set 3 with the effective binary yield (dashed line), maximum binary yield (purple dotted line), and minimum binary yield (teal dotted line) for Set 4 for ^{19}F and ^{22}Ne in panel b and d. The yields for the separate binary systems are given in Table 6.3. The coloured area indicates the potential binary yields, assuming that they are between the effective binary yield and the single star yield. The red lines in panels a and c indicate the initial amounts of ^{19}F and ^{22}Ne in the stars.

compared to ^{19}F, at 30 $M_\odot$.

For the stable isotopes, there is another interesting trend. The effective binary yields decrease from 10 $M_\odot$ to 25 $M_\odot$, and then increase again after this initial mass. This is because at the lowest masses the increase in mass loss is very significant, but for 20 and 25 $M_\odot$, the increased mass loss due to the binary interactions has the same effect as the mixing due to the formation of a convective envelope. This is illustrated in Figure 6.12, showing the KHDs for three initial masses are shown, $10M_\odot$, $20M_\odot$, and $40M_\odot$, single stars on the left (panels a, c, and e), binary stars on the right (panels b, d, and f). For the 10 $M_\odot$ star, the mass loss of the primary star is significantly more than for the single star, which leads to a large increase of the yield, though either yield is still too low to give a positive net yield. For the 20 $M_\odot$ models, even though the primary star loses more mass, the layers uncovered by the binary mass-transfer do not have a large ^{22}Ne mass fraction and thus the increase between the single star and the binary star is much smaller than for the 10 $M_\odot$ model. Finally, for the 40 $M_\odot$ models, the extra mass loss due to the binary interactions uncover the deeper layers of the star and the winds strip off the upper layer of the region that belonged to the helium burning core. This increases the yield of the primary star significantly as compared to the single star, even leading to a positive net yield for the primary star, while only the fastest rotating single star model has a positive net yield. This shows that while for the SLRs, the impact of the binary interactions already tapers off around 40 $M_\odot$, for the stable isotopes, the effect is still significant for the higher masses considered here (40-50 $M_\odot$). The impact of binary interactions on the yields of the stable isotopes will therefore need further investigation, and extension to higher initial masses for the primary stars.

For ^{19}F, the effect is less pronounced, mainly due to the destruction of this isotope during helium burning. Even though the yields increase strongly for the binary models between 40-50 $M_\odot$, the effective binary yields still do not lead to a positive net yield, though the maximum binary yields for these models are close to the initial amount of ^{19}F present in the stars. This makes these yields especially sensitive to changes in the stellar winds and the internal mixing.

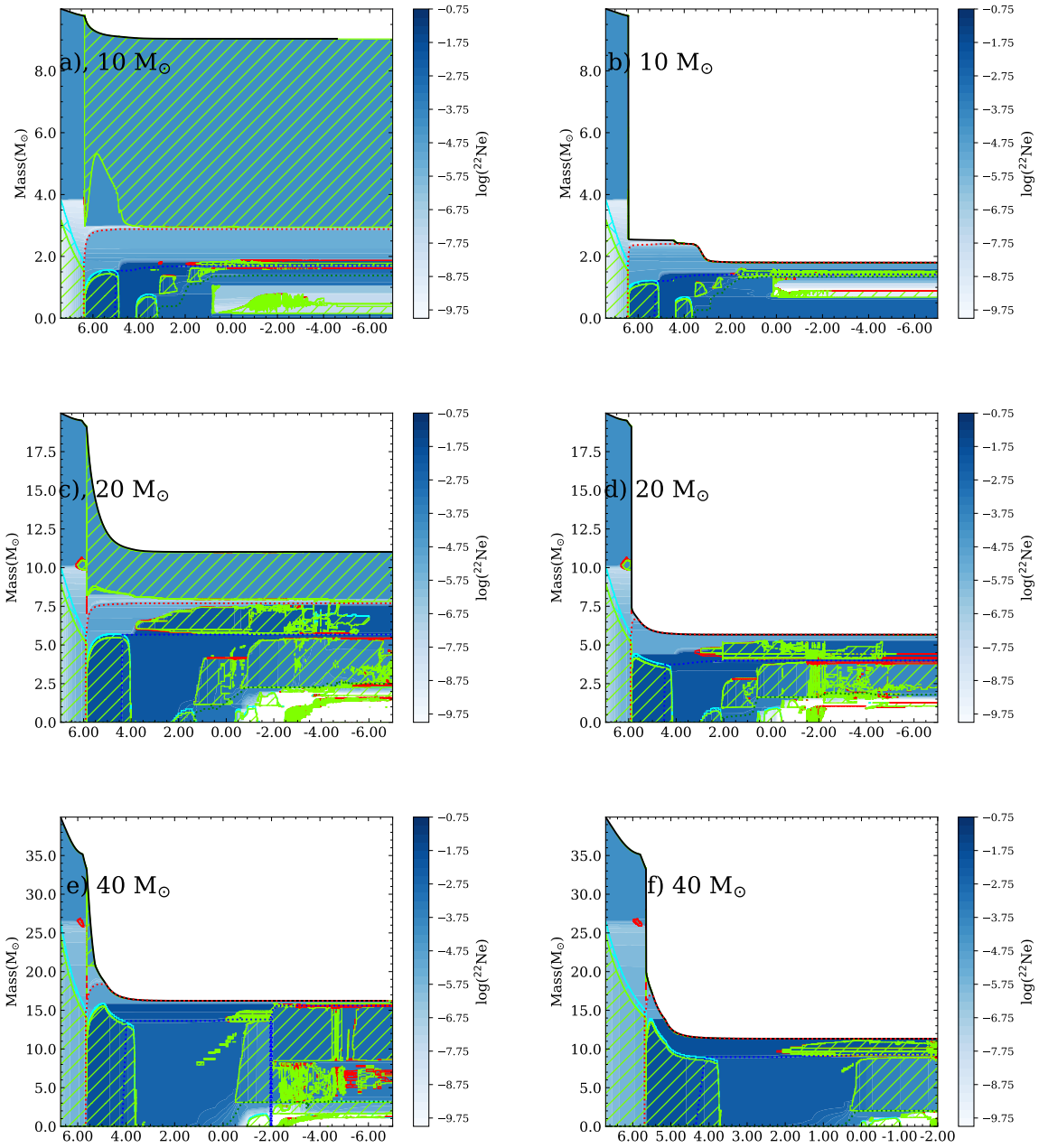

Figure 6.12: KHDs for a 10, 20, and 40 $M_\odot$, single stars on the left (panels a, c, and e), binary stars on the right (panels b, d, and f). The initial periods are 4.9 days for the 10 $M_\odot$ model (panel b), ?? days for the 15 $M_\odot$ model (panel d), and 15.8 days for the 40 $M_\odot$ model. All three systems undergo Case B mass-transfer. The colour scale shows the ^{22}Ne mass fraction in the stars. All other colours and shadings are the same as in Figure 2.1.

Table 6.3: Wind yields for the binary models of Set 4: ^{19}F, ^{22}Ne, ^{26}Al, ^{36}Cl, ^{41}Ca, and ^{60}Fe. $M_{\rm ini}$ is the initial mass in $M_\odot$. $P_{\rm ini}$ is the initial period of the binary system in days. The yields per isotope are given in $M_\odot$. For the stable isotopes, the initial amount present in the star is given as well. The yields given here are not corrected for radioactive decay that might take place during the evolution of the star, and neither have I corrected the yields for the initial amounts of the stable isotopes present in the stars, i.e., the total yields are given. The top line gives the non-rotating yield from Set 3

$M_{\rm ini}$ ($M_\odot$)	$P_{\rm ini}$ (days)	$^{19}F_{\rm ini}$ ($M_\odot$)	^{19}F ($M_\odot$)	$^{22}Ne_{\rm ini}$ ($M_\odot$)	^{22}Ne ($M_\odot$)	^{26}Al ($M_\odot$)	^{36}Cl ($M_\odot$)	^{41}Ca ($M_\odot$)	^{60}Fe ($M_\odot$)
10	-	5.28e-06	4.61e-07	9.82e-4	8.47e-05	7.19e-11	8.82e-23	7.90e-23	4.11e-41
	2.8[3]	5.28e-06	3.28e-06	9.82e-4	6.23e-4	5.85e-08	3.53e-08	1.29e-07	1.83e-15
	4.9[4]	5.28e-06	3.27e-06	9.82e-4	6.05e-4	1.59e-07	1.12e-08	4.76e-08	1.44e-15
	13.1[4]	5.28e-06	3.27e-06	9.82e-4	6.01e-4	1.57e-07	4.61e-11	2.31e-10	5.94e-20
15	0	7.93e-06	1.69e-06	1.47e-3	3.12e-4	8.85e-09	3.00e-22	1.41e-21	1.81e-40
	3.8	7.93e-06	4.39e-06	1.47e-3	8.10e-4	3.90e-07	1.03e-20	1.35e-19	1.06e-41
	6.7	7.93e-06	4.39e-06	1.47e-3	8.10e-4	4.69e-07	3.06e-15	1.22e-14	3.29e-29
	16.8	7.93e-06	4.39e-06	1.47e-3	8.08e-4	4.58e-07	2.73e-15	61.09e-14	2.63e-29
20	0	1.06e-05	4.01e-06	1.96e-3	7.43e-4	1.81e-07	1.94e-21	1.28e-20	7.40e-39
	2.5[2,5]	1.06e-05	5.24e-06	1.96e-3	9.74e-4	1.53e-06	7.43e-17	2.60e-16	7.36e-32
	5.1[5]	1.06e-05	5.24e-06	1.96e-3	9.83e-4	2.42e-06	3.05e-12	1.41e-11	1.38e-23
	6.2	1.06e-05	5.24e-06	1.96e-3	9.90e-4	2.13e-06	4.47e-12	2.08e-11	2.17e-23
	7.4	1.06e-05	5.24e-06	1.96e-3	9.80e-4	2.12e-06	4.44e-12	2.07e-11	2.17e-23
	18.4	1.06e-05	5.24e-06	1.96e-3	9.80e-4	2.07e-06	4.27e-12	1.99e-11	2.01e-23
	66.2	1.06e-05	5.24e-06	1.96e-3	9.81e-4	2.01e-06	3.85e-12	1.79e-11	1.65e-23
	132.4	1.06e-05	5.24e-06	1.96e-3	9.81e-4	2.00e-06	3.84e-12	1.79e-11	1.65e-23
25	0	1.32e-05	5.87e-06	2.46e-3	1.09e-3	1.17e-06	2.80e-21	6.27e-20	6.56e-39
	2.7[2]	1.32e-05	5.88e-06	2.46e-3	1.11e-3	5.11e-06	1.75e-11	8.10e-11	3.26e-22
	6.7[2]	1.32e-05	5.88e-06	2.46e-3	1.11e-3	6.31e-06	3.46e-10	1.72e-09	8.64e-20
	8.9	1.32e-05	5.88e-06	2.46e-3	1.11e-3	5.93e-06	4.60e-10	2.30e-09	1.60e-19
	17.8	1.32e-05	5.88e-06	2.46e-3	1.11e-3	5.86e-06	4.41e-10	2.20e-09	1.37e-19
	71.3[5]	1.32e-05	5.88e-06	2.46e-3	1.11e-3	5.76e-06	3.94e-10	1.96e-09	9.74e-20
30	0	1.59e-05	6.38e-06	2.95e-3	1.19e-3	3.41e-06	6.76e-21	2.22e-19	7.10e-39
	2.8[1]	1.59e-05	6.41e-06	2.95e-3	1.19e-3	5.59e-07	1.44e-22	4.87e-22	4.21e-40
	8.4[2]	1.59e-05	9.46e-06	2.95e-3	6.63e-3	1.17e-05	9.78e-08	3.11e-07	1.56e-13
	10.1[2]	1.59e-05	8.98e-06	2.95e-3	5.46e-3	1.17e-05	7.88e-08	2.57e-07	1.31e-13
	12.2[2]	1.59e-05	9.06e-06	2.95e-3	5.53e-3	1.18e-05	7.94e-08	2.60e-07	1.35e-13
	30.3[2]	1.59e-05	8.42e-06	2.95e-3	4.67e-3	1.16e-05	6.74e-08	2.20e-07	1.24e-13
	75.4[2]	1.59e-05	9.33e-06	2.95e-3	6.05e-3	1.15e-05	8.95e-08	2.87e-07	2.20e-13
35	0	1.85e-05	6.77e-06	3.44e-3	1.27e-3	8.44e-06	4.70e-16	1.96e-15	1.08e-30
	2.9[1]	1.85e-05	6.80e-06	3.44e-3	1.27e-3	1.20e-06	1.86e-22	1.50e-21	6.23e-40
	8.8[2]	1.85e-05	1.84e-05	3.44e-3	2.31e-2	1.87e-05	4.84e-07	1.35e-06	8.06e-13
	10.6[2]	1.85e-05	1.81e-05	3.44e-3	2.24e-2	1.82e-05	4.83e-07	1.31e-06	8.61e-13
	12.7[2]	1.85e-05	1.86e-05	3.44e-3	2.21e-2	1.84e-05	4.75e-07	1.30e-06	8.37e-13
	31.5[2]	1.85e-05	1.68e-05	3.44e-3	2.03e-2	1.79e-05	4.55e-07	1.21e-06	8.64e-13
	78.6[2]	1.85e-05	1.54e-05	3.44e-3	1.90e-2	1.73e-05	4.39e-07	1.16e-06	8.73e-13

Table 6.3 continued.

$M_{\rm ini}$ ($M_\odot$)	$P_{\rm ini}$ (days)	$^{19}F_{\rm ini}$ ($M_\odot$)	^{19}F ($M_\odot$)	$^{22}Ne_{\rm ini}$ ($M_\odot$)	^{22}Ne ($M_\odot$)	^{26}Al ($M_\odot$)	^{36}Cl ($M_\odot$)	^{41}Ca ($M_\odot$)	^{60}Fe ($M_\odot$)
40	0	2.11e-05	7.06e-06	3.93e-3	1.36e-3	1.88e-05	7.99e-11	4.015e-10	6.37e-21
	3.1[1]	2.11e-05	7.13e-06	3.93e-3	1.33e-3	2.20e-06	2.64e-22	4.51e-21	1.56e-39
	7.6[2]	2.11e-05	2.42e-05	3.93e-3	3.72e-2	2.74e-05	9.07e-07	2.30e-06	2.094e-12
	15.8[2]	2.11e-05	2.17e-05	3.93e-3	3.44e-2	2.66e-05	8.81e-07	2.18e-06	2.24e-12
	20.4[2]	2.11e-05	2.19e-05	3.93e-3	3.47e-2	2.64e-05	8.91e-07	2.21e-06	2.20e-12
	32.8[2]	2.11e-05	2.15e-05	3.93e-3	3.44e-2	2.60e-05	8.96e-07	2.19e-06	2.43e-12
	81.7[2]	2.11e-05	1.54e-05	3.93e-3	2.65e-2	2.40e-05	7.81e-07	1.75e-06	2.88e-12
45	0	2.38e-05	7.40e-06	4.42e-3	5.18e-3	2.94e-05	1.45e-07	2.44e-07	3.09e-11
	3.2[1]	2.38e-05	7.41e-06	4.42e-3	1.39e-3	3.43e-06	3.43e-22	9.69e-21	6.7e-40
	7.8[5]	2.38e-05	7.40e-06	4.42e-3	1.41e-3	2.73e-05	9.51e-19	7.77e-18	1.14e-35
	19.5[2]	2.38e-05	2.39e-05	4.42e-3	4.91e-3	3.61e-05	1.4e-06	3.22e-06	5.27e-12
	23.4[2]	2.38e-05	2.36e-05	4.42e-3	4.92e-3	3.59e-05	1.41e-06	3.23e-06	5.31e-12
	42.0[2]	2.38e-05	2.14e-05	4.42e-3	4.64e-3	3.52e-05	1.37e-06	3.08e-06	5.66e-12
	69.9[2]	2.38e-05	1.7e-05	4.42e-3	3.98e-3	3.34e-05	1.27e-06	2.68e-06	6.61e-12
50	0	2.64e-05	7.82e-06	4.91e-3	1.21e-2	4.00e-05	4.18e-07	6.89e-07	6.88e-11
	8.1[2]	2.64e-05	2.56e-05	4.91e-3	6.57e-2	4.9e-05	1.95e-06	4.36e-06	7.90e-12
	14.0[2]	2.64e-05	2.5e-05	4.91e-3	6.83e-2	4.79e-05	2.04e-06	4.56e-06	8.42e-12
	21.7[2]	2.64e-05	2.44e-05	4.91e-3	6.62e-2	4.73e-05	2.01e-06	4.43e-06	9.13e-12
	29.1[2]	2.64e-05	2.32e-05	4.91e-3	6.26e-2	4.71e-05	1.95e-06	4.22e-06	9.83e-12
	72.3[2]	2.64e-05	1.7e-05	4.91e-3	5.21e-2	4.40e-05	1.77e-06	3.54e-06	1.55e-11
	144.6[2]	2.64e-05	1.07e-05	4.91e-3	3.33e-2	4.09e-05	1.26e-06	2.21e-06	2.61e-11

[1] Terminated due to the formation of a common envelope initiated by the primary star
[2] The primary star of this system was uncoupled and further evolved as a single star
[3] This primary star has lost such a significant amount of mass that its final state will be a white dwarf
[4] The final core mass of this star is such that it is a potential electron-capture supernova
[5] This run was terminated before the core collapse due to numerical difficulties.

Chapter 7

Summary, conclusions, and future work

7.1 Summary and conclusions

The summary, conclusions, and part of the future work were presented in Brinkman et al. (2019) and Brinkman et al. (2021).

During their lives and deaths stars turn the lightest elements, hydrogen and helium, into heavier elements, such as carbon and oxygen, the building blocks of life. Many stars have lived and died since the beginning of the Universe, and their nuclear burning products have been ejected into the interstellar medium and incorporated into new generations stars. Eventually, this process led to the formation of the Sun and the Solar System. To understand where the isotopes that formed the Sun and the Solar System come from, here I studied a special group of isotopes; short-lived radio-active isotopes. These are radioactive isotopes with half-lives up to a few Myr, which makes them short-lived compared to the Galaxy and the lifetimes of most stars. Because of their relative short half-lives compared to the age of the Universe and their production in specific processes, these short-lived radioactive isotopes can point us to the sources that polluted the early Solar System. They can provide us information about the environment and circumstances of the birth of the Sun, as they represent the fingerprint of the local nucleosynthesis that occurred nearby at the time and place of the birth of the Sun. Their presence and abundances in the early Solar System have been inferred from meteoretic data reporting excesses in their daughter nuclei. In this work I studied four short-lived radioactive isotopes, and specifically the heating source ^{26}Al with a half life of 0.72 Myr. The other three short-lived radioactive isotopes considered are ^{36}Cl, ^{41}Ca, and ^{60}Fe.

The four short-lived radioactive isotopes are all produced in massive stars and they can be expelled into the interstellar medium by the stellar winds, by mass-transfer between the components of massive binary systems, and by the final explosions of such stars. Massive stars are one of the main contributors to the conversion of elements and the production of these isotopes, because they undergo all burning phases until their cores become made of iron-group elements. At this point, fusion does not generate any more energy to counter the gravitational collapse of the core. The core then contracts further until it turns into

a neutron star. The material outside of the core falls onto the neutron star and bounces back, which is observed as the supernova explosion. If enough material is accreted onto the neutron star, it will turn into a black hole instead of a neutron star. In some other cases, the star will directly turn into a black hole. The outcome of the evolution depends therefore on the initial mass of the star. My work focused on the production of ^{26}Al in massive binaries, and then the production of ^{26}Al, ^{36}Cl, ^{41}Ca, and ^{60}Fe in massive rotating and non-rotating single stars, and the resulting wind yields, and I did not consider the contribution of the supernovae. I also considered the wind yields of the stable isotopes that are part of the CNO-cycle, as well as ^{19}F and ^{22}Ne, for which the astrophysical sources are still uncertain.

For this work, I have used the MESA stellar evolution code with a nuclear network of 63 isotopes for the first part of my research, and of 209 isotopes for the second part, to compute massive (10-80 $M_\odot$), rotating (with initial velocities of 150 and 300 km/s, and non-rotating single stars at solar metallicity (Z=0.014), as well as non-rotating binary stars with initial masses 10-50 $M_\odot$. First, the models were evolved up to the onset of carbon burning to study only ^{26}Al. Then I computed a second set of models to study the four short-lived radioactive isotopes and the stable isotopes, which were evolved to the onset of core collapse. In Chapter 3, I presented the results of the stellar evolution of the different sets of models, and compared them to studies from the literature. In Chapter 4, I presented the wind yields for the various isotopes, discussed the trends in their yields, and again compared them to studies from the literature. In Chapter 5, I discussed the impact of the binary wind yields on the overall galactic budget of ^{26}Al, and how massive stars might be the source of ^{26}Al, ^{41}Ca, and ^{36}Cl in the early Solar System. In Chapter 6, I discussed various uncertainties connected to binary evolution, as well as uncertainties connected to the reaction rates involved in the production and destruction of the short-lived radioactive isotopes. I also presented the first results of binaries evolved up to the onset of core-collapse. In the next part of this section, I briefly repeat the goals of the two parts of my research, as presented in Brinkman et al. (2019) and Brinkman et al. (2021), and the main conclusions from these works.

For the first part of my research, presented in Brinkman et al. (2019), I have computed the ^{26}Al yields from massive non-rotating single and binary stars with the aim of investigating the potential impact of binary interactions on the ^{26}Al yields of massive stars. I compared the results of the single stars with the results of the binary stars and to the results of various other single non-rotating star studies from the literature. I also compared the results of two of the binary systems (with initial primary masses of 20 and 50 $M_\odot$) to the results found by Braun & Langer (1995). The main conclusions of this first part of my research are:

- Primary stars in binary systems give a higher ^{26}Al yield, by up to a factor 100, than

single stars for masses up to 35-40 $M_\odot$, above 45 $M_\odot$ instead, the yields become comparable to, or lower, than the yields found for the single stars.

- My synthetic approach (semi-numerical scheme), where I artificially removed the envelope to simulate binary mass-transfer, provides an upper limit to the ^{26}Al yield, since this method strips away more mass than the fully evolved numerical binaries do and this ejection happens instantaneously in the synthetic scheme instead of gradually over time. The numerical binary yields also represent an upper limit with respect to the use of fully non-conservative mass transfer, where all the mass transferred is lost from the system.

- When considering the effect of binary yields on the total ^{26}Al abundance produced by a stellar population, the preliminary conclusion is that the total ^{26}Al abundance in the Galaxy is still dominated by production during the core-collapse supernovae rather than by the winds.

For the second part of my research, presented in Brinkman et al. (2021), I investigated the production of more stable and radioactive isotopes in the winds of massive rotating stars. The selected short-lived radioactive isotopes of interest for the early Solar System are: ^{26}Al, ^{36}Cl, and ^{41}Ca, while the selected stable isotopes are: ^{19}F and ^{22}Ne. These results have been compared to various studies in the literature. Using the calculated yields, I determined which models could self-consistently explain the early Solar System abundances of ^{26}Al, ^{36}Cl, and ^{41}Ca. The main conclusions are:

- For the short-lived radioactive isotopes, it is mostly the Wolf-Rayet stars in the mass-range 40-80 $M_\odot$ that give significant yields. As expected, the ^{60}Fe yields are always insignificant as compared to the supernova yields, even for the highest initial masses.

- Only my most massive rotating star produces a net positive ^{19}F yield (80 $M_\odot$ for an initial rotation rate of 150 km/s). For ^{22}Ne, more stars give a net positive yield, from masses $\geq$40-45 $M_\odot$, depending on the initial rotational velocity.

- The main effect of rotation is that it lowers the initial mass for which the stars become Wolf-Rayet stars. For ^{26}Al the effect of rotation on the yields is minimal, and only noticeable around the Wolf-Rayet limit. For ^{36}Cl and ^{41}Ca, a higher rotation rate leads to an increase in the yields at lower masses, shifting from $\sim$30 $M_\odot$ to $\sim$20 $M_\odot$. From $\sim$45 $M_\odot$ the yields become again comparable for all models. For the stable isotopes, the rotational mixing leads to lower yields below 50 $M_\odot$ and 35 $M_\odot$ for ^{19}F and ^{22}Ne, respectively.

- Overall, the yields from my models compare well to those from the literature. There are some differences caused by a different prescription of the mass loss and/or a different approach to rotational mixing. This clearly shows that the treatment of stellar winds and the increase of mass-loss due to rotation, as well as the treatment of rotation and rotational mixing, have still a large impact on the yields.

- Depending on their initial rotational velocity, stars with an initial mass of 40-45 $M_\odot$ and higher could explain the ^{26}Al and ^{41}Ca abundances in the early Solar System. However, only the most massive models ($\geq$60 $M_\odot$) can also explain the ^{36}Cl abundances. I remind that also the following core collapse supernovae of massive star models will expel a significant amount of these isotopes, however, they produce an overabundance of ^{60}Fe relatively to its early Solar System value.

- To better match the current recommended isotopic ratios for the three short-lived radioactive isotopes in the early Solar System, more ^{36}Cl and/or less ^{41}Ca is needed. To test this hypothesis, I changed the neutron-capture rates of ^{36}Cl and ^{41}Ca. I conclude that to obtain a better match for all three short-lived radioactive isotopic ratios, a decrease in the amount of ^{41}Ca, derived from increasing its (n,α) reaction rate, has more impact than the increase in the amount of ^{36}Cl, derived from decreasing its (n,p) reaction rate.

- When comparing my models with the oxygen isotopic ratios in Solar System material rich and poor in ^{26}Al, which are known to high precision, I find that the high mass models decrease the oxygen isotopic ratios, ^{17}O/^{16}O and ^{18}O/^{16}O, too much relative to the observations, while the lower mass models stay within the error margins of the measurements.

In conclusion, my work shows that massive stars, and especially massive binary stars, are interesting sites for nucleosynthesis and their yields can contribute to disentangling the sources of short-lived radioactive isotopes in the early Solar System. Future work, see below, will be needed to investigate the impact on galactic chemical evolution.

7.2 Future work

Based on the research presented in this thesis and the conclusions presented above, much work still needs to be done to obtain a full understanding of the yields from massive binary stars, how they impact the galactic chemical evolution, and how they can be sources of the short-lived radioactive isotopes found in the early Solar System. This future work can be separated into different topics: stellar evolution including binary evolution, post-processing of the models, including supernova explosions, nucleosynthesis uncertainties,

and comparison to stardust grains and the early Solar System. For the stellar evolution, both single and binary, future work includes more analysis of:

- the influence of rotation, in both the single and the binary stars, and more specifically the interplay between the increased mass loss from rotation as seen in the models of Set 3 and mass transfer, as this both has an effect on increasing the yields, though the two processes might be competing,
- the influence of metallicity, in both the single and binary stars, to complete the set of models for galactic chemical evolution,
- nycleosynthetic post-processing of the pre-supernova phase such that the yields for all relevant isotopes can be determined for the single stars and the primary stars of the binary systems,
- supernova explosions for the single stars and the primary stars of the binary systems and nucleosynthetic post-processing of the supernova explosions for the full nucleosynthetic yields,
- the influence of the reverse mass-transfer, the mass-transfer efficiency, and different the initial mass ratios,
- the yields for the secondary stars of the binary systems, which includes investigation of whether the binary system survives supernova explosion of the primary star. These models also need to be post-processed for the pre- and post-supernova phase.

The combination of all these models, and specifically having both the pre- and post-supernova yields at all metallicities, for both the single stars and the components of the binary systems, will give a self-consistent set that could be used for galactic chemical evolution and early Solar System predictions.
For the nucleosynthesis, future work includes:

- Testing how the uncertainties in the nuclear reaction rate linked to neutron sources, mainly ^{13}C(α,n)^{16}O and ^{22}Ne(α,n)^{25}Mg, impacts the short-lived radioactive isotopes,
- Continued investigation how the uncertainties in the neutron-capture reactions responsible for the creation and destruction of the short-lived radioactive isotopes impact the yields, and also for other key reactions connected to the production and destruction of the stable isotopes of interest, such as ^{19}F and ^{22}Ne,

- Expanding the nuclear network to 287 isotopes to cover the production of ^{107}Pd, which happens through the s process, the sequence of neutron captures and β-decays that form the isotopes above the iron group, and more specifically the weak s process, which produces the nuclei up to A$\sim$50 and takes place in massive stars.

The results of these future sets of models need to be put into context of the early Solar System and galactic chemical evolution. Also, to input the material from the stars into the early Solar System, the formation of dust around massive stars and massive binary stars needs to be investigated. Finally, a comparison to stardust grains, dust grains that carry the isotopic signature of a single source should also be made, also to the CNO ratios found in the winds of the massive stars, since the sources of the short-lived radioactive isotopes should not impact the ratios of the stable isotopes.

Chapter 8

Összefoglalás, következtetések és további tervek

8.1 Összefoglalás és következtetések

A csillagok életük és haláluk során a legkönnyebb elemeket, azaz hidrogént és héliumot alakítják át nehezebb elemekké - például szénné és oxigénné, azaz az élet építőköveivé is. A Világegyetem kezdete óta számos csillag élt és halt már meg, a nukleáris égéstermékeik pedig a csillagközi anyagba kerültek ki, ahol csillagok új generációiba épültek be. Végül ez a folyamat vezetett a Nap és a Naprendszer kialakulásához. Az izotópok egy speciális csoportját, a rövid életű radioaktív izotópokat tanulmányoztam annak érdekében, hogy megértsük, honnan származnak a Napot és a Naprendszert alkotó izotópok. Ezen speciális izotópok élete a Galaxis és a legtöbb csillag életéhez képest rövid, a felezési idejük néhány millió évig terjed. A Világegyetem korához képest rövid felezési idejük és a különleges folyamatok általi keletkezésük miatt ezen rövid életű radioaktív izotópok segíthetnek rámutatni a korai Naprendszert beszennyező forrásokra. Információt szolgáltathatnak továbbá a Nap születésekor uralkodó környezetről és körülményekről, mivel ezen izotópok a Nap keletkezése idején, annak környezetében történt helyi atomfizikai folyamatok nyomjelzői. A jelenlétükre és az elemgyakoriságukra a korai Naprendszerben olyan meteoritok adataiból következtettek, amelyekben a leányelemeik atommagjainak többletét fedeztek fel. Jelen dolgozatban négy rövid életű radioaktív izotópot tanulmányoztam, különös tekintettel a 0,72 millió év felezési idejű hőforrásra, a ^{26}Al-ra. A másik három tanulmányozott rövid életű radioaktív izotóp a ^{36}Cl, ^{41}Ca és a ^{60}Fe.

Mind a négy rövid életű radioaktív izotóp nagy tömegű csillagokban keletkezik és csillagszél által, nagy tömegű kettőscsillagok közötti tömegátadás során vagy ezen csillagok végső robbanása által jut ki a csillagközi anyagba. A nagytömegű csillagok az elemek előállításának egyik fő hozzájárulói, mivel minden égési fázison keresztülmennek, egészen addig, amíg a magjuk át nem alakul a vas-csoport elemeivé. Ezen a ponton a fúzió már nem termel energiát a mag gravitációs összeomlása ellen. A mag addig folytatja összehúzódását, amíg neutroncsillagá nem válik. A magon kívüli anyag ekkor a neutronc-

sillagra esik rá és visszapattan, amit szupernóva robbanásként figyelünk meg. Amennyiben elég anyag akkretálódik a neutroncsillagra, neutroncsillag helyett fekete lyukká válik. Néhány egyéb esetben a csillag rögtön fekete lyukká válik. A fejlődés kimenetelét tehát a csillag kezdeti tömege határozza meg. Munkám középpontjában a nagytömegű kettőscsillagok ^{26}Al termelése állt, majd a ^{26}Al, ^{36}Cl, ^{41}Ca és ^{60}Fe termelése forgó és nem forgó egyedülálló csillagokban, és az általuk keletkezett csillagszél hozamának vizsgálata, anélkül, hogy figyelembe venném a szupernóvák hozzájárulását. Emellett figyelembe vettem a CNO-ciklusban részt vevő stabil izotópok szél hozamát, valamint a ^{19}F-ét és a ^{22}Ne-ét is, amely izotópok asztrofizikai forrása mindmáig bizonytalan.

Jelen munkában a MESA csillagfejlődési kódot használtam, a kutatásom első felében 63 izotópból álló nukleáris hálózattal, második felében 209 izotóppal nagytömegű (10-80 $M_\odot$), forgó (150 és 300 km/s kezdeti forgási sebességgel bíró) és nem forgó egyedülálló, Nap fémességű (Z=0,014) csillagok, valamint 10-50 $M_\odot$-ű, nem forgó kettőscsillag modellek számítására. Először a modellek fejlődése a szén égető fázisig tartott, csak a ^{26}Al tanulmányozása érdekében. Ezután újabb modelleket futtattam a négy rövid életű radioaktív izotóp és stabil izotópok tanulmányozására, amelyeket a magösszeomlás kezdetéig számítottam. A 3. fejezetben mutattam be a különböző paraméterű modellek fejlődésének eredményét és ezeket összehasonlítottam irodalmi vizsgálatokkal. A 4. fejezetben bemutattam a különböző izotópok szél hozamait, tárgyaltam a hozamok trendjeit és ezeket ismét összehasonlítottam irodalmi vizsgálatokkal. Az 5. fejezetben a kettősök szél hozamának hatását tárgyaltam a ^{26}Al teljes galaktikus hozzájárulására nézve és hogy hogyan lehetnek a nagytömegű csillagok a ^{26}Al, a ^{41}Ca és a ^{36}Cl forrásai a korai Naprendszerben. A 6. fejezetben a kettősök fejlődéséhez, valamint a rövid életű radioaktív izotópok termelésében és megsemmisítésében közreműködő reakciórátákhoz kapcsolódó bizonytalanságokat tárgyaltam. Szintén bemutattam az első eredményeket olyan kettősökről, amelyek a magösszeomlás kezdetéig fejlődtek. Ennek a fejezetben a következő részében röviden megismételtem a kutatásom két részének céljait, melyeket Brinkman et al. (2019) és Brinkman et al. (2021) cikkekben publikáltam, valamint ezen munkák fő következtetéseit. Kutatásom első részében (Brinkman et al. 2019 cikkben bemutatva) nagytömegű, forgó és nem forgó egyedüli és kettőscsillagok ^{26}Al hozamát számoltam ki azzal a céllal, hogy megtudjam, nagytömegű csillagok esetén a kettősök közötti kölcsönhatás milyen lehetséges hatással van a ^{26}Al hozamára. Az egyedüli és kettőscsillagok eredményeit összehasonlítottam egymással, valamint további irodalmi vizsgálatok eredményével forgó és nem forgó csillagok esetére is. Továbbá összehasonlítottam két kettőscsillag rendszer (20 és 50 $M_\odot$ kezdeti tömegű csillagokkal) eredményeit Braun & Langer (1995) eredményeivel. Kutatásom első részének főbb következtetései az alábbiak:

- 35-40 $M_\odot$-ig a kettőscsillag rendszerek fő komponense nagyobb ^{26}Al hozamot ad, akár százszorosat, mint az egyedülálló csillagok; 45 $M_\odot$ felett azonban a kettősök

hozama hasonló mértékű, vagy akár alacsonyabb lesz, mint ami az egyedülálló csillagoknál megfigyelhető.

- A szintetikus megközelítésem (szemi-numerikus séma), ahol mesterségesen eltávolítottam a köpenyt a kettős rendszerben történő tömegátadás szimulálása érdekében, felső határt ad a ^{26}Al hozamra, mivel ez a módszer több tömeget von el a teljesen végig fejlesztett numerikus kettőscsillagok szimulálása esetén, és ez a kidobódás az időbeli fokozatosság helyett a szintetikus sémában azonnal megtörténik. A numerikus kettős hozamok továbbá felső határt jelentenek a teljesen nemkonzervatív tömegátadás használatát figyelembe véve is, ahol a teljes átadott tömeg elveszik a rendszerből.

- A csillagpopulációkban kettőscsillagok által termelt ^{26}Al hozam teljes ^{26}Al elemgyakoriságra vonatkoztatott hatása előzetes következtetéseim szerint az, hogy a Tejútrendszerben található teljes ^{26}Al elemgyakoriságot még mindig inkább a kollapszár szupernóva-robbanás során termelt ^{26}Al dominálja a szél által termelttel szemben.

Kutatásom második felében további stabil és radioaktív izotópok keletkezését vizsgáltam nagytömegű forgó csillagok által kibocsátott csillagszélben. A kiválasztott, korai Naprendszer szempontjából érdekesnek ítél rövid életű radioaktív izotópok a következők: ^{26}Al, ^{36}Cl és ^{41}Ca, míg a stabil izotópok a ^{19}F és a ^{22}Ne. Ezeket az eredményeket számos irodalmi vizsgálattal hasonlítottam össze. Felhasználva a számolt hozamokat meghatároztam, mely modellek magyarázhatják meg önkonzisztens módon a korai Naprendszer ^{26}Al, ^{36}Cl és ^{41}Ca elemgyakoriságait. A fő következtetések a következők:

- A rövid életű radioaktív izotópokra főleg a 40-80 $M_{\odot}$-ű Wolf-Rayet csillagok adnak jelentős hozamot. A várakozásoknak megfelelően a szupernóva hozamokkal összehasonlítva a ^{60}Fe hozamok mindig jelentéktelenek, még a legnagyobb tömegekre is.

- Csak a legnehezebb forgó csillagaim termelnek nettó pozitív ^{19}F hozamot (80 $M_{\odot}$ 150 km/s kezdeti forgási sebességnél). A ^{22}Ne-ra több csillag ad nettó pozitív hozamot 40-45 $M_{\odot}$ felett, a kezdeti forgási sebességüktől függően.

- A forgás fő hatása, hogy csökkenti azt a kezdeti tömeget, ahol a csillagok Wolf-Rayet csillagokká válnak. A ^{26}Al esetében a forgás hatása a hozamokra minimális, és csak a Wolf-Rayet határ környékén észlelhető. A ^{36}Cl és a ^{41}Ca esetében a nagyobb forgási sebesség kisebb tömegek esetén a hozam növekedéséhez vezet, $\sim$30 $M_{\odot}$-ról $\sim$20 $M_{\odot}$-ra tolódva. $\sim$45 $M_{\odot}$ felett a hozamok ismét egymással összevethetőek minden

tömegértékre. A stabil izotópok esetében a forgás okozta keveredés csökkenti a hozamokat, ^{19}F esetén 50 $M_\odot$ alá, míg ^{22}Ne esetén 35 $M_\odot$ alá.

- Összességében a modelljeim által kapott hozamok jó egyezést mutatnak az irodalomban található modellekkel. Néhány eltérés tapasztalható a tömegvesztés eltérő előírása és/vagy a forgási keveredés eltérő megközelítése okán. Ez egyértelműen mutatja, hogy a csillagszél kezelése és a forgás okozta megnövekedett tömegvesztés, valamint a forgás és a forgási keveredés kezelése még mindig nagy befolyással bír a hozamokra.

- A kezdeti forgási sebességtől függően a 40-45 $M_\odot$és nagyobb kezdeti tömegű csillagok megmagyarázhatják a korai Naprendszer ^{26}Al és ^{41}Ca elemgyakoriságait. Azonban csak a legnehezebb ($\geq$60 $M_\odot$) modellek tudják megmagyarázni a ^{36}Cl elemgyakoriságokat is. Emlékeztetőül, a nagy tömegű csillagok modelljeit követő kollapszár szupernóvák ezekből az izotópokból szintén nagy mennyiséget bocsátanak ki, azonban ^{60}Fe-ból többet termelnek annak korai Naprendszer-beli értékénél.

- Ahhoz, hogy jobb egyezést kapjunk a három, rövid életű radioaktív izotóp jelenleg ajánlott, korai Naprendszer-beli izotóparányára, több ^{36}Cl-ra és/vagy kevesebb ^{41}Ca-ra van szükség. Ezen feltételezés tesztelésére megváltoztattam a ^{36}Cl és a ^{41}Ca neutronbefogási rátáit. Eredményül azt kaptam, hogy a mindhárom rövid életű radioaktív izotóparánnyal való jobb egyezés érdekében a ^{41}Ca mennyiség csökkenésének - megnövelt (n,α) reakciórátája által - nagyobb hatása van, mint a ^{36}Cl növelésének, utóbbi csökkentett (n,p) reakciórátája eredményeképp.

- Modelljeimet összehasonlítva a ^{26}Al-ban gazdag és szegény Naprendszer anyagának oxigén izotóp arányaival, melyek nagy pontossággal ismertek, azt találtam, hogy a nagy tömegű modellek túlságosan csökkentik a ^{17}O/^{16}O és a ^{18}O/^{16}O izotóp arányok értékét a megfigyelésekhez képest, míg a kisebb tömegű modellek a megfigyelések hibáinak határán belül maradnak.

8.2 További tervek

A dolgozatban bemutatott kutatás és a fent részletezett következtetések nyomán még mindig sok munka szükséges annak tisztázásához, hogy a nagytömegű kettőscsillag rendszerek hozama hogyan hat a galaktikus kémiai evolúcióra, valamint hogy ezek a csillagok hogyan lehetnek a korai Naprendszerben talált izotópok forrásai. Ez a további munka több különböző témára osztható fel: csillagfejlődés, ezen belül kettőscsillagok fejlődése, és a modellek utófeldolgozása, szupernóva robbanások, a nukleoszintézis bizonytalanságai, és a korai Naprendszer valamint csillagokból származó porszemcsék összehasonlítása. A

csillagfejlődés, mind egyedülálló, mind kettőscsillagokra további vizsgálatokat igényel a következő témákban:

- a forgás hatása mind egyedülálló, mind kettőscsillagokra,
- a fémesség hatása mind egyedülálló, mind kettőscsillagokra,
- a szupernóva előtti fázis teljes izotóphozamának nukleoszintézis utófeldolgozása mind egyedülálló, mind a kettős rendszerek fő csillagára.

Összefoglalásul, a munkámban bemutattam hogy a nagytömegű csillagok, és legfőképp a nagytömegű kettőscsillagok a nukleoszintézis érdekes színterei és hozamuk hozzájárulhat a korai Naprendszerben előforduló rövid életű radioaktív izotópok forrásának azonosításához. A galaktikus kémiai evolúcióra gyakorolt hatásukról további kutatások szükségesek.

Publications

Publications associated with this thesis:
Brinkman, H.E.; den Hartogh, J. W.; Doherty, C. L.; Pignatari, M.; Lugaro, M;, *Aluminium-26 from massive binary stars II.; rotating stars and extended nuclear network*, The Astrophysical Journal, Volume 923, Issue 1, id.47, 14 pp. DOI: 10.3847/1538-4357/ac25ea, IF: 5.874

Brinkman, H. E.; Doherty, C. L.; Pols, O. R.; Li, E. T.; Côté, B.; Lugaro, M., *Aluminium-26 from Massive Binary Stars. I. Nonrotating Models*, The Astrophysical Journal, Volume 884, Issue 1, article id. 38, 19 pp. (2019)., DOI: 10.3847/1538-4357/ab40ae, IF: 5.745

den Hartogh, J. W.; Peto, M.; Lawson, T.; Sieverding, A.; **Brinkman, H. E.**; Pignatari, M.; and Lugaro, M., *Comparison between core-collapse supernova yields and stardust grains: investigating Magnesium, Aluminium, and Chromium*, The Astrophysical Journal, Volume 927, Issue 2, article id. 220, 24 pp. (2022)., DOI: 10.3847/1538-4357/ac4965, IF: 5.874

Conference proceedings:
Brinkman, H. E.; Doherty, C. L.; Li, E. T.; Côté, B.; Lugaro, M.,*Aluminium-26 from Massive Binary Stars*, Nuclei in the Cosmos XV, held 24-29 June, 2018 in L'Aquila, Italy. Edited by A. Formicola, M. Junker, L. Gialanella, G. Imbriani. Springer Proceedings in Physics, Vol. 219, 2019, p.289-292, DOI: 10.1007/978-3-030-13876-9_49

Li, E. T.; Lugaro, M.; **Brinkman, H. E.**; Doherty, C. L.; Côté, B., *The Effects of 26Al Isomeric State on Its Ground State Production*, Nuclei in the Cosmos XV, held 24-29 June, 2018 in L'Aquila, Italy. Edited by A. Formicola, M. Junker, L. Gialanella, G. Imbriani. Springer Proceedings in Physics, Vol. 219, 2019, p.393-396, DOI: 10.1007/978-3-030-13876-9_73

Other publications:
Lugaro, M; Côté, B.; Pignatari, M.; Yagüe López, A.; **Brinkman, H. E.**; Cseh, B.; den Hartogh, J. W.; Doherty, C. L.; Karakas, A. I.; Kobayashi, C.; Lawson, T; Peto, M.; Soós, B.; Trueman, T.; Világos, B. *The RADIOSTAR Project*, Universe 2022, 8, 130. DOI: 10.3390/universe8020130, IF: 2.278

Diehl, R.; Lugaro, M.; Heger, A.; Sieverding, A.; Tang, X.; Li, K. A.; Li, E. T.; Doherty, C. L.; Krause, M. G. H.; Wallner, A.; Prantzos, N.; **Brinkman, H. E.**; den Hartogh, J. W.; and Wehmeyer, B.; Yagüe López, A.; Pleintinger, M. M. M.; and Banerjee, P.; Wang, W., *The Radioactive Nuclei ^{26}Al and ^{60}Fe in the Cosmos and in the Solar System*, Publications of the Astronomical Society of Australia, Volume 38, article id. e062, DOI: 10.1017/pasa.2021.48, IF: 5.571

Submitted works:
Laird, A.; ... **Brinkman, H. E.**; ..., *Nuclear reactions affecting the ^{26}Al abundance in the Galaxy*, submitted to JPhysG

MTMT number: 10066760

Acknowledgements

Here, I want to take the opportunity to thank everyone who has helped me while I was working on my research and my thesis. First of all, I want to thank my supervisor, Dr. Maria Lugaro, for giving me the opportunity to do my PhD, for being my guide into doing scientific research, not only by teaching me how to do research itself, but also by patiently teaching me how to write my research down in a comprehensive way, being supportive and understanding, allowing me a lot of freedom in my research, and introducing me to my now favourite isotope ^{26}Al. I have learned a lot over the past almost five years, and I am very grateful for all the guidance, advice, and patience I have received. I also want to thank Dr. Carolyn Doherty for all her assistance with my research, for the countless hours of planning world domination, but also for being a voice of reason when the stress of doing research and everything surrounding it tended to become too much. And Dr. József Vinkó for helping me navigate the Hungarian PhD system at the University of Szeged, and without whom the road to obtaining my PhD would have been a lot harder, and Dr. Tamás Szalai who helped me with the last steps.
I want to thank all the people at the Konkoly Observatory who have been kind, friendly, and very welcoming. Thank you for all chats in the coffee room or random encounters on the bus to or from work. For not blaming me that I did not learn Hungarian in all the years living here. For listening to me, and giving me advice, or sometimes simply telling me that it is normal to feel the way I feel. I especially want to thank Dr. András Pál for dragging me outside for runs, to help me clear my head, though I still hate running uphill, for all the chats during those runs, ranging from my own research to being taught about radio communication and satellites, and for all the advice given over the years. I want to thank Borbála Cseh for translating the summary of this thesis in Hungarian. I want to thank all the other members of the RADIOSTAR group who made my stay in Hungary a lot of fun, both at work and outside of the Observatory.
Finally, I want to thank Prof. Roland Diehl for all his advice, research related, but also practical. And Prof. George Meynet for his advice at the beginning of my PhD and for hosting me for two weeks in Geneva. And Dr. Marco Pignatari for hosting me in Hull for a week, and then for all advice and kind words here in Budapest. I also extend my thanks to Dr. Onno Pols, for introducing me into the world of research, to stellar modelling, and most importantly to binary stars.
Aside from those who have guided me in my research, I want to thank some people who have been essential to me in the years living in Budapest. I want to thank everyone at St. Columba's Scottish Church for welcoming me in their community. I went there the first Sunday after moving to Budapest and never felt the need to find another church. I especially want to thank Rev. Aaron Stevens, John and Janet Barber, and Jeremy Strangward for being there for me not only during the easy times, but also when things got rough, for being kind, understanding, and patient while helping me back on my feet. I also want to thank everyone attending the Midweek Bible Study for allowing me to speak my mind and help me deepen my faith with discussion and new insights. I want to thank Lucia of Apucome Hurray Coffee, the owner of the tiny coffee shop around the corner of my apartment, who has been a great support during the pandemic, and makes the best caramel lattes in the city.
Last, but definitely not least, I want to thank my parents for supporting me for all this time, during my studies in Nijmegen and during my time away from home pursuing my PhD. I want to thank my siblings for their support, putting up with my stress-levels, and

being there for me even if it is for something as silly as a broken keyboard.

This work is supported by the ERC via CoG-2016 RADIOSTAR (Grant Agreement 724560). I also acknowledge support from "ChETEC" COST Action(CA16117), supported by COST (European Cooperation in Science and Technology). The work in this thesis would not been possible without the MESA stellar evolution code. Therefore, I want to thank the MESA team for making their stellar evolution code publicly available, and especially Bill Paxton for starting the code in the first place and for clarifying pieces of the code, Frank Timmes for his support with the pre-supernova models, Josiah Schwab for his kind words of advice regarding MESA, Zsolt Keszthelyi for his help with implementing the new rotational boost into MESA, and everyone else who has made their inlists and scripts public.

References

Abbott, B. P., Abbott, R., Abbott, T. D., et al. 2016, Physical Review Letters, 116, 061102

—. 2017, Physical Review Letters, 119, 161101

Adams, F. C. 2010, ARA&A, 48, 47

Adsley, P., Battino, U., Best, A., et al. 2021, Phys. Rev. C, 103, 015805

Aerts, C. 2013, in EAS Publications Series, Vol. 64, EAS Publications Series, ed. K. Pavlovski, A. Tkachenko, & G. Torres, 323–330

Aerts, C., Mathis, S., & Rogers, T. M. 2019, ARA&A, 57, 35

Allen, B., Boldeman, J., Musgrove, A. L., & Macklin, R. 1977

Angulo, C., Arnould, M., Rayet, M., et al. 1999, Nuclear Physics A, 656, 3

Arnould, M., Goriely, S., & Meynet, G. 2006, A&A, 453, 653

Arnould, M., Paulus, G., & Meynet, G. 1997, A&A, 321, 452

Asplund, M., Grevesse, N., Sauval, A. J., & Scott, P. 2009, ARA&A, 47, 481

Austin, S. M., West, C., & Heger, A. 2017, ApJLetters, 839, L9

Banerjee, P., Misch, G. W., Ghorui, S. K., & Sun, Y. 2018, Phys. Rev. C, 97, 065807

Basunia, M., & Hurst, A. 2016, Nuclear Data Sheets, 134, 75

Belczynski, K., Klencki, J., Fields, C. E., et al. 2020, A&A, 636, A104

Björklund, R., Sundqvist, J. O., Puls, J., & Najarro, F. 2021, A&A, 648, A36

Böhm-Vitense, E. 1958, ZAp, 46, 108

Braun, H., & Langer, N. 1995, in IAU Symposium, Vol. 163, Wolf-Rayet Stars: Binaries; Colliding Winds; Evolution, ed. K. A. van der Hucht & P. M. Williams, 305

Brinkman, H. E., den Hartog, H., Doherty, C. L., Pignatari, M., & Lugaro, M. 2021, ApJ, 923, 47

Brinkman, H. E., Doherty, C. L., Pols, O. R., et al. 2019, ApJ, 884, 38

Brott, I., de Mink, S. E., Cantiello, M., et al. 2011, A&A, 530, A115

Burbidge, E. M., Burbidge, G. R., Fowler, W. A., & Hoyle, F. 1957, Reviews of Modern Physics, 29, 547

Caughlan, G. R., & Fowler, W. A. 1988, Atomic Data and Nuclear Data Tables, 40, 283

Chieffi, A., & Limongi, M. 2013, ApJ, 764, 21

Claret, A. 2007, A&A, 475, 1019

Claret, A., & Torres, G. 2016, A&A, 592, A15

Conti, P. S. 1975, Memoires of the Societe Royale des Sciences de Liege, 9, 193

Côté, B., Lugaro, M., Reifarth, R., et al. 2019a, ApJ, 878, 156

Côté, B., O'Shea, B. W., Ritter, C., Herwig, F., & Venn, K. A. 2017, ApJ, 835, 128

Côté, B., Yagüe, A., Világos, B., & Lugaro, M. 2019b, ApJ, 887, 213

Cristallo, S., Straniero, O., Gallino, R., et al. 2009, ApJ, 696, 797

Crowther, P. A. 2007, ARA&A, 45, 177

Cyburt, R. H., Amthor, A. M., Ferguson, R., et al. 2010, ApJS, 189, 240

de Jager, C., Nieuwenhuijzen, H., & van der Hucht, K. A. 1988, A&AS, 72, 259

De Marco, O., & Izzard, R. G. 2017, PASA, 34, e001

de Mink, S. E., Pols, O. R., & Hilditch, R. W. 2007, A&A, 467, 1181

de Mink, S. E., Sana, H., Langer, N., Izzard, R. G., & Schneider, F. R. N. 2014, ApJ, 782, 7

de Smet, L., Wagemans, C., Goeminne, G., Heyse, J., & van Gils, J. 2007, Phys. Rev. C, 75, 034617

den Hartogh, J., Petö, M. K., Lawson, T., et al. 2022, ApJ, 927, 220

Diehl, R. 2013, Reports on Progress in Physics, 76, 026301

Diehl, R., Lang, M. G., Martin, P., et al. 2010, A&A, 522, A51

Diehl, R., Lugaro, M., Heger, A., et al. 2021, PASA, 38, e062

Dillmann, I., Heil, M., Käppeler, F., et al. 2006, in American Institute of Physics Conference Series, Vol. 819, Capture Gamma-Ray Spectroscopy and Related Topics, ed. A. Woehr & A. Aprahamian, 123–127

Doherty, C. L., Gil-Pons, P., Siess, L., & Lattanzio, J. C. 2017, PASA, 34, e056

Doherty, C. L., Gil-Pons, P., Siess, L., Lattanzio, J. C., & Lau, H. H. B. 2015, MNRAS, 446, 2599

Dominik, M., Belczynski, K., Fryer, C., et al. 2012, ApJ, 759, 52

Duchêne, G., & Kraus, A. 2013, ARA&A, 51, 269

Dwarkadas, V. V., Dauphas, N., Meyer, B., Boyajian, P., & Bojazi, M. 2017, ApJ, 851, 147

Eggleton, P. P. 1983, ApJ, 268, 368

Ekström, S., Meynet, G., Georgy, C., et al. 2019, in Dwarf Galaxies: From the Deep Universe to the Present, ed. K. B. W. McQuinn & S. Stierwalt, Vol. 344, 153–160

Ekström, S., Georgy, C., Eggenberger, P., et al. 2012, A&A, 537, A146

Eldridge, J. J., & Vink, J. S. 2006, A&A, 452, 295

Endal, A. S., & Sofia, S. 1976, ApJ, 210, 184

Farmer, R., Fields, C. E., Petermann, I., et al. 2016, ApJS, 227, 22

Farmer, R., Laplace, E., de Mink, S. E., & Justham, S. 2021, ApJ, 923, 214

Gaidos, E., Krot, A. N., Williams, J. P., & Raymond, S. N. 2009, ApJ, 696, 1854

Georgy, C. 2012, A&A, 538, L8

Glebbeek, E., Gaburov, E., de Mink, S. E., Pols, O. R., & Portegies Zwart, S. F. 2009, A&A, 497, 255

Götberg, Y., de Mink, S. E., Groh, J. H., et al. 2018, A&A, 615, A78

Gounelle, M., & Meibom, A. 2007, ApJLetters, 664, L123

Gounelle, M., & Meynet, G. 2012, A&A, 545, A4

Gupta, S. S., & Meyer, B. S. 2001, Phys. Rev. C, 64, 025805

Hamann, W. R., & Koesterke, L. 1998, A&A, 335, 1003

Hamann, W.-R., Koesterke, L., & Wessolowski, U. 1995, A&A, 299, 151

Heger, A., Fryer, C. L., Woosley, S. E., Langer, N., & Hartmann, D. H. 2003, ApJ, 591, 288

Heger, A., Langer, N., & Woosley, S. E. 2000, ApJ, 528, 368

Heger, A., Woosley, S. E., Rauscher, T., Hoffman, R. D., & Boyes, M. M. 2002, New A Rev., 46, 463

Heger, A., Woosley, S. E., & Spruit, H. C. 2005, ApJ, 626, 350

Herwig, F. 2000, A&A, 360, 952

—. 2005, ARA&A, 43, 435

Herwig, F., Bloecker, T., Schoenberner, D., & El Eid, M. 1997, A&A, 324, L81

Hunter, I., Brott, I., Lennon, D. J., et al. 2008, ApJLetters, 676, L29

Hurley, J. R., Tout, C. A., & Pols, O. R. 2002, MNRAS, 329, 897

Hut, P. 1981, A&A, 99, 126

Iliadis, C., Buchmann, L., Endt, P. M., Herndl, H., & Wiescher, M. 1996, Phys. Rev. C, 53, 475

Iliadis, C., Champagne, A., Chieffi, A., & Limongi, M. 2011, ApJS, 193, 16

Iliadis, C., Longland, R., Champagne, A. E., & Coc, A. 2010, Nuclear Physics A, 841, 323

Imbriani, G., Costantini, H., Formicola, A., et al. 2005, European Physical Journal A, 25, 455

Ivanova, N., Justham, S., Chen, X., et al. 2013, A&A Rev., 21, 59

Izzard, R. G., Dray, L. M., Karakas, A. I., Lugaro, M., & Tout, C. A. 2006, A&A, 460, 565

Izzard, R. G., Preece, H., Jofre, P., et al. 2018, MNRAS, 473, 2984

Jacobsen, B., Yin, Q.-z., Moynier, F., et al. 2008, Earth and Planetary Science Letters, 272, 353

Jones, S. W., Möller, H., Fryer, C. L., et al. 2019, MNRAS, 485, 4287

Kaeppeler, F., Wiescher, M., Giesen, U., et al. 1994, ApJ, 437, 396

Karakas, A. I., & Lattanzio, J. C. 2014, PASA, 31, e030

Kato, S. 1966, PASJ, 18, 374

Kenny, M., Macklin, R., Halperin, J., et al. 1977

Keszthelyi, Z., Meynet, G., Shultz, M. E., et al. 2020, MNRAS, 493, 518

Kiminki, D. C., & Kobulnicky, H. A. 2012, ApJ, 751, 4

Kippenhahn, R., & Weigert, A. 1967, ZAp, 65, 251

Kobayashi, C., Karakas, A. I., & Lugaro, M. 2020, ApJ, 900, 179

Kobulnicky, H. A., Smullen, R. A., Kiminki, D. C., et al. 2012, ApJ, 756, 50

Kobulnicky, H. A., Kiminki, D. C., Lundquist, M. J., et al. 2014, ApJS, 213, 34

Koehler, P. E., Graff, S. M., O'brien, H. A., Gledenov, Y. M., & Popov, Y. P. 1993, Phys. Rev. C, 47, 2107

Kopal, Z. 1955, Annales d'Astrophysique, 18, 379

Kroupa, P. 2001, MNRAS, 322, 231

Krumholz, M. R. 2015, in Astrophysics and Space Science Library, Vol. 412, Very Massive Stars in the Local Universe, ed. J. S. Vink, 43

Kudritzki, R. P., Pauldrach, A., Puls, J., & Abbott, D. C. 1989, A&A, 219, 205

Lamers, H. J. G. L. M., Maeder, A., Schmutz, W., & Cassinelli, J. P. 1991, ApJ, 368, 538

Lamers, H. J. G. L. M., Snow, T. P., & Lindholm, D. M. 1995, ApJ, 455, 269

Langer, N. 1998, A&A, 329, 551

—. 2012, ARA&A, 50, 107

Langer, N., & Maeder, A. 1995, A&A, 295, 685

Lauterborn, D. 1970, A&A, 7, 150

Lawson, T. V., Pignatari, M., Stancliffe, R. J., et al. 2022, MNRAS, 511, 886

Lee, T., Papanastassiou, D. A., & Wasserburg, G. J. 1977, ApJLetters, 211, L107

Li, Z., Su, J., Li, Y., et al. 2015, Science China Physics, Mechanics, and Astronomy, 58, 82002

Lichtenberg, T., Golabek, G. J., Gerya, T. V., & Meyer, M. R. 2016, Icarus, 274, 350

Limongi, M., & Chieffi, A. 2006, ApJ, 647, 483

—. 2018, ApJS, 237, 13

Liu, M.-C. 2017, Geochim. Cosmochim. Acta, 201, 123

Lodders, K. 2003, ApJ, 591, 1220

Longland, R., Iliadis, C., & Karakas, A. I. 2012, Phys. Rev. C, 85, 065809

Lugaro, M., Ott, U., & Kereszturi, Á. 2018, Progress in Particle and Nuclear Physics, 102, 1

Luu, T.-H., Hin, R. C., Coath, C. D., & Elliott, T. 2019, Earth and Planetary Science Letters, 522, 166

Maeder, A. 2009, Physics, Formation and Evolution of Rotating Stars, doi:10.1007/978-3-540-76949-1

Maeder, A., & Meynet, G. 1994, A&A, 287, 803

—. 2000a, A&A, 361, 159

—. 2000b, ARA&A, 38, 143

Maeder, A., & Zahn, J.-P. 1998, A&A, 334, 1000

Makide, K., Nagashima, K., Krot, A. N., et al. 2011, ApJLetters, 733, L31

Martin, P., Knödlseder, J., Diehl, R., & Meynet, G. 2009, A&A, 506, 703

McKee, C. F., & Ostriker, E. C. 2007, ARA&A, 45, 565

Meynet, G., & Arnould, M. 2000, A&A, 355, 176

Meynet, G., & Maeder, A. 1997, A&A, 321, 465

—. 2005, A&A, 429, 581

Moe, M., & Di Stefano, R. 2017, ApJS, 230, 15

Mohamed, S., & Podsiadlowski, P. 2007, in Astronomical Society of the Pacific Conference Series, Vol. 372, 15th European Workshop on White Dwarfs, ed. R. Napiwotzki & M. R. Burleigh, 397

Mohamed, S., & Podsiadlowski, P. 2012, Baltic Astronomy, 21, 88

Montalbán, J., Miglio, A., Noels, A., et al. 2013, ApJ, 766, 118

Motte, F., Bontemps, S., & Louvet, F. 2018, ARA&A, 56, 41

Murray, N. 2011, ApJ, 729, 133

Nesaraja, C., & McCutchan, E. 2016, Nuclear Data Sheets, 133, 120

Nica, N., Cameron, J., & Singh, J. 2012, Nuclear Data Sheets, 113, 25

Nieuwenhuijzen, H., & de Jager, C. 1990, A&A, 231, 134

Nittler, L. R., O'D. Alexander, C. M., Liu, N., & Wang, J. 2018, ApJLetters, 856, L24

Nugis, T., & Lamers, H. J. G. L. M. 2000, A&A, 360, 227

O'Connor, E., & Ott, C. D. 2011, ApJ, 730, 70

Packet, W. 1981, A&A, 102, 17

Paczynski, B. 1976, in Structure and Evolution of Close Binary Systems, ed. P. Eggleton, S. Mitton, & J. Whelan, Vol. 73, 75

Palacios, A., Arnould, M., & Meynet, G. 2005a, A&A, 443, 243

Palacios, A., Meynet, G., Vuissoz, C., et al. 2005b, A&A, 429, 613

Paxton, B., Bildsten, L., Dotter, A., et al. 2011, ApJS, 192, 3

Paxton, B., Cantiello, M., Arras, P., et al. 2013, ApJS, 208, 4

Paxton, B., Marchant, P., Schwab, J., et al. 2015, ApJS, 220, 15

Paxton, B., Schwab, J., Bauer, E. B., et al. 2018, ApJS, 234, 34

Petrovic, J., Langer, N., Yoon, S.-C., & Heger, A. 2005, A&A, 435, 247

Pignatari, M., Gallino, R., Heil, M., et al. 2010, ApJ, 710, 1557

Pignatari, M., Herwig, F., Hirschi, R., et al. 2016, ApJS, 225, 24

Pinsonneault, M. H., Kawaler, S. D., Sofia, S., & Demarque, P. 1989, ApJ, 338, 424

Podsiadlowski, P., Langer, N., Poelarends, A. J. T., et al. 2004, ApJ, 612, 1044

Poelarends, A. J. T., Wurtz, S., Tarka, J., Cole Adams, L., & Hills, S. T. 2017, ApJ, 850, 197

Pols, O. R., Cote, J., Waters, L. B. F. M., & Heise, J. 1991, A&A, 241, 419

Prialnik, D. 2009, An Introduction to the Theory of Stellar Structure and Evolution

Puls, J., Vink, J. S., & Najarro, F. 2008, A&A Rev., 16, 209

Rauscher, T. 2008, Online code NON-SMOKERWEB,version 5.0w and higher

Rauscher, T., Heger, A., Hoffman, R. D., & Woosley, S. E. 2002, ApJ, 576, 323

Reifarth, R., Fiebiger, S., Göbel, K., et al. 2018, International Journal of Modern Physics A, 33, 1843011

Renzo, M., Ott, C. D., Shore, S. N., & de Mink, S. E. 2017, A&A, 603, A118

Ritter, C., Côté, B., Herwig, F., Navarro, J. F., & Fryer, C. L. 2018a, ApJS, 237, 42

Ritter, C., Herwig, F., Jones, S., et al. 2018b, MNRAS, 480, 538

Robertson, J. W., & Faulkner, D. J. 1972, ApJ, 171, 309

Romano, D., & Matteucci, F. 2003, Memorie della Societa Astronomica Italiana Supplementi, 3, 163

Romano, D., Matteucci, F., Zhang, Z.-Y., Ivison, R. J., & Ventura, P. 2019, MNRAS, 490, 2838

Salaris, M., & Cassisi, S. 2017, Royal Society Open Science, 4, 170192

Sana, H., de Mink, S. E., de Koter, A., et al. 2012a, Science, 337, 444

Sana, H., Dunstall, P. R., Hénault-Brunet, V., et al. 2012b, in Astronomical Society of the Pacific Conference Series, Vol. 465, Proceedings of a Scientific Meeting in Honor of Anthony F. J. Moffat, ed. L. Drissen, C. Robert, N. St-Louis, & A. F. J. Moffat, 284

Sander, A. A. C., & Vink, J. S. 2020, MNRAS, 499, 873

Schaller, G., Schaerer, D., Meynet, G., & Maeder, A. 1992, A&AS, 96, 269

Schneider, F. R. N., Podsiadlowski, P., & Müller, B. 2021, A&A, 645, A5

Schootemeijer, A., Götberg, Y., de Mink, S. E., Gies, D., & Zapartas, E. 2018, A&A, 615, A30

Schootemeijer, A., & Langer, N. 2018, A&A, 611, A75

Schroder, K.-P., Pols, O. R., & Eggleton, P. P. 1997, MNRAS, 285, 696

Sedyshev, P. V., Mohr, P., Beer, H., et al. 1999, Phys. Rev. C, 60, 054613

Sevior, M., Mitchell, L., Tingwell, C., & Sargood, D. 1986, Nuclear Physics A, 454, 128

Shao, Y., & Li, X.-D. 2016, ApJ, 833, 108

Sieverding, A., Martínez-Pinedo, G., Huther, L., Langanke, K., & Heger, A. 2018, ApJ, 865, 143

Smith, N. 2014, ARA&A, 52, 487

Soberman, G. E., Phinney, E. S., & van den Heuvel, E. P. J. 1997, A&A, 327, 620

Stancliffe, R. J., Fossati, L., Passy, J. C., & Schneider, F. R. N. 2015, A&A, 575, A117

Straniero, O., Imbriani, G., Strieder, F., et al. 2013, ApJ, 763, 100

Strieder, F., Rolfs, C., Spitaleri, C., & Corvisiero, P. 2001, Naturwissenschaften, 88, 461

Sukhbold, T., Ertl, T., Woosley, S. E., Brown, J. M., & Janka, H.-T. 2016, ApJ, 821, 38

Talwar, R., Adachi, T., Berg, G. P. A., et al. 2016, Phys. Rev. C, 93, 055803

Tan, J. C., Beltrán, M. T., Caselli, P., et al. 2014, in Protostars and Planets VI, ed. H. Beuther, R. S. Klessen, C. P. Dullemond, & T. Henning, 149

Tang, H., & Dauphas, N. 2012, Earth and Planetary Science Letters, 359, 248

Tang, H., Liu, M.-C., McKeegan, K. D., Tissot, F. L. H., & Dauphas, N. 2017, Geochim. Cosmochim. Acta, 207, 1

Tauris, T. M., Langer, N., & Podsiadlowski, P. 2015, MNRAS, 451, 2123

Trappitsch, R., Boehnke, P., Stephan, T., et al. 2018, ApJLetters, 857, L15

Tur, C., Heger, A., & Austin, S. M. 2010, ApJ, 718, 357

van Loon, J. T., Cioni, M. R. L., Zijlstra, A. A., & Loup, C. 2005, A&A, 438, 273

van Rensbergen, W., de Greve, J. P., Mennekens, N., Jansen, K., & de Loore, C. 2011, A&A, 528, A16

Vink, J. S. 2017, A&A, 607, L8

—. 2021, arXiv e-prints, arXiv:2109.08164

Vink, J. S., de Koter, A., & Lamers, H. J. G. L. M. 1999, A&A, 350, 181

—. 2000, A&A, 362, 295

—. 2001, A&A, 369, 574

von Zeipel, H. 1924, MNRAS, 84, 665

Voss, R., Martin, P., Diehl, R., et al. 2012, A&A, 539, A66

Wang, W., Siegert, T., Dai, Z. G., et al. 2020, ApJ, 889, 169

Wasserburg, G. J., Busso, M., Gallino, R., & Nollett, K. M. 2006, Nucl. Phys. A, 777, 5

Wellstein, S., Langer, N., & Braun, H. 2001, A&A, 369, 939

Woosley, S. E., & Heger, A. 2007, Phys. Rep., 442, 269

Woosley, S. E., Heger, A., & Weaver, T. A. 2002, Reviews of Modern Physics, 74, 1015

Yoon, S. C., Langer, N., & Norman, C. 2006, A&A, 460, 199

Young, E. D. 2014, Earth and Planetary Science Letters, 392, 16

Zahn, J. P. 1977, A&A, 500, 121

Zinnecker, H., & Yorke, H. W. 2007, ARA&A, 45, 481